Contents

List of Figures

List of Tables

Frequently Used Acronyms

AC	Analysis Center
AIUB	Astronomical Institute of the University of Berne, Switzerland
AS	Anti-Spoofing
BKG	Bundesamt für Kartographie und Geodäsie, Federal Agency of Cartography and Geodesy, Frankfurt, Germany
C/A-code	Coarse-Acquisition, Clear-Access,or Civil-Access code (1.023 MHz)
CDDIS	Crustal Dynamics Data Information System, Goddard Space Flight Center, NASA, USA
CHAMP	CHAllenging Minisatellite Payload
CNES	Centre Nationale d'Etudes Spatiale, France
CODE	Center for Orbit Determination in Europe
CONAE	Comisión National de Actividades Espaciales, National Commission on Space Activities, Argentina
DCB	Differential Code Bias
DOP	Dilution Of Precision
DORIS	Doppler Orbitography and Radio positioning Integrated by Satellite
doy	Day of Year
ERP	Earth Rotation Parameter
GFO	GEO Follow On
GFZ	GeoForschungsZentrum, Potsdam, Germany
GLONASS	GLObal NAvigation Satellite System
GOCE	Gravity field and steady-state Ocean Circulation Explorer
GPS	Global Positioning System
GRACE	Gravity Recovery And Climate Experiment
ICESat	Ice, Cloud, and land Elevation Satellite
IGS	International GPS Service
JPL	Jet Propulsion Laboratory, Pasadena, California, USA
LC	Linear Combination
LEO	Low Earth Orbiter
NASA	National Aeronautics and Space Administration, USA
NAVSTAR	NAVigation Satellite Timing and Ranging
ONERA	Office National d'Études et de Recherches Aérospatiales, Toulouse, France
P-code	Precise or Protected code (10.23 MHz)
POD	Precise Orbit Determination
PPN	Parametrized Post-Newtonian
RINEX	Receiver-INdependent EXchange Format
RMS	Root-mean-square (error)

RSO	Rapid Science Orbit
SA	Selective Availability
SLR	Satellite Laser Ranging

1. Introduction

The Global Positioning System (GPS) has been serving as a satellite system for global navigation and positioning for at least twenty years. It is operated by the U.S. Department of Defense and consists of nominally 24 satellites. They are distributed in six orbital planes at an altitude of about 20,000 km above the Earth's surface. The GPS satellites emit coherent microwave signals on two frequencies. A big variety of applications using these signals have been developed during the last twenty years. They range from navigation to highest precision geodetic applications.

A few of the main topics in global geodetic research using the GPS are, e.g., the determination of precise orbit information for the GPS satellites, the establishment of a global reference frame, the determination of high-resolution Earth rotation parameters, and the monitoring of plate motions. GPS data of a global station network are used for most of these applications. This network is part of the International GPS Service (IGS).

The IGS was established by the International Association of Geodesy (IAG) in order to promote international standards for GPS data acquisition and analysis, to deploy and operate a common, comprehensive global GPS tracking network, and to provide GPS orbits of highest achievable accuracy. The IGS is based on the voluntary contribution of a large number of organizations, agencies, and universities.

The Astronomical Institute of the University of Bern (AIUB) in Switzerland contributes to the IGS since its official start in 1994. The institute hosts the Center for Orbit Determination in Europe (CODE), one of eight analysis centers of the IGS. The products delivered to the IGS are computed with the Bernese GPS Software which is developed at the AIUB. The work presented here was developed in this environment of concentrated knowledge of GPS and its application to Earth's science.

Already in the early 1980's GPS receivers were mounted on satellites orbiting in low Earth orbits (up to about 2000 km). They aimed at demonstrating the capability of tracking the GPS signals with receivers on-board low Earth orbiting satellites. LANDSAT 5 (1984) was one of the first satellites carrying a GPS receiver, which tracked, however, only the pseudorange. With the launch of the radar altimeter satellite TOPEX/Poseidon in 1992, the era of GPS receivers delivering data for precise orbit determination of the satellite has begun. Presently several satellites use the GPS data as the primary measurements for precise orbit determination (e.g., CHAMP (launched in 2000), SAC-C (2000), JASON-1 (2001), GRACE A and B (2002), and ICESat (2003)).

Many orbit determination procedures based on the GPS observations were developed since the advent of spaceborne GPS receivers. The large variety of approaches may be divided in two groups. One group deals with the dynamic modeling based on the physical properties of the satellite and its orbit (*dynamic and reduced-dynamic strategies*). These strategies were developed already before GPS data became available for satellites and the models are elaborate. The second group deals with the determination of kinematic positions for the satellite (*kinematic strategies*). These strategies were developed as soon as the GPS as a first continuous tracking system became available for the satellites.

The Low Earth Orbiters (LEOs) nowadays (e.g., CHAMP, SAC-C, JASON-1) are equipped with many different scientific instruments. Some applications of these instruments need precise orbit infor-

mation for the processing of their data. The requirements in quality, latency, and availability of the precise orbit are different. Radar altimetry (TOPEX/Poseidon, JASON-1), e.g., needs a precise knowledge (few centimeters) mainly of the radial component of the orbit. The highest quality of the orbit is important, e.g., for the determination of the Earth gravity field. This is one main purpose of the CHAMP, GRACE, and GOCE missions. The latency of the orbit product is not important for this purpose because the gravity field coefficients are determined in a post-processing mode. A short latency of the orbit is an important requirement for near real-time applications aiming at providing the corresponding product as soon as possible after the measurement (e.g., deriving temperature and pressure profiles from the measurements of GPS limb sounding antennas as input for weather forecasting).

On many LEOs the GPS receiver is not the only instrument available for precise orbit determination. Usually the satellites are equipped with a laser retro-reflector array to allow for SLR (Satellite Laser Ranging) measurements (e.g., TOPEX/Poseidon, CHAMP, JASON-1, GRACE, GOCE). Some satellites are equipped in addition with the DORIS system (TOPEX/Poseidon, JASON-1), which is an orbit determination system based on microwaves developed by the Centre Nationale d'Etudes Spatiale (CNES, France). Such independent measuring systems allow for an independent evaluation of the orbits resulting from the different orbit determination procedures. External quality control in general improves the quality of each procedure.

The goal of this work is the development of efficient methods for precise orbit determination of LEOs using the GPS. The orbits also have to be of a sufficient quality for a big variety of applications.

The focus is on a procedure based on undifferenced observations of the GPS receiver on-board the LEO satellite. A kinematic strategy is underlying the determination of a precise orbit. The kinematic approach provides identical orbital accuracies regardless of the altitude of the satellite, because no dynamic models are used. The accuracy of the kinematic positions is mainly given by the quality of the GPS observations.

In the zero-difference point positioning approach the screening of the LEO GPS observations plays an important role. An elaborate pre-screening procedure was developed here. The options, which may be selected for the pre-screening procedure, have an impact on the kinematically determined orbits. This impact was extensively studied in order to evaluate the optimal options for processing GPS data of different LEO satellites. A reduced-dynamic orbit determination procedure was used and tested in connection with this pre-screening procedure, because a priori information about the orbit of the LEO is needed for the data screening in the kinematic approach. The kinematic and the reduced-dynamic procedures are therefore linked. Kinematic and reduced-dynamic solutions of comparably good quality are achieved using efficient methods.

In Chapter 2, *General Information*, the basic facts of the GPS system, institutions relevant to this work, Low Earth Orbiters (LEOs) carrying a GPS receiver, and different orbit determination strategies for LEOs are discussed.

Chapter 3, *Kinematic Point Positioning on the Zero-difference Level*, develops a kinematic procedure which is based on zero-difference GPS observations. Simulations are performed to evaluate the procedure.

In Chapter 4, *Data Pre-processing*, the screening algorithm used in our kinematic point positioning procedure is introduced.

Chapter 5, *Dynamic and Reduced-dynamic Orbit Modeling*, presents the implementation of the dynamic and reduced-dynamic orbit modeling for LEOs. The options to parametrize a dynamic orbit are explained.

In Chapter 6, *Results and Applications*, the algorithms developed for this work are tested extensively and evaluated using GPS data from the LEO satellites CHAMP and SAC-C. For CHAMP two time inter-

vals in 2001 and in 2002 are used and for SAC-C one in 2002 (the same as for CHAMP). Comparisons with external solutions are performed for the 2001 campaign for CHAMP. Different gravity field models are used for the generation of reduced-dynamic orbits of the two satellites and the impact on the reduced-dynamic orbits is studied. The accelerometer measurements available for CHAMP may be introduced in the reduced-dynamic orbit determination procedure instead of modeling the non-gravitational forces. The impact on the achievable orbit quality is considered, as well. The final section of the chapter uses the tools developed for spaceborne receivers to screen the GPS observations of receivers in a permanent tracking network. The performance of this by-product is remarkable.

Chapter 7, *Summary and Outlook*, summarizes our results and discusses possible future developments and directions of research.

2. General Information

2.1 The Global Positioning System – GPS

The space observation technique used for this work is the microwave technique of the NAVSTAR GPS (NAVigation by Satellite Timing And Ranging Global Positioning System), or shortly GPS, operated by the U.S. Department of Defense. The GPS is a satellite navigation system widely used also for various Earth Sciences applications.

The space segment of the system nominally consists of 24 satellites (21 operational satellites plus three active spares). Currently 29 satellites are active. The satellites are distributed over six orbital planes separated by 60° on the equator. The almost circular orbits are inclined by 55° w.r.t. the equatorial plane and the semi-major axis of the orbits is about 26 500 km. The revolution period is half a sidereal day ($11^{\mathrm{h}}58^{\mathrm{m}}$), which means that for a given observation point on the Earth's surface the satellite constellation repeats itself after one sidereal day ($23^{\mathrm{h}}56^{\mathrm{m}}$). The GPS observation technique is based on the microwave signals emitted by the satellites. The signals are derived from the fundamental frequency ($f_0 = 10.23$ MHz) of the satellites' oscillator. The two carrier frequencies f_1 (wavelength λ =19 cm, $f_1 = 154 \cdot f_0$) and f_2 (λ =24 cm, $f_2 = 120 \cdot f_0$) are modulated with the codes and the navigation message to transmit information such as the readings of the satellite clocks, the orbital parameters, etc. The C/A-code (Coarse-Acquisition, Clear-Access, or Civil-Access) is modulated on the L_1 carrier only. The P-code (Precise or Protected) is modulated on both carriers. There exist two possibilities for limiting the achievable accuracy for civilian users, namely Selective Availability (SA) and Anti-Spoofing (AS).

Selective Availability (SA), the deterioration of the satellite clock frequency (dither), was switched off on May 2, 2000, 4:00 UTC. This fact facilitates the estimation of the satellite clock corrections and they can be better predicted. The zero-difference applications requiring the satellite clock information for processing in particular have taken profit out of this change of policy.

Anti-Spoofing (AS) is a protection against "fake" transmissions by encrypting the P-code to form the Y-code. AS is fully active, but nowadays methods are known to get rid of part of the deteriorating effects.

Pseudorange and carrier phase measurements can be acquired on both frequencies (f_1 and f_2). The pseudorange observation has an accuracy of a few decimeters while the carrier phase is accurate to a few millimeters. In order to relate the phase measurement with the geometric range, an unknown, but integer number of wavelengths has to be estimated in the data processing. The data processing is a complex task and cannot be described in detail here. For a detailed description of the whole GPS satellite system and fundamental processing aspects we refer to, e.g. [*Hofmann-Wellenhof et al.*, 2001; *Springer*, 2000; *Schaer*, 1999]. The basic facts needed in the context of this work will be described and explained in Chapter 3.

2.2 Institutions Relevant to this Work

2.2.1 The International GPS Service

The International GPS Service (IGS) was established by the International Association of Geodesy (IAG) between 1991 and 1993 and began with its official operations in January 1994. The IGS is part of the effort of the international scientific community to promote international standards for GPS data acquisition and analysis, and to deploy and operate a common, comprehensive global GPS tracking network. This was done as a result of the continued growth and diversification of GPS applications.

The IGS is based on the voluntary contributions of a large number of organizations, agencies, and universities. The following products, based on the contributions of eight analysis centers (ACs), are made available by the IGS:

- a set of GPS satellite ephemerides, namely final, rapid, ultra-rapid (started in March 2000), and predicted (terminated in March 2001) ephemerides,
- Earth rotation parameters (ERPs),
- IGS tracking station coordinates and velocities,
- GPS satellite and IGS tracking station clock information,
- station-specific tropospheric zenith path delay estimates (since January 1997), and
- ionosphere maps and other ionosphere products.

In addition, the IGS provides ephemerides of the Russian GLONASS (GLObal Navigation Satellite System) satellites. A detailed description of the IGS products, their accuracy and latency may be found, e.g., in [*Weber and Springer,* 2002] and [*IGSCB,* 2002].

2.2.2 The Center for Orbit Determination in Europe – CODE

The Center for Orbit Determination in Europe (CODE) is one of eight analysis centers of the IGS. It is located at the Astronomical Institute of the University of Berne (AIUB) and is a joint venture of:

- the Federal Office of Topography (swisstopo), Wabern, Switzerland,
- the Federal Agency of Cartography and Geodesy (BKG), Frankfurt, Germany,
- the Institut Géographique National (IGN), Paris, France, and
- the Astronomical Institute of the University of Berne (AIUB), Berne, Switzerland.

All CODE solutions and results for the IGS are produced with the Bernese GPS Software [*Hugentobler et al.,* 2001]. Currently the development version 5.0 of the software is used. This software version is also used for the computations made in the context of this work. The official CODE products delivered to the IGS or the official IGS products are used as input for the data processing, where needed.

For more information about CODE, its involvement in the IGS and the routine data processing we refer, e.g., to [*Schaer,* 1999; *Springer,* 2000; *Hugentobler et al.,* 2002].

2.2.3 The IGS LEO Pilot Project

Many scientific projects are initiated by the IGS. Due to our interest in Low Earth Orbiter (LEO) GPS data processing, we focus merely on the IGS LEO Pilot Project. Due to upcoming LEO missions carrying GPS receivers it was recommended at the *Joint IGS-GFZ-JPL Workshop on Low Earth Orbiter Missions* in March 1999 at the GeoForschungsZentrum (GFZ) Potsdam, Germany, to initiate a pilot project for the use of GPS flight receiver data. In January 2000 the "Call for participation" was issued. The IGS LEO Pilot Project started at the *IGS Pilot Project Meeting*, February 6-8, 2001, GFZ Potsdam, Germany. The goals of the IGS LEO Pilot Project are [*Boomkamp*, 2002]

- to establish and maintain a clear listing of all differences between LEO flight receiver data and terrestrial GPS data,
- to compare GPS orbits, clocks and EOP (Earth Orientation Parameters) as generated by routine IGS operations for cases with and without the inclusion of LEO data in the analysis,
- to develop the capability for combined LEO + GPS data processing at a representative number of Analysis Centers,
- to improve the processing of LEO flight receiver data at points where available processing systems still prevent a positive impact of LEO data on IGS products,
- to compare the IGS troposphere products for cases with and without LEO data, with the aim of analyzing benefits that may be obtained
    1. from LEO-based GPS observables, e.g., difference data for a LEO that passes through the line of sight between a ground station and a GPS satellite,
    2. from the inclusions of other LEO tracking data types, e.g., DORIS (Doppler Orbitography and Radio positioning Integrated by Satellite) or SLR (Satellite Laser Ranging), in simultaneous processing of GPS and LEO satellites,
- to establish and maintain a list of required analysis capabilities for using LEO data in IGS processing,
- to monitor the existing processing capabilities, compare them with the required analysis capabilities, and take steps to correct deficiencies as far as necessary for completion of the Pilot Project analysis, and
- to extrapolate the processing requirements that emerge during the Pilot Project into a set of conditions for operational implementation of LEO data in IGS processing.

The starting phase of the project was problematic because prior to mid 2001 new LEO GPS data were only available from the SAC-C satellite (Section 2.3.5). After the release of the CHAMP (Section 2.3.4) data in June 2001, the Associate Analysis Centers of the LEO Pilot Project could start to process the data based on a CHAMP test campaign of eleven days (20-30 May, 2001, doy 140-150). This test campaign gives to all institutions involved in POD (Precise Orbit Determination) for LEOs the opportunity to compare their results. The summary of this comparison may be found in [*TEST CAMPAIGN*, 2002]. The contributions of the AIUB to the CHAMP test campaign will be described in Section 6.3.

Table 2.1: Summary of LEOs equipped with GPS receivers.

Satellite	Altitude (km)	Inclination (degree)	Launch date
TOPEX/Poseidon	1336	66	10 August 1992
MicroLab-1/GPS/MET	715	70	9 April 1995
GFO	785	108	10 February 1998
ØRSTED	640/850	96.5	23 February 1999
SUNSAT	640/850	96.5	23 February 1999
CHAMP	470-300	87	15 July 2000
SAC-C	702	98	23 November 2000
JASON-1	1336	66	7 December 2001
GRACE	500-300	89	17 March 2002
ICESat	600	94	12 January 2003
GOCE	250-200	∼97	2006

2.3 Low Earth Orbiters Tracking GPS Signals

Satellites in a so-called Low Earth Orbit (LEO) are perfectly suited to be equipped with a tracking system based on GPS signals. As LEOs we understand satellite orbits with a height below 2000 km above the Earth's surface [*Martin et al.*, 2001]. At these altitudes the orbital period varies between less than 90 minutes and two hours. In the Low Earth Orbit the most important non-gravitational force acting on the satellite is the atmospheric drag decreasing, however, rapidly with increasing height. Atmospheric drag depends on the atmospheric density which is in turn governed by, e.g., altitude, solar activity, daytime, season, and geographical longitude and latitude. A large number of satellites can be found in Low Earth Orbits. The Earth observation satellites of the ERS-, SPOT-, and LANDSAT-missions are, e.g., in Low Earth Orbits. The Iridium satellites, a satellite constellation for mobile telephone communication purposes and many scientific missions studying different subjects, e.g., the gravity field or magnetic field of the Earth, are located in the LEO belt, as well.

The era of GPS receivers used for spaceborne applications began in the early 1980's. Initially they were launched into orbit only for demonstration of the concept of satellite tracking with GPS. The first receivers tracked only the pseudorange (e.g., LANDSAT 5 [*Heuberger*, 1984]). The first mission using pseudorange and carrier phase measurements of GPS for orbit determination is the radar altimeter mission TOPEX/Poseidon. Some LEOs carrying a GPS receiver put into orbit since the launch of TOPEX/Poseidon in August, 1992, are summarized in Table 2.1. They are listed in the order of their launch date. The list is not complete, but gives an overview of different LEO missions using GPS. We will describe each satellite briefly which should give an impression of the wide field of science objectives of the different missions. Figures 2.1 to 2.11 give an idea of the physical shape of the satellites. The satellites CHAMP and SAC-C and in particular the performance of their GPS receivers will be described in more detail in Chapters 4 and 6.

2.3.1 TOPEX/Poseidon

TOPEX/Poseidon [*Fu et al.*, 1994] is a joint mission coordinated and operated by NASA (National Aeronautics and Space Administration, USA) and CNES (Centre Nationale d'Etudes Spatiale, France). It was launched on August 10, 1992 and is still in operation today. The main purpose of the mission is to measure the ocean topography using a radar altimeter. In addition to the main radar instruments

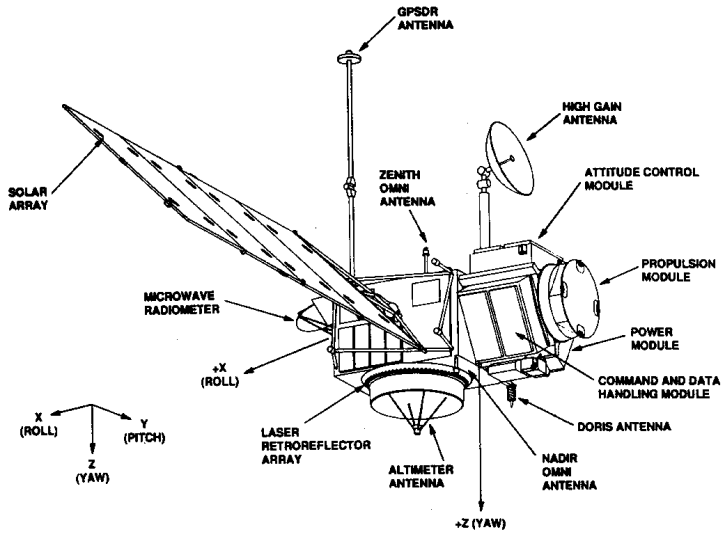

Figure 2.1: TOPEX/Poseidon satellite.

the satellite is equipped with a laser retro-reflector array for SLR measurements, a DORIS receiver, and a GPS Demonstration Receiver (GPSDR). The three latter devices are all used for orbit determination of the TOPEX/Poseidon satellite. The plane of the circular orbit is inclined by $66°$ with respect to the equator and the satellite is orbiting at an altitude of 1336 km. A sketch of TOPEX/Poseidon may be found in Figure 2.1 showing that the GPS antenna is mounted on top of a 4.3 m mast. The GPSDR tracks (only) up to six satellites simultaneously. Unfortunately, due to the receiver construction, it can track both frequencies only during periods when AS is turned off [*Bertiger et al.*, 1994].

2.3.2 MicroLab-1/GPS/MET

The MicroLab-1 satellite is carrying the GPS/MET-receiver. The receiver is part of a proof-of-concept system to generate atmospheric profiles based on observations from GPS satellites occulting at the Earth's atmospheric limb as seen from the satellite. For more details on the technique we refer, e.g., to [*Melbourne et al.*, 1994]. In order to serve the sounding experiment the GPS antenna is placed at the rear side of the satellite. As a result only half of the GPS satellites above the horizon of the satellite can be tracked. The observational geometry for determining the position of the satellite is, therefore, comparatively poor and the resulting orbit is not representative for the potential of GPS POD techniques. The satellite was launched on April 9, 1995. The nearly circular orbit with an inclination of $70°$ has an altitude of about 715 km. Figure 2.2 shows the small MicroLab-1 satellite with the GPS antenna at the rear side. The TurboRogue receiver tracks up to six satellites simultaneously. Data problems occurred during periods, when AS was turned on [*Bertiger and Wu*, 1996].

2.3.3 GFO, ØRSTED and SUNSAT

The satellite GFO (Geosat Follow On) (Figure 2.3, [*GFO*, 2002]) was launched on February 10, 1998, into an orbit with an altitude of 785 km and an inclination of $108°$. It is equipped with instruments for the precise measurement in the domain of both, mesoscale and basin-scale oceanography. The satellite carries a GPS receiver which did, however, never work. The same is unfortunately true for the GPS re-

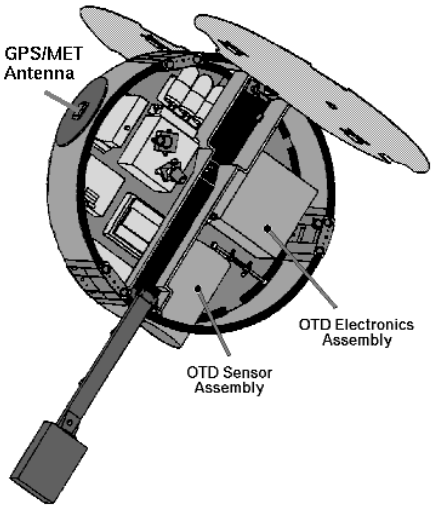

Figure 2.2: MicroLab-1 satellite.

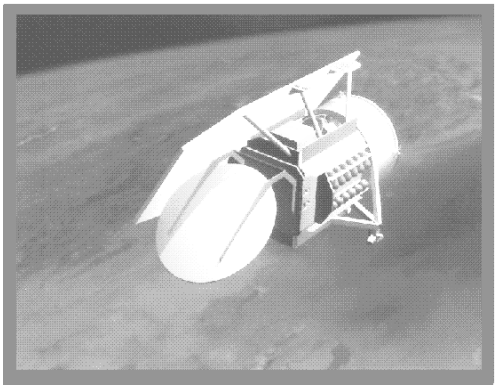

Figure 2.3: GFO satellite.

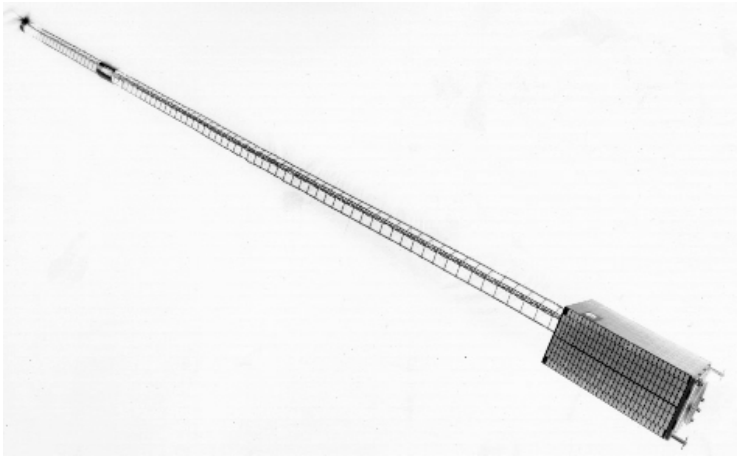

(a) ØRSTED satellite.

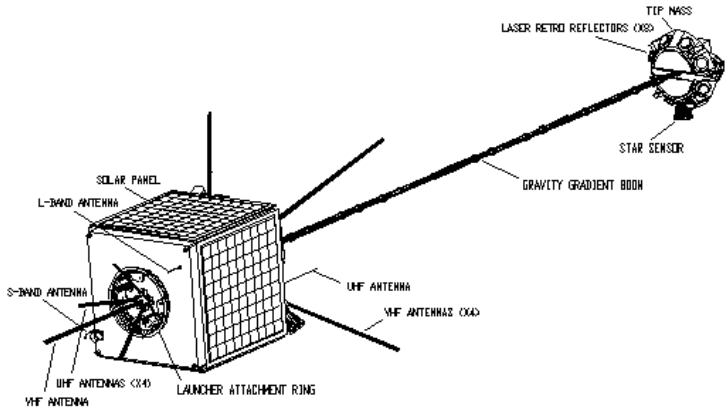

(b) SUNSAT satellite.

Figure 2.4: Two satellites launched together on February 23, 1999.

ceiver on the South African satellite SUNSAT [*SUNSAT*, 2002] launched on February 23, 1999, together with the Danish satellite ØRSTED (Figure 2.4(a), [*ØRSTED*, 2002]). SUNSAT is a micro-satellite developed by graduate students at Stellenbosch University in South Africa. It is shown in Figure 2.4(b). In addition to the TurboRogue GPS receiver and a laser retro-reflector array, the satellite is equipped with a CCD (Charged Couple Device) sensor and two different school experiments which were developed by High School students (see also [*SUNSAT*, 2002]). Unfortunately, the GPS receiver did not work for the entire lifetime of the satellite and on February 1, 2001, the functional life of the satellite was ended. The Danish satellite ØRSTED, launched with the same launch vehicle as SUNSAT, has been developed for studying the magnetic field of the Earth. The GPS receiver on-board ØRSTED is working well but the measurements are not sufficient in quantity and quality to be used for reliable POD.

2.3.4 CHAMP

CHAMP (CHAllenging Minisatellite Payload) ([*Reigber et al.*, 1998] and [*CHAMP*, 2002]) is a German mission under the leadership of the GFZ in Potsdam, Germany. The partners of this satellite project are NASA, CNES and AFRL (Air Force Research Laboratories, USA). The main purpose of the satellite is the study of the Earth's magnetic and gravity fields. In addition to the BlackJack GPS receiver provided by NASA/JPL (Jet Propulsion Laboratory), it carries a STAR accelerometer provided by CNES and manufactured by ONERA (Office National d'Etudes et de Recherches Aérospatiales) in Toulouse, France. The new instrument measures the non-gravitational accelerations acting on the satellite which are mainly due to atmospheric drag, solar radiation pressure, Earth albedo radiation, and attitude maneuvers. The usage of these accelerometer measurements allows it to generate a dynamic orbit of the LEO without modeling the non-gravitational forces which is very helpful for gravity field recovery. A cold gas propulsion system has been employed in order to control the attitude and to perform orbit change maneuvers. The attitude of the spacecraft is not stable over a long time period due to the design of the satellite. The attitude is corrected by thruster pulses of the cold gas propulsion system, which may happen between 70 and 200 times per day. Figures 2.5(a) and 2.5(b) [*CHAMP*, 2002] show the satellite system and its payload.

CHAMP was launched on July 15, 2000. The satellite is orbiting in a nearly circular orbit with an inclination of $87°$. The initial altitude was about 470 km. Within its lifetime it will decay to about 300 km due to atmospheric drag and orbital maneuvers. The actual rate of this decay depends on the solar activity. In Figure 2.6 [*CHAMP*, 2002] the predicted orbital decay is shown as a function of high and low solar activity.

In addition to the GPS receiver, the CHAMP satellite is equipped with a laser retro-reflector array for SLR measurements. The SLR technique is a completely independent technique to determine precise orbits for the LEO. SLR observations are accurate ($\sim$ 1 cm), unambiguous and free of atmospheric propagation effects due to water vapor. This is why the SLR technique is very useful for calibrating the orbit resulting from the GPS tracking.

A detailed description of the instruments important for POD (GPS receiver, laser retro-reflector array, accelerometer instrument, and attitude sensor) may be found in [*Grunwaldt and Meehan*, 2003].

2.3.5 SAC-C

The Earth observation satellite SAC-C was launched on November 23, 2000 [*SAC-C*, 2002]. It is an international cooperative mission with the main responsibility at CONAE (Comisión National de Actividades Espaciales, National Commission on Space Activities), Argentina and NASA, USA. The SAC-C

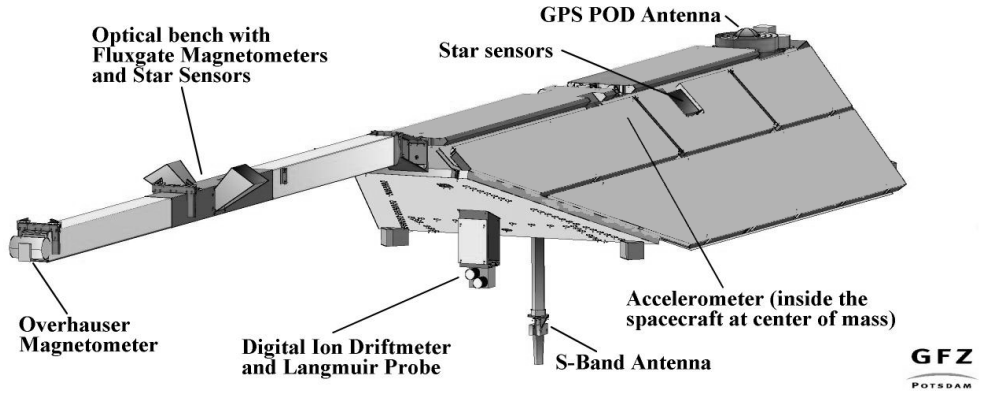

(a) Front.

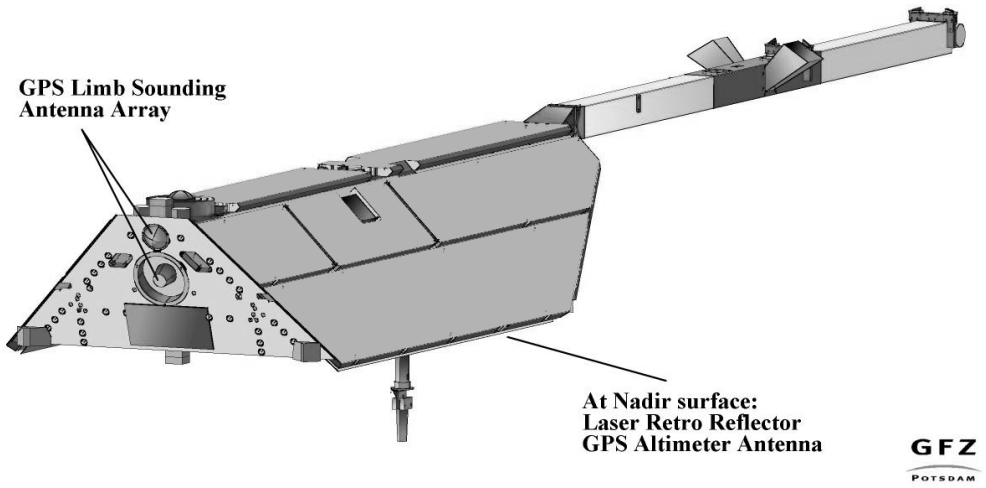

(b) Rear.

Figure 2.5: CHAMP satellite.

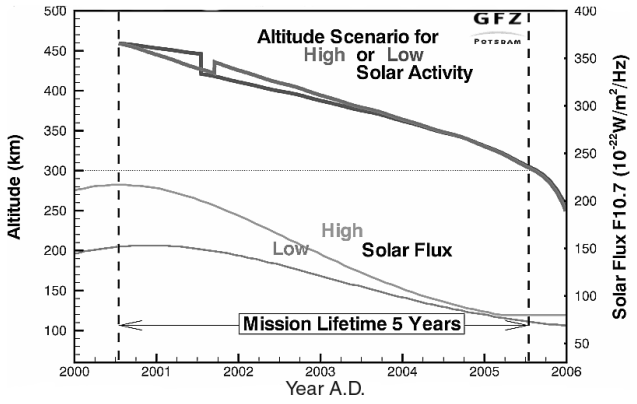

Figure 2.6: Altitude of CHAMP dependent on solar activity.

mission comprises eleven different instruments. The instrument of interest for POD is the BlackJack GPS receiver provided by JPL. In addition, the satellite is equipped with a Lagrange GPS/GLONASS demonstration receiver, which is part of the INES (Italian Navigation Experiment) and should demonstrate the capability of a secondary attitude determination sensor. The BlackJack GPS receiver has four antennas, "looking" into the up, down, fore and aft directions. Therefore, the GPS signals may be used for POD (up), for radio occultations (fore and aft), and for GPS altimetry (down) making use of the GPS signals reflected by the Earth's oceans. Figure 2.7 contains a sketch of the SAC-C satellite. SAC-C is orbiting at an altitude of 702 km and the sun-synchronous orbit has an inclination of $98°$ with respect to the equator. Unfortunately the satellite has no SLR reflector or DORIS receiver, rendering independent comparisons between different POD techniques impossible. The interest of most institutions working in the field of POD for LEOs in SAC-C tracking data is, therefore, limited – despite the facts that the data is of good quality and that the modeling of the orbit is simpler than for CHAMP because of the satellite's orbital height.

2.3.6 JASON-1

JASON-1 [*JASON-1*, 2003], the follow-on mission of TOPEX/Poseidon, is equipped with more or less the same but revised instruments as TOPEX/Poseidon. For JASON-1 the BlackJack GPS receiver is a primary instrument for orbit determination. In addition, the satellite carries, like its predecessor TOPEX/Poseidon, a SLR reflector array and a DORIS receiver. The GPS antenna is placed at the side of the satellite body and is tilted with respect to the axes of the satellite. JASON-1 was launched on December 7, 2001, and is orbiting at an altitude of 1336 km in an almost circular orbit with an inclination of $66°$. Figure 2.8 shows the JASON-1 satellite. The GPS data are available since fall 2002.

2.3.7 GRACE

GRACE (Gravity Recovery And Climate Experiment) [*GRACE*, 2003] may be viewed as the follow-on mission of CHAMP. The mission consists of two satellites orbiting the Earth in the same orbital trajectory following each other in a distance of 220 km $\pm$ 50 km. A K-band link between the two spacecrafts provides a new and independent observation type for mapping the gravity field of the Earth. The satellites were launched on March 17, 2002, and are equipped both, with a BlackJack GPS receiver,

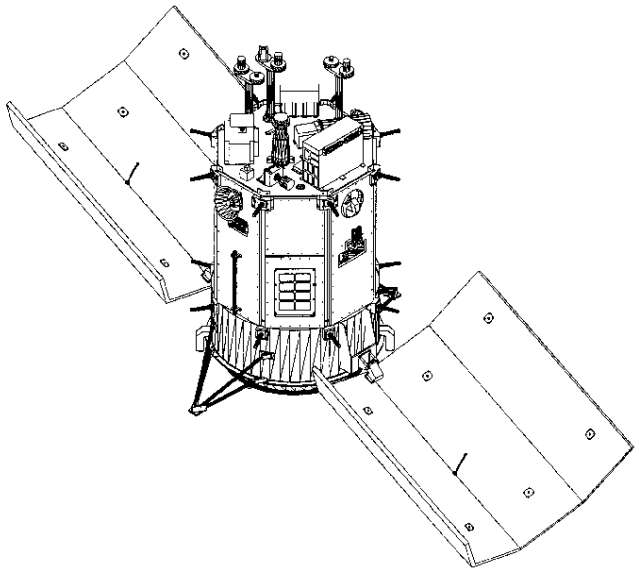

Figure 2.7: SAC-C satellite.

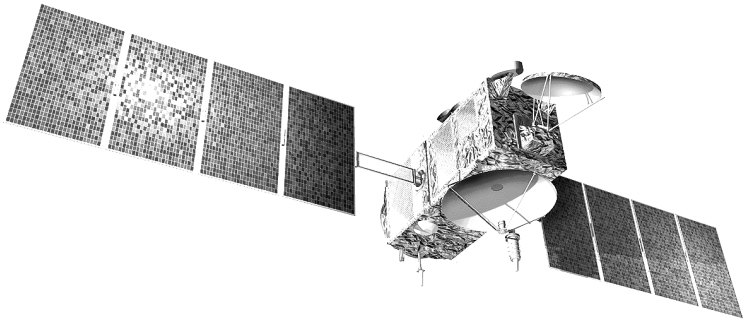

Figure 2.8: JASON-1 satellite.

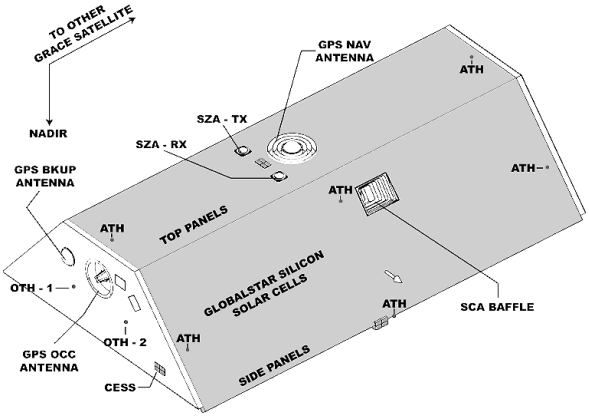

Figure 2.9: GRACE satellite from above.

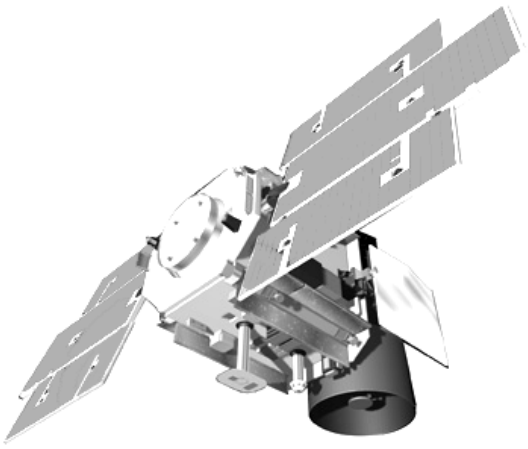

Figure 2.10: ICESat satellite.

with a laser retro-reflector array, and with an accelerometer instrument. The inclination of the orbit is $89°$ and the orbit altitude was initially 500 km. As can be seen in Figure 2.9 the GRACE satellites are similar in construction to the CHAMP satellite (apart from the boom which is not required in the case of the GRACE satellites). The GPS POD antenna is placed in the middle of the satellite body and not at its aft end as in the case of CHAMP. The GPS tracking data of the twin satellites are expected to be available in mid of 2003.

2.3.8 ICESat

The ICESat (Ice, Cloud, and land Elevation Satellite) mission is designed for measuring the mass balance of ice sheets, cloud and aerosol heights, optical densities, vegetation and land topography. The Geoscience Laser Altimeter System (GLAS) and the GPS receiver are the only scientific instruments on board the ICESat spacecraft. The satellite (Figure 2.10, [*ICESAT*, 2002]) was launched on January 12, 2003 into an orbit of 600 km height and an inclination of $94°$. The GPS tracking data will be available in summer 2003.

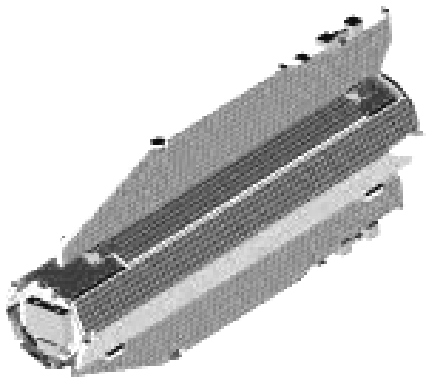

Figure 2.11: GOCE - computer aided drawing.

2.3.9 GOCE

The GOCE (Gravity field and steady-state Ocean Circulation Explorer) mission will be the first Earth Explorer Mission in the Living Planet Programme of the European Space Agency (ESA) [*Visser and Van den IJssel*, 2000; *GOCE*, 2002]. The two key instruments are a three-axis gradiometer and a GPS/GLONASS receiver. The baseline mission duration is 20 months and the reference orbit is a dawn-dusk sun-synchronous orbit at a mean altitude of 250 km during the first half of the mission, and approximately 240 km during the second half [*Battrick*, 1999]. Figure 2.11 shows a computer-aided drawing of the GOCE satellite.

2.4 Precise Orbit Determination for LEOs Using GPS

The LEOs carrying GPS receivers have in general also other scientific instruments on-board. The purpose of the GPS receiver is in most cases to provide data for a precise orbit determination of the LEO. The scientific exploitation of the data of the other instruments often requires precise satellite positions. Having continuous GPS tracking data available for POD is a big advantage over alternative POD methods, where a precise trajectory may be reconstructed only through elaborate orbit models.

Much work was performed in the last decade to develop and evaluate different orbit determination strategies for LEOs using GPS. The approach depends on requirements like precision, latency, and availability. The orbital altitudes of the satellites range between about 300 km and 2000 km, leading to different perturbation characteristics. The orbit determination strategies may be divided into two main groups, the *dynamic* and *reduced-dynamic strategies* on one hand and the *kinematic strategies* on the other hand. The GPS data processing procedures for the LEO are common to both groups. These procedures may be distinguished by their differencing level namely the zero-difference (ZD), double-difference (DD), or triple-difference (TD) level of the original observations. All strategies make direct or indirect use of the GPS ground network, the IGS network. Direct use is made if the observations of the ground stations are used together with the LEO GPS data for the processing (DD and TD). Indirect use is made if the observations of the ground stations are not used for the LEO GPS data processing (ZD), in which case the ground based observations are required to estimate GPS clock corrections. In any case ground station data are required to compute precise GPS satellite orbits.

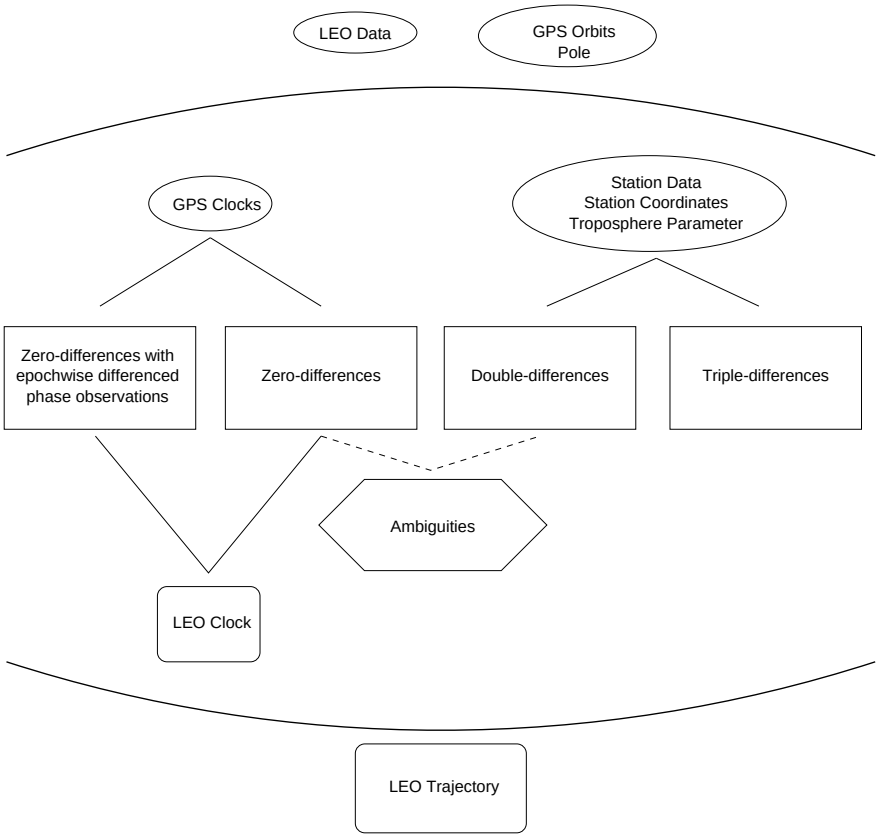

Figure 2.12: Scheme of different processing strategies for LEO GPS data.

The different procedures for the LEO GPS data processing are illustrated by Figure 2.12. All procedures require GPS orbits, Earth rotation information, and LEO GPS data as input for the processing. The GPS orbits and Earth rotation parameters are taken either from the IGS (or one of its analysis centers) or they may be estimated together with the LEO orbit. On the right hand side Figure 2.12 shows the TD and DD approaches requiring GPS data of an array of terrestrial receivers as well as the coordinates and troposphere information of these stations. The two ZD approaches on the left hand side do not need these data, but precise GPS clock corrections at a high sampling rate (30 seconds) are required. In the two approaches in the center of the figure, the well-known ZD and the DD procedures, the ambiguities have to be estimated as real values making the procedures complex and time-consuming. The ZD approach displayed in the leftmost part of Figure 2.12 is the approach developed in this work. Subsequently the two groups of orbit determination strategies are described in more detail.

2.4.1 Dynamic and Reduced-dynamic Strategies

The dynamic and reduced-dynamic orbit determination strategies are the best-known strategies for LEO POD based on GPS tracking data. They are both demonstrated for the first time for TOPEX/Poseidon, see, e.g., [*Bertiger et al.*, 1994], [*Schutz et al.*, 1994]. The principles described in the two references are based on double-differencing the LEO GPS data using GPS data of an array of terrestrial receivers. The parameters for the LEO and for all GPS satellites are then estimated simultaneously. The parameters for the LEO are related to a dynamical orbit model. Some of the recent missions (CHAMP (Section 2.3.4), GRACE (Section 2.3.7)) are equipped with an accelerometer measuring the non-gravitational forces acting on the satellite. Using the measurements of the new instrument type allows it to replace the modeling of the non-gravitational forces by the measurements of the accelerometer. This approach was demonstrated for the first time for CHAMP [*Koenig et al.*, 2001] and is used for GRACE, as well.

Mathematical models of the forces acting on the LEO and mathematical models of the physical properties of the LEO are required for the dynamic and reduced-dynamic strategies. The equation of motion is solved using the technique of numerical integration (see, e.g., [*Beutler*, 2004]). The GPS measurements are represented by a particular orbit which is in turn established by a least squares adjustment with the initial conditions and the dynamical parameters as unknowns. The model errors limit the dynamic strategies. They result in systematic errors growing with the arc length. Introducing empirical parameters, e.g., once-per-revolution parameters or stochastic pulses, in the parameter estimation process allows it to attenuate these errors. This is the key element of the reduced-dynamic strategies. Empirical parameters reduce the influence of possible deficiencies of the dynamical models on the estimated orbit. Lower orbits require more empirical parameters than higher ones because it is virtually impossible to use adequate models for the atmosphere and for the Earth's gravity field (at least initially). The gravity models developed prior to the data of the recent gravity missions CHAMP or GRACE are, e.g., not capable of providing the higher order terms of the gravity field with sufficient precision for low orbits.

Subsequently we will develop a reduced-dynamic strategy for LEO orbit determination to provide, on the one hand, good a priori orbit information for our kinematic point positioning procedure and to generate, on the other hand, reduced-dynamic orbits based on kinematic positions as the best orbit product which is possible with the two procedures developed in this work. In Chapter 5 the particular reduced-dynamic strategy and the algorithms behind it will be explained in more detail.

2.4.2 Kinematic Strategies

Kinematic POD procedures estimate the satellite position for each observation epoch based on the GPS observations only. Kinematic strategies do not need any information concerning the gravity field and other parameters of the dynamical orbit models. The precision of the kinematic positions therefore uniquely depends on the precision of the observations, on the strength of the observation geometry, and on the quality of the GPS orbit and clock products used. The number (and distribution) of the GPS satellites observed simultaneously by the spaceborne receiver is of crucial importance for the accuracy of the kinematic positions. If less than four observations are available per epoch no position can be determined. These missing positions as well as data gaps, e.g., due to receiver resets, lead to interrupts in the trajectory of the LEO which in turn may cause problems when using the kinematic positions as orbit information for an independent analysis of other data of the satellite. This is not the case for a dynamical orbit solution, because this orbit is continuous by construction and has no gaps no matter whether there are data gaps or not.

An example for a kinematic strategy using TD observations may be found, e.g., in [*Grejner-Brzezinska et al.*, 2002] and [*Byun*, 2003]. In [*Svehla and Rothacher*, 2002], e.g., we may find both a ZD and a DD approach including the fixing of ambiguities to integer numbers. The ZD approach which may be found in [*Bisnath and Langley*, 2001] uses filtering techniques for determining the kinematic positions. It is an approach using epoch-differenced phase observations. The kinematic point positioning procedure developed for this work is a ZD approach, as well. Epoch-differenced zero-difference phase observations are used to establish the position-differences between subsequent observation epochs with a conventional least squares adjustment technique. This procedure will be explained in more detail in Chapter 3.

2.5 Data Pre-processing

Pre-processing GPS data is an important issue for all applications. In order to have cleaned data available for the kinematic point positioning approach we have to find a suitable procedure for pre-processing the ZD LEO GPS data. Screening differenced GPS data is much easier because common errors may be removed or greatly reduced by forming the differences. Receiver and satellite clocks are prominent examples. Different procedures are available for screening ZD data of terrestrial stations. One of them is the code smoothing implemented in the program RNXSMT [*Springer*, 2000] of the Bernese GPS Software. At CODE ZD observations of the IGS stations are processed to estimate clock corrections. Screening of ZD observations is currently based on this RNXSMT program. The program MAUPRP will replace it, however, in the near future. The original purpose of the program MAUPRP [*Hugentobler et al.*, 2001] in the Bernese GPS Software is the data screening of phase DD observations. The program is now extended to screen phase ZD observations, as well. It promises to be more reliable than RNXSMT. The ZD screening algorithm in MAUPRP is based on the epoch-differences of the phase observations to individual satellites. Information concerning the GPS orbits and the satellite clock corrections are required for the screening procedure, station coordinates are required as well as a priori information.

The program MAUPRP is also able to pre-process ZD LEO data but we decided to develop a completely new screening algorithm. It is based on a receiver- and epoch-wise cleaning of the data and requires IGS products like orbits and clock corrections, and a priori information about the receiver. We developed this pre-screening algorithm primarily for the data pre-processing of LEO data (Chapter 4). Since the pre-processing works very well for spaceborne receivers its application to the data of ground based receivers was logical. Results for terrestrial receiver data (Section 4.4) are presented and compared

with results of the program MAUPRP (Section 6.7).

3. Kinematic Point Positioning on the Zero-difference Level

3.1 Principles of Processing

As mentioned in Section 2.4.2 a special zero-difference approach was developed for kinematic point positioning of a GPS receiver. Before providing a detailed description of the developed procedure, we have to discuss the requirements and assumptions made.

As a first prerequisite we assume that the GPS orbits and ERPs are known from the IGS or from one of its analysis centers (e.g., CODE). The GPS clock corrections are provided by the IGS, as well, but unfortunately, except of JPL, only with a sampling rate of five minutes. As will be shown in the following sections we need the precise clock corrections every 30 seconds if we want to reach the best possible result with our kinematic point positioning procedure. JPL provides 30-second clock corrections to the IGS (since May 1999). They are not ideal for our application, however, because many epochs are missing. We need clock information for the GPS satellites for each epoch the GPS satellites are observed. To get such continuous 30-seconds clock corrections for the GPS satellites an efficient procedure was developed and described by [*Bock et al.*, 2000] and [*Bock et al.*, 2003]. The procedure is based on the same zero-difference approach as the kinematic point positioning procedure to be explained in this chapter.

Let us first give an overview of the principles of the processing approach in order to get a better understanding of the data flow, the processing steps, and the dependencies between different steps, which will be described in more detail in the following sections. The processing scheme required for the processing of GPS data from a LEO is shown as a flow diagram in Figure 3.1. The approach may be applied to moving receivers such as LEOs, but also to stationary receivers. Subsequently the processing of LEO data is taken as an example because the procedures were initially developed for LEOs and because more complex algorithms are required for the kinematic point positioning of a LEO than for a terrestrial station.

GPS orbits, ERPs and clock corrections are assumed to be known and held fixed in our kinematic solutions. Based on this information the kinematic orbit is determined in an iterative procedure composed of three steps:

- In a first processing step only the code observations of the LEO are used to estimate kinematic positions without knowledge of a priori positions (see Section 3.2.1). The estimated positions have an accuracy of the order of the code observations (i.e. a few meters). They are used as pseudo-observations to determine a reduced-dynamic orbit (see Chapter 5). This reduced-dynamic orbit is then used as a priori orbit for the second step.
- The second processing step consists of a screening procedure using only the code observations of the LEO. A second reduced-dynamic orbit, determined with the resulting positions, is then used as a priori orbit for the third and final step.

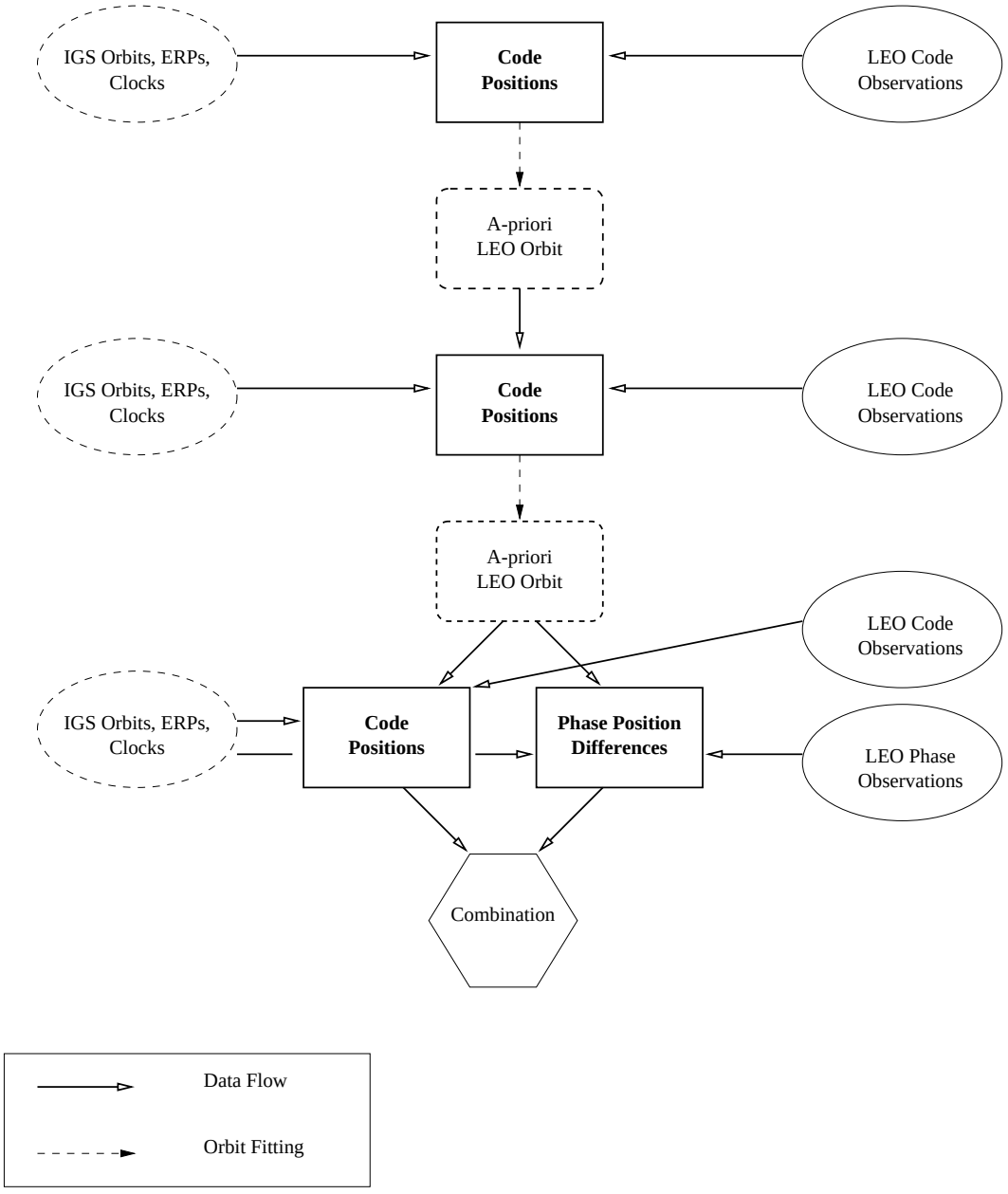

Figure 3.1: Processing scheme for kinematic point positioning of a LEO with GPS data.

- In the third step the phase and the code observations are used. From the phase measurements time-differenced observations are formed to eliminate the phase ambiguities. As a consequence only position-differences can be estimated (see Section 3.3). These position-differences have accuracies corresponding to the accuracy of the phase observations (mm to cm). Positions and position-differences can be combined to precise kinematic positions by an efficient algorithm described in Section 3.4.

The second and third processing step allow for a data screening based on the knowledge of an a priori orbit (see Chapter 4).

An alternative procedure to get a good a priori orbit within two steps is to use phase-difference observations already in the second step of the described procedure. The first a priori orbit is the same but in the second step we produce directly combined positions based on the first a priori orbit. These combined positions may then be used for the generation of a new a priori orbit. This a priori orbit is then used for the third step, the final kinematic positioning of the receiver.

The two different procedures are compared in Chapter 6 and evaluated to find the more efficient and more reliable one for our requirements.

The processing sequence explained by Figure 3.1 is designed for kinematic point positioning of a LEO. In the following sections we will develop the algorithms behind this processing scheme for the code (Section 3.2) and for the phase observations (Section 3.3) in a more general way. The procedure may be well suited for processing GPS observations stemming from any moving object carrying a GPS receiver.

3.2 Code Solution

Let us use the following notation:

j	is the index (superscript) of a particular GPS satellite, $j = 1, \ldots, n_s$, where n_s is the number of satellites observed at one epoch.
m	is the index of the frequency used (m =1, 2).
t	is the signal reception time (in GPS time).
τ^j	is the signal propagation time between satellite j and the receiver.
ϱ^j	is the geometrical distance between satellite j (at signal emission time $t-\tau^j$) and the receiver (at signal reception time t), also called "slant range" $\left\|\boldsymbol{r}^j - \boldsymbol{r}\right\|$.
$\boldsymbol{r}^j(t-\tau^j)$	is the position of the satellite j at signal emission time $t-\tau^j$.
$\boldsymbol{r}(t)$	is the position of the receiver at signal reception time t.
c	is the speed of light.
t'	is the reading of the receiver clock at signal reception time.
δ	is the error of the receiver clock at time t with respect to GPS time. The true signal reception time t may be written as $t = t' - \delta$.
δ^j	is the error of the clock of satellite j at time $t-\tau^j$ w.r.t. GPS time.
δ_r	is the periodic relativistic effect on the receiver due to the eccentricity of its orbit (varying velocity and height in the Earth's potential).
δ_r^j	is the periodic relativistic effect on the GPS satellite j due to the eccentricity of its orbit (varying velocity and height in the Earth's potential).
T^j	is the signal delay due to tropospheric refraction.

I_m^j is the signal delay on carrier m due to ionospheric refraction, $I_1^j = I^j$, $I_2^j = \frac{f_1^2}{f_2^2} I^j$.

The pseudorange between GPS satellite j and the receiver then reads as

$$p_m^j = \varrho^j - c \cdot \delta^j + c \cdot \delta - c \cdot \delta_r^j + c \cdot \delta_r + T^j + I_m^j. \tag{3.1}$$

The above observation equation is written in a very general form. Not all terms in this equation are required to model a particular type of data. The signal delay due to tropospheric refraction T^j, e.g., is not relevant for a spaceborne receiver because the troposphere extends only up to an altitude of about 20 kilometers and the satellite is orbiting well above this height. To process data from a terrestrial receiver we introduce the tropospheric delay, e.g., from an official IGS solution or we model it using a standard model, e.g., the Saastamoinen model. The periodic relativistic effect δ_r, on the other hand, is only relevant for a spaceborne receiver. This relativistic effect for a receiver is due to the varying receiver velocity and height in the Earth's potential as a consequence of the eccentricity of the orbit and is computed according to [*McCarthy*, 1996]

$$\delta_r = \frac{-2 \cdot \boldsymbol{r} \cdot \dot{\boldsymbol{r}}}{c^2}, \qquad \delta_r^j = \frac{-2 \cdot \boldsymbol{r}^j \cdot \dot{\boldsymbol{r}}^j}{c^2}. \tag{3.2}$$

The periodic effect with an amplitude of some 4 nanoseconds (1.3 meters) is small for a typical LEO when compared to the same effect for GPS satellites (50 nanoseconds or 15 meters). Without applying the correction the effect will be absorbed as a periodic signal into the clock correction of the spaceborne receiver. The clock rates of the GPS satellites are offset by $\Delta f/f = -4.4647 \cdot 10^{-10}$[*ICD*, 2000] to compensate for the constant relativistic effects. For spaceborne LEO receivers it is not clear from the data whether the frequency offset is applied to the receiver clock. For a receiver orbiting in a Low Earth Orbit the offset is about $\Delta f/f = \nabla 2.9 \cdot 10^{-10}$.

The terms for the tropospheric delay and the periodic relativistic correction of the receiver clock will be left in the observation equation. Depending on whether spaceborne or terrestrial data are processed, one of the terms is set to zero.

As mentioned already, GPS orbits and ERPs (and, if necessary, the tropospheric delays) are fixed to the official solutions of the IGS or of one of its analysis centers. The official 5-minutes GPS clock corrections are used in a densification step to constrain the 30-seconds clock corrections [*Bock et al.*, 2003]. Apart from the position and the clock correction of the receiver, the delay due to the ionospheric refraction I_m^j is the only remaining unknown in eqn. (3.1). As opposed to the tropospheric refraction, the ionospheric refraction affects the signal received by a spaceborne receiver, because the ionosphere extends to an altitude of 1500 kilometers, well above the orbital altitude of most of the LEOs. The signals received by a LEO are, therefore, delayed due to ionospheric refraction. The absolute delay is not as large as for GPS signals arriving on the Earth's surface but the short-period variations are more pronounced than those caused by the lower regions of the ionosphere [*Schaer*, 1999]. In addition, the high velocity of the LEO (of about 7 km/s) implies more rapid variations of the ionospheric refraction than those observed by a receiver on the Earth's surface. Since the ionospheric refraction is frequency-dependent, the so-called "ionosphere-free" linear combination p^j of the P1- and P2-measurements may be formed using the formula

$$p^j = \frac{1}{f_1^2 - f_2^2} \cdot \left(f_1^2 \cdot p_1^j - f_2^2 \cdot p_2^j \right). \tag{3.3}$$

The resulting observation equation for one code measurement to satellite j then reads as

$$p^j = \varrho^j - c \cdot \delta^j + c \cdot \delta - c \cdot \delta_r^j + c \cdot \delta_r + T^j. \tag{3.4}$$

The unknowns in this equation (3.4) are the three Cartesian coordinates x, y and z of the position vector $\boldsymbol{r}$ and the clock correction δ of the receiver. If more than four GPS satellites are observed simultaneously, we may estimate these parameters using a least squares adjustment for each individual epoch. To this purpose we have to linearize eqn. (3.4) for each satellite j. The linearization is a Taylor series of first order which, using the model function $F(\boldsymbol{x}) = F(x, y, z, c \cdot \delta)$, looks like

$$\begin{aligned} p^j &= F(\boldsymbol{x}) + \frac{\partial F(\boldsymbol{x})}{\partial \boldsymbol{x}} \\ &= \varrho^j + c \cdot \delta - c \cdot \delta^j + c \cdot \delta_r - c \cdot \delta_r^j + T^j \\ &\quad - \frac{x^j - x}{|\boldsymbol{r}^j - \boldsymbol{r}|} \cdot dx - \frac{y^j - y}{|\boldsymbol{r}^j - \boldsymbol{r}|} \cdot dy - \frac{z^j - z}{|\boldsymbol{r}^j - \boldsymbol{r}|} \cdot dz + c \cdot d\delta, \end{aligned} \tag{3.5}$$

with the corrections of the model parameters dx, dy, dz, and $c \cdot d\delta$. We use the following notation:

$\boldsymbol{l}$	is the vector of the observations.
$\boldsymbol{v}$	is the vector of residuals.
$\boldsymbol{A}$	is the first design matrix with the elements $\frac{\partial F(\boldsymbol{x})}{\partial \boldsymbol{x}}\Big\|_{\boldsymbol{x}=\boldsymbol{x_0}}$.
$\boldsymbol{x} = \boldsymbol{x_0} + \boldsymbol{dx}$	is the vector of the unknown model parameters.
$\boldsymbol{dx}$	is the vector with the corrections of the model parameters (i.e., $dx, dy, dz, c \cdot d\delta$).
$\boldsymbol{x_0}$	is the vector with approximate (a priori) model parameters.
$\boldsymbol{l - F(x_0)}$	is the vector with the "observed-minus-computed" terms (O-C).

The scheme for the least squares adjustment may be written as

$$(\boldsymbol{l - F(x_0)}) + \boldsymbol{v} = \boldsymbol{A} \cdot \boldsymbol{dx}. \tag{3.6}$$

The corresponding normal equation (NEQ) system is

$$\boldsymbol{A}^T \boldsymbol{A} \cdot \boldsymbol{dx} = \boldsymbol{A}^T \cdot (\boldsymbol{l - F(x_0)}) \tag{3.7}$$

with

$$\boldsymbol{l} = (p^1, p^2, \ldots, p^{n_s})^T \tag{3.8}$$

$$\boldsymbol{A} = \begin{pmatrix} -(\boldsymbol{e}^1)^T & 1 \\ -(\boldsymbol{e}^2)^T & 1 \\ \ldots & \ldots \\ \ldots & \ldots \\ -(\boldsymbol{e}^{n_s})^T & 1 \end{pmatrix} \tag{3.9}$$

$$\boldsymbol{dx} = (dx, dy, dz, c \cdot d\delta)^T \tag{3.10}$$

$$\begin{aligned} \boldsymbol{F(x_0)} = (& \left|\boldsymbol{r}^1 - \boldsymbol{r_0}\right| + c \cdot \delta_0 - c \cdot \delta^1 + c \cdot \delta_r - c \cdot \delta_r^1 + T^1, \\ & \left|\boldsymbol{r}^2 - \boldsymbol{r_0}\right| + c \cdot \delta_0 - c \cdot \delta^2 + c \cdot \delta_r - c \cdot \delta_r^2 + T^2, \\ & \ldots, \\ & |\boldsymbol{r}^{n_s} - \boldsymbol{r_0}| + c \cdot \delta_0 - c \cdot \delta^{n_s} + c \cdot \delta_r - c \cdot \delta_r^{n_s} + T^{n_s})^T \end{aligned} \tag{3.11}$$

and

$$(\boldsymbol{e}^j)^T = (\frac{x^j - x}{|\boldsymbol{r}^j - \boldsymbol{r}|}, \frac{y^j - y}{|\boldsymbol{r}^j - \boldsymbol{r}|}, \frac{z^j - z}{|\boldsymbol{r}^j - \boldsymbol{r}|}). \tag{3.12}$$

$\boldsymbol{e}^j$ is the unit vector pointing from the receiver at $\boldsymbol{r}(t)$ to satellite j at $\boldsymbol{r}^j(t - \tau^j)$. The specific form of matrix $\boldsymbol{A}$ in column four implies that we are actually introducing $c \cdot \delta$ as parameter (and not the clock correction δ itself). The dimension of matrix $\boldsymbol{A}$ is n_s x 4, where 4 is the number of epoch-specific unknowns ($x, y, z, c \cdot \delta$). Let us furthermore assume that all code observations have the same standard deviation σ_c

$$\begin{aligned} \text{var}(p) &= \sigma_c^2 \\ \boldsymbol{P}_c &= \frac{1}{\sigma_c^2} \cdot \boldsymbol{E}. \end{aligned} \tag{3.13}$$

Matrix $\boldsymbol{E}$ is a unit matrix of dimension n_s x n_s. The weight matrix $\boldsymbol{P}_c$ has the dimension n_s x n_s. From the functional model in eqn. (3.6), the stochastic model in eqn. (3.13), and the O-C terms $\boldsymbol{l} - \boldsymbol{F}(\boldsymbol{x_0}) = \tilde{\boldsymbol{p}}$ (vector with n_s elements) we obtain the final form of the NEQ system for the code positioning procedure for one epoch

$$\boldsymbol{A}^T \boldsymbol{P}_c \boldsymbol{A} \cdot \boldsymbol{dx} = \boldsymbol{A}^T \boldsymbol{P}_c \cdot \tilde{\boldsymbol{p}}. \tag{3.14}$$

$\boldsymbol{A}^T \boldsymbol{P}_c \boldsymbol{A}$ is the NEQ matrix $\boldsymbol{N}$ and the inverse of the NEQ matrix ($\boldsymbol{N}^{-1}$) is the variance-covariance matrix of the estimated parameters.The solution of eqn. (3.14) is an array containing the three coordinates of the position vector and the clock correction of the receiver.

$$\boldsymbol{dx} = \boldsymbol{N}^{-1} \cdot \boldsymbol{A}^T \boldsymbol{P}_c \cdot \tilde{\boldsymbol{p}}. \tag{3.15}$$

The accuracy obtained is limited by the code observations quality (0.5 m to few meters). This point positioning is done independently for each observation epoch. Data screening issues, which are very important for the data processing, will be dealt with in Chapter 4.

3.2.1 Code Point Positioning Without A priori Information

So far we assumed that the position of the receiver is approximately known a priori. When processing the observations of a terrestrial station we may normally assume that a priori coordinates of the station are available. If we process data stemming from a moving object carrying a GPS receiver, e.g., data of a LEO, no a priori information concerning the position of the moving object may be available. Therefore we need an initial run of point positioning (using the code observations), where the a priori position is not needed. For this purpose we use the so-called "Bancroft"- algorithm [*Bancroft*, 1985], explained also in [*Kleusberg and Teunissen*, 1996]. The algorithm is based on squaring the observation equation (3.4). Two solutions of this quadratic equation result for each observation epoch. When using the "Bancroft"-algorithm no data pre-processing can be performed prior to the least squares adjustment. Plausibility checks may make use of the estimated root-mean-square (RMS) error of the code observations a posteriori. It may be, however, that few errors in the code observations are not detected.

The orbit may now be used as a priori orbit for a second point positioning step with the algorithm explained above. Within this second step we may now invoke an efficient data screening to be explained in detail in Chapter 4. The question arises why we have to determine a dynamical orbit using the positions

of the first and second step in order to obtain an a priori orbit instead of taking directly the code positions as a priori information for the code and phase-difference processing. The complicated procedure is necessary because the code positions are affected by outliers and because of the relatively high measurement noise of one to three meters. The accuracy of the positions is not sufficient for pre-processing the phase-differences with the approach developed subsequently. In the case of processing data from another moving receiver, e.g., on an airplane or a car, the code positions have to be smoothed, e.g., by a low-pass filter, before using them as a priori positions for the phase-difference processing.

3.3 Phase-difference Solution

The algorithm for processing the phase observations is in principle the same as that for the code observations. The observation equations of the phase measurement contain, however, in addition the initial phase ambiguity N_m^j as an unknown parameter

$$\phi_m^j = \varrho^j - c \cdot \delta^j + c \cdot \delta - c \cdot \delta_r^j + c \cdot \delta_r + T^j - I_m^j + \lambda_m \cdot N_m^j. \tag{3.16}$$

The ionosphere-free linear combination ϕ^j may be used for the phase observations. The equation for the observation referring to satellite j then reads as

$$\phi^j = \varrho^j - c \cdot \delta^j + c \cdot \delta - c \cdot \delta_r^j + c \cdot \delta_r + T^j + \frac{1}{f_1^2 - f_2^2}(f_1^2 \cdot \lambda_1 \cdot N_1^j - f_2^2 \cdot \lambda_2 \cdot N_2^j). \tag{3.17}$$

The phase ambiguity term may be eliminated by taking the difference of subsequent phase observations. The epoch-difference between epoch i and $i-1$ ($i = 2, \ldots, n$ number of epochs) of the ionosphere-free linear combination of a phase measurement $\Delta\phi_i^j$ from the receiver to satellite j reads as

$$\begin{aligned} \Delta\phi_i^j = \phi_i^j - \phi_{i-1}^j &= \varrho_i^j - \varrho_{i-1}^j - c \cdot (\delta_i^j - \delta_{i-1}^j) + c \cdot (\delta_i - \delta_{i-1}) \\ &\quad - c \cdot (\delta_{r_i}^j - \delta_{r_{i-1}}^j) + c \cdot (\delta_{r_i} - \delta_{r_{i-1}}) + T_i^j - T_{i-1}^j \\ &= \Delta\varrho_i^j - c \cdot \Delta\delta_i^j + c \cdot \Delta\delta_i - c \cdot \Delta\delta_{r_i}^j + c \cdot \Delta\delta_{r_i} + \Delta T_i^j. \end{aligned} \tag{3.18}$$

The phase-difference observations to different GPS satellites are, by construction, independent. We may thus study the stochastic model independently for each satellite. Subsequent phase-difference observations are mathematically correlated because observation ϕ_{i-1}^j is contained in $\Delta\phi_i^j$ and $\Delta\phi_{i-1}^j$. Let the O-C term be $\tilde{\phi}_i^j$ and let us define

$$(\boldsymbol{\Delta}\tilde{\boldsymbol{\phi}}^j)^T \doteq \left(\tilde{\phi}_2^j - \tilde{\phi}_1^j, \tilde{\phi}_3^j - \tilde{\phi}_2^j, \ldots, \tilde{\phi}_n^j - \tilde{\phi}_{n-1}^j\right). \tag{3.19}$$

The vector $\boldsymbol{\Delta}\tilde{\boldsymbol{\phi}}^j$ has $n-1$ elements. Obviously, we may compute the difference observations from the undifferenced ones through the matrix operation

$$\boldsymbol{\Delta}\tilde{\boldsymbol{\phi}}^j = \boldsymbol{C} \cdot \tilde{\boldsymbol{\phi}}^j \tag{3.20}$$

where

$$\boldsymbol{C} = \begin{pmatrix} -1 & 1 & 0 & 0 & \dots & \dots & 0 & 0 \\ 0 & -1 & 1 & 0 & \dots & \dots & 0 & 0 \\ 0 & 0 & -1 & 1 & \dots & \dots & 0 & 0 \\ \dots & \dots & \dots & \dots & \dots & \dots & \dots & \dots \\ \dots & \dots & \dots & \dots & \dots & \dots & \dots & \dots \\ \dots & \dots & \dots & \dots & \dots & \dots & \dots & \dots \\ 0 & 0 & 0 & 0 & \dots & \dots & -1 & 1 \end{pmatrix}. \tag{3.21}$$

Assuming that var$(\phi) = \sigma_\phi^2 \cdot \boldsymbol{E}$, the basic rule to compute the variance-covariance matrix of a linear combination of a random vector says that

$$\text{var}(\boldsymbol{\Delta}\tilde{\boldsymbol{\phi}}^j) = \text{var}(\boldsymbol{\Delta}\boldsymbol{\phi}^j) = \boldsymbol{C} \cdot \text{var}(\phi) \cdot \boldsymbol{C}^T = \sigma_\phi^2 \cdot \boldsymbol{C}\boldsymbol{C}^T \tag{3.22}$$

where

$$\boldsymbol{C}\boldsymbol{C}^T = \begin{pmatrix} 2 & -1 & 0 & 0 & \dots & 0 & 0 \\ -1 & 2 & -1 & 0 & \dots & 0 & 0 \\ 0 & -1 & 2 & -1 & \dots & 0 & 0 \\ \dots & \dots & \dots & \dots & \dots & \dots & \dots \\ \dots & \dots & \dots & \dots & \dots & \dots & \dots \\ \dots & \dots & \dots & \dots & \dots & 2 & -1 \\ 0 & 0 & 0 & 0 & \dots & -1 & 2 \end{pmatrix}. \tag{3.23}$$

Using the standard deviation of the code observable as weight unit, we may compute the weight matrix for the phase-difference array of the observations to one satellite j as follows:

$$\boldsymbol{P}_{\Delta\phi^j} = \frac{\sigma_c^2}{\sigma_\phi^2} \cdot (\boldsymbol{C}\boldsymbol{C}^T)^{-1}. \tag{3.24}$$

The matrix $(\boldsymbol{C}\boldsymbol{C}^T)^{-1}$ has the simple structure

$$(\boldsymbol{C}\boldsymbol{C}^T)^{-1} = \frac{1}{n} \cdot \begin{pmatrix} n-1 & n-2 & \dots & 1 \\ n-2 & 2(n-2) & \dots & 2 \\ n-3 & 2(n-3) & \dots & 3 \\ \dots & \dots & \dots & \dots \\ \dots & \dots & \dots & \dots \\ \dots & \dots & \dots & n-1 \end{pmatrix}. \tag{3.25}$$

This weight matrix has to be symmetric. Its general element is computed as

$$(\boldsymbol{C}\boldsymbol{C}^T)^{-1}_{ik} = \frac{i \cdot (n-k)}{n},\ k \geq i. \tag{3.26}$$

The weight matrix $\boldsymbol{\mathcal{P}}$ for all phase observations and all epochs is a superposition of the matrices $\boldsymbol{P}_{\Delta\phi^j}$ for all satellites $j = 1, 2, \dots, n_s$ with dimension $n_s(n-1)$ x $n_s(n-1)$ and may be written as

$$\boldsymbol{\mathcal{P}} = \frac{\sigma_c^2}{n \cdot \sigma_\phi^2} \cdot \begin{pmatrix} (n-1) \cdot \boldsymbol{E} & (n-2) \cdot \boldsymbol{E} & \dots & 1 \cdot \boldsymbol{E} \\ (n-2) \cdot \boldsymbol{E} & 2(n-2) \cdot \boldsymbol{E} & \dots & 2 \cdot \boldsymbol{E} \\ (n-3) \cdot \boldsymbol{E} & 2(n-3) \cdot \boldsymbol{E} & \dots & 3 \cdot \boldsymbol{E} \\ \dots & \dots & \dots & \dots \\ \dots & \dots & \dots & \dots \\ \dots & \dots & \dots & (n-1) \cdot \boldsymbol{E} \end{pmatrix}. \tag{3.27}$$

For simplicity, we assume that all n_s satellites are observed for all n epochs in which case $\boldsymbol{E}$ above is a unit matrix of dimension n_s x n_s. The realistic case, where this assumption is no longer true, will be handled in Section 3.4.2. The observation equation for the n_s phase-difference observations pertaining to epoch i may be written as

$$-\boldsymbol{A}_{i-1} \cdot \boldsymbol{dx}_{i-1} + \boldsymbol{A}_i \cdot \boldsymbol{dx}_i - (\tilde{\boldsymbol{\phi}}_i - \tilde{\boldsymbol{\phi}}_{i-1}) = \boldsymbol{w}_i, \quad i = 2, \ldots, n, \tag{3.28}$$

where $\boldsymbol{w}_i$ is the array of residuals. The matrices $\boldsymbol{A}_i$ have the same form as the first design matrix in eqn. (3.9) for the code observations. All phase-difference observation equations may then be written in the following convenient matrix form

$$\boldsymbol{\mathcal{A}} \cdot \boldsymbol{dx} - \boldsymbol{\Delta}\tilde{\boldsymbol{\phi}} = \boldsymbol{w} \tag{3.29}$$

with

$$\boldsymbol{\mathcal{A}} = \begin{pmatrix} -\boldsymbol{A}_1 & +\boldsymbol{A}_2 & \boldsymbol{0} & \ldots & \boldsymbol{0} & \boldsymbol{0} \\ \boldsymbol{0} & -\boldsymbol{A}_2 & +\boldsymbol{A}_3 & \ldots & \ldots & \boldsymbol{0} \\ \ldots & \ldots & \ldots & \ldots & \ldots & \ldots \\ \ldots & \ldots & \ldots & \ldots & \ldots & \ldots \\ \ldots & \ldots & \ldots & \ldots & \ldots & \ldots \\ \ldots & \ldots & \ldots & \ldots & -\boldsymbol{A}_{n-1} & +\boldsymbol{A}_n \end{pmatrix}. \tag{3.30}$$

$\boldsymbol{\mathcal{A}}$ has the dimension $n_s \cdot (n-1)$ x $4 \cdot n$, where n is the number of epochs considered. Most of the elements of matrix $\boldsymbol{\mathcal{A}}$ are zero as can be seen in the defining eqn. (3.30). The entire NEQ system for the phase-difference observations then reads as

$$\boldsymbol{\mathcal{A}}^T \boldsymbol{\mathcal{P}} \boldsymbol{\mathcal{A}} \cdot \boldsymbol{dx} = \boldsymbol{\mathcal{A}}^T \boldsymbol{\mathcal{P}} \cdot \boldsymbol{\Delta}\tilde{\boldsymbol{\phi}}. \tag{3.31}$$

Inserting $\boldsymbol{\mathcal{A}}$ from eqn. (3.30) and $\boldsymbol{\mathcal{P}}$ from eqn. (3.27) one may show that

$$\boldsymbol{\mathcal{A}}^T \boldsymbol{\mathcal{P}} \boldsymbol{\mathcal{A}} = \begin{pmatrix} \alpha \cdot \boldsymbol{N}_{11} & \beta \cdot \boldsymbol{N}_{12} & \ldots & \beta \cdot \boldsymbol{N}_{1n} \\ \beta \cdot \boldsymbol{N}_{12}^T & \alpha \cdot \boldsymbol{N}_{22} & \ldots & \beta \cdot \boldsymbol{N}_{2n} \\ \ldots & \ldots & \ldots & \ldots \\ \ldots & \ldots & \ldots & \ldots \\ \ldots & \ldots & \ldots & \ldots \\ \ldots & \ldots & \ldots & \alpha \cdot \boldsymbol{N}_{nn} \end{pmatrix} \tag{3.32}$$

with

$$\begin{aligned} \boldsymbol{N}_{lm} &= \boldsymbol{A}_l^T \boldsymbol{A}_m, \\ & \quad l, m = 1, 2, \ldots, n \\ \alpha &= \frac{\sigma_c^2}{\sigma_\phi^2} \cdot \frac{n-1}{n} \\ \beta &= \frac{\sigma_c^2}{\sigma_\phi^2} \cdot \frac{-1}{n} \end{aligned} \tag{3.33}$$

and

$$\boldsymbol{\mathcal{A}}^T\boldsymbol{\mathcal{P}}\cdot\boldsymbol{\Delta}\tilde{\boldsymbol{\phi}} = \begin{pmatrix} \boldsymbol{b}_1 \\ \boldsymbol{b}_2 \\ \dots \\ \dots \\ \boldsymbol{b}_n \end{pmatrix} \tag{3.34}$$

with

$$\begin{aligned} \boldsymbol{b}_1 &= \sum_{i=1}^{n-1} -\boldsymbol{P}_{1,i}\cdot\boldsymbol{A}_1^T\cdot\boldsymbol{\Delta}\tilde{\boldsymbol{\phi}}_i \\ \boldsymbol{b}_m &= \sum_{i=1}^{n-1}\left[\boldsymbol{P}_{m-1,i}-\boldsymbol{P}_{m,i}\right]\cdot\boldsymbol{A}_m^T\cdot\boldsymbol{\Delta}\tilde{\boldsymbol{\phi}}_i, \\ & \quad m = 2,3,\dots,n-1. \\ \boldsymbol{b}_n &= \sum_{i=1}^{n-1} +\boldsymbol{P}_{n-1,i}\cdot\boldsymbol{A}_n^T\cdot\boldsymbol{\Delta}\tilde{\boldsymbol{\phi}}_i. \end{aligned} \tag{3.35}$$

The $\boldsymbol{P}_{ik}$ matrices are the sub-matrices of matrix $\boldsymbol{\mathcal{P}}$ defined by eqn. (3.27) and are proportional to the unit matrix.

One has to take into account that there is not enough information in the epoch-differenced phase observations to reconstruct the trajectory or positions of the receiver. For n epochs there are $4\cdot n$ unknown parameters and $n_s\cdot(n-1)$ observations. Assuming one measurement per 30 seconds result in 2880 epochs per day. Assuming furthermore that eight satellites are observed simultaneously (for each epoch), we obtain $4\cdot 2880$ unknown parameters and $8\cdot 2879$ observations. Theoretically, there are more than enough observations to estimate the parameters. We estimate, however, only position-differences and have, therefore, no information available about the absolute position of the receiver. The NEQ system is therefore singular. We have to add at least one initial position to make the system regular. A better option is to add the corresponding code observations to make the parameter estimation procedure regular. This is done by a combination of the results associated with the two different measurement types.

3.4 Combination of Code and Phase

According to the assumptions made we have n independent code point positioning solutions corresponding to the n epochs. To simplify the equations we may use σ_c as weight unit which is the reason why in the following no weight matrices will show up in the NEQ system associated with the code observations. Formally, we may write all our epoch-wise code solutions into one NEQ system (eqn. (3.14))

$$\boldsymbol{\mathcal{A}}^T\boldsymbol{\mathcal{A}}\cdot\boldsymbol{dx} = \boldsymbol{\mathcal{A}}^T\cdot\tilde{\boldsymbol{p}} \tag{3.36}$$

where

$$\boldsymbol{\mathcal{A}}^T\boldsymbol{\mathcal{A}} = \begin{pmatrix} \boldsymbol{A}_1^T\boldsymbol{A}_1 & \boldsymbol{0} & \dots & \boldsymbol{0} \\ \boldsymbol{0} & \boldsymbol{A}_2^T\boldsymbol{A}_2 & \dots & \boldsymbol{0} \\ \dots & \dots & \dots & \dots \\ \dots & \dots & \dots & \dots \\ \dots & \dots & \dots & \dots \\ \boldsymbol{0} & \boldsymbol{0} & \dots & \boldsymbol{A}_n^T\boldsymbol{A}_n \end{pmatrix}. \tag{3.37}$$

The dimension of the entire system is $4 \cdot n$ x $4 \cdot n$. From the construction of this NEQ system we know that it is actually broken up into n independent systems of dimension four.

The NEQ system containing the code and phase-difference observations to all satellites – assuming exactly identical observation scenarios for code and phase measurements, e.g. no cycle slips – eventually results by adding the (block diagonal) code NEQ system (3.36) to the superposition of all phase-difference contributions (3.31). The resulting NEQ matrix assumes the form:

$$\boldsymbol{\mathcal{N}} = \begin{pmatrix} (\alpha+1) \cdot \boldsymbol{N}_{11} & \beta \cdot \boldsymbol{N}_{12} & \dots & \beta \cdot \boldsymbol{N}_{1n} \\ \beta \cdot \boldsymbol{N}_{12}^T & (\alpha+1) \cdot \boldsymbol{N}_{22} & \dots & \beta \cdot \boldsymbol{N}_{2n} \\ \dots & \dots & \dots & \dots \\ \dots & \dots & \dots & \dots \\ \dots & \dots & \dots & \dots \\ \dots & \dots & \dots & (\alpha+1) \cdot \boldsymbol{N}_{nn} \end{pmatrix}. \tag{3.38}$$

In view of the structure (eqns. (3.32) and (3.33)) of the phase-difference contributions, and in view of the actual definition of the original first design matrix in eqn. (3.9) we may safely state that the off-diagonal blocks in the resulting NEQ are small in absolute value when compared to the diagonal terms, as long as the number n of epochs without cycle slips is "big" which makes the factors β small w.r.t. α (see eqn. (3.33)). This fact allows it to come up with a good approximation of the correct solution.

Let us write the structure of the correct NEQ system including all code and phase-difference observations in the following symbolic way:

$$\boldsymbol{\mathcal{N}} \cdot \boldsymbol{dx} = \boldsymbol{b} \tag{3.39}$$

where

$$\boldsymbol{\mathcal{N}} = \boldsymbol{\mathcal{N}}_0 + \delta\boldsymbol{\mathcal{N}}. \tag{3.40}$$

$\boldsymbol{\mathcal{N}}_0$ contains only the 4×4 diagonal blocks of type $\boldsymbol{A}_i^T \boldsymbol{A}_i$. It can thus be said that $\boldsymbol{\mathcal{N}}_0$ can easily be inverted step by step, one step corresponding to one epoch. We will further address this problem in Section 3.4.3, where we discuss an approximate solution of eqn. (3.39). In Sections 3.4.1, 3.4.2, and 3.4.3 we develop algorithms to combine code observations and phase-difference observations with increasing levels of statistical correctness.

3.4.1 Neglecting the Correlations

Although it is not correct from the statistical point of view to disregard the mathematical correlations between subsequent phase-difference observations, it is nevertheless instructive to develop the resulting NEQ contribution from the observations based on this assumption. Moreover, and often this is a sufficient justification, the resulting structure of the NEQ system becomes comparatively simple, allowing for a straight-forward and efficient solution. We consider this approach as a *zero-order approximation*, which is also useful for the development of the correct solution.

We thus assume in this subsection that the weight matrix associated with the phase-differences is not given by eqn. (3.24) for all n_s satellites per epoch, but rather by

$$\boldsymbol{\mathcal{P}} = \frac{\sigma_c^2}{2 \cdot \sigma_\phi^2} \cdot \boldsymbol{E} \tag{3.41}$$

where $\boldsymbol{E}$ is the unit matrix. The factor of two results because of the difference of two independent phase observations with variance σ_ϕ^2.

Obviously, the contributions of the phase-differences to the resulting NEQ system formally are identical with eqn. (3.31), with the understanding, however, that the weight matrix is given by the relation in eqn. (3.41). The right hand side of the resulting NEQ system is given by

$$\begin{array}{rcll} \boldsymbol{b}_1 & = & \boldsymbol{A}_1^T \cdot \tilde{\boldsymbol{p}}_1 - \frac{\sigma_c^2}{2 \cdot \sigma_\phi^2} \cdot \boldsymbol{A}_1^T \cdot \boldsymbol{\Delta}\tilde{\boldsymbol{\phi}}_1 & \\ \boldsymbol{b}_l & = & \boldsymbol{A}_l^T \cdot \tilde{\boldsymbol{p}}_l + \frac{\sigma_c^2}{2 \cdot \sigma_\phi^2} \cdot \boldsymbol{A}_l^T \cdot \left(\boldsymbol{\Delta}\tilde{\boldsymbol{\phi}}_{l-1} - \boldsymbol{\Delta}\tilde{\boldsymbol{\phi}}_l \right), & \\ & & l = 2, 3, \ldots, n-1 & \\ \boldsymbol{b}_n & = & \boldsymbol{A}_n^T \cdot \tilde{\boldsymbol{p}}_n + \frac{\sigma_c^2}{2 \cdot \sigma_\phi^2} \cdot \boldsymbol{A}_n^T \cdot \boldsymbol{\Delta}\tilde{\boldsymbol{\phi}}_{n-1}. & \end{array} \tag{3.42}$$

The matrix of the NEQ system is slightly different from the form in eqn. (3.38):

$$\boldsymbol{\mathcal{A}}^T \boldsymbol{\mathcal{P}} \boldsymbol{\mathcal{A}} = \begin{pmatrix} (\gamma+1) \cdot \boldsymbol{N}_{11} & -\gamma \cdot \boldsymbol{N}_{12} & \boldsymbol{0} & \ldots & \boldsymbol{0} \\ -\gamma \cdot \boldsymbol{N}_{12}^T & (2\gamma+1) \cdot \boldsymbol{N}_{22} & \ldots & \ldots & \boldsymbol{0} \\ \boldsymbol{0} & -\gamma \cdot \boldsymbol{N}_{23}^T & \ldots & \ldots & \boldsymbol{0} \\ \boldsymbol{0} & \boldsymbol{0} & \ldots & \ldots & \boldsymbol{0} \\ \ldots & \ldots & \ldots & \ldots & \ldots \\ \ldots & \ldots & \ldots & \ldots & \ldots \\ \boldsymbol{0} & \boldsymbol{0} & \ldots & \ldots & \boldsymbol{0} \\ \boldsymbol{0} & \boldsymbol{0} & \ldots & (2\gamma+1) \cdot \boldsymbol{N}_{n-1,n-1} & -\gamma \cdot \boldsymbol{N}_{n-1,n} \\ \boldsymbol{0} & \boldsymbol{0} & \ldots & -\gamma \cdot \boldsymbol{N}_{n-1,n}^T & (\gamma+1) \cdot \boldsymbol{N}_{nn} \end{pmatrix} \tag{3.43}$$

with

$$\begin{array}{rcll} \gamma & = & +\frac{\sigma_c^2}{2 \cdot \sigma_\phi^2} & \\ \boldsymbol{N}_{ii} & = & \boldsymbol{A}_i^T \boldsymbol{A}_i, & i = 1, 2, \ldots, n \\ \boldsymbol{N}_{i,i+1} & = & \boldsymbol{A}_i^T \boldsymbol{A}_{i+1} & \\ \boldsymbol{N}_{i,i+k} & = & \boldsymbol{0}, & k > 1. \end{array} \tag{3.44}$$

The NEQ matrix has a band structure with one diagonal and seven parallels to the diagonal on each side (corresponding to two position and two clock parameters). All other elements are zero. The solution of the NEQ system thus may be found by very efficient algorithms, despite the fact that the number of parameters may be rather large (see, e.g., [*Press et al.*, 1992]). The explicit inversion of the NEQ matrix (eqn. (3.43)) may be neglected under these circumstances. In a first step, the NEQ matrix is stored in a compact form to save space. This form is used to perform a LU (Lower-Upper) decomposition, which is then followed by a back-substitution step in order to obtain the solution vector.

3.4.2 Estimating Position-differences

Let us introduce here a modification of the task leading to an algorithm of comparable efficiency. The idea is to perform the estimation of the kinematic positions in three steps:

- The first consists of the estimation of positions of the receiver using only the code observations.
- The second step consists of the estimation of position-differences using only the phase-difference observations.
- The third and last step consists of the combination of positions and position-differences.

Due to the separation of the procedure we have to find a possibility to estimate position-differences using the phase-difference observations. Let us, therefore, have a closer look at the structure of the phase-difference observation at epoch t_i. By the decomposition

$$\boldsymbol{dx}_i \doteq \boldsymbol{dx}_{i-1} + \boldsymbol{d\Delta x}_i \tag{3.45}$$

of the vector $\boldsymbol{dx}_i$, where $\boldsymbol{d\Delta x}_i$ obviously is the improvement of the vector $\boldsymbol{x}_i - \boldsymbol{x}_{i-1}$, we may rewrite the observation equation (3.28) as

$$\boldsymbol{A}_i \cdot \boldsymbol{d\Delta x}_i + \boldsymbol{\delta A}_i \cdot \boldsymbol{dx}_{i-1} - (\tilde{\boldsymbol{\phi}}_i - \tilde{\boldsymbol{\phi}}_{i-1}) = \boldsymbol{w}_i \tag{3.46}$$

with $\boldsymbol{\delta A}_i = \boldsymbol{A}_i - \boldsymbol{A}_{i-1}$. Assuming an error of one meter in the position of $\boldsymbol{x}_{i-1}$ ($\boldsymbol{dx}_{i-1} \approx 1$ m), the absolute value $\boldsymbol{\delta A}_i \cdot \boldsymbol{dx}_{i-1}$ is at maximum one centimeter for a spacing of 10-30 seconds between the observations and a typical velocity of $|\dot{\boldsymbol{r}}| \approx 7$ km/s for a LEO. The neglect of the term $\boldsymbol{\delta A}_i \cdot \boldsymbol{dx}_{x-1}$ in eqn. (3.46) would, therefore, cause a maximum error of one centimeter in the resulting position-difference. Let us therefore neglect the term for the further processing.

The NEQ system resulting for all $n-1$ vectors $\boldsymbol{d\Delta x}_i,\ i = 2, 3, \ldots, n$ has a block diagonal structure with $n-1$ blocks for the $n-1$ epoch differences $t_i - t_{i-1}$. We obtain an estimate for the difference vector $\boldsymbol{d\Delta x}_i$ as a solution of the system

$$(\boldsymbol{A}_i^T \boldsymbol{A}_i) \cdot \boldsymbol{d\Delta x}_i = \boldsymbol{A}_i^T \cdot \boldsymbol{\Delta}\tilde{\boldsymbol{\phi}}_i, \qquad i = 2, 3, \ldots, n. \tag{3.47}$$

The position- (and clock correction-) differences between subsequent epochs t_{i-1} and t_i are obtained as the sum of the a priori differences and the solution of the simple, epoch-specific NEQ system (eqn. (3.47)). The similarity and the analogy to the absolute position and clock correction estimates at epochs $t_i,\ i = 1, 2, \ldots, n$ are striking when comparing the NEQ system (eqn. (3.36)) for the code observations with the system in eqn. (3.47) for phase-difference observations. Let us use the following notation:

- $\boldsymbol{x}_{c,i}$ is the position estimate as obtained from the code observations of epoch t_i,
- $\boldsymbol{x}_{\phi,i} - \boldsymbol{x}_{\phi,i-1}$ is the position-difference as obtained from the phase-difference observations of epochs t_i and t_{i-1}.

How are the n position estimates resulting from eqn. (3.36) combined with the $n-1$ position-difference estimates from eqn. (3.47)? The adjusted positions and position-differences are simply interpreted as observations of the positions (with identity matrices as first design matrices) and with the inverses of the variance-covariance matrices of the position and position-difference estimates as weight matrices.

The "observation equations" read as

$$\begin{array}{lcl} \boldsymbol{E} \cdot \hat{\boldsymbol{x}}_i - \boldsymbol{x}_{c,i} & = & \tilde{\boldsymbol{v}}_{c,i} \\ \boldsymbol{E} \cdot [\hat{\boldsymbol{x}}_i - \hat{\boldsymbol{x}}_{i-1}] - [\boldsymbol{x}_{\phi,i} - \boldsymbol{x}_{\phi,i-1}] & = & \tilde{\boldsymbol{v}}_{\phi,i}, \end{array} \tag{3.48}$$

where we denote the estimated positions and clock corrections at time t_i resulting from the combination of all code position and phase position-difference estimates as $\hat{\boldsymbol{x}}_i$. $\tilde{\boldsymbol{v}}_{c,i}$ and $\tilde{\boldsymbol{v}}_{\phi,i}$ are the residuals of the corresponding code positions and phase position-differences.

Using the standard deviation of the code observation as weight unit and using the inverse of the variance-covariance matrix of each epoch of the code positioning as weight matrix, we obtain the following NEQ contributions from the code observations

$$(\boldsymbol{E}^T \boldsymbol{P} \boldsymbol{E}) \cdot \hat{\boldsymbol{x}} = \boldsymbol{E}^T \boldsymbol{P} \cdot \boldsymbol{x}_c \tag{3.49}$$

where

$$\begin{aligned} \boldsymbol{x}_c^T &= \left(\boldsymbol{x}_{c,1}^T, \boldsymbol{x}_{c,2}^T, \ldots, \boldsymbol{x}_{c,n}^T\right) \\ \hat{\boldsymbol{x}}^T &= \left(\hat{\boldsymbol{x}}_1^T, \hat{\boldsymbol{x}}_2^T, \ldots, \hat{\boldsymbol{x}}_n^T\right) \end{aligned} \tag{3.50}$$

and

$$\boldsymbol{P} = \begin{pmatrix} \boldsymbol{P}_1 & \boldsymbol{0} & \ldots & \ldots & \ldots \\ \boldsymbol{0} & \boldsymbol{P}_2 & \boldsymbol{0} & \ldots & \ldots \\ \ldots & \ldots & \ldots & \ldots & \ldots \\ \ldots & \ldots & \ldots & \ldots & \ldots \\ \ldots & \ldots & \ldots & \ldots & \boldsymbol{P}_n \end{pmatrix} \tag{3.51}$$

with

$$\boldsymbol{P}_i = \boldsymbol{A}_i^T \boldsymbol{A}_i. \tag{3.52}$$

The NEQ contribution from the phase observations may be given by the form

$$(\boldsymbol{\mathcal{E}}^T \boldsymbol{P} \boldsymbol{\mathcal{E}}) \cdot \hat{\boldsymbol{x}} = \boldsymbol{\mathcal{E}}^T \boldsymbol{P} \cdot \boldsymbol{\Delta x}_\phi \tag{3.53}$$

where

$$\boldsymbol{P} = \begin{pmatrix} \boldsymbol{P}_2 & \boldsymbol{0} & \ldots & \ldots & \ldots \\ \boldsymbol{0} & \boldsymbol{P}_3 & \boldsymbol{0} & \ldots & \ldots \\ \ldots & \ldots & \ldots & \ldots & \ldots \\ \ldots & \ldots & \ldots & \ldots & \ldots \\ \ldots & \ldots & \ldots & \ldots & \boldsymbol{P}_n \end{pmatrix} \tag{3.54}$$

with

$$\boldsymbol{P}_i = \frac{\sigma_c^2}{2 \cdot \sigma_\phi^2} \cdot \boldsymbol{A}_i^T \boldsymbol{A}_i \tag{3.55}$$

and

$$\boldsymbol{\Delta x}_\phi^T = \left(\boldsymbol{x}_{\phi,2} - \boldsymbol{x}_{\phi,1}, \ldots\ldots, \boldsymbol{x}_{\phi,n} - \boldsymbol{x}_{\phi,n-1}\right). \tag{3.56}$$

At last we have

$$\boldsymbol{\mathcal{E}} = \begin{pmatrix} -\boldsymbol{E} & +\boldsymbol{E} & \ldots & \ldots & \ldots \\ \boldsymbol{0} & -\boldsymbol{E} & +\boldsymbol{E} & \ldots & \ldots \\ \ldots & \ldots & \ldots & \ldots & \ldots \\ \ldots & \ldots & \ldots & \ldots & \ldots \\ \ldots & \ldots & \ldots & -\boldsymbol{E} & +\boldsymbol{E} \end{pmatrix}. \tag{3.57}$$

The resulting system of equations for the determination of $\hat{\boldsymbol{x}}_i$ is again a NEQ system. It follows in an elementary way from the above NEQ systems for position and position-differences as

$$\boldsymbol{\mathcal{M}} \cdot \hat{\boldsymbol{x}} = \boldsymbol{b} \tag{3.58}$$

where $\boldsymbol{\mathcal{M}}$ is of band-diagonal structure

$$\boldsymbol{\mathcal{M}} = \begin{pmatrix} \boldsymbol{M}_{11} & \boldsymbol{M}_{12} & \boldsymbol{0} & \dots & \boldsymbol{0} \\ \boldsymbol{M}_{12}^T & \boldsymbol{M}_{22} & \dots & \dots & \boldsymbol{0} \\ \boldsymbol{0} & \boldsymbol{M}_{23}^T & \dots & \dots & \boldsymbol{0} \\ \boldsymbol{0} & \boldsymbol{0} & \dots & \dots & \boldsymbol{0} \\ \dots & \dots & \dots & \dots & \dots \\ \dots & \dots & \dots & \dots & \dots \\ \boldsymbol{0} & \boldsymbol{0} & \dots & \dots & \boldsymbol{0} \\ \boldsymbol{0} & \boldsymbol{0} & \dots & \boldsymbol{M}_{n-1,n-1} & \boldsymbol{M}_{n-1,n} \\ \boldsymbol{0} & \boldsymbol{0} & \dots & \boldsymbol{M}_{n-1,n}^T & \boldsymbol{M}_{nn} \end{pmatrix} \tag{3.59}$$

with

$$\begin{aligned} \boldsymbol{M}_{11} &= \boldsymbol{A}_1^T \boldsymbol{A}_1 + \tfrac{\sigma_c^2}{2 \cdot \sigma_\phi^2} \cdot \boldsymbol{A}_2^T \boldsymbol{A}_2 \\ \boldsymbol{M}_{ii} &= \boldsymbol{A}_i^T \boldsymbol{A}_i + \tfrac{\sigma_c^2}{2 \cdot \sigma_\phi^2} \cdot \left[\boldsymbol{A}_i^T \boldsymbol{A}_i + \boldsymbol{A}_{i+1}^T \boldsymbol{A}_{i+1} \right], \quad i = 2, 3, \dots, n-1 \\ \boldsymbol{M}_{nn} &= \boldsymbol{A}_n^T \boldsymbol{A}_n + \tfrac{\sigma_c^2}{2 \cdot \sigma_\phi^2} \cdot \boldsymbol{A}_n^T \boldsymbol{A}_n \\ \boldsymbol{M}_{i,i+1} &= -\tfrac{\sigma_c^2}{2 \cdot \sigma_\phi^2} \cdot \boldsymbol{A}_{i+1}^T \boldsymbol{A}_{i+1}, \qquad i = 1, 2, \dots, n-1 \\ \boldsymbol{M}_{i,i+k} &= \boldsymbol{0}, \qquad i = 1, 2, \dots, n-2, k > 1 \end{aligned} \tag{3.60}$$

The right hand sides of eqn. (3.58) may be written as

$$\boldsymbol{b}^T = \left(\boldsymbol{b}_1^T, \boldsymbol{b}_2^T, \dots, \boldsymbol{b}_n^T \right), \tag{3.61}$$

where the epoch-specific arrays $\boldsymbol{b}_i$ have to be computed as:

$$\begin{aligned} \boldsymbol{b}_1 &= (\boldsymbol{A}_1^T \boldsymbol{A}_1) \cdot \boldsymbol{x}_{c,1} - \tfrac{\sigma_c^2}{2 \cdot \sigma_\phi^2} \cdot (\boldsymbol{A}_2^T \boldsymbol{A}_2) \cdot [\boldsymbol{x}_{\phi,2} - \boldsymbol{x}_{\phi,1}] \\ \boldsymbol{b}_i &= (\boldsymbol{A}_i^T \boldsymbol{A}_i) \cdot \boldsymbol{x}_{c,i} + \tfrac{\sigma_c^2}{2 \cdot \sigma_\phi^2} \cdot (\boldsymbol{A}_i^T \boldsymbol{A}_i) \cdot [\boldsymbol{x}_{\phi,i} - \boldsymbol{x}_{\phi,i-1}] - \\ &\quad \tfrac{\sigma_c^2}{2 \cdot \sigma_\phi^2} \cdot (\boldsymbol{A}_{i+1}^T \boldsymbol{A}_{i+1}) \cdot [\boldsymbol{x}_{\phi,i+1} - \boldsymbol{x}_{\phi,i}], \qquad i = 2, 3, \dots, n-1 \\ \boldsymbol{b}_n &= (\boldsymbol{A}_n^T \boldsymbol{A}_n) \cdot \boldsymbol{x}_{c,n} + \tfrac{\sigma_c^2}{2 \cdot \sigma_\phi^2} \cdot (\boldsymbol{A}_n^T \boldsymbol{A}_n) \cdot [\boldsymbol{x}_{\phi,n} - \boldsymbol{x}_{\phi,n-1}] \end{aligned} \tag{3.62}$$

The NEQ system (3.58) has band-diagonal structure with one diagonal and seven non-zero parallels to the diagonal on both sides of the diagonal. The system is, as every NEQ system, symmetric. The solution of this special NEQ system follows the same pattern as described in Section 3.4.1.

In the above derivations we have assumed that we have identical observation scenarios for phase and code and that the same n_s satellites have been observed at all n epochs. In the general case we should allow for different first design matrices $\boldsymbol{A}_{i_c}$ and $\boldsymbol{A}_{i_p}$ for code and phase and for different epochs.

Kinematic procedures have the disadvantage that a "jump" may occur in the kinematic trajectory if the phase-connection is lost between two subsequent epochs. For our procedure this is the case if no phase-derived position-difference is available for one or more epoch-differences. In this case the connection between two subsequent epochs is missing, leading to two separate sequences of positions. The two sequences derive their absolute definition from the code positions of the two sequences. The NEQ matrix $\boldsymbol{\mathcal{M}}$ is then actually divided into several independent matrices $\boldsymbol{\mathcal{M}}_1, \boldsymbol{\mathcal{M}}_2, \dots, \boldsymbol{\mathcal{M}}_{g+1}$, where g is the number of gaps in the phase-difference processing. The code accuracy is not sufficient to assure

the connection to the previous sequence and therefore a jump of some ten centimeters may occur. The results of Section 3.6.2 give an impression of the size of these jumps and of the effect on the quality of the combined kinematic positions.

3.4.3 Correct Correlations

Despite the fact that we will not focus on the statistically correct solutions, but rather on approximate treatments, we nevertheless develop the correct formulae.

The NEQ system emerging from the correct combination of code and phase-difference observations is of the form of eqn. (3.40), where the absolute values of the elements of matrix $\boldsymbol{\delta N}$ are small compared to the (absolute values of the) non-zero elements of matrix $\boldsymbol{N}_0$. For the subsequent matrix inversion it is convenient to write the matrix $\boldsymbol{N}$ as

$$\boldsymbol{N} = \boldsymbol{N}_0 + \boldsymbol{\delta N} = \boldsymbol{N}_0 \cdot \left(\boldsymbol{E} + \boldsymbol{N}_0^{-1} \cdot \boldsymbol{\delta N} \right) \tag{3.63}$$

with

$$\boldsymbol{\delta N} = \begin{pmatrix} \alpha \cdot \boldsymbol{N}_{11} & \beta \cdot \boldsymbol{N}_{12} & \dots & \beta \cdot \boldsymbol{N}_{1n} \\ \beta \cdot \boldsymbol{N}_{12}^T & \alpha \cdot \boldsymbol{N}_{22} & \dots & \beta \cdot \boldsymbol{N}_{2n} \\ \dots & \dots & \dots & \dots \\ \dots & \dots & \dots & \dots \\ \dots & \dots & \dots & \dots \\ \dots & \dots & \dots & \alpha \cdot \boldsymbol{N}_{nn} \end{pmatrix}. \tag{3.64}$$

In view of the assumptions concerning the size of the elements of the matrices we may write the inverted matrix $\boldsymbol{N^{-1}}$ approximately as follows

$$\boldsymbol{N^{-1}} \;\; = \;\; \left(\boldsymbol{E} - \boldsymbol{N}_0^{-1} \cdot \boldsymbol{\delta N} \right) \cdot \boldsymbol{N}_0^{-1}. \tag{3.65}$$

By construction, $\boldsymbol{N}_0$ is of a block-diagonal structure with blocks of dimension 4 x 4. The inverse thus may be computed easily, block by block, where we have to assume that the individual blocks are regular. For later use we write the individual blocks of matrix $\boldsymbol{N}_0$ in the following way:

$$\boldsymbol{N}_0^{-1} = \begin{pmatrix} \boldsymbol{N}_{0,11}^{-1} & \boldsymbol{0} & \dots & \dots & \dots \\ \boldsymbol{0} & \boldsymbol{N}_{0,22}^{-1} & \boldsymbol{0} & \dots & \dots \\ \dots & \dots & \dots & \dots & \dots \\ \dots & \dots & \dots & \dots & \dots \\ \dots & \dots & \dots & \dots & \boldsymbol{N}_{0,nn}^{-1} \end{pmatrix} \tag{3.66}$$

Using the approximation of eqn. (3.65) and taking into account the actual form of matrix $\boldsymbol{N}_0^{-1}$ the solution of the NEQ system (eqn. (3.39)) may be written as

$$\boldsymbol{dx} = \boldsymbol{N}_0^{-1} \cdot \boldsymbol{b} - \boldsymbol{N}_0^{-1} \cdot \boldsymbol{\delta N} \cdot \boldsymbol{N}_0^{-1} \cdot \boldsymbol{b}. \tag{3.67}$$

Denoting by

$$\boldsymbol{dx}_0 \doteq \boldsymbol{N}_0^{-1} \cdot \boldsymbol{b} = \begin{pmatrix} \boldsymbol{N}_{0,11}^{-1} \cdot \boldsymbol{b}_1 \\ \boldsymbol{N}_{0,22}^{-1} \cdot \boldsymbol{b}_2 \\ \dots \\ \dots \\ \dots \\ \boldsymbol{N}_{0,nn}^{-1} \cdot \boldsymbol{b}_n \end{pmatrix} \doteq \begin{pmatrix} \boldsymbol{dx}_{01} \\ \boldsymbol{dx}_{02} \\ \dots \\ \dots \\ \dots \\ \boldsymbol{dx}_{0n} \end{pmatrix} \tag{3.68}$$

we may write the solution $\boldsymbol{dx}$ as

$$\boldsymbol{dx} = \boldsymbol{dx}_0 - \boldsymbol{N}_0^{-1} \cdot \boldsymbol{\delta N} \cdot \boldsymbol{dx}_0, \tag{3.69}$$

where we may write

$$\boldsymbol{N}_0^{-1} \cdot \boldsymbol{\delta N} \cdot \boldsymbol{dx}_0 = \begin{pmatrix} \boldsymbol{N}_{0,11}^{-1} \cdot \sum_{i=1}^{n} \boldsymbol{\delta N}_{1i} \cdot \boldsymbol{dx}_{0i} \\ \boldsymbol{N}_{0,22}^{-1} \cdot \sum_{i=1}^{n} \boldsymbol{\delta N}_{2i} \cdot \boldsymbol{dx}_{0i} \\ \cdots \\ \cdots \\ \cdots \\ \boldsymbol{N}_{0,nn}^{-1} \cdot \sum_{i=1}^{n} \boldsymbol{\delta N}_{ni} \cdot \boldsymbol{dx}_{0i} \end{pmatrix}. \tag{3.70}$$

The $\boldsymbol{\delta N}_{1i}$ matrices are the sub-matrices of matrix $\boldsymbol{\delta N}$ defined by eqn. (3.64). Eqn. (3.70) shows how the solution vector may be computed in an efficient way by first computing a first order approximation $\boldsymbol{dx}_0$ of the solution $\boldsymbol{dx}$. In the following section we will summarize the approximations for kinematic point positioning on the zero-difference level with the epoch-wise differenced phase observations, which were implemented and tested in the context of this work.

3.5 Practical Realization

It is our stated goal to develop an efficient approach for kinematic point positioning on the zero-difference level. Therefore, we will focus on the solution of eqn. (3.58) for the combination of the code positions and phase position-differences. This solution promises to meet our requirements. The disadvantage of this approach is the neglect of the correlations between subsequent phase-difference observations.

For a better understanding of the studies made in this context we will briefly and schematically explain the flowchart (Figure 3.2) of the program LEOKIN we have developed for the kinematic point positioning for a moving GPS receiver. Figure 3.1 shows the general scheme for processing LEO data. Figure 3.2 now illustrates the flow of the data within our program LEOKIN performing a zero-difference kinematic point positioning.

LEOKIN is based on an epoch-by-epoch processing. In the main epoch loop both, the code and the phase-difference processing, take place. After the pre-screening of the code observations (the algorithm will be explained in Chapter 4) the receiver clock is synchronized to GPS time. The receiver clock has to be known with an accuracy better than one microsecond and the approximate value is saved for the phase processing. The position of the receiver and an improved receiver clock correction are then estimated using the code observations of the current epoch corrected by the approximate receiver clock correction. The matrix $\boldsymbol{A}_i^T \boldsymbol{A}_i$ is saved for the combination of the code with the phase-difference solutions. In a second block the phase-differences are processed. For this purpose the observations of the previous epoch have been saved and the differences are formed for the satellites observed in the current and the previous epoch. The phase-differences are pre-screened in a similar way as the code observations (see Chapter 4). In the next step the position-difference for the current epoch-difference is estimated and the phase observations of the actual epoch are saved for the next epoch-difference. The matrix $\boldsymbol{A}_i^T \boldsymbol{P} \boldsymbol{A}_i$ of the phase-difference processing is saved for the later combination, too. The processing of the next epoch starts again with code processing. When the code positions and phase position-differences for all epochs have been estimated, the matrix $\boldsymbol{\mathcal{M}}$ and the vector $\boldsymbol{b}$ are set up according to eqns. (3.60) and (3.62). At

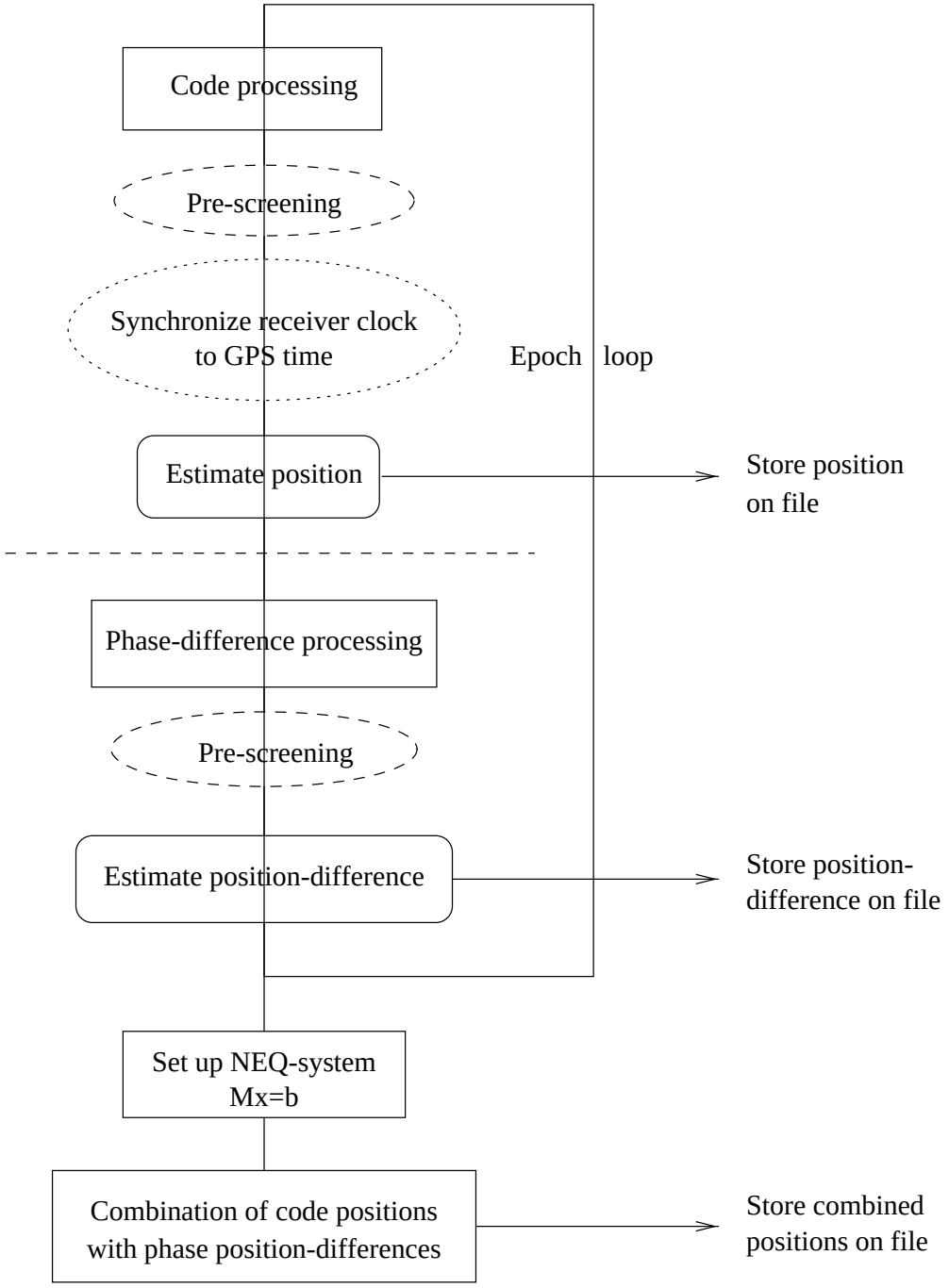

Figure 3.2: Flowchart of program LEOKIN.

the same time the matrix $\mathcal{M}$ is stored in a space-saving way and the algorithm described in [*Press et al.*, 1992] is applied to the band-diagonal NEQ system in order to solve for the combined positions.

Figure 3.2 is the skeleton for our kinematic point positioning approach. Program LEOKIN saves both the combined positions and the estimated positions (derived from the code observations) and the estimated position-differences (derived from the phase-difference observations). The combined positions as well as the positions and position-differences may be used by an orbit determination program as pseudo-observations to determine a fully deterministic or a reduced-dynamic orbit (see Chapter 5).

In the following sections we will refer to this skeleton to explain modified procedures or studies made within a special step. In the next sections we will validate the developed approach based on simulations.

3.6 Simulations

3.6.1 Code

Terrestrial Station

Our approach is designed for processing data of any roving or static station carrying a GPS receiver. The simplest roving station is a fixed terrestrial station. The receiver is, in fact, not moving w.r.t. an Earth-fixed system, which makes it well-suited for validating the procedure. We simulate in a first step data for a terrestrial receiver to validate the code point positioning procedure. The input data for the simulation for doy (day of year) 034/2002 (February 3, 2002) are

- CODE rapid orbits,
- Earth rotation parameters of the CODE rapid processing,
- broadcast clock corrections for the GPS satellites, and
- IGS2000-coordinates [*Ferland,* 2002] for station ALGO (ALGOnquin Park, Ontario, Canada).

With these input data we simulate error-free code observations for station ALGO to validate the point positioning approach. The result of a point positioning using the program LEOKIN has to be compared with the a priori coordinates of the station ALGO used in the simulation. The result of this test is satisfactory: the "true" coordinates of Algonquin are reproduced virtually error-free.

In a second step we simulate code observations with an a priori standard deviation of $\sigma_{apr} = 1.0$ m for the two frequencies L1 and L2. The differences of these positions in comparison to the "true" values are shown in Figure 3.3(a) (North-, East-, and Up-direction). Figure 3.3(b) shows the differences for a simulation of observations with $\sigma_{apr} = 0.5$ m and Table 3.1 summarizes mean and standard deviation values of these two simulations using the ionosphere-free linear combination (P3) of the observations. The third row of this table are mean and standard deviation values for the same observations simulated with $\sigma_{apr} = 0.5$ m but only the P1-code measurements are used for the point positioning. Taking into account that the noise of the ionosphere-free linear combination is three times larger than that for P1- or P2-measurements [*Beutler et al.*, 1990], we get for the simulation with $\sigma_{apr} = 1.0$ m a standard deviation of $\sigma_{P3} \approx 3$ m. The expected precision σ_{pos} for a point position is then $\sigma_{pos} = \sigma_{P3} \cdot$ DOP (Dilution Of Precision) [*Kleusberg and Teunissen,* 1996]. The DOP-value is an indicator for the geometry defined by the GPS satellite constellation above the observing site. The better the satellite geometry, the smaller the DOP-value, and the better the expected positioning accuracy. The DOP-value can be separated in three

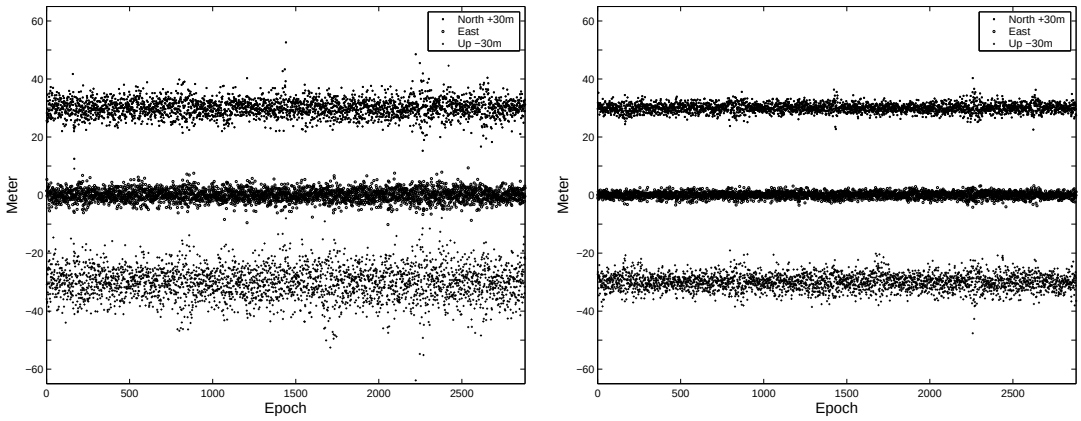

(a) $\sigma_{apr} = 1.0$ m (b) $\sigma_{apr} = 0.5$ m

Figure 3.3: Differences of coordinates computed from simulated observations w.r.t. the "true" coordinates of ALGO.

Table 3.1: Mean (μ) and standard deviation (σ) of the differences to the "true" values (of ALGO) of a point positioning with simulated code observations using different σ_{apr} and different linear combinations (LC).

σ_{apr}	LC	$\mu_N \pm \sigma_N$ (m)	$\mu_E \pm \sigma_E$ (m)	$\mu_U \pm \sigma_U$ (m)	$\mu_{c\cdot\delta_A} \pm \sigma_{c\cdot\delta_A}$ (m)
1.0 m	P3	0.1189 ± 3.4043	0.0058 ± 2.2379	-0.0867 ± 6.0409	-0.0416 ± 4.2241
0.5 m	P3	0.0267 ± 1.5150	0.0270 ± 1.0146	0.03012 ± 2.7197	0.0253 ± 1.8879
0.5 m	P1	0.0059 ± 0.5007	0.0030 ± 0.3449	0.0161 ± 0.9057	0.0066 ± 0.6307

components (North, East, and Up). The mean DOP-values and the corresponding values of the expected precision for the station ALGO are ($\sigma_{apr} = 1.0$ m)

$$\begin{aligned} \mu_{NDOP} &= 1.4625 \quad \Rightarrow \quad \sigma_N \approx 4.4\,m \\ \mu_{EDOP} &= 0.9478 \quad \Rightarrow \quad \sigma_E \approx 2.8\,m \\ \mu_{UDOP} &= 2.6189 \quad \Rightarrow \quad \sigma_U \approx 7.9\,m. \end{aligned} \tag{3.71}$$

Table 3.1 shows that the accuracy of the positions of ALGO derived from simulated code observations meet the expectations. The different noise of the three components is due to the constellation and the design of the GPS satellite system. The inclination of the satellite orbits of $i = 55°$ causes, e.g., for stations at mid-latitude on the Northern hemisphere a bad satellite coverage of the Northern sky. Thus the North-component of the station is worse than the East-component. The Up-component shows the largest error. This is expected due to the observation geometry (and the necessity to estimate a receiver clock correction).

Low Earth Orbiter

The focus of this subsection is the recovery of the kinematic trajectory for a LEO using simulated observations. The same input characteristics as in the case of the terrestrial station are used for the simulation.

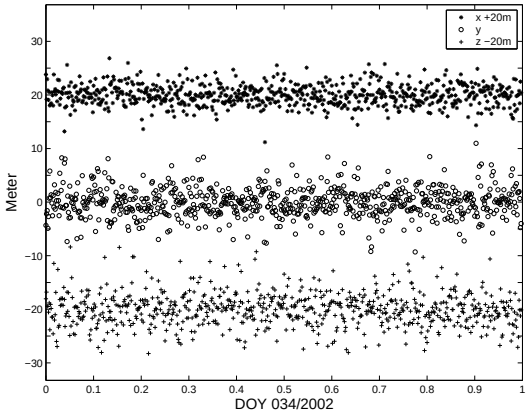

Figure 3.4: Differences of satellite positions w.r.t. the "true" a priori orbit from a code point positioning with program LEOKIN using simulated data with $\sigma_{apr} = 1.0$ m.

Instead of the coordinates of the station we use an a priori orbit of a LEO, in this case the Rapid Science Orbit (RSO) [*Koenig et al.*, 2002] of CHAMP computed by GFZ for doy 034/2002. In a first step we simulate error-free code observations. The simulated CHAMP data are then used for a code point positioning procedure. The point positioning starts from an a priori orbit, where the same orbit was used as in the simulation. The "true" a priori orbit is reproduced within one to two millimeters difference. This result is expected because the orbits compared here are stored in the precise orbit format (SP3, [*Remondi*, 1989]) where the last significant digit of the coordinates is one millimeter. Even if no a priori orbit, but the "Bancroft"-algorithm is used in program LEOKIN for the point positioning, the solutions agree within one to two millimeters with the orbit used for the simulation, as well.

In a second step we simulate data with an a priori sigma $\sigma_{apr} = 1.0$ m for the P1- and P2-code observations. After the point positioning using an a priori orbit we compare the resulting positions with the a priori orbit used for the simulation of the data. The differences are shown in Figure 3.4 and in Table 3.2, where we find the mean and standard deviation values of these differences. Both, the mean and the standard deviation values correspond to the expected values considering that the ionosphere-free linear combination of the P1- and P2-measurements is used. As mentioned above the noise of the ionosphere-free linear combination is three times larger than that for P1 and in addition the DOP-values have to be taken into account. The mean DOP-values (X, Y, Z) and the expected accuracies for CHAMP on doy 034 are

$$\begin{aligned} \mu_{XDOP} &= 0.6566 \quad \Rightarrow \quad \sigma_X \approx 2.0\,m \\ \mu_{YDOP} &= 0.8759 \quad \Rightarrow \quad \sigma_Y \approx 2.6\,m \\ \mu_{ZDOP} &= 1.0181 \quad \Rightarrow \quad \sigma_Z \approx 3.0\,m. \end{aligned} \tag{3.72}$$

These values are reflected by the values in Table 3.2.

3.6.2 Combined Positions and Phase Only Positions

Simple Example: Static Positioning

Before analyzing our methods for kinematic point positioning using GPS code and phase-difference observations with program LEOKIN we apply our algorithms to a very simple static example.

Table 3.2: Mean (μ) and standard deviation (σ) of the differences of the single point positioning solutions w.r.t the "true" a priori LEO orbit.

σ_{apr}	$\mu_x \pm \sigma_x$ (m)	$\mu_y \pm \sigma_y$ (m)	$\mu_z \pm \sigma_z$ (m)
1.0 m	0.140 ± 1.966	0.141 ± 2.735	0.098 ± 3.118

For this purpose we "freeze" one particular observation scenario (station Algonquin, doy 055/2002, $2^{\mathrm{h}}40^{\mathrm{m}}00^{\mathrm{s}}$ UTC), when eleven GPS satellites were observed. With this frozen scenario 2880 observations are simulated with a noise of $\sigma_c = 1.0$ m for the code and $\sigma_p = 0.01$ m for the phase observations. This means that the results are not affected by the movements of the satellites and the Earth, and by different satellite constellations (leading to different DOP-values). In addition we assume that the observations are not affected by tropospheric or ionospheric refraction. The algorithms explained previously for estimating the code point positions, for estimating the phase position-differences, and for the combination of the two results are used. The relative weight between code and phase-differences for the combination is $(1 \cdot \sqrt{2} : 100)^2 = 2 : 100^2$. Subsequently, we confine ourselves to showing only the development of the North-component of the station. The figures for the East- and the Up-component show in principle the same pattern except for the noise level, which is larger for the North- than for the East-component and larger for the Up- than for the North-component.

The differences of the combined positions w.r.t. the "true" position of ALGO are shown in Figure 3.5 (top), where the correct relative weight ($2 : 100^2$) between the code positions and the position-differences for the combination was used. Obviously, there is a signal in the residuals which is not expected. We reduce the weight of the code positions in order to reduce the impact of the code positions on the combined positions. Figure 3.5 shows the differences for solutions with increasing reduction of the weight of the code positions from the second (factor 10) to the fifth figure (factor 10'000). The signal disappears the more the weight of the code positions is reduced.

These examples (Figures 3.5) demonstrate that the code positions have a big impact on the combined positions if they are used with their normal relative weight w.r.t. the phase position-differences. The main purpose of using the code positions for the combination is the regularization of the NEQ-system. But for the regularization we need in principle only one position for one phase-connected observation series. As we have, on the other hand, a series of code positions we would like to profit from all of them and therefore we introduce all code positions into the combination process but with a lower weight. If we use a too low weight of the code positions (Figure 3.5 (bottom), factor 10'000) the absolute definition is lost and the combined positions may have an offset w.r.t. the true solution. Figure 3.5 (second) shows that a reduction with a factor 10 is not sufficient to reduce the signal of the code positions. One of the solutions with reduction factor of 100 or 1'000 seems to be the most reasonable solution. The sequences with continuous phase position-differences are in practice rather shorter than 2880 epochs. Data gaps and data problems in the phase are causing interrupts in the series of phase-differences. The shorter the sequences with connected phase-differences the less the code positions help to provide the absolute definition of the combined positions. We will, therefore, use the factor of 100 to reduce the code weight in order to avoid the appearance of a code-induced signal in the combined positions, but also to avoid loosing too much strength of the absolute definition of the combined positions by the code. In practice this means that the contributions of the code ($\boldsymbol{A}_i^T \boldsymbol{A}_i$) for the combination in eqns. (3.60) and (3.62) are reduced by a factor of 100. This simple example of static positioning shows that our approach based on zero-difference code and epoch-wise differenced phase observations gives reliable results if we downweight the contribution of the code positions. Subsequently we will focus on the recovery of the kinematic trajectory of both, a

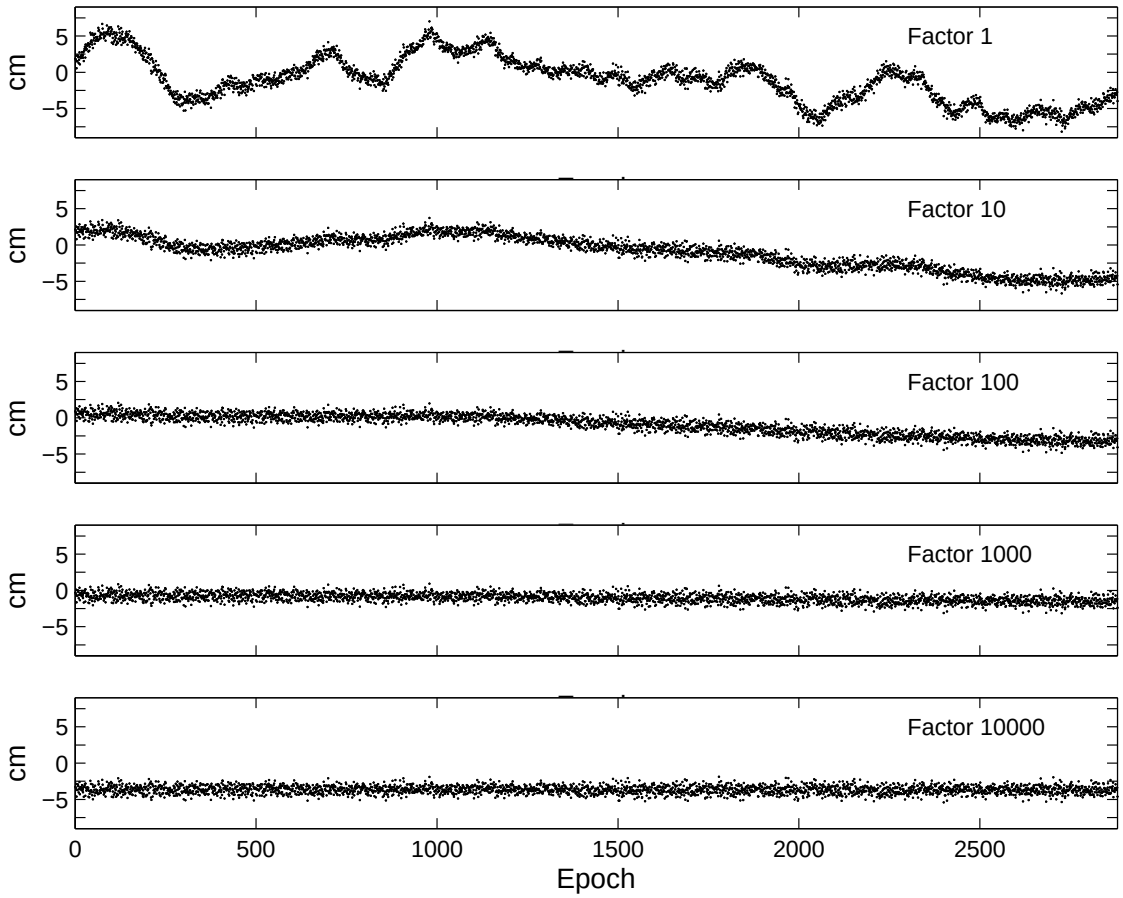

Figure 3.5: Differences between positions combined with different weight ratios and the true position of ALGO (North-component).

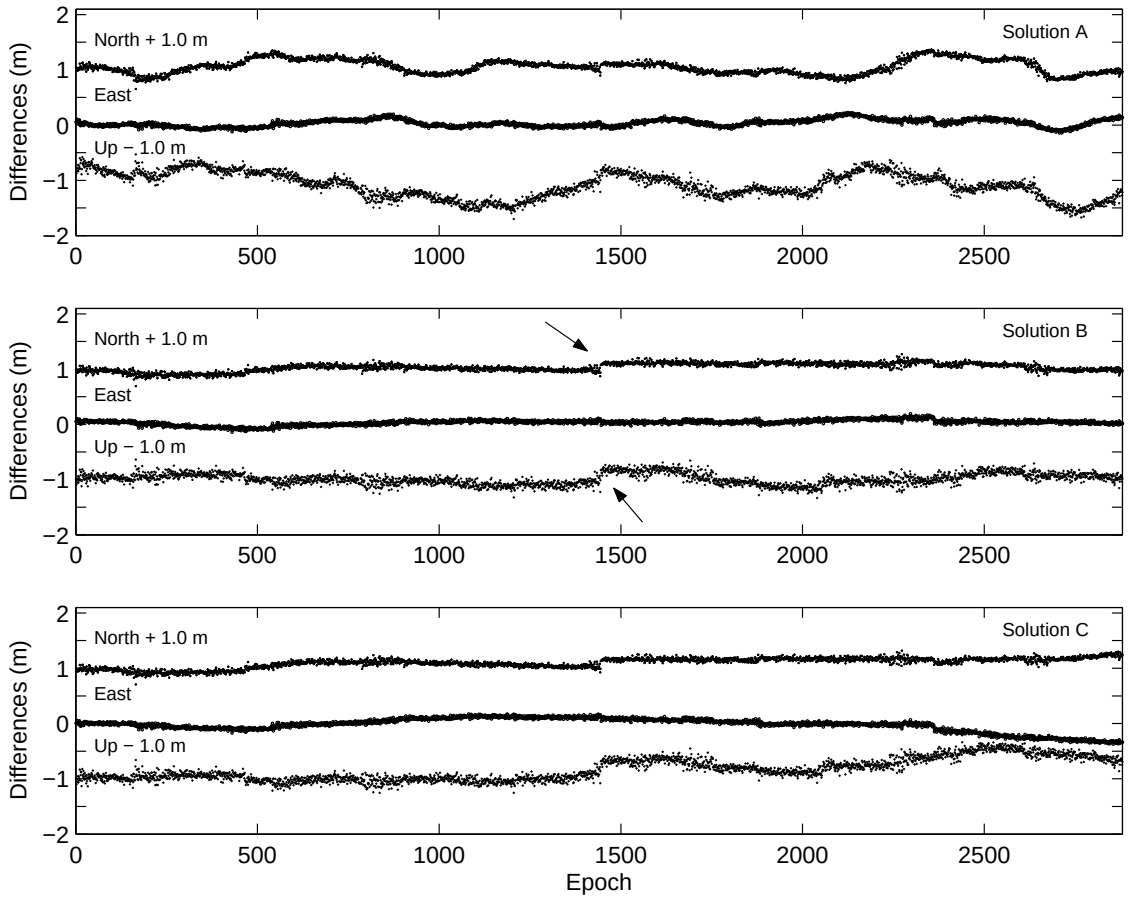

Figure 3.6: Differences of combined positions w.r.t. "true" ALGO coordinates for different weighting options.

terrestrial station and a LEO, using simulated code and phase-difference observations.

Terrestrial Station

The simulations made for the kinematic code point positioning of a terrestrial station in Section 3.6.1 can be repeated for the combined code and phase-difference point positioning. As a zero-test we start with the simulation of error-free code and phase observations for the terrestrial station ALGO. The combined kinematic positions resulting from the error-free observations show a noise w.r.t. the coordinates of ALGO due to rounding errors, which is expected for the zero-test. Subsequently we use three different solutions, named A, B, and C, based on the experience we gained with the static positioning example. The three solutions are characterized as follows:

- Solution A: The relative weight for the combination between code positions and phase position-differences is given by the ratio $\sigma_c^2 : 2 \cdot \sigma_p^2$.
- Solution B: The weight of the code positions is reduced by a factor 100.
- Solution C: Only the position-differences derived from the phase-difference observations are used

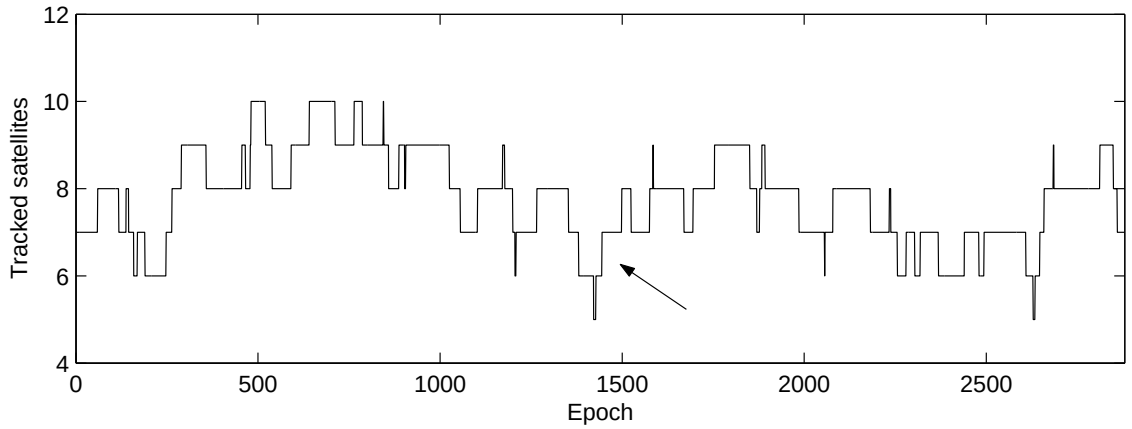

Figure 3.7: Number of tracked satellites in the simulated observations of ALGO for doy 034/2002.

for the combination (only the first position is fixed to the a priori position to regularize the NEQ system.)

If we look at simulated data with $\sigma_p = 0.01$ m for the phase observations ($\sigma_{\Delta p} = \sqrt{2} \cdot 0.01$ m) and $\sigma_c = 1.0$ m for the code observations, the differences between the combined positions and the true coordinates of ALGO (Figure 3.6 (top)) reveal the following pattern: Solution A shows a clear signal. Figure 3.6 (middle) shows the results for Solution B. The strong signal in the differences has disappeared, but there are small "jumps" in the differences, e.g., at epoch 1445 (arrows in Figure 3.6). This jump is due to the fact that the observation geometry has changed by a "new" (rising) satellite at this epoch. Prior to epoch 1445 six satellites were tracked, afterwards seven. During one day, the satellite constellation and therefore the observation geometry changes rather often. Figure 3.7 shows the number of tracked satellites in the simulated data of ALGO. All "jumps" in the differences are connected with such constellation changes but not all constellation changes lead to visible "jumps" in the differences.

As a last test only the phase-derived position-differences were used to determine the position of ALGO (Solution C). Since the NEQ system for the combination then becomes singular, we introduce the a priori position of ALGO for the position at the first epoch. The combination algorithm is in this case a simple algorithm summing up the position-differences. The differences of Solution C w.r.t. the true position of ALGO are reproduced in Figure 3.6 (bottom). Similar characteristics as in Solution B are observed for Solution C. The difference to Solution B resides in a small drift in the differences. The position-differences have an error specified by the observation accuracy of the phase observations. In this phase-only solution the position-differences are added up as well as the errors according to the error propagation. This leads to the drifts in the differences for Solution C. In Solution B the code positions have still a high enough weight to prevent that the combined positions are drifting away from the "true" position due to the summing up of the errors. The compromise is, as already mentioned in the previous section, to reduce the code weight by a factor 100 for the combination of the code positions with the phase position-differences. By this means we obtain an absolute definition of the coordinates which is strong enough, but we avoid a signal in the combined positions stemming from the quality of the code positions.

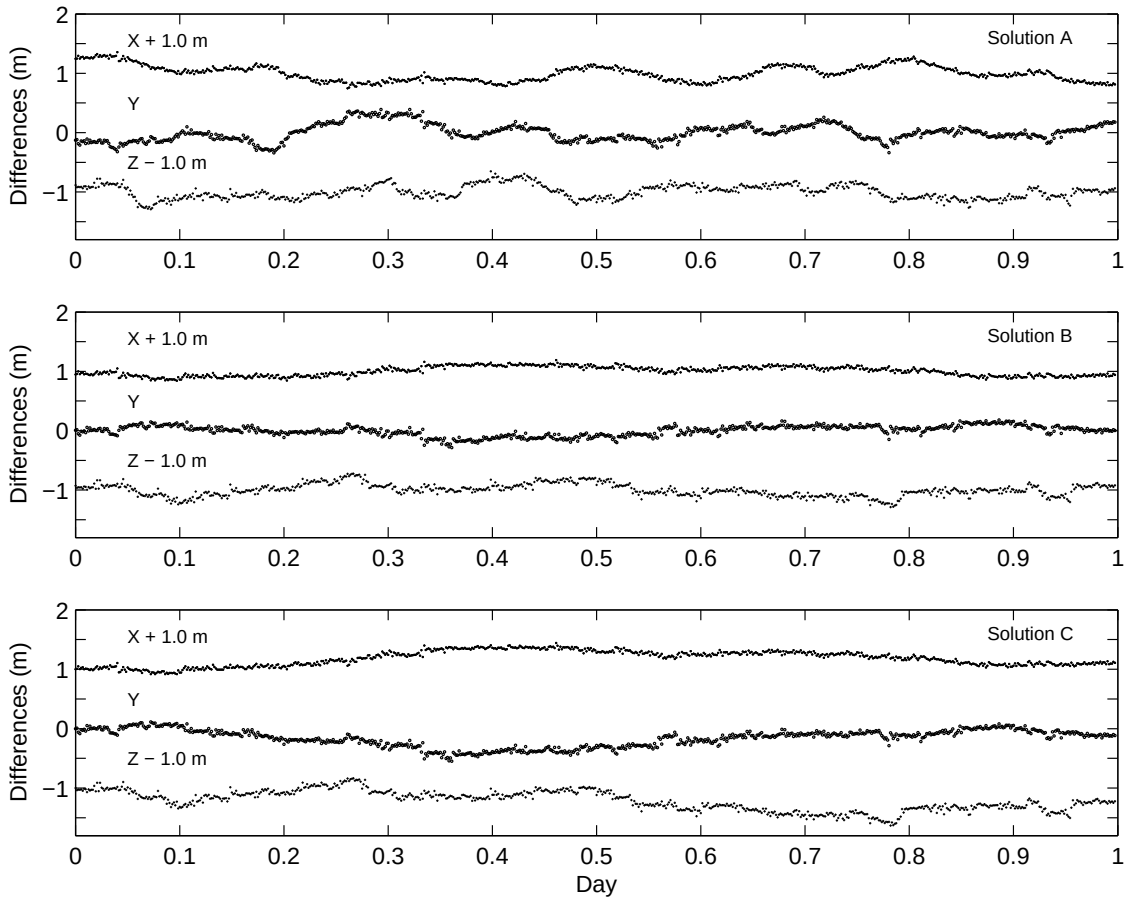

Figure 3.8: Differences of combined kinematic positions from simulated code and phase observations of CHAMP to the a priori orbit used for the simulation.

Low Earth Orbiter

Together with the simulation of the error-free code observations of CHAMP error-free phase observations are simulated for doy 034/2002. Using these error-free code and phase observations to reproduce the orbit by the combined kinematic positions results in differences w.r.t. the a priori orbit used for the simulation of up to one millimeter – an expected result.

For the simulation of normally-distributed phase observations we choose a root mean square error of $\sigma_p = 0.01$ m for the L1- and L2-frequency ($\sigma_{\Delta p} = \sqrt{2} \cdot 0.01$ m). For the code observations σ_c is 1.0 m for L1 and L2. Solutions A, B, and C are computed and compared to the a priori orbit of CHAMP used for the simulation of the data. For this purpose a Helmert transformation with three translation parameters is performed between the orbits.

Figure 3.8 (top) shows the differences between the combined positions of Solution A and the a priori CHAMP orbit. Figure 3.8 (middle) shows the corresponding differences for Solution B. The signals in the differences for Solution A stem from the code positions. In Solution B the code signals are smoothed but the differences show not only white noise. The small jumps and the remaining signals are caused by constellation changes and a bad observation geometry. Figure 3.9 shows the number of

Table 3.3: RMS errors (cm) per component of Helmert transformation between combined kinematic trajectories and "true" a priori orbit (Figure 3.8).

	x (cm)	y (cm)	z (cm)
Solution A	13.1	14.2	11.6
Solution B	7.9	8.6	10.4
Solution C	12.7	14.3	16.6

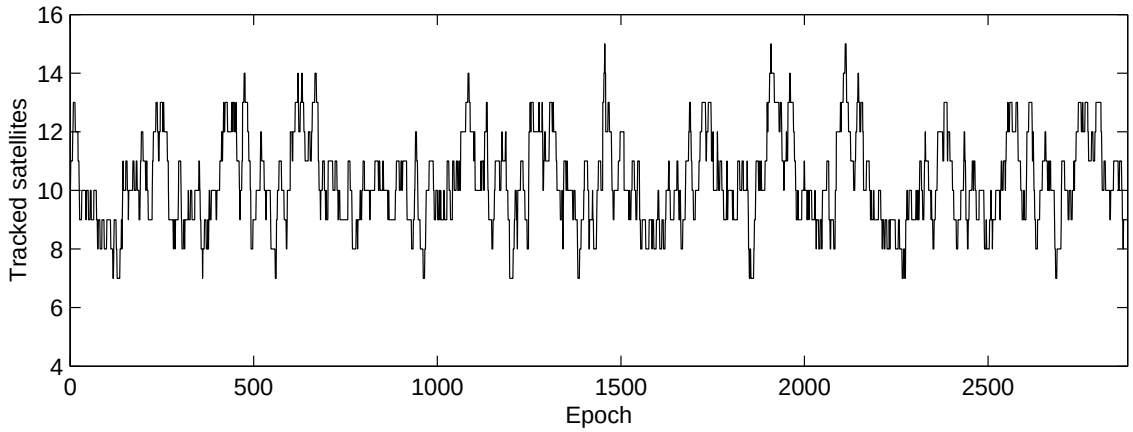

Figure 3.9: Number of satellites tracked by CHAMP for simulated observations of doy 034/2002.

tracked satellites for the simulated data of CHAMP on doy 034/2002. One clearly sees that the number of tracked satellites and therefore the satellite constellation changes more rapidly than for a terrestrial station (Figure 3.7), a fact which is due to the rapid movement of the satellite. The LEO revolves around the Earth in approximately 90 to 100 min and therefore sees nearly the entire GPS constellation within this time interval.

Figure 3.8 (bottom) shows the differences for Solution C. The influence of the code positions in Figure 3.8 (top) and the reduced signal in Figure 3.8 (middle) is obvious. The differences between Solution B (middle) and C (bottom) are not as pronounced as between Solution A (top) and B (middle). The tendency of Solution C in the case of a LEO is the same as for Solution C for the terrestrial station. The differences show a slight drift w.r.t. the line representing the true solution. The RMS errors of the Helmert transformations in Figure 3.8 are summarized in Table 3.3. The same conclusions as for the terrestrial station may be drawn. Solution B is the most reasonable choice for the combination of code positions with phase position-differences. These examples with simulated GPS code and phase observations of a LEO show that the kinematic trajectory of a LEO could be reconstructed to within a decimeter (assuming a noise of 0.01 m for the phase observations) by the kinematic point positioning procedure developed here.

3.6.3 Further Studies

Subsequently, two further studies have been performed using simulated LEO GPS data. These are studies on the impact

- of enforced interrupts and

- of using different a priori orbit/position.

Enforced Interrupts

As mentioned in Section 3.4.2 one deficiency of kinematic point positioning procedures reside in the fact that jumps occur if the connection between two subsequent epochs is not given by the phase measurements. In the case of the LEOKIN procedure a jump occurs in the combined kinematic positions if there is no phase-derived position-difference available for one or more epoch-differences. The problem is not only caused by missing position-differences due to data quality but also because of data gaps due to receiver resets or due to interrupts during data download periods. In this section we will simulate such interrupts in order to study the size of the resulting jumps and in order to see how these jumps affect the combined positions.

The simulated code and phase data used for the computations of the previous section are used here again. We enforce interrupts in the phase-difference processing in order to introduce a jump in the combined positions. We simulate two different cases. We enforce interrupts in the phase-difference processing

- after 1'000 subsequent epochs (500 minutes) and
- after 700 subsequent epochs (350 minutes).

Figure 3.10 shows the differences of Solution A (top) and Solution B (bottom) for the first case (interrupts after 1'000 epochs) w.r.t. the a priori orbit used for the simulation. Figure 3.11 shows the differences for the second case with enforced interrupts after 700 epochs (Solution A (top) and Solution B (bottom)). Solutions A and B have been computed for both cases to show the different impact of the interrupts on the sequences of connected positions. The effect of the interrupts is obviously different for the two cases and for the two solutions A and B. The size of the jumps in the coordinates reaches values up to 30 centimeters while some of the interrupted position-differences do not at all affect the coordinate results of the combined positions. These jumps in the kinematic trajectory are of course not real, but a characteristic feature of this zero-difference approach with phase-differencing from one epoch to the next. We have to be aware of this issue during the data processing and we have to find ways to reduce the number and the size of these jumps.

Different A priori Orbit or Position

Up to now all results for simulated observations of the LEO have been derived by using the "true" orbit used for the simulation as a priori orbit for the kinematic point positioning in LEOKIN. An additional test was performed in order to study the impact of the quality of the a priori orbit. In practice, the a priori orbit used is a deterministic or reduced-dynamic orbit defined by code positions or combined positions (see Section 3.1). This orbit has an accuracy of about half a meter, a fact which may have an influence on the resulting positions. For our test we use an a priori orbit, which was generated by an orbit determination procedure using the code-derived positions. Figure 3.12 (top) shows the differences between this a priori orbit and the orbit (RSO) used for the simulation. The RMS error of a Helmert transformation between the two orbits is 13.9 cm. Figure 3.12 (middle) shows the differences of the estimated positions using the new a priori orbit w.r.t. the estimates when using the "true" orbit. To this scale the differences are rather small. Figure 3.12 (bottom) shows, however, that differences up to a few centimeters do exist. The differences are attributed to the pre-processing which critically depends on the quality of the a priori orbit (see also Chapter 4). The example shows that the quality of the a priori orbit

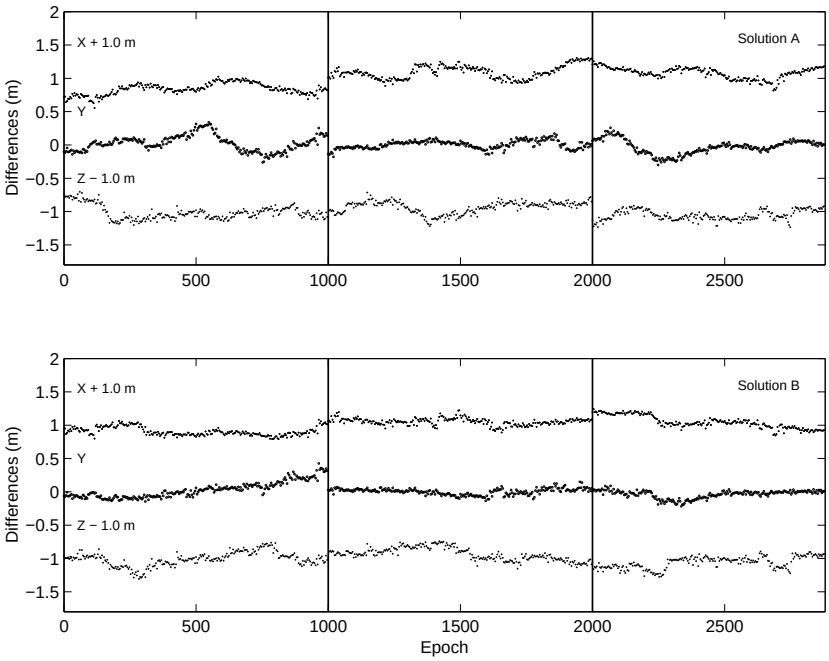

Figure 3.10: Differences of kinematic positions from simulated code and phase observations of CHAMP w.r.t. the "true" a priori orbit; Enforced interrupts after 1000 epochs.

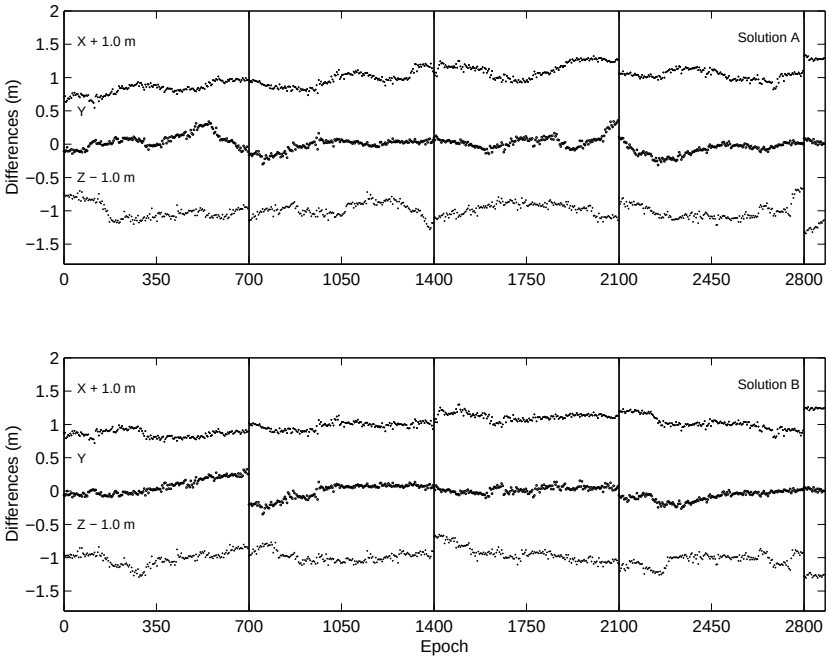

Figure 3.11: Differences of kinematic positions from simulated code and phase observations of CHAMP w.r.t. the "true" a priori orbit; Enforced interrupts after 700 epochs.

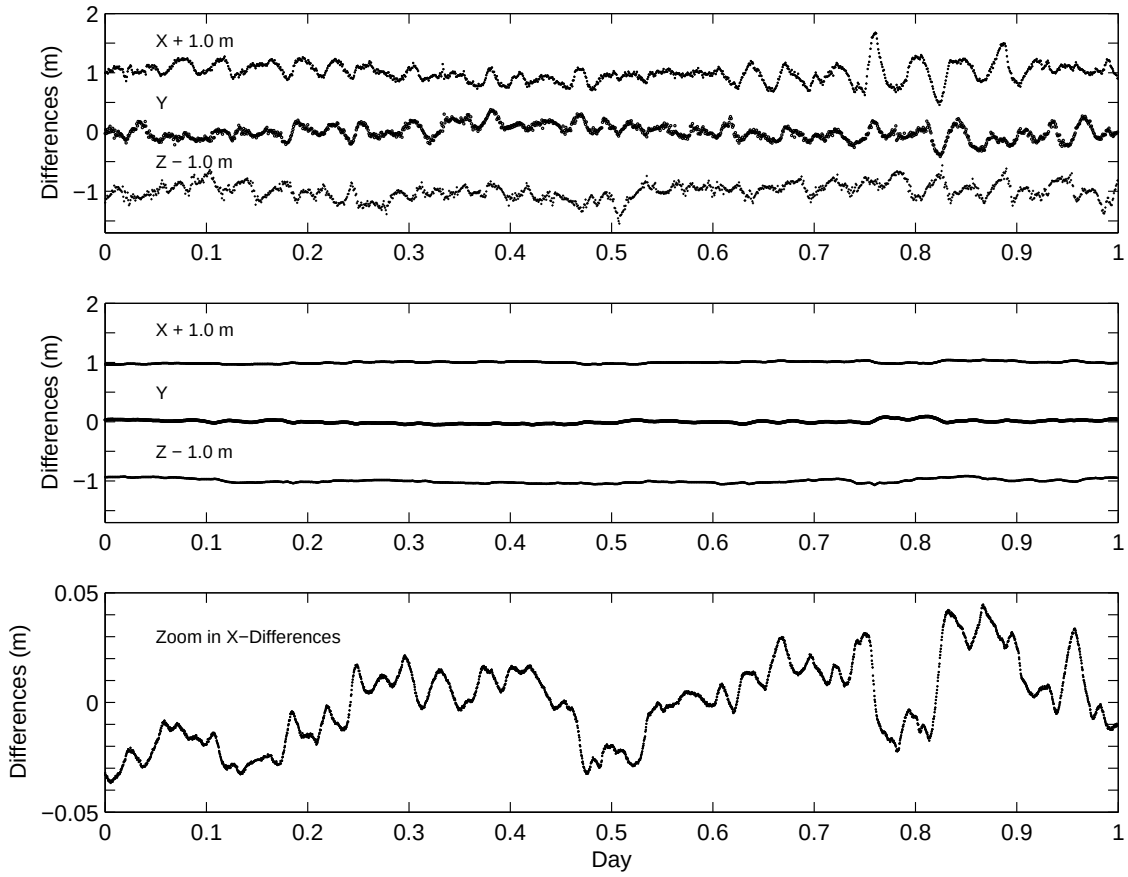

Figure 3.12: Influence of using an a priori orbit different from the "true" orbit used for the simulation of the data; Top: Differences between original a priori orbit and new a priori; Middle: Differences in resulting kinematic positions; Bottom: Zoom of x-component.

is a critical issue in our kinematic point positioning procedure. We should produce the best possible a priori orbit with our dynamic orbit determination procedure. This is in a first approximation an orbit derived from code positions or an orbit derived from combined positions (described in the second step of Figure 3.1). The more we iterate the procedure described in Figure 3.1 using combined positions the better the kinematic positions and therefore the a priori orbit gets. In order to meet our goal of developing an efficient procedure we confine ourselves to using the three steps described in Section 3.1.

3.7 Satellite Clock Interpolation

Our method depends on the availability of highly accurate GPS satellite clock corrections. These corrections should be available at 30-second intervals if we want to process 10-second (or even higher rate) data. Such satellites clock corrections currently are only available from JPL. The deficiency of these JPL clock corrections is that many epochs are missing. This is why an efficient procedure to generate 30-second clock corrections was developed [*Bock et al.*, 2000, 2003]. The procedure was developed at a time when SA was still switched on, i.e., when the satellite clock frequency was dithered in order to limit

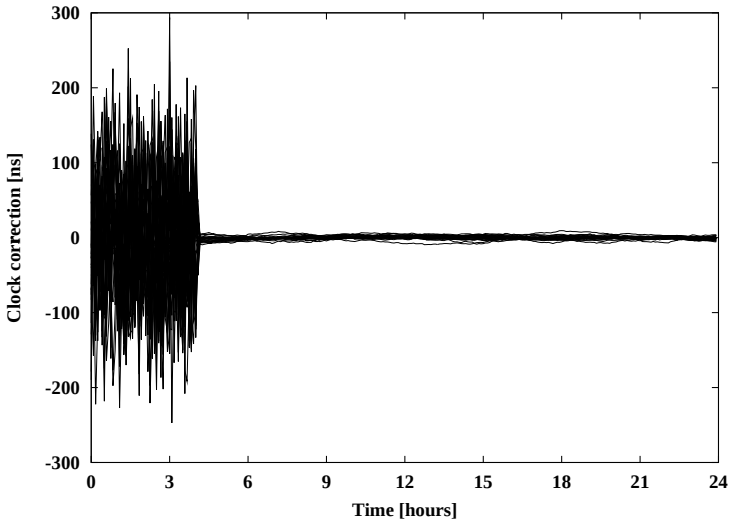

Figure 3.13: SA switched off on May 2, 2000 – effect on GPS satellite clocks.

the accuracy of unauthorized real-time positioning. With SA enabled an interpolation of the available 5-minute clock corrections from IGS to 30-second clock corrections was not possible with an acceptable accuracy. On May 2, 2000, SA was switched off and the satellite clocks are no longer disturbed by the dithering (see Figure 3.13). The question arises whether it is now possible to (linearly) interpolate the 5-minute clock corrections to 30-second intervals to process zero-difference data with a 30-second or even 10-second sampling without loosing accuracy. The question shall be answered using 5-minute, 30-second, and 10-second clock correction estimates. Our starting point are the CODE Rapid GPS satellite clock corrections of doy 034/2002 with a sampling of 5 minutes. These clock corrections are derived from a global network of up to 90 stations. In addition we have downloaded 1-second GPS data available at the IGS data center at CDDIS (Crustal Dynamics Data Information Center) [*CDDIS*, 2002] for doy 034/2002, $0^{\mathrm{h}}00^{\mathrm{m}}00^{\mathrm{s}}$ to $4^{\mathrm{h}}45^{\mathrm{m}}00^{\mathrm{s}}$ (21 stations). In a first step we compute 30-second clock corrections based on phase-difference observations and constrain them to the CODE Rapid 5-minute clock corrections [*Bock et al.*, 2003]. In a next step we repeat the procedure with 10-second sampling of the 1 Hz observations and constrain the resulting corrections to the 30-second clock corrections obtained in the previous step. From now on we have three sets of clock corrections with different sampling rates, namely 5-minute, 30-second, and 10-second available. We can now simulate GPS data for CHAMP based on the 10-second clock corrections together with the other input data already used for the simulations in Sections 3.6.1 and 3.6.2. For the simulation no observation noise is introduced for code and phase on the two frequencies in order to isolate the effect of the interpolation of the clock corrections on the resulting kinematic positions. No pre-screening of the data is performed for the same reason. We use a linear interpolation of the satellite clock corrections (Figures 3.14(a) to 3.14(d)) and an interpolation with a polynomial of degree three (Figures 3.15(a) and 3.15(b)). Figures 3.14(a), 3.14(c), and 3.15(a) show the results for the combined positions from error-free code and phase-difference observations. The plots show the differences w.r.t. the CHAMP orbit used for the simulation. Figures 3.14(b), 3.14(d), and 3.15(b) are the corresponding "zooms" of the y-component of the differences from $1^{\mathrm{h}}00^{\mathrm{m}}00^{\mathrm{s}}$ to $2^{\mathrm{h}}00^{\mathrm{m}}00^{\mathrm{s}}$. The structure of the differences is better visible in these figures. Table 3.4 summarizes the corresponding RMS errors of the Helmert transformations. In the first line the RMS errors for the "zero-

Table 3.4: RMS errors (mm) of the Helmert transformation between kinematic positions derived by error-free code and phase-difference observations and the a priori orbit used for the simulation.

	x (mm)	y (mm)	z (mm)
10 second	0.6	0.5	0.4
30 second	3.4	4.6	5.4
5 minutes	24.5	35.9	38.8
5 minutes (2)	25.0	34.9	41.3

test" solution with the 10-second clock corrections are listed.

Clearly, the linear interpolation of the 5-minute clock corrections to 30-second intervals is not sufficient if highest accuracy is the goal. The position errors introduced by the clock interpolation are up to 20 cm, which is not acceptable for a point positioning with phase observations. The interpolation of the 5-minute clock corrections with a polynomial of degree three is not significantly better (see bottom line in Table 3.4). On the other hand, one recognizes that a linear interpolation of the 30-second clock corrections to the 10-second intervals is sufficient to obtain 10-second clock corrections of sufficient accuracy. The RMS errors of the Helmert transformation between the a priori orbit and the kinematic positions are of the order of three to five millimeters (Table 3.4) using the interpolated 30-second clock correction to the 10-second intervals.

Interpolation is a good alternative considering the fact that the widely used sampling rate within the IGS is 30 second and that at present only a network of about 40 stations delivers one second data (each 15 minutes) to the IGS data centers. These are the only data which might be used for computing 10-second clock corrections. The effort to compute 10-second clock corrections is of course considerably higher than that of computing 30-second clock corrections using up to 120 stations and constraining these estimates to the official IGS 5-minute clock corrections. The clock corrections interpolated from 30-second values have an accuracy that is comparable to the original derived 10-second clock corrections. In addition the interpolated 10-second clock corrections have less gaps than the 10-second clock corrections. It may even happen that some satellites are not tracked by more than two stations of the small network of 40 stations. In this case we cannot estimate a clock correction for this particular epoch and for this particular satellite (which depends on redundant observations). When estimating the 30-second clock corrections using a network of up to 120 stations the redundancy is high and the estimation of clock corrections robust.

Highest accuracy may not be achieved by interpolating the 5-minute clock corrections to a 10-second interval but the results are promising that it should be possible without a big loss in accuracy. This could be very important because the 5-minute clock corrections are officially available at the IGS and the 30-second clock corrections have to be produced by our own procedure. In order to evaluate the effect of interpolated 5-minute clock corrections in comparison to the usage of interpolated 30-second clock corrections on real data we will compute a series of data with both clock informations and show the results in Section 6.4.

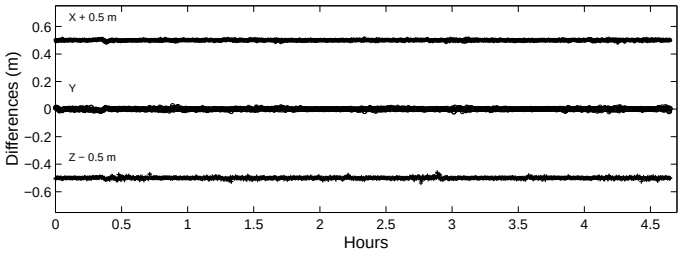

(a) Linear interpolated 30-second clock corrections.

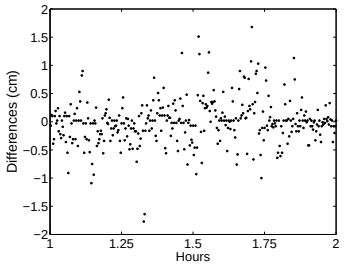

(b) Zoom in y-component 1:00-2:00.

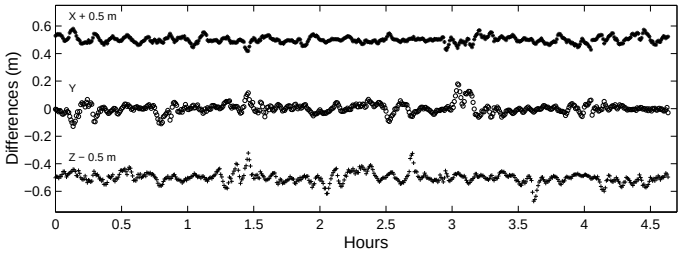

(c) Linear interpolated 5-minute clock corrections.

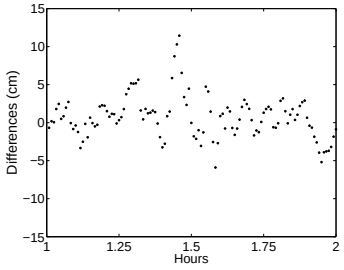

(d) Zoom in y-component 1:00-2:00.

Figure 3.14: Differences between kinematic positions and the a priori orbit of CHAMP (1) with linearly interpolated satellite clock corrections.

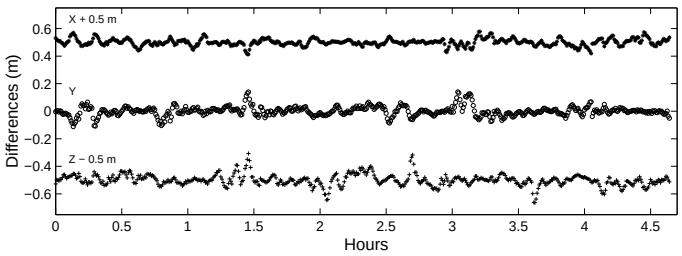

(a) Interpolated 5-minute clock corrections with a polynomial of degree 3.

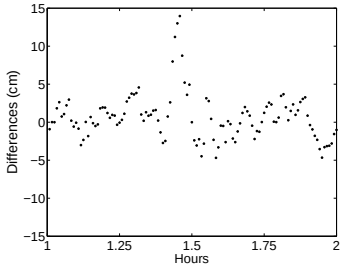

(b) Zoom in y-component 1:00-2:00.

Figure 3.15: Differences between kinematic positions and the a priori orbit of CHAMP (2) with polynomial interpolated satellite clock corrections.

4. Data Pre-processing

For all applications of GPS data an efficient pre-processing and data screening of the observations is essential. It is in particular an important issue for the processing of spaceborne receiver data. The data screening of the GPS observations in the program LEOKIN consists of two steps:

1. The data are pre-screened based on a priori information about the position of the receiver combined with a "majority voting" algorithm. Observations which are detected as outliers in this step are excluded from the following processing.

2. The least-squares adjustment step includes an iterative procedure where bad observations may be detected and can be excluded from the processing.

In Section 4.1 we explain in detail the first step of the screening which has been newly developed for the program LEOKIN. Section 4.2 describes the second step. The options to modify the performance of the pre-screening algorithm as well as other pre-processing issues of particular importance for the determination for LEO orbits are outlined (Section 4.3). Eventually, we will present a complete data screening procedure for zero-difference applications of permanent networks (Section 4.4).

4.1 Outlier Detection - Principle of Majority Voting

Outlier rejection is based on the principle of "majority voting". In order to explain the principles underlying the algorithm we briefly review the general principles of the program LEOKIN as shown in Figure 3.2. In a first step the code observations are processed for each epoch and the receiver clock is synchronized to GPS time (Section 3.2). In the second step the phase-differences between subsequent epochs are processed (Section 3.3). Both processing steps are preceded by the screening procedure.

Let us have a look at the code observations of the receiver for a particular epoch. The unknowns in the code observation equations (3.1) pertaining to one epoch are the three coordinates x, y, z, and the clock correction $c \cdot \delta$ of the receiver. For our data pre-screening algorithm we do not only use precise GPS orbits and clock corrections but also the a priori information available concerning the position of the receiver. If reliable and accurate information of this kind is available, only the receiver clock correction $c \cdot \delta$ remains as unknown in eqn. (3.1). The fact that the receiver clock correction should be, within the accuracy of the code, the same for all code observations of one epoch is the key assumption for the data pre-screening procedure. The procedure is robust due to only one unknown (receiver clock correction) and promises to find reliably the outliers. From the statistical point of view normally distributed measurements with a standard deviation σ are within $3 \cdot \sigma$ of the expected value with a probability of 99.73%. This means that the difference between two clock corrections derived from the observations to satellites i and j, respectively, should with the same probability lie within $3 \cdot \sqrt{2} \cdot \sigma_c = 3 \cdot \sigma_{c_{scr}}$, where σ_c is the standard deviation of the ionosphere-free linear combination of the code observations. Our algorithm is set up in the following way:

1. All possible differences are formed between the receiver clock corrections $\gamma_i = (c \cdot \delta)_i, i = 1, \ldots, n_s$ computed for each satellite i. A check is performed whether the absolute value of each difference is smaller than $3 \cdot \sigma_{c_{scr}}$:

$$\Delta\gamma_{ij} = |\gamma_i - \gamma_j| \leq 3 \cdot \sigma_{c_{scr}}, \quad i = 1, 2, \ldots, n_s - 1; \quad j = i + 1, i + 2, \ldots, n_s. \tag{4.1}$$

All γ_j meeting the above condition with a particular γ_i are assigned to the same group as γ_i. Figure 4.1 shows that different groups may result for the observations of one epoch. It may happen that two clock corrections (A $= \gamma_i$ and B$= \gamma_j$) meeting the above condition are already assigned to a particular group, e.g., A to group one (X) and B to group two (O) (Figure 4.1). In this case all members of the second group are assigned to the first group. In our example this means that all values γ_i are finally in one group. The example illustrates that not all differences between the $\gamma_i's$ of one group are necessarily within the limits of $3 \cdot \sigma_{c_{scr}}$. In this example the largest difference between the $\gamma_i's$ is about $10 \cdot \sigma_{c_{scr}}$. In the worst case this difference is $3 \cdot (n_s - 1) \cdot \sigma_{c_{scr}}$. This is due to the design of the pre-screening algorithm and we may influence the size of the group with matching clock corrections (γ_i) by changing the value of $\sigma_{c_{scr}}$. The smaller $\sigma_{c_{scr}}$ the smaller the absolute difference between the smallest and the largest γ_i of a group will be.

2. The values γ_i' of the group with the largest number of members ("majority voting") are used to compute a mean value $\bar{\gamma}'$ and a standard deviation $\sigma_{\gamma'}$.

3. Each receiver clock correction γ_i of the processed epoch is compared with this mean value $\bar{\gamma}'$ ($\Delta\bar{\gamma}_i = |\gamma_i - \bar{\gamma}'|$).

$$\gamma_i = \begin{cases} \text{b} & : \quad \Delta\bar{\gamma}_i \leq \beta \cdot \sigma_{\gamma'} \\ \text{c} & : \quad \Delta\bar{\gamma}_i > \beta \cdot \sigma_{\gamma'} \end{cases} \tag{4.2}$$

   where

   - b means that the observation is accepted, but has to be checked within the following iterative least squares adjustment step, and
   - c means that the observation is definitely an outlier.

If the difference $\Delta\bar{\gamma}_i$ is larger than a given multiple β of the computed $\sigma_{\gamma'}$ (e.g., $\beta = 10$) the observation is marked as an outlier and not used in the following point positioning procedure. β is a defining parameter of the algorithm. If the data would have no systematic errors, all differences $\Delta\bar{\gamma}_i$ would be with a probability of 99.73% within $3 \cdot \sigma_{\gamma'}$ ($\rightarrow \beta = 3$). Since we cannot completely avoid systematic errors in the data (insufficient a priori information, biased GPS clock corrections, etc.), this assumption

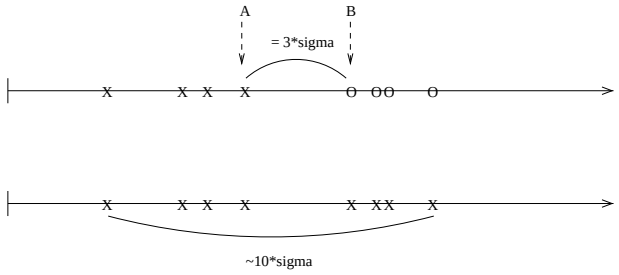

Figure 4.1: Example for the grouping of γ_i.

is not met. That is why we provide the possibility to select the value for β manually. If we would choose a large value for β (e.g., $\beta = 30$) the pre-screening will only detect extreme outliers and the other bad observations remaining in the processing have to be found in the second step, the iterative least squares adjustment step. The data quality after the pre-screening depends therefore on the screening options. The performance of the algorithm may be influenced by modifying the following input parameters:

- the σ_c for arranging the observations γ_i into groups (depends on the code data quality),
- the standard deviation for setting the rejection threshold (it may either be derived from the observations $\gamma_i' \rightarrow \sigma_{\gamma'}$ or specified as fixed value $\sigma_{\gamma_{fix}}$), and
- the factor β.

The same pre-screening algorithm is applied to the phase-difference observations where the σ_c is replaced by $\sqrt{2} \cdot \sigma_p$ (the factor $\sqrt{2}$ arises because the difference of two phase observations is analyzed) and where γ_i is the receiver clock correction difference of subsequent epochs derived from the phase observations to satellite i.

The key factor limiting the performance of the pre-screening approach is the quality of the a priori information. This is in particular the case when processing LEO data. For the point positioning with the code this is not a serious problem, but for the screening of the phase-differences the quality of the a priori information is critical (see Section 3.4). Bad a priori information may "mimic" bad phase observations which would then be erroneously removed as outliers by the screening algorithm. To be sure that this does not happen the rejection threshold should not be set too small. This implies that a second screening step has to follow in order to find all observations deteriorating the solution.

4.2 Iterative Screening Procedure

The second data screening step is included in the least-squares adjustment step. It follows the same scheme for the code as for the phase-difference processing. We will explain it based on the code processing.

1. The code observations of the processed epoch which have been accepted by the pre-screening procedure are used to generate a position estimate. No solution can be computed for a particular epoch if the number of satellites per epoch is $n_s < 4$ and the procedure stops.
2. The solution is checked whether the RMS error of the position estimate is smaller than an externally specified threshold. If yes, the solution is accepted. If not, a series of n_{s_a} solutions (n_{s_a} is the number of accepted observations in the processing) is computed, where one observation is removed in each attempt.
3. The solution with the smallest RMS error is selected and the observation which was excluded for this solution is marked as an outlier.
4. Point 2 and 3 are iterated as long as the solution is not accepted and more than four observations are available.

It is clear, that this second data screening step is not as robust as the first pre-screening step. We have four unknowns ($x, y, z, c \cdot \delta$) and between five and eight or ten observations depending on the number of tracked satellites. This means that the degree of freedom of this adjustment is small and the identification of outliers is difficult.

4.3 Processing Issues Related to LEOs

The processing issues of particular importance for LEOs include not only the pre-screening based on the principle of "majority voting". Other issues, such as cut-off angle and elevation-dependent weighting of the observations have to be considered as well.

The zenith direction of a LEO spacecraft may be defined by the unit vector

$$\boldsymbol{e}_z \doteq \frac{\boldsymbol{r}}{|\boldsymbol{r}|}, \tag{4.3}$$

where $\boldsymbol{r}$ is the geocentric unit vector of the satellite. This definition is independent of the attitude of the satellite and of the place where the GPS antenna is mounted. The limit of the zenith angle is given by the Earth's limb at approximately 110 to 115 degrees for a satellite at 400 to 700 km altitude.

The zenith direction of the GPS antenna is defined as the normal to the receiving antenna's micro-chip array. This zenith direction must be given in the body-fixed coordinate system of the satellite. We thus need information about the attitude of the satellite, i.e., the orientation of the satellite body in the inertial system to relate the two zenith directions. This second zenith angle is relevant for the discussion of multipath caused by the surface of the satellite body or for the use of GPS antenna patterns to model phase center variations.

If the GPS antenna is placed on the top of the satellite body both definitions may be identical. If the antenna is not on the top of the satellite body as, e.g., in the case of GPS/MET (Section 2.3.2) and JASON-1 (Section 2.3.6), the two zenith angles are different.

The nominal orientation of a typical body-fixed system of a LEO (e.g., of CHAMP) is given schematically in Figure 4.2. The body-fixed Cartesian coordinate system is defined by the X-, Y-, and Z-axis. Normally the body-fixed Z-axis is pointing towards the geocenter of the Earth. The body-fixed X-axis is perpendicular to the Z-axis and is pointing approximately into the flight direction (only approximately because of the orbital eccentricity). The body-fixed Y-axis completes the Cartesian right-handed system. For CHAMP the difference between the real and the nominal attitude (the real Z-axis of the body-fixed system and the direction to the geocenter) is in most cases at maximum two degrees (maximum five centimeters for the antenna offset vector) and is corrected if it is getting too large by the cold gas propulsion system which leads to several attitude maneuvers during one day. In the case of CHAMP the differences are small enough that normally the nominal attitude may be used for the determination of the orientation of the GPS antenna and for the correction of the antenna offsets to the center of mass. Real attitude data are available for CHAMP, as well.

To get an idea what can be expected concerning quantity and quality of the GPS data for a LEO we will first have a look at the performance of the GPS receivers of CHAMP and SAC-C. We focus on the performance of these satellites because most LEO GPS data analyzed here stem from the two spacecrafts.

4.3.1 GPS Receiver Performance

CHAMP

The CHAMP satellite is orbiting in a near-circular orbit with an inclination of $i = 87°$ and an orbit altitude between 470 km (at the beginning) and 300 km (at the end of the mission). The BlackJack GPS receiver on-board CHAMP has 16 channels for each frequency. They are not only dedicated to the POD antenna on top of the satellite but also to the GPS limb sounding antenna at the rear side of the satellite body and to the experimental GPS altimetry antenna at the bottom of the satellite body. At maximum twelve channels are available for the POD antenna. At the beginning of the mission only the

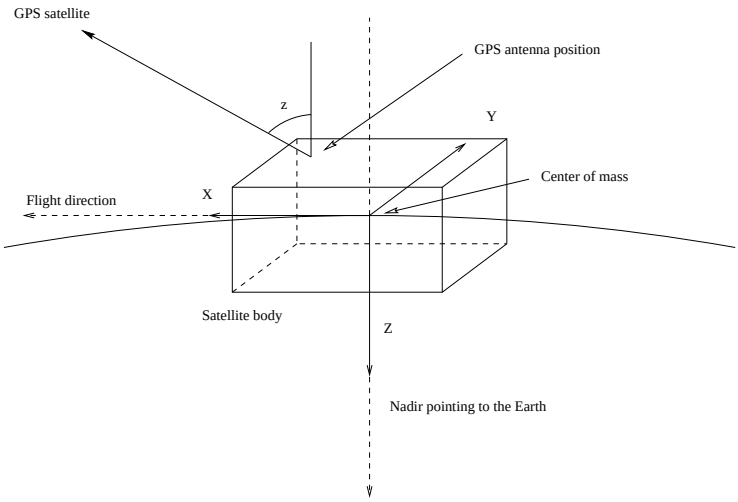

Figure 4.2: Satellite body-fixed system (schematically).

Table 4.1: Summary of switches in the tracking software of the GPS receiver on CHAMP [*Grunwaldt,* 2002].

Switch at doy	Max. number of tracked satellites	Switch for a short period	Max. number of tracked satellites
199/2000	7		
		026/2001 - 027/2001	8
		041/2001 - 042/2001	8
		047/2001	6
		054/2001 - 056/2001	8
081/2001	8		
		129/2001 (24 h test)	9
064/2002	10		

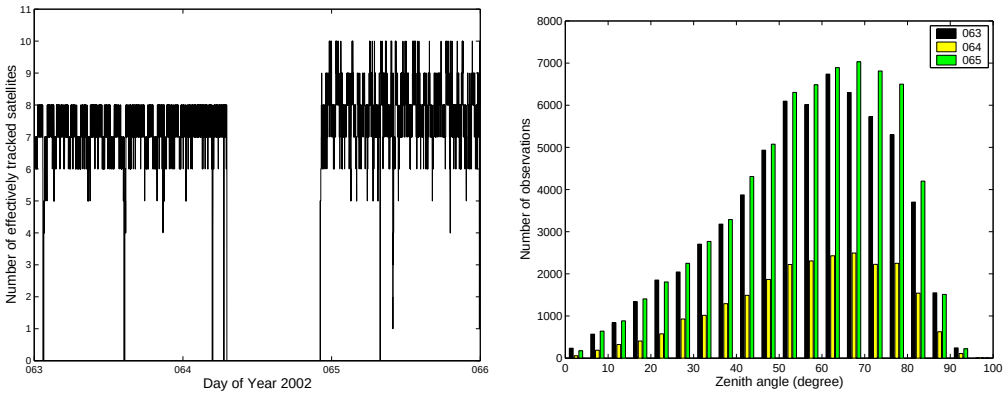

(a) Number of effectively tracked satellites.

(b) Histogram of the observations vs. zenith angle for three days.

Figure 4.3: CHAMP receiver performance for doy 063 to 065, 2002 (software switch during break).

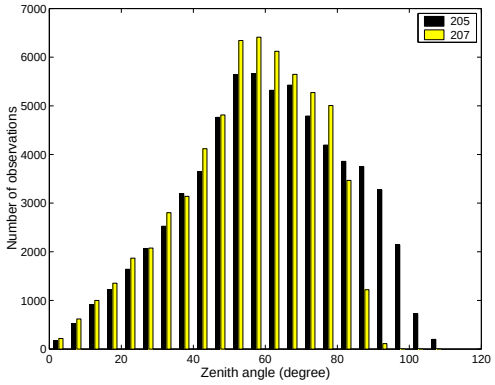

Figure 4.4: Change in tracking performance after software upload on doy 206/2001.

POD antenna was switched on; because of software problems the tracking capability was limited to seven satellites [*Loyer*, 2000]. In the meantime the receiver tracks up to ten satellites simultaneously (Status: April 10, 2003).

For all zero-difference kinematic approaches at least four good observations must be available because otherwise no position can be determined. Therefore, it is important to know how many satellites can be tracked at maximum by the receiver on-board a LEO. Table 4.1 lists the maximum number of satellites tracked by the GPS receiver on-board CHAMP for different time periods. After the activation of the GPS receiver on doy 199/2000 (July 17, 2000) the receiver tracked up to seven satellites with its POD antenna. The receiver was then commanded to track up to eight satellites simultaneously on doy 081/2001 (March 22, 2001). On doy 064/2002 (March 5, 2002) the receiver was eventually able to track up to ten satellites.

Figure 4.3(a) shows the number of tracked satellites for doy 063 to 065/2002. The receiver actually tracked up to eight satellites until it stopped tracking on doy 064 for several hours. After this break, during which the software change took place, it started again with tracking up to ten satellites simulta-

Table 4.2: Summary of switches in the tracking software of the GPS receiver on SAC-C.

Switch at doy	Max. number of tracked satellites	Switch for a short period	Max. number of tracked satellites
327/2000	8		
191/2001	6		
		220/2001 - 222/2001	9
		222/2001	6
223/2001	7		
036/2002	12		
089/2002	8		

neously. Figure 4.3(b) shows the histogram of the observations for doy 063 to 065/2002 as a function of the zenith angles of the observed satellites. Each day is represented by one of the three bars for each bin. On doy 064 few observations were made due to the interruption lasting for several hours. Furthermore we recognize the increased number of tracked satellites on doy 065 by a larger number of observations with zenith distances between 65 and 85 degrees. The increase of the maximum possible number of tracked satellites improves the observation geometry and is therefore very useful for the kinematic POD approaches for CHAMP.

Another very useful change in the tracking performance of the CHAMP receiver was made on doy 206/2001. On this day an upload of the tracking software was made [*Grunwaldt,* 2002] and the effects can be seen in Figure 4.4. Before doy 206 the receiver tracked satellites also below the local horizon (90 degrees), but after the upload it tracked only satellites above the local horizon. This fact is important for the data processing as will be seen in Section 4.3.3.

SAC-C

The Earth observation satellite SAC-C (Section 2.3.5) is orbiting at an altitude of 702 km and the sun-synchronous orbit has an inclination of $i = 98°$. The BlackJack GPS receiver on-board SAC-C has twelve channels. Table 4.2 lists the most important changes of the tracking software on SAC-C we have identified. At present the SAC-C receiver is tracking up to eight satellites simultaneously (Status: April 10, 2003).

Figures 4.5(a) and 4.5(b) display the same information for SAC-C as Figures 4.3(a) and 4.3(b) for CHAMP. The two related figures to SAC-C show, as expected, a more balanced performance for the three days because no software switch was made during this time interval for the SAC-C receiver.

4.3.2 Data Quality and Pre-screening Options

Data quantity is in general a good indication for the performance of a GPS receiver and therefore, in a certain sense, also for the quality of the results to be expected. The number and lengths of data gaps are an important criterion for the performance of a GPS receiver, as well. In particular for kinematic point positioning we absolutely need observations to determine the position at a specific epoch. This is an essential difference w.r.t. the approaches based on dynamic orbit modeling, where gaps may be bridged (to some extent) by the equation of motion of the satellite. The data sets of both satellites, CHAMP and SAC-C, have data gaps which may be attributed to receiver resets or to the downlink periods.

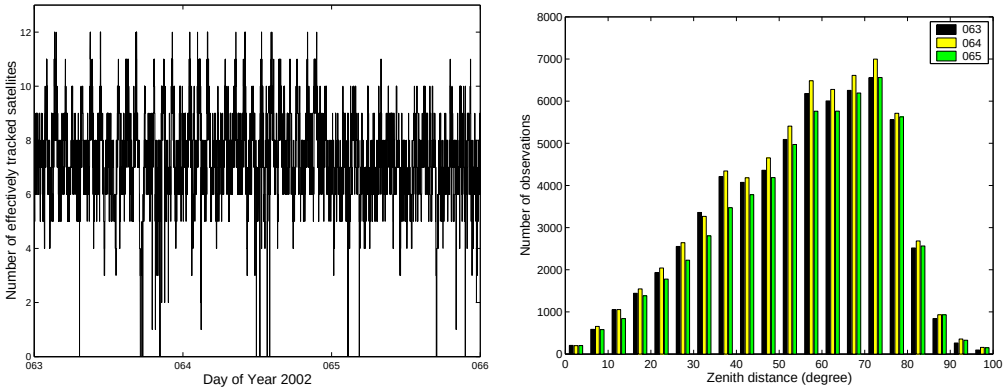

(a) Number of effectively tracked satellites.

(b) Histogram of the observations vs. zenith distances for three days.

Figure 4.5: SAC-C receiver performance for doy 063 to 065, 2002.

We have seen that different screening options may be needed to optimize the pre-processing procedure. Studies were performed to get insight concerning the effect of the options. The following tests are based on data stemming from SAC-C of doy 051/2001 (February 20, 2001). From CHAMP we use the GPS data of doy 152, 2001 (June 1, 2001). Figure 4.6 shows the number of effectively tracked satellites for the two days considered. The SAC-C data have no gap and the CHAMP data have one gap of about 15 minutes and in addition two single epochs are missing.

The data sets are ideal for studying the pre-processing options outlined in Section 4.1 and other processing issues.

Let us first study the numerical values for $\sigma_{\gamma'}$, the RMS error of the clock correction terms γ'_i of the biggest group of "good" observations. As $\sigma_{\gamma'}$ is actually computed from the clock corrections it is a measure for the data quality. All available data were used for this test, implying that the observations tracked below the local horizon were used, as well. Figures 4.7(a) to 4.7(d) give the histograms of $\sigma_{\gamma'}$ for all epochs of the day considered. The a priori standard deviation used for the code and phase screening are $\sigma_{c_{scr}} = 1.0$ m ($\sigma_c \approx 0.7$ m) and $\sigma_{p_{scr}} = 0.01$ m ($\sigma_p = 0.005$ m), respectively, for both satellites. The selected value for $\sigma_{obs_{scr}}$ is marked by a vertical line. The percentage of observations in total used for the determination of the values for $\sigma_{\gamma'}$ are given in the figures, too.

The histograms of $\sigma_{\gamma'}$ are different for the two receivers. Obviously, the data of the CHAMP receiver are noisier than those of the SAC-C receiver. For SAC-C $\sigma_{c_{scr}} = 1.0$ m is representative for the histogram of $\sigma_{\gamma'}$ (Figure 4.7(a)). For the phase observations the histogram of $\sigma_{\gamma'}$ is narrower than expected from the introduction of $\sigma_{p_{scr}} = 0.01$ m. For CHAMP, on the other hand, $\sigma_{\gamma'}$ of the code observations show a broader histogram. The same is true for $\sigma_{\gamma'}$ obtained from the phase observations.

For SAC-C the values of $\sigma_{c_{scr}} = 1.0$ m and $\sigma_{p_{scr}} = 0.01$ m seem to be appropriate, but for CHAMP these values seem to be too optimistic. This behavior may be due to the observations gathered below local horizon. The conclusion from this test is to adopt the values to $\sigma_{c_{scr}} = 1.5$ m and $\sigma_{p_{scr}} = 0.015$ m for CHAMP.

Figures 4.7(e) and 4.7(f) show the histogram of $\sigma_{\gamma'}$ using $\sigma_{c_{scr}} = 1.5$ m and $\sigma_{p_{scr}} = 0.015$ m. A broader histogram is obtained for $\sigma_{\gamma'}$ than in the corresponding Figures 4.7(c) and 4.7(d) for both, the code and the phase observations. The percentage of observations used for the determination of $\sigma_{\gamma'}$

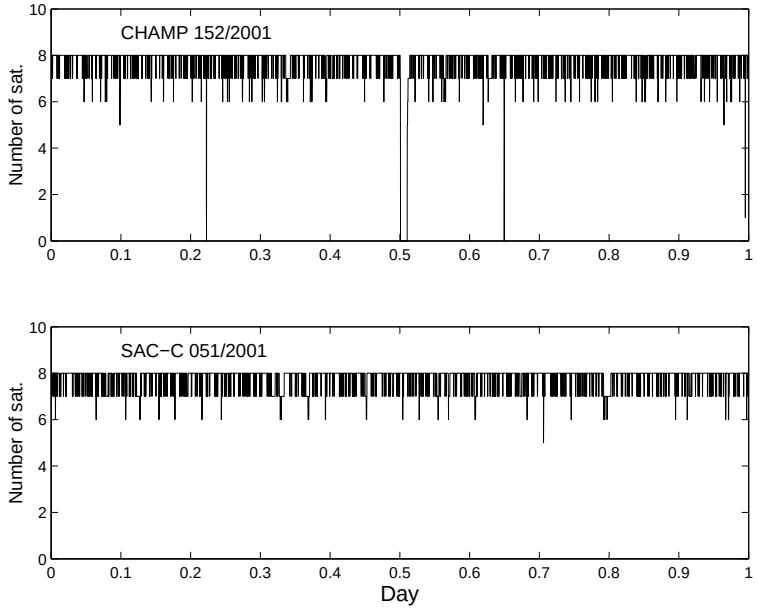

Figure 4.6: Number of effectively tracked satellites for CHAMP 152/2001 and SAC-C 051/2001.

is, on the other hand, ten percent higher for the code observations and five percent higher for the phase observations, if we use the bigger value for $\sigma_{obs_{scr}}$. The question whether the values of 1.0 m and 0.01 m, or, alternatively, 1.5 m and 0.015 m should be used in practice, will be answered at the end of this section after having studied all options relevant for the performance of the pre-screening algorithm.

One day of data for each satellite is of course not representative for a long data set of the two satellites. Figures 4.8(a) and 4.8(b) for instance show the histograms of $\sigma_{\gamma'}$ using $\sigma_{c_{scr}} = 1.0$ m and $\sigma_{p_{scr}} = 0.01$ m for SAC-C on doy 067/2002. These more recent data of SAC-C show a similar performance as the data of doy 051/2001 with the difference that approximately ten percent more observations are used for the determination of $\sigma_{\gamma'}$. The difference between the two days is that the receiver tracked up to twelve satellites simultaneously on doy 067/2002 instead of eight on doy 051/2001.

Figures 4.8(c) and 4.8(d) show the histograms of the $\sigma_{\gamma'}$ values using $\sigma_{c_{scr}} = 1.0$ m and $\sigma_{p_{scr}} = 0.01$ m for CHAMP on doy 145/2001. This day is only one week before doy 152/2001, the data analyzed in Figure 4.7, but shows a rather different behavior. As the last example we include the histogram of the $\sigma_{\gamma'}$ values for CHAMP on doy 067/2002 (Figures 4.8(e) and 4.8(f)). This day falls into the time period where the receiver did no longer track below the local horizon and where up to ten satellites were observed simultaneously. The histograms are similar to the histograms of doy 145/2001 with the difference that the percentage of observations used for the determination of the corresponding $\sigma_{\gamma'}$ is higher and the histogram of $\sigma_{\gamma'}$ of the code observations is slightly narrower than for doy 145/2001. The two examples of CHAMP seem to indicate that the data quality of doy 152/2001 is worse than normal. We will nevertheless use this data set for further studies to get insight into the performance of the pre-screening algorithm for data of a relatively bad quality.

Next, we study $\Delta\bar{\gamma}_i$, the difference between each γ_i and the mean value $\bar{\gamma}'$ defined by eqn. (4.2). The pre-screening procedure checks whether the values of $\Delta\bar{\gamma}_i$ lie within the limits defined by $\beta \cdot \sigma_{\gamma'}$ of eqn. (4.2). Therefore, we study histograms of the ratios $\Delta\bar{\gamma}_i / \sigma_{\gamma'}$.

These histograms may be found in Figures 4.9(a) and 4.9(b) for SAC-C 051/2001. For CHAMP

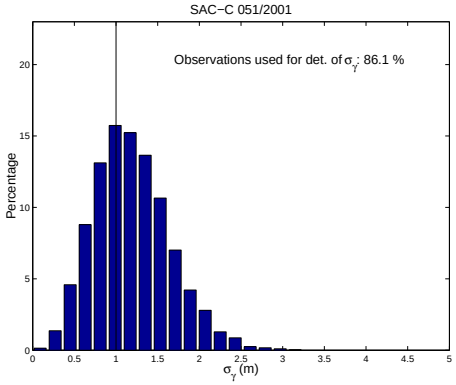

(a) Code - $\sigma_{c_{scr}} = 1.0$ m.

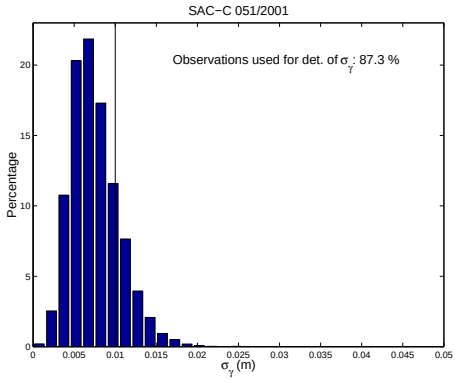

(b) Phase - $\sigma_{p_{scr}} = 0.01$ m.

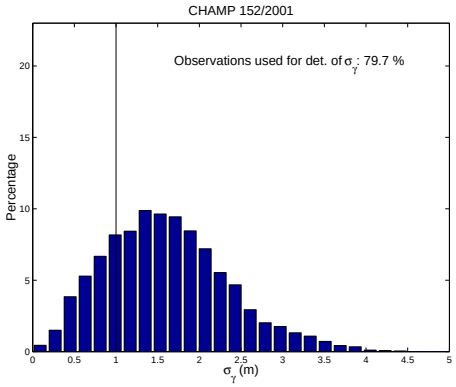

(c) Code - $\sigma_{c_{scr}} = 1.0$ m.

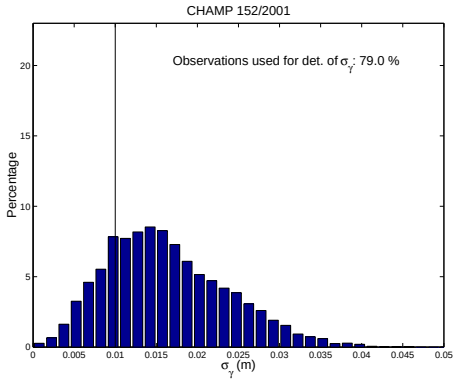

(d) Phase - $\sigma_{p_{scr}} = 0.01$ m.

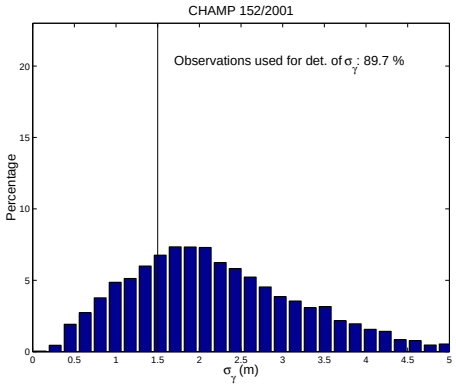

(e) Code - $\sigma_{c_{scr}} = 1.5$ m.

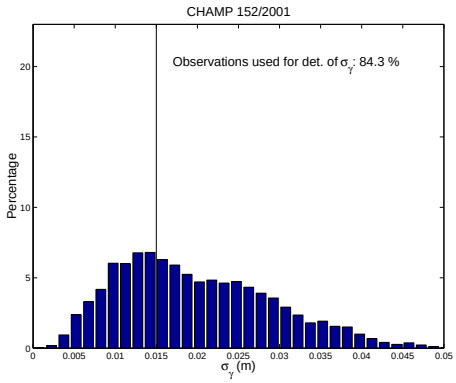

(f) Phase - $\sigma_{p_{scr}} = 0.015$ m.

Figure 4.7: Histograms of $\sigma_{\gamma'}$ values for SAC-C 051/2001 and CHAMP 152/2001; Vertical line at $\sigma_{obs_{scr}}$.

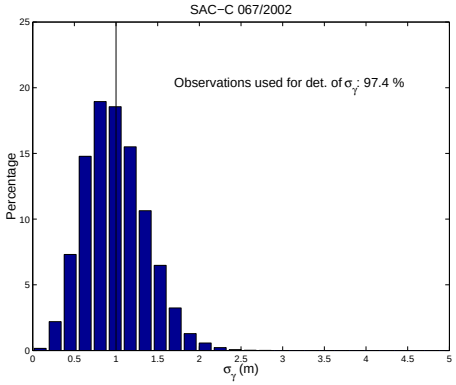

(a) Code - $\sigma_{c_{scr}} = 1.0$ m.

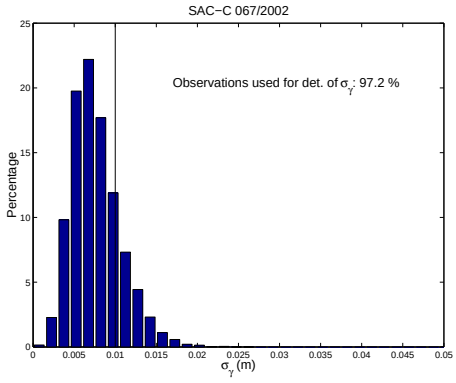

(b) Phase - $\sigma_{p_{scr}} = 0.01$ m.

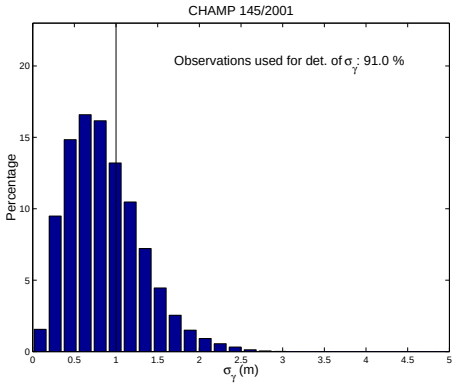

(c) Code - $\sigma_{c_{scr}} = 1.0$ m.

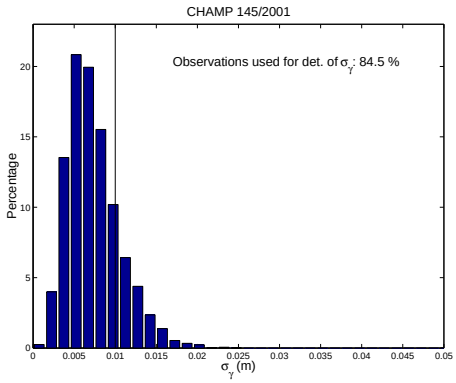

(d) Phase - $\sigma_{p_{scr}} = 0.01$ m.

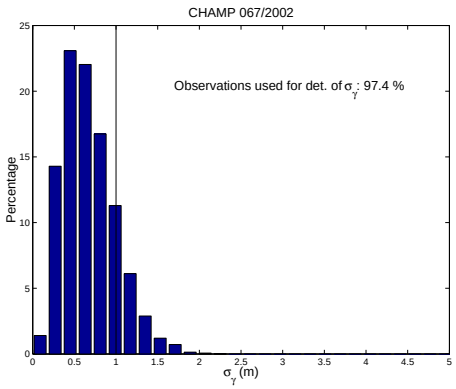

(e) Code - $\sigma_{c_{scr}} = 1.0$ m.

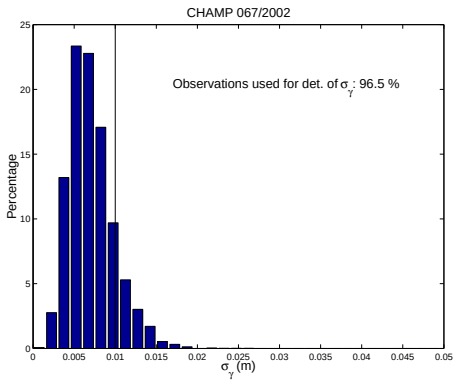

(f) Phase - $\sigma_{p_{scr}} = 0.01$ m.

Figure 4.8: Histogram of $\sigma_{\gamma'}$ values for SAC-C 067/2002 and for CHAMP 145/2001 and 067/2002.

152/2001 both examples (the first using $\sigma_{c_{scr}} = 1.0$ m and $\sigma_{p_{scr}} = 0.01$ m and the second using $\sigma_{c_{scr}} = 1.5$ m and $\sigma_{p_{scr}} = 0.015$ m) are included in Figures 4.9(c) and 4.9(d) and in Figures 4.9(e) and 4.9(f). The ratios on the horizontal axes are given in units of β (see eqn. (4.2)). The bar on the right hand side in each figure is the sum of all ratios larger than $\beta = 20$. Two versions are given for each histogram, where the one to the left contains the entire information, the one on the right is cut at three percent on the vertical axis.

The values of the ratios depend directly on the distribution of the $\sigma_{\gamma'}$ (Figures 4.7(a) to 4.7(f)). The histograms of code and phase-differences are different. There are differences between the histograms for CHAMP and SAC-C, as well. As a consequence, the proper choice of the factor β determining the rejection threshold ($\beta \cdot \sigma_{\gamma'}$) for outliers depends also on the data quality. As expected the histograms for the two examples for CHAMP are different. The histograms of the first example are broader for both, the code and the phase, when compared to the second example. For the phase-differences the distribution is the same for the bins $\beta >$12, implying that the rejection of large outliers is the same no matter which $\sigma_{p_{scr}}$ is selected. For the code observations a similar conclusion cannot be drawn due to the higher percentage of the ratios in all bins $\beta > 3$.

The question is whether it is reasonable to select a threshold of, e.g., $\beta = 3$ or one with $\beta \gg 3$, in which case observations of a moderate quality are included and would contribute to a more stable point positioning solution. On the other hand, if the rejection threshold is set to a big value, bad observations can deteriorate the quality of the point positions. Tests were carried out using $\beta = 2$, 3, 5, 10, 20, 30 and 40 to identify the optimum value.

Figures 4.10(a) and 4.10(b) show the percentage of deleted observations for SAC-C on doy 051/2001 for different values of the threshold value β for code and for phase-difference observations. Figures 4.10(c) and 4.10(d) give the same information for CHAMP on doy 152/2001 for the first example ($\sigma_{c_{scr}} = 1.0$ m, $\sigma_{p_{scr}} = 0.01$ m), Figures 4.10(e) and 4.10(f) for the second example ($\sigma_{c_{scr}} = 1.5$ m, $\sigma_{p_{scr}} = 0.015$ m). The lower curves correspond to the percentage of observations deleted by the pre-screening procedure. The upper curves correspond to the percentage of observations removed by the complete point positioning procedure, i.e., they include the observations marked due to the rejection criterion in the iterative least squares adjustment step.

The figures show a very different behavior for SAC-C and for CHAMP, as could be expected from inspecting Figures 4.9(a) to 4.9(f). For the code observations of SAC-C in Figure 4.10(a) the difference between the two curves is above 3% for all values of β. A larger value of β means that many observations, which are actually outliers, pass the pre-screening algorithm. In this case the bad observations have to be found during the least squares adjustment step. The flattening of the upper curve in Figure 4.10(a) indicates that most of them are found for $\beta > 10$. The decrease of the percentage from $\beta = 2$ to $\beta = 10$ is remarkable. The curves give no information on which is the correct percentage of deleted observations. It seems, however, that the percentage for $\beta =$2 or 3 is too large.

On the other hand, Figure 4.10(b) for the phase-difference processing shows that both curves are flatter than for the code processing and nearly coincide. This means that in the case of the phase-difference processing most bad observations are already rejected by the pre-screening algorithm almost independently of the value of β. This indicates that the phase observations show more or less only extreme outliers due to cycles slips or phase resets. For CHAMP the curves look different. The decrease of the percentage of removed code observations with increasing values of β is more pronounced than for SAC-C, but the difference between the upper and lower curve is less pronounced. For the phase observations this difference is larger than for SAC-C and the percentage of deleted observations is also larger. For $2 \leq \beta \leq 10$, the percentage is clearly larger for the first example (Figure 4.10(d)) of CHAMP than for the second one (Figure 4.10(f)). These diagrams underline once more that there are significant

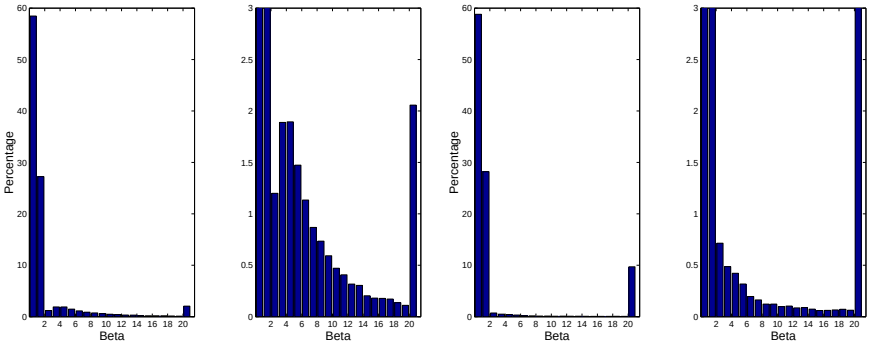

(a) Code – $\sigma_{c_{scr}} = 1.0$ m – SAC-C 051/2001.

(b) Phase-differences – $\sigma_{p_{scr}} = 0.01$ m – SAC-C 051/2001.

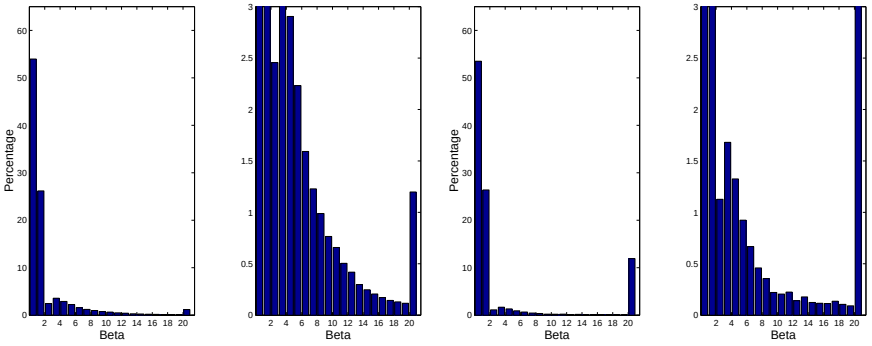

(c) Code – $\sigma_{c_{scr}} = 1.0$ m – CHAMP 152/2001.

(d) Phase-differences – $\sigma_{p_{scr}} = 0.01$ m – CHAMP 152/2001.

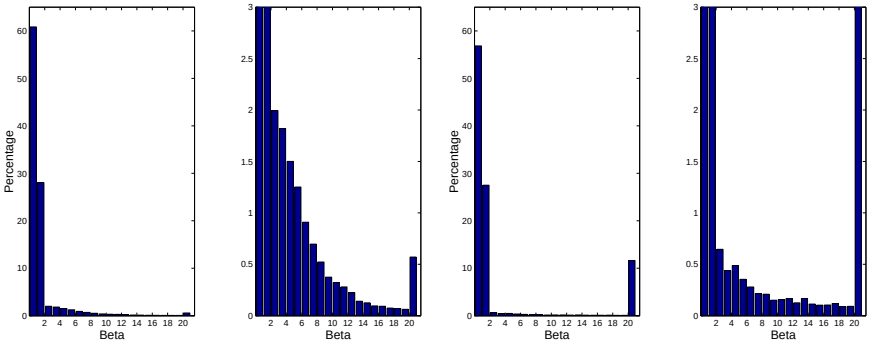

(e) Code – $\sigma_{c_{scr}} = 1.5$ m – CHAMP 152/2001.

(f) Phase-differences – $\sigma_{p_{scr}} = 0.015$ m – CHAMP 152/2001.

Figure 4.9: Histograms of $\Delta\bar{\gamma}_i/\sigma_{\gamma'}$ in units of β for code and phase-difference observations in the pre-screening algorithm.

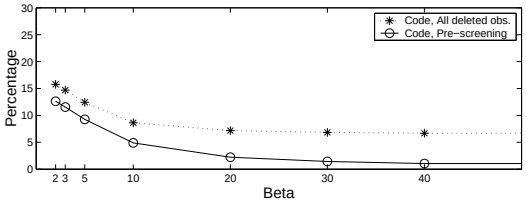

(a) Percentage of deleted code observations – SAC-C 051/2001 – $\sigma_{c_{scr}} = 1.0$ m.

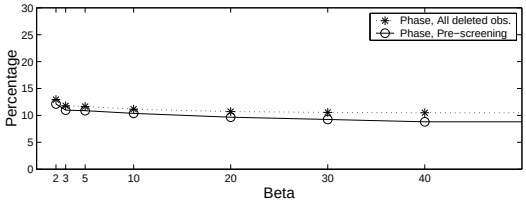

(b) Percentage of deleted phase-difference observations – SAC-C 051/2001 – $\sigma_{p_{scr}} = 0.01$ m.

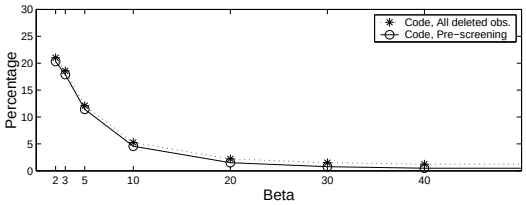

(c) Percentage of deleted code observations – CHAMP 152/2001 – $\sigma_{c_{scr}} = 1.0$ m.

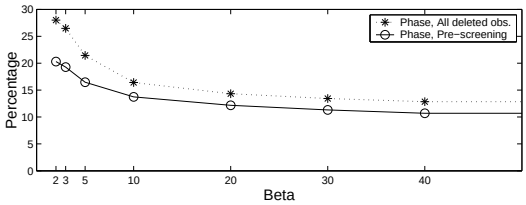

(d) Percentage of deleted phase-difference observations – CHAMP 152/2001 – $\sigma_{p_{scr}} = 0.01$ m.

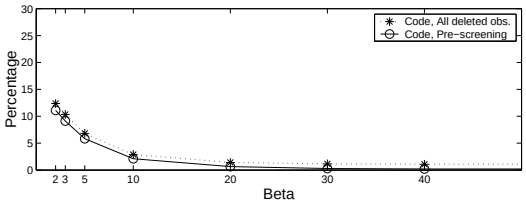

(e) Percentage of deleted code observations - CHAMP 152/2001 - $\sigma_{c_{scr}} = 1.5$ m.

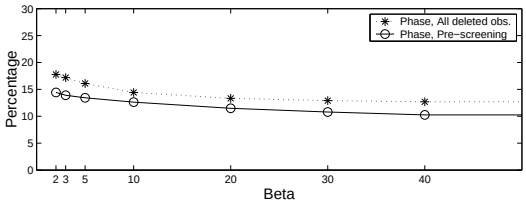

(f) Percentage of deleted phase-difference observations - CHAMP152/2001 - $\sigma_{p_{scr}} = 0.015$ m.

Figure 4.10: Percentage of deleted observations for different values of β.

differences of data quality of the two receivers on CHAMP and on SAC-C, respectively, for the days considered. If we compare the two CHAMP examples we recognize that there are remarkable differences in the two curves for $\beta < 20$. For $\beta \geq 20$ the differences are marginal and it does not matter which value for $\sigma_{obs_{scr}}$ was used.

In summary we may state that the pre-screening algorithm is working reliably for different receiver data. To make the procedure robust we have to take the data quality into account, i.e., the pre-screening options have to be selected according to the data performance and quality of the receiver. The studies performed to test the pre-screening options let us conclude that in the case of CHAMP and SAC-C the choice of $\sigma_{c_{scr}} = 1.0$ m, $\sigma_{p_{scr}} = 0.01$ m, and $10 \leq \beta \leq 20$ seems to be appropriate. This choice is appropriate for CHAMP, too, because we have seen that the lower data quality on doy 152/2001 is an exception, but that the pre-screening algorithm with the above recommended values still gives satisfactory results. Nevertheless these are only preliminary results because we looked only at the performance of the pre-screening algorithm itself. Whether the kinematic point positioning solution is better with a small or a large value for β can be concluded only when we study the impact of the values on the resulting kinematic positions in Chapter 6.

4.3.3 Elevation-dependent Weighting and Cut-off Angle

The cut-off angle as well as the function used for the elevation-dependent weighting of observations significantly influence the resulting kinematic positions. [*Rothacher et al.*, 1998] propose to give an observation at zenith distance z of a terrestrial station a weight of

$$w(z) = \cos^2(z). \tag{4.4}$$

It is an open question whether this weighting scheme is appropriate for LEO GPS data, as well. LEO observations at low elevations are not corrupted by tropospheric refraction (only directly at the Earth's limb they are corrupted), but multipath effects may nevertheless be an important source for degradation of low-elevation data quality – in particular because a LEO may track satellites at zenith angles significantly larger than 90° (up to $105^\circ - 110^\circ$). In fact, CHAMP and SAC-C tracked in their early mission times satellites below the local horizon, which raised the question whether such observations are of any use at all. This question is implicitly answered for CHAMP by the fact that today (since doy 206/2001) no observations are gathered below the local horizon of the spacecraft.

Studies were nevertheless made to see whether low elevation observations improve the point positioning, if an appropriate weighting is used. A simple modification of the weighting function (4.4) allows it to include observations at $z \geq 90^\circ$

$$w(z) = \cos^2(\alpha \cdot z), \tag{4.5}$$

Figure 4.11 shows the weighting function $w(z)$ for $\alpha = 1$ and $\alpha = 0.75$, where the weights down to $z = 120^\circ$ are given. The "stretching factor" α is obviously useful.

Multipath may heavily degrade the observations at low elevations. It is therefore also important to study the contribution of observations at zenith angles $80^\circ \leq z \leq 90^\circ$. Further studies and results made by using different modifications of the developed pre-screening algorithm, different weighting functions and different cut-off angles for LEO data are presented in detail in Chapter 6.

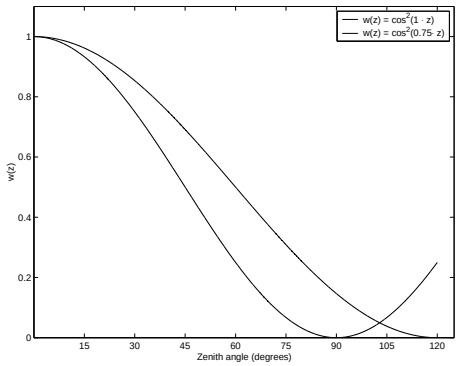

Figure 4.11: Different weighting functions $w(z)$.

4.4 Development of a Data Screening Procedure for a Permanent Network

A new pre-processing procedure based on the observations of one roving receiver had to be developed for processing GPS observations of spaceborne GPS receivers. As the trajectory of the spaceborne receiver may be modeled over long time spans (hours or even days) with accuracies on the level of few centimeters, this particular case of kinematic positioning is very closely related to static positioning. It is thus tempting to apply the pre-processing algorithms developed for LEOs to the case of static positioning, as well.

Excellent a priori information concerning the "trajectory" of a fixed receiver is available for stations included in the IGS network. The algorithm allows it to develop a data screening procedure for code and phase observations based on a station- and epoch-wise processing of the data. The requirements for such a procedure are the availability of:

- precise station coordinates in the ITRF,
- precise orbit information for the GPS satellites in the Earth-fixed system (ITRF),
- precise 30-seconds clock corrections for the GPS satellites (including DCBs, Differential Code Biases), and
- tropospheric delay estimates for the stations – not mandatory.

These requirements are met, e.g., by the stations of the IGS network and the products delivered by CODE (Section 2.2.2) to the IGS. These products include station coordinates, orbits, ERPs, DCBs, and troposphere estimates. The 30-seconds clock corrections are computed by the procedure described in [*Bock et al.*, 2000] and [*Bock et al.*, 2003] using the 5-minutes clock corrections computed by CODE.

The original program LEOKIN for zero-difference kinematic point positioning as shown in its simple form in Figure 3.2 is not yet capable of serving as a self-contained data screening tool. We have to add the options to

- generate a list of the code and phase observations excluded by the pre-screening algorithm and the least squares adjustment in the code or the phase-difference processing, and to
- generate a list of the epochs where new ambiguities for specified satellites have to be set up for the phase observations.

With this concatenated list of problem cases we may then use the program SATMRK of the Bernese GPS Software [*Hugentobler et al.*, 2001] to modify the observation files accordingly.

Thanks to the excellent a priori information concerning the station coordinates it was possible to modify the pre-screening algorithm for the phase-difference observations. For the data screening of the phase observations of terrestrial stations we classify the values γ_i not according to relation (4.2) but according to

$$\gamma_i = \begin{cases} \text{a} & : \quad \Delta\bar{\gamma} \leq 3 \cdot \sigma_{\gamma'} \\ \text{b} & : \quad \Delta\bar{\gamma} \leq \beta \cdot \sigma_{\gamma'} \\ \text{c} & : \quad \Delta\bar{\gamma} > \beta \cdot \sigma_{\gamma'} \end{cases} \tag{4.6}$$

where

a means that the observation is accepted,

b means that the observation is accepted, but has to be checked within the following iterative least-squares adjustment step, and

c means that the observation is definitely an outlier.

Subsequently observations meeting the condition “a” of eqn. (4.6) will be accepted without further control, implying that these observations cannot be rejected by the estimation process for the position-differences after the pre-screening. The observation is so to speak “protected against rejection”. Observations corresponding to the values of γ_i meeting condition “b”, on the other hand, are checked again during the estimation process. It may be that they are helpful for a stable determination of the position-difference or they may disturb the solution. In the case of a terrestrial station the a priori information is more precise than in the case of a LEO. That is why we protect the observations meeting the condition “a” against rejection. These observations have to be okay. The least squares adjustment step becomes more robust due to this protection. It may be that we have eight observations passing the pre-screening algorithm. Six of them meet condition “a” and two meet condition “b”. In the least squares adjustment now only the two observations of condition “b” may be responsible for a possible deterioration of the solution. It may be that both have to be excluded but it may also be that one is remaining in the processing because it stabilizes the position. Observations classified in “c” in the test of eqn. (4.6) are marked as outliers and added to the above mentioned list.

This modification of the pre-screening algorithm of the phase observations has the advantage that unnecessary iterations in the kinematic point positioning procedure are avoided and that the detection of bad observations disturbing the solution gets more reliable. The modification is not made for the code processing because the quality of the code observations is very different for different GPS receivers. Since we screen all code data with the same $\sigma_{c_{scr}}$ the usage of the modification would be not as reasonable as for the phase-difference processing.

The actions performed due to bad observations are slightly different for code and phase observations. Therefore, we explain both procedures separately.

4.4.1 Screening of Code Observations

Since the point positioning and therefore also the pre-screening algorithm is based on a station- and epoch-wise processing of the data it is sufficient to outline the procedure of code observations for an epoch and one station. If the following criteria are not met by the observations, the $P1$- and $P2$-measurement of the specified satellite and epoch are marked and excluded from the further processing of the data:

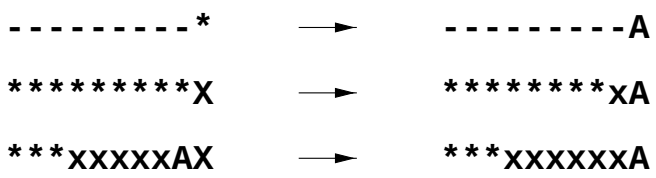


```
- ... No observation
x ... Marked observation
* ... Good observation
A ... Ambiguity
X ... Difference to previous epoch is not okay
```

Figure 4.12: Actions performed for phase observations.

- The difference between $P1$ and $P2$ has to be smaller than a specified value (e.g., 30 m).
- Orbit and clock correction information has to be available for the observed GPS satellite of the processed epoch.
- The test value γ_i has to be in category "b" in eqn. (4.2); the point positioning procedure has to confirm that the observation is okay and useful.
- At least four observations have to be available for the epoch.

4.4.2 Screening of Phase Observations

When screening phase observations, observations may be marked or flagged for setting up a new ambiguity. The criteria which have to be met by a good phase observation of one epoch-difference are the following:

- Orbit and clock correction information have to be available for the observed GPS satellite for both epochs.
- The test value γ_i has to be classified as "a" or "b" in eqn. (4.6). If the second condition "b" is met the estimation process has to confirm that the observation-difference is okay.
- At least four observation-differences have to be available for the epoch-difference considered.
- The satellite has to be observed at both epochs in order to form the difference.

If one of the above conditions is not met, the case-dependent actions illustrated in Figure 4.12 are invoked. The first line in Figure 4.12 stands for the case that no observations are available to a satellite for a longer period before the receiver starts to track the satellite. In this case we have to set up a new ambiguity at the first epoch the satellite is observed. At this moment it is not clear, however, whether this observation is of acceptable quality. This may not be checked until the difference with the observation of the next epoch is formed. If the observations then should be rejected the third line of Figure 4.12 applies. The second line illustrates the case where the observation-difference for the considered epoch-difference is recognized as an outlier. In this case the observation of the first epoch of the epoch-difference is marked as bad and at the second, the current epoch we set up a new ambiguity.

If a cycle slip has occurred between these two epochs for this satellite we have marked the observation of the first epoch unnecessarily. But with our processing strategy of forming independent differences from one epoch to the next we may not recognize whether a bad observation-difference is due to an outlier or to a cycle slip. To be on the safe side, we mark in all these cases the observation of the first epoch.

The third line of the figure can just be seen as the continuation to the second line. If we found a bad observation-difference related to a particular epoch-difference, where at the first epoch a new ambiguity already was set up, we mark this first observation and "move" the new ambiguity flag to the observation of the current epoch.

The validation and application of this data screening procedure for zero-difference observations of a terrestrial network is presented in Section 6.7.

5. Dynamic and Reduced-dynamic Orbit Modeling

Kinematic point positions (e.g., from LEOKIN) may be used as pseudo-observations in an orbit determination process based on a physical orbit model in order to generate a dynamic or reduced-dynamic orbit. Our work also deals with dynamic and reduced-dynamic strategies for LEO precise orbit determination (LEO-POD). As already mentioned in Section 2.4 the physical models for the perturbing forces are more complicated for low Earth orbiting satellites than for satellites orbiting at higher altitudes, such as GPS or GLONASS. The orbit of a high orbiting satellite is in general sufficiently well parametrized by initial conditions and a few dynamical parameters. For LEOs the force field is usually not known with sufficient precision (e.g., the higher degree and order terms of the gravity field or the atmospheric drag) and the orbit determination procedure has to allow for a stochastic component in the satellite motion [*Beutler*, 2004].

Table 5.1 [*Rothacher*, 1992] lists the perturbing accelerations acting on a GPS satellite and Table 5.2 those acting on a LEO. Obviously, the perturbations due to the gravity field of the Earth are larger by several orders of magnitude for LEOs. The impact of lunar and solar gravitational attraction, on the other hand, is slightly smaller for LEOs because only the relative acceleration w.r.t. the geocenter defines the perturbation. The effect of the radiation pressure depends mainly on the factor $\frac{Q}{m}$ (ratio area-to-mass) of the satellite. The perturbation due to atmospheric drag mainly depends on the altitude of the satellite and the $\frac{Q}{m}$ ratio.

Dynamical orbits (when compared to the kinematic orbits) have the advantage of being continuous and without gaps. For applications requiring continuous precise orbit information a kinematic solution may not be the optimum. On the other hand, precise knowledge of the physical models describing the forces acting on the satellite is required in order to generate a dynamical solution.

Table 5.1: Perturbing accelerations acting on a GPS satellite.

Perturbation	Acceleration m/s^2
Two-Body Term of Earth's Gravity Field	0.59
Oblateness of the Earth	$5 \cdot 10^{-5}$
Lunar Gravitational Attraction	$5 \cdot 10^{-6}$
Solar Gravitational Attraction	$2 \cdot 10^{-6}$
Other Terms of Earth's Gravity Field	$3 \cdot 10^{-7}$
Radiation Pressure (direct)	$9 \cdot 10^{-8}$
Y-Bias	$5 \cdot 10^{-10}$
Solid Earth Tides	$1 \cdot 10^{-9}$

Table 5.2: Perturbing accelerations acting on a LEO satellite.

Perturbation	Acceleration m/s^2
Two-Body Term of Earth's Gravity Field	8.6
Oblateness of the Earth	$2 \cdot 10^{-2}$
Other Terms of Earth's Gravity Field	$2 \cdot 10^{-4}$
Lunar Gravitational Attraction	$1 \cdot 10^{-6}$
Solar Gravitational Attraction	$4 \cdot 10^{-7}$
Atmospheric Drag	$5 \cdot 10^{-7}$
Radiation Pressure (direct)	$3 \cdot 10^{-8}$
Albedo	$4 \cdot 10^{-10}$

5.1 Program SATORB

The program SATORB is the tool used subsequently for the dynamic and reduced-dynamic orbit determination procedure. Positions and, possibly, position-differences are used as observations in the orbit determination process. For our applications the positions (and position-differences) are the result of program LEOKIN. The positions may either be derived only from code observations or they are the result of the combination of code positions with phase-derived position-differences (Section 3.4). Alternatively, positions and position-differences (also from LEOKIN), may be introduced as separate observation types into the orbit determination process. They are weighted in program SATORB according to their estimated RMS errors in program LEOKIN or according to a user-defined weight ratio between positions and position-differences. To make use of these two separate observation types has an advantage compared to using the combined positions. The artificial jumps in the combined positions due to interrupts in the phase-difference processing or due to data gaps are not present in the positions and position-differences. They are combined in the dynamic orbit determination process following the physical models. Pseudo-stochastic pulses may compensate insufficiencies of the model and do not have to compensate for artificial problems in the combined positions due to the jumps. The better the physical models the fewer stochastic pulses have to be set up.

The equations of motion of the LEO are based on the parametrized post-Newtonian mechanics (PPN-approximation) and integrated using a collocation technique described in [*Beutler*, 2004]. Models for the following perturbing forces are implemented in SATORB:

- Gravitational forces (and gravity-related effects):
  - Earth gravity field,
  - solid Earth tides,
  - ocean tides,
  - third-body perturbations of the Sun and the Moon,
  - relativistic PPN corrections,
  - precession, nutation, and polar motion.
- Non-gravitational forces:
  - atmospheric drag,

  - direct radiation pressure, and
  - Earth albedo radiation pressure.

Non-gravitational forces may also be taken into account by analyzing accelerometer measurements in the orbit determination process.

The following parameters may be estimated optionally and in addition to the six osculating elements:

- up to nine empirical parameters,
- scale factor for atmospheric drag,
- scale factor for direct radiation pressure,
- albedo parameter, or
- pseudo-stochastic pulses at pre-defined epochs.

When using accelerometer measurements one may in addition solve for

- scale factors and
- biases for the accelerometer data.

Subsequently, the models and algorithms are explained in detail.

5.2 Gravitational Forces

5.2.1 Earth Potential

The gravity field of the Earth is usually represented by spherical harmonic functions. A consequent use of normalized Legendre polynomials avoids numerical problems related to high degree and order terms. Several sets of coefficients are available and can be used for the orbit determination. The models used for our studies in dynamical orbit determination are the JGM-3 [*Tapley et al.*, 1996], GRIM5-S1 [*Biancale et al.*, 2000], EGM96 [*Lemoine et al.*, 1998], TEG-4 [*Tapley et al.*, 2000] and EIGEN-1S [*Reigber et al.*, 2002]. The maximum degree and order can be selected depending on the satellite being processed. The perturbations due to the gravity field for the higher satellites like GPS are modeled with sufficient accuracy by using the spherical harmonics up to degree and order eight. For the LEOs this is not sufficient and we have to use expansions of degree and order 70 or more. For LEO orbits it proved to be problematic that most gravity models do not provide sufficiently accurate high degree and order coefficients. As gravity models are available using CHAMP data for the computation of the model (TEG-4 and EIGEN-1S), the situation improved and the new models represent the gravity field much better than the older gravity models. The issue of using different gravity models is addressed in Section 6.5.

5.2.2 Solid Earth and Ocean Tides

The tidal potential used in SATORB conforms to the IERS Standards 1996 [*McCarthy*, 1996]. In total 17 constant and frequency-dependent terms are used with a harmonic expansion up to degree and order four. The permanent tide is handled according to the gravity field used and the solid Earth pole tide is applied. The gravity potential added by ocean tides are represented by constant and frequency-dependent terms from the CSR3.0 global ocean tide model [*Eanes and Bettadpur*, 1995].

5.2.3 Third-body Perturbations

The perturbations due to Sun and Moon are computed using the DE200 JPL Development ephemerides [*Standish,* 1990]. The perturbations from major planets are not implemented.

5.2.4 Precession, Nutation and Polar Motion

Precession and nutation are implemented following the IAU resolutions 1976 and 1980, respectively ([*Seidelmann,* 1992]), and for the polar motion the IERS Bulletin A or the IGS values are used.

5.3 Non-gravitational Forces

The modeling of the non-gravitational forces is not standardized to the same extent as the modeling of the gravitational forces. In the following sections the models used in SATORB for the non-gravitational forces are briefly characterized.

5.3.1 Atmospheric Drag

The determination of the perturbation due to the atmospheric drag acting on the satellite is one of the most difficult tasks in modeling the low Earth orbiting satellites, because the atmospheric density along the satellite orbit is not precisely predictable. In these heights not many measurements are available to determine an exact model of the density of the higher atmosphere and its time variation. Nevertheless, several models exist and we use the MSISe-90 (Mass Spectrometer and Incoherent Scatter) [*Hedin,* 1987, 1991] model for computing the density of the higher atmosphere. The MSISe-90 gives the density as a function of the

- height above the Earth's surface,
- day of year,
- geodetic longitude and latitude,
- daytime,
- true solar time,
- solar flux F10.7 cm, and the
- planetary magnetic index Ap.

The MSISe-90 model thus takes seasonal variations of the air density, variations with local time and geographic location as well as with solar activity into account.

With the density $\rho(\boldsymbol{r})$ based on the MSISe-90, the perturbing acceleration $\boldsymbol{a}_{\text{at}}$ for a spherical satellite due to the atmosphere may be expressed as [*Beutler,* 2004]

$$\boldsymbol{a}_{\text{at}} = -\frac{C}{2} \cdot \rho(\boldsymbol{r}) \cdot \frac{Q}{m} \cdot \dot{\boldsymbol{r}}^2 \cdot \frac{\dot{\boldsymbol{r}}}{|\dot{\boldsymbol{r}}|}. \tag{5.1}$$

C is the drag coefficient for the atmospheric drag, $2 \leq C \leq 2.5$.

Q is the cross-sectional area of the satellite in the relevant direction for the atmospheric drag.
m is the mass of the satellite.
$\dot{\boldsymbol{r}}$ is the velocity vector of the satellite in the Earth-fixed frame.

We may choose constant values for C, Q and m using a spherical satellite model (cannon ball model). The three parameters are different for each satellite being processed. More realistic satellite models requiring knowledge of the satellite dimensions, surface properties, and attitude are not currently implemented. In addition to the a priori model (eqn. (5.1)) program SATORB offers the possibility to estimate a scale factor s_{at} for the atmospheric drag

$$\boldsymbol{a'}_{\text{at}} = s_{\text{at}} \cdot \boldsymbol{a}_{\text{at}} \tag{5.2}$$

in order to adapt the atmospheric drag computed by eqn. (5.1) to the actual properties (C, Q, m) of the satellite. The main uncertainty of the model is the atmospheric density and its variations with time and location at the altitude of the satellite.

5.3.2 Direct Solar Radiation Pressure

The acceleration due to solar radiation pressure mainly depends on the shape and on the reflection characteristics of the satellite body. For a spherical satellite it may be expressed as [*Beutler*, 2004]

$$\boldsymbol{a}_{\text{rp}} = -\frac{\tilde{C}}{2} \cdot \frac{A_e^2}{|\boldsymbol{r} - \boldsymbol{r}_s|^2} \cdot \frac{S}{c} \cdot \frac{\tilde{Q}}{m} \cdot \frac{\boldsymbol{r} - \boldsymbol{r}_s}{|\boldsymbol{r} - \boldsymbol{r}_s|}. \tag{5.3}$$

$\tilde{C}$ is the coefficient for direct radiation pressure.
$\boldsymbol{r}$ is the geocentric vector of the satellite.
$\boldsymbol{r}_{\text{s}}$ is the geocentric vector of the Sun.
A_{e} is the astronomical unit, $A_{\text{e}} = 149'597'870'610$ m [*Lang*, 1992].
S is the Solar constant, $S = 1'368 \frac{\text{W}}{\text{m}^2}$ [*Lang*, 1992].
c is the velocity of light.
$\tilde{Q}$ is the cross-sectional area of the satellite in the relevant direction for solar radiation pressure (direction Sun $\rightarrow$ satellite).
m is the mass of the satellite.

As opposed to atmospheric drag affecting the satellite continuously, solar radiation pressure acts only if the Sun is not eclipsed (as seen by the satellite). If the satellite is in the Earth's shadow, the perturbation due to the solar radiation pressure is zero. In the same way as for the atmospheric drag we have the possibility to choose the numbers $\tilde{C}, \tilde{Q}$, and m corresponding to the satellite considered in SATORB. A scale factor s_{rp} for the direct radiation pressure may be estimated

$$\boldsymbol{a'}_{\text{rp}} = s_{\text{rp}} \cdot \boldsymbol{a}_{\text{rp}}. \tag{5.4}$$

5.3.3 Empirical Parameters

In addition to the direct radiation pressure represented by eqn. (5.3) we may introduce empirical radiation pressure parameters in the DYX-directions (D: direction to the sun, Y: direction of the solar panel axis, X: perpendicular to D and Y (right-handed system)). Such a decomposition of the perturbing accelerations

may, however, even make sense for a satellite without solar panels. The Y-direction is perpendicular to the direction to the line Sun – satellite and perpendicular to the direction satellite – geocenter. The parametrization consists of three constant terms (D_0, Y_0, X_0) and one once-per-revolution cosine- and sin-term ($D_C, D_S, Y_C, Y_S, X_C, X_S$) in each direction. The acceleration is set to zero if the satellite is in the shadow. The model is given by

$$\begin{pmatrix} a_D \\ a_Y \\ a_X \end{pmatrix} = \begin{pmatrix} D_0 & + & D_C \cdot \cos u & + & D_S \cdot \sin u \\ Y_0 & + & Y_C \cdot \cos u & + & Y_S \cdot \sin u \\ X_0 & + & X_C \cdot \cos u & + & X_S \cdot \sin u \end{pmatrix} \tag{5.5}$$

where u is the argument of latitude at the time t considered. This model corresponds to the so-called CODE Extended Radiation pressure model used at the CODE Analysis Center which was originally developed to account for the solar radiation pressure for the modeling of GPS satellite orbits [*Beutler et al.*, 1994].

We may also set up similar empirical parameters in an orbit-fixed reference frame in RSW-directions (R: radial, S: in flight direction, perpendicular to R (alongtrack), W: perpendicular to R and S (crosstrack)), [*Colombo,* 1989]. The model for the RSW-directions is

$$\begin{pmatrix} a_R \\ a_S \\ a_W \end{pmatrix} = \begin{pmatrix} R_0 & + & R_C \cdot \cos u & + & R_S \cdot \sin u \\ S_0 & + & S_C \cdot \cos u & + & S_S \cdot \sin u \\ W_0 & + & W_C \cdot \cos u & + & W_S \cdot \sin u \end{pmatrix}. \tag{5.6}$$

These parameters ($R_0, S_0, W_0, R_C, S_C, W_C, R_S, S_S, W_S$) are estimated as constants for the arc considered.

5.3.4 Earth Albedo

The Earth albedo perturbation $\boldsymbol{a}_{al}$ (due to the sunlight reflected by the Earth's surface) is small compared to the direct radiation pressure. It depends on the position of the satellite relative to the sunlit hemisphere of the Earth. The same input parameters ($\tilde{C}, \tilde{Q}, m$) and a spherical satellite model with homogeneous surface properties are assumed to model the effect. The area of the Earth visible from the satellite is divided into a given number of surface elements. For each surface element illuminated by the Sun the amount of light scattered into the direction of the satellite is computed using the Lambert reflection law. This very simple model assumes a constant albedo for the entire Earth's surface. The Earth's albedo may be estimated in the orbit improvement procedure.

5.4 Measuring the Non-gravitational Forces: Accelerometer Data

CHAMP carries a three-axes accelerometer instrument on-board (Section 2.3.4). An accelerometer measures all non-gravitational forces acting on the satellite, e.g., atmospheric drag, radiation pressure, Earth albedo, the movements of the satellite due to maneuvers, etc. in a particular direction. The instrument measures (in essence) the movements of a proof-mass in a self-contained cage. This is realized in the case of CHAMP by measuring the electrostatic forces acting on the proof-mass placed in a cage in the center of mass of the satellite. The maximum deviation of the proof-mass from the center of mass is two millimeters. The six pairs of electrodes (three for linear and three for angular accelerations) placed in the walls of the cage are used for both the generation of the electrostatic field keeping the proof-mass at its location and for measuring the changes of the capacitance due to position changes of the proof-mass. Based on the measurement of the capacitance, the electrostatic field is stabilized by applying the

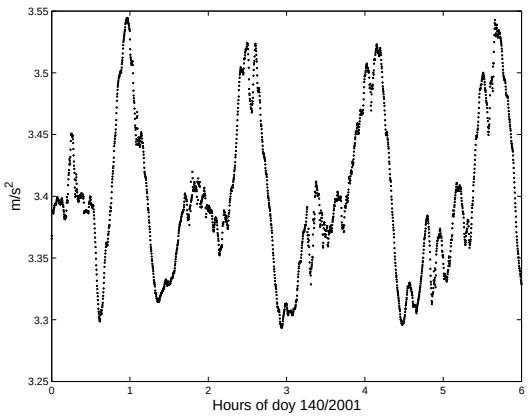

Figure 5.1: Accelerometer measurements in alongtrack direction for CHAMP, doy 140/2001, 0:00-6:00.

corresponding voltage on the opposite electrodes [*CHAMP*, 2002]. The output of the instrument are the six accelerations (three linear and three angular). For orbit modeling the linear accelerations are relevant because they may be used to calculate the surface forces (in particular atmospheric drag). The measured values may, however, not directly be interpreted as accelerations but need to be modified using the transformation

$$F_{\text{acc}}(i) = a(i) \cdot m(i) + b(i), \quad i = 1, 2, 3. \tag{5.7}$$

The constants $a(i)$ (scale factor) and $b(i)$ (bias) are applied to the measurements $m(i)$ of direction i. For CHAMP these are the radial-, alongtrack-, and crosstrack-direction. The values for $a(i)$ and $b(i)$ may either be introduced as known – from a calibration procedure – into the orbit model or they may be estimated in the parameter estimation process.

The original measurements provided by the instrument have a sampling rate of one second and show spikes which are partly related to thruster pulses and boom oscillations. The pre-processing of the acceleration measurements is performed at GFZ prior to data release [*Foerste*, 2001]. Pre-processing is performed in two steps. In a first step a second-degree polynomial is fitted to the 1-Hz data for 10-second intervals in order to identify and remove spikes and outliers. After a second fit with a polynomial of second degree a normal point is constructed for each 10-second interval. These normal points are released as Level 2 data to the users of the accelerometer data.

Figure 5.1 shows these pre-processed accelerations in the alongtrack direction for a time window of six hours for doy 140/2001. A signal related to the orbital revolution of CHAMP (about 93 minutes for doy 140/2001) can clearly be identified. The main non-gravitational forces acting on the satellite in alongtrack direction are the atmospheric drag and, depending on the position w.r.t. the Sun, the direct solar radiation pressure.

Figure 5.2 compares the accelerometer measurements and the models for non-gravitational forces implemented in SATORB for the first twelve hours of doy 150/2001. The argument of latitude is used as independent argument. The three components, radial, alongtrack, and crosstrack, are shown separately. The left-hand figures are the accelerometer measurements in the corresponding directions and the right-hand figures are the accelerations given by the models for the same time interval. The radial component of the accelerometer measurements shows a strange pattern. One accelerometer diode in radial direction failed but the information can be recovered by forming a specific linear combination of the other measurements [*Perosanz et al.*, 2003]. The signal in the radial direction has, therefore, not the same accuracy

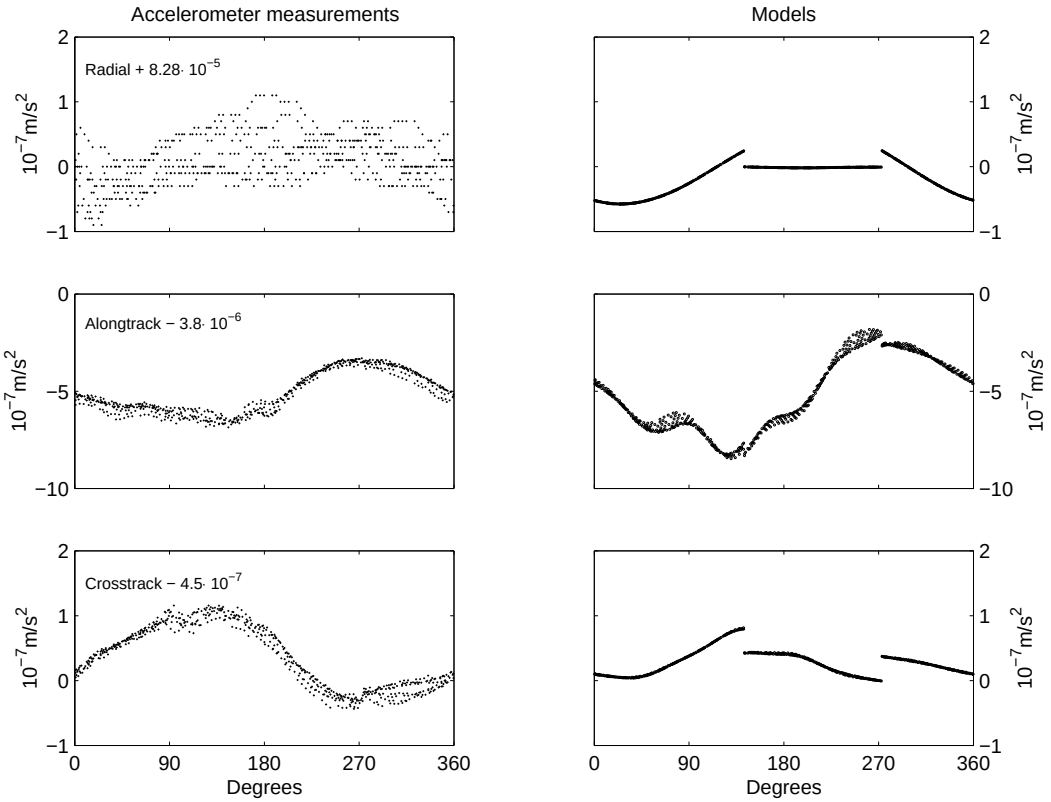

Figure 5.2: Comparison of accelerometer measurements and models for non-gravitational forces as a function of the argument of latitude (CHAMP, doy 150/2001, 0:00-12:00).

as that in the other two directions. The alongtrack and the crosstrack components show a similar behavior for the accelerometer measurements and the models. The differences are mainly due to the insufficient accuracy of the models for the non-gravitational forces. The jumps in the model accelerations are due to eclipses. They are barely visible in the accelerometer measurements.

Accelerometer data were used for some tests. Results may be found in Section 6.6.

5.5 Pseudo-stochastic Pulses

The orbit determination procedure has to allow for a stochastic component in the orbit movement because the parametrization of a low satellite orbit with the initial conditions and dynamical parameters is usually not sufficient. The procedure implemented in SATORB may be characterized as follows [*Beutler,* 2004]:

- Each resulting orbit (or arc) is continuous.
- Each arc is represented piece-wise by conventional ordinary differential equation systems (deterministic equations of motion).
- At pre-determined epochs the orbit is allowed to suffer velocity changes δv_i in pre-determined directions i. These velocity changes are a consequence of *pseudo-stochastic pulses.*
- Pseudo-stochastic pulses δv_i are conventional parameters of a classical least squares adjustment process.
- Each pseudo-stochastic pulse is characterized by an a priori variance.

The part of the NEQ system containing the contributions of the pulses may be formed by linear combinations from a reduced NEQ system (including only the initial osculating elements and the dynamical parameters). This feature is extremely time saving because no variational equations have to be integrated for the stochastic pulse parameters. Additional optimization of processing time is achieved by only saving the reduced NEQ component for each pulse epoch. Based on that information the NEQ is reconstructed for the full parameter vector just before inverting the NEQ system.

The pseudo-stochastic pulses may be set up in the R-, S-, and W-directions. They may be set up at pre-determined epochs with a specified spacing (e.g., every 30 minutes) or at epochs which are defined, e.g., to maneuvers of the satellite.

The CHAMP satellite, e.g., frequently performs maneuvers. Usually, they are due to the satellites' attitude. The maneuvers may nevertheless have a non-negligible effect on the orbit, e.g., due to a misalignment of thruster pairs or due to not fully balanced firings of the thruster pairs. Figure 5.3 shows the number and duration of the thruster pulses for four different days. The duration of the pulses is limited to three seconds. A maneuver is initiated when the real attitude of the satellite differs by more than a certain value from the nominal attitude. The circles in Figure 5.3 correspond to maneuvers which have happened according to accelerometer measurements but were initially not recorded by the satellite system. After a pre-processing of the maneuver and accelerometer data (performed at GFZ, Potsdam, Germany) these maneuver epochs are added to the list of pulses with an unknown duration and direction. Figure 5.3 shows that the attitude maneuvers normally take place at regular time intervals. There are several maneuvers directly following each other which are performed for the fine-tuning of the attitude. Stochastic pulses may be set up at the maneuver epochs to absorb possible orbit movements caused by the pulses. A few studies made in this context are outlined in Sections 6.6.

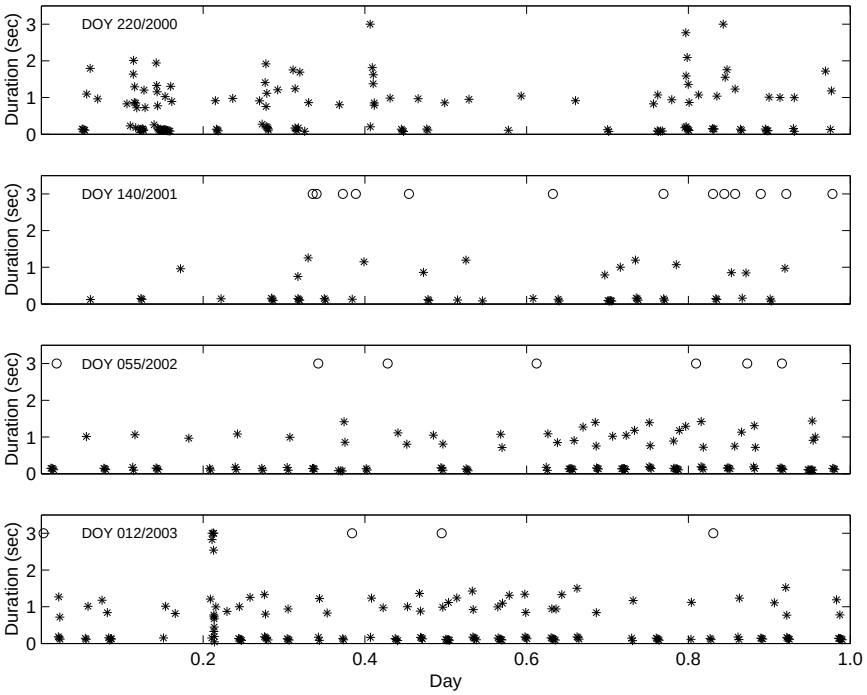

Figure 5.3: Number and duration of thruster pulses for CHAMP for different days ($*$: maneuver recorded by the satellite system; $\circ$: additional maneuver with unknown duration added after pre-processing of the data).

6. Results and Applications

The quality of kinematic orbits of LEOs computed by the program LEOKIN as explained in Chapter 3 strongly depends on the pre-processing of the observations. A first part of this chapter is, therefore, devoted to the impact of different pre-processing options on the resulting kinematic positions (see Chapter 4). The kinematic trajectories are compared with reduced-dynamic orbits (see Chapter 5) or, if available, with orbits from external sources.

The first section introduces the criteria used for the evaluation of kinematic solutions. It is followed by results from different pre-processing options applied to data sets for CHAMP and SAC-C covering different time intervals. The first example is based on data from one day of CHAMP (doy 152/2001) and one day of SAC-C (doy 051/2001). The second example is based on the data set of the IGS CHAMP test campaign in May 2001 (doy 140 to 150/2001). The third example is based on a data set spanning 35 days in 2002 (doy 055 to 089/2002) of SAC-C and CHAMP.

In subsequent sections different gravity field models are compared based on dynamic orbit solutions for CHAMP and SAC-C. The impact of stochastic pulses, which may be set up in the reduced-dynamic orbit procedure, are studied. The use of accelerometer measurements instead of models for the non-gravitational forces is the topic of one section. Results and comparisons of the data screening approaches for zero-difference observations for ground stations (see Section 4.4) are presented in the final section.

6.1 Evaluation of Kinematic Solutions

The evaluation of kinematic solutions is difficult without external comparisons. We have to define criteria to evaluate the results from program LEOKIN. Two criteria are important quality indicators for kinematic solutions:

1. the number of interrupts in the combined solution due to missing phase position-differences and
2. the number of jumps in the kinematic trajectory exceeding a specified threshold.
3. RMS error of a Helmert transformation between kinematic and reduced-dynamic orbit.

Jumps are caused by position-differences corrupted by bad observations. Such jumps may be identified by comparing the kinematic trajectory with a dynamic or reduced-dynamic orbit. These orbits have no gaps and are continuous for the entire arc. Jumps in the kinematic trajectory may therefore be detected by analyzing the difference between the kinematic and a dynamic orbit, e.g., the a priori or the post-fit orbit. The procedure used to find these jumps is the following:

1. Form the differences between three-dimensional positions of kinematic and dynamic trajectories.
2. Form the differences of these difference vectors between two subsequent epochs. A jump in the kinematic positions will then manifest itself as an outlier in an otherwise smooth curve.

3. For a moving interval of ten epochs:
   - Exclude each of the ten points one after the other,
     - fit a polynomial of degree two through the remaining nine points,
     - check the residuals of the excluded points,
     - mark a point as outlier if the absolute value of its residual is larger than a specified limit.
   - If a position was marked as an outlier the procedure is repeated with the remaining points of the interval. Eventually all outliers in the interval are identified.
4. If the same point is showing a residual of more than the specified limit in more than eight successive moving intervals, a jump in the kinematic trajectory is assigned to the corresponding epoch-difference.

An interrupt in the kinematic trajectory due to a missing position-difference always occurs if there is a data gap. An interrupt may also occur if not enough phase-difference observations are left due to outliers such that no position-difference can be computed for this epoch-difference. In general, an interrupt may lead to a large jump in the trajectory (Section 3.6.3). If the jump is larger than the specified limit (we used eleven centimeters for this purpose), this interrupt is included in the number of jumps of the kinematic trajectory w.r.t. the dynamic orbit. If the interrupt does not result in a large jump in the kinematic trajectory, it does not appear in the number of jumps of the kinematic trajectory.

These two criteria defined above are used to evaluate the kinematic solutions computed by LEOKIN. The smaller the number of interrupts and the number of jumps the better the solution.

In addition, the percentage of observations deleted by the pre-screening algorithm is an important criterion for the evaluation of a kinematic solution. If the kinematic trajectory has few interrupts and jumps but if instead a big number of observations is excluded due to a too narrow pre-screening threshold the corresponding options may not be correct.

The resulting kinematic trajectories and the reduced-dynamic orbits are saved as tabular positions in the SP3-format ([*Remondi*, 1989]). For comparison purposes a Helmert transformation with estimating a translation (three unknown parameters) is performed between these positions. If we compare several orbits with a ”reference” orbit, the resulting RMS errors of the Helmert transformation indicate the quality of the orbits considered w.r.t. the ”reference” orbit.

The kinematic trajectory resulting from LEOKIN which is supposed to be the best is used for generating a reduced-dynamic orbit with SATORB. The code positions and phase position-differences of the kinematic solution are used as independent observation types in SATORB (see Section 5.1) in order to avoid data problems stemming from the jumps in the combined positions. This reduced-dynamic orbit is the best result we may produce with LEOKIN and SATORB. This orbit then may be used as “reference“ orbit for comparison purposes in order to evaluate the quality of all other kinematic and reduced-dynamic orbits produced for a particular data set.

6.2 CHAMP 152/2001 and SAC-C 051/2001

We compare different pre-screening and -processing options for the two satellites CHAMP and SAC-C. The data used for this example (doy 051/2001 for SAC-C, doy 152/2001 for CHAMP) are described in Section 4.3.2. Input data for each day are

- GPS orbits and ERPs of the CODE Rapid processing,

- 30-second clock corrections for the GPS satellites [*Bock et al.*, 2000] (GPS broadcast clock corrections used for alignment to GPS time), and
- the corresponding reduced-dynamic orbit for CHAMP or SAC-C derived by the procedure explained in Figure 3.1 (only code observations).

The data are processed with the following basic options:

1. $\sigma_{c_{scr}} = 1.0$ m and $\sigma_{p_{scr}} = 0.01$ m,
2. the weight of the code positions is reduced by a factor 100 for the combination (in addition to the normal weight ratio of $w_c : w_p = 2 : 100^2$),
3. no cut-off angle is used for the observations, and
4. an elevation-dependent weighting is applied to the observations with the weighting function $w(z) = \cos^2(\frac{3}{4} \cdot z)$.

In Section 4.3.2 we have studied the influence of different pre-processing options on the pre-processing itself. In this section we compute different solutions with one or two options changed in order to get an impression of the influence of the options on the kinematic solution.

6.2.1 Different Values for Threshold β

The threshold value β is an important pre-screening option. It decides which observations are excluded from the further processing in the pre-screening step (see eqn. (4.2)). The remaining observations are used for the kinematic point positioning. This is done iteratively in order to find the observations which passed erroneously the pre-screening procedure and disturb the solution. The question is therefore whether a narrow pre-screening with a small value for β is preferable or a pre-screening which excludes only the extreme outliers due to a large value for β. The observations which pass the pre-screening and still disturb the solution should then be found in the iterative least squares adjustment step. It may be possible that in the case of a larger value for β, observations which would be excluded with a smaller β may contribute to a more stable point position. We have to remember that the GPS receivers on-board the LEO satellites often do not track many satellites and the degree of freedom f (number of observations minus number of parameters) is rather small for the epoch-wise kinematic point positioning ($f \sim 0-3$). Therefore each observation is important for a controlled solution. The small value for f is, on the other hand, the problem why we need the described pre-screening procedure. In this procedure, only the receiver clock parameter has to be estimated while the position is fixed at its a priori value. This makes the procedure much more robust to find the outliers than the iterative least squares adjustment step with four unknowns and a corresponding small degree of freedom. The requirement for the pre-screening algorithm is, however, that a priori orbit information of sufficient accuracy (better than half a meter) is available.

Solutions with different values for β are computed in order to study the effect on the resulting kinematic positions. Table 6.1 characterizes the solutions. The value β is varied from 3 to 40. Figure 6.1 shows the results for SAC-C 051/2001 (top) and for CHAMP 152/2001 (bottom). It shows for each solution C1 to C6 two bars. The left bar represents the number of interrupts in the kinematic trajectory due to missing phase position-differences and the right bar represents the number of jumps in the kinematic trajectory w.r.t. a reduced-dynamic orbit due to incorrect position-differences.

Table 6.1: Solutions with different threshold value β.

Solution	C1	C2	C3	C4	C5	C6
$\beta =$	3	5	10	20	30	40

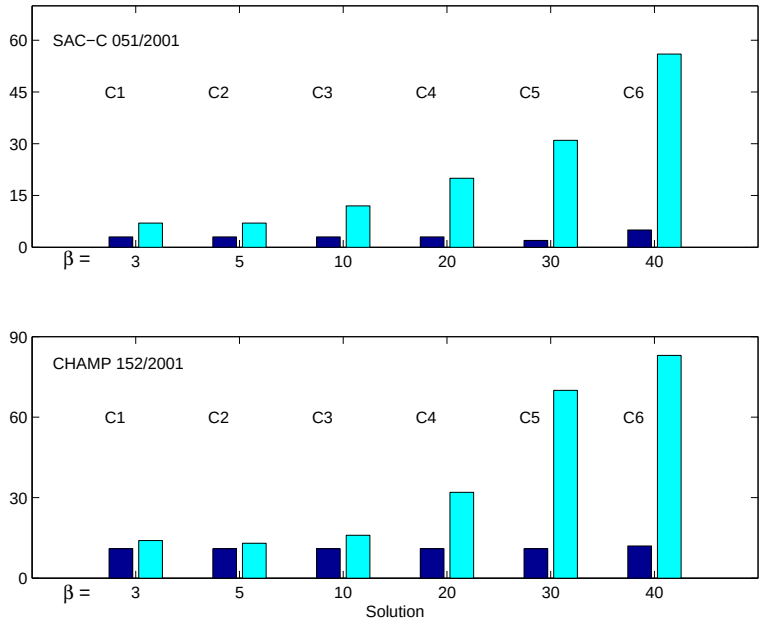

Figure 6.1: Number of interrupts due to missing phase position-differences (left bar) and number of jumps in the kinematic trajectory (right bar) for solutions C1 to C6, SAC-C 051/2001 (top) and CHAMP 152/2001 (bottom).

Table 6.2: RMS errors (m) of Helmert transformation between kinematic solutions C2 to C6 and C1 and between C1 to C6 and reduced-dynamic solution C1S.

		C1	C2	C3	C4	C5	C6
SAC-C	C1	-	0.04	0.15	0.35	0.30	0.43
	C1S	0.16	0.16	0.22	0.40	0.34	0.45
CHAMP	C1	-	0.02	0.16	0.64	0.72	0.71
	C1S	0.10	0.11	0.20	0.65	0.73	0.72

The number of jumps in the kinematic trajectory is increasing with increasing threshold value β for both satellites. This means that bad observations which are not excluded by the pre-screening due to a big value of β are not identified as outliers by the iterative least squares adjustment. These bad observations deteriorate the solution and lead to the jumps in the kinematic trajectory. The number of interrupts due to missing position-differences, on the other hand, does not depend much on β for both satellites. This means that no additional interrupts are produced due to the different pre-processing option.

We use the positions and position-differences from solution C1 in order to fit a reduced-dynamic orbit through these "pseudo-observations". This reduced-dynamic orbit C1S (1-day arc) is parametrized as follows:

- six osculating elements,
- nine empirical parameters in RSW-directions, and
- pseudo-stochastic pulses every ten minutes.

The gravity field model EIGEN-1S (120x120) and models for atmospheric drag and direct radiation pressure are used. Eight iterations are performed to guarantee convergence of the solution.

Table 6.2 shows the RMS errors of a Helmert transformation with three translation parameters between the kinematic trajectories of C2 to C6 and C1 and the kinematic trajectories C1 to C6 and C1S. It seems that only solutions C1 and C2 are of comparably good quality. Figure 6.2(a) shows the differences between solution C1 and C2 and Figure 6.2(b) between C1 and C5 for SAC-C. Figure 6.3(a) shows the differences between the kinematic trajectory C1 and the reduced-dynamic orbit C1S for SAC-C 051/2001 and Figure 6.3(b) those between C2 and C1S. The differences between C1 and C2 for SAC-C are small (up to 15 cm). Those between C1 and C5 are ten times larger underlining that C5 with a $\beta = 30$ is not of good quality. The differences between the kinematic trajectories C1 and C2 are so small that the differences of these kinematic trajectories w.r.t. the reduced-dynamic orbit C1S (Figure 6.3) do not allow to prefer one of the solutions.

Figures 6.4(a) and 6.4(b) show the differences between the kinematic trajectories C1 and C2 and between C1 and C5 for CHAMP. The differences between C1 and C2 for CHAMP have the same magnitude as the corresponding differences for SAC-C except for a small sequence at the end of the day which reaches up to 35 cm (z-component). The differences between C1 and C5 show three major problem sequences, i.e., at the beginning, between 9^{h} and 12^{h}, and at the end of the day.

Figure 6.5 shows the differences between the kinematic trajectory C1 and C1S (left) and between C2 and C1S (right) for CHAMP 152/2001. The differences between C1 and C2 are also in the case of CHAMP so small that no solutions may be preferable when inspecting the differences to C1S. One thing can be recognized however: The big jump between the kinematic trajectories C1 and C2 (Figure 6.4(a)) at the end of the day stems from the kinematic solution C2 (compare with Figure 6.5(b)).

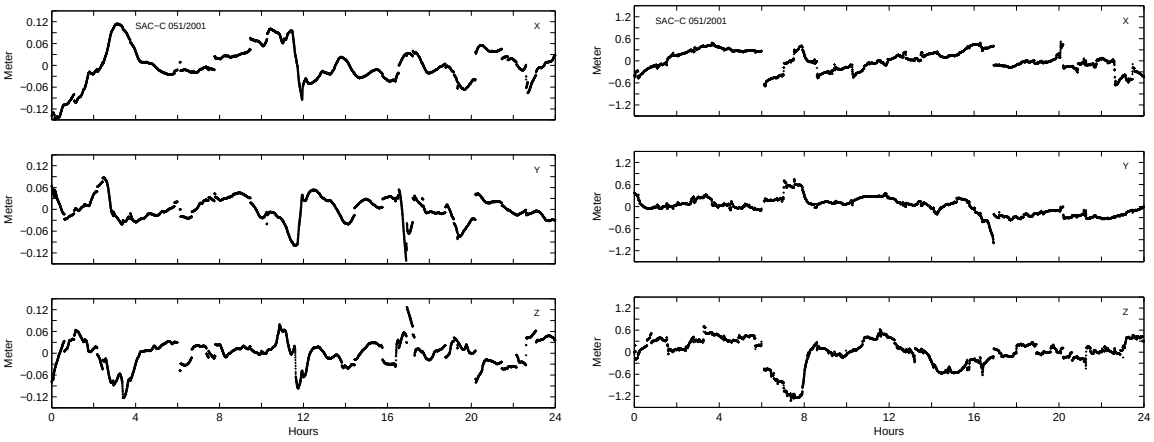

(a) Kinematic trajectories C1 – C2, RMS 0.04 m.

(b) Kinematic trajectories C1 – C5, RMS 0.30 m.

Figure 6.2: Orbit differences between kinematic trajectories C1 and C2 (left) and C1 and C5 (right) for SAC-C 051/2001.

Some observations included in C5 significantly deteriorate the kinematic solution. Decimeter accuracy of a kinematic solution with LEOKIN is not possible with $\beta \geq 30$ (C5 and C6). The studies underline the importance of the pre-screening. The iterative least squares adjustment step following the pre-screening is obviously not reliable enough to find all bad observations disturbing the solution. The results heavily depend on the pre-screening option β.

The percentage of deleted observations is an additional indication on how to select the optimum options. This is already illustrated by Figures 4.10(a) and 4.10(b) for SAC-C and by Figures 4.10(c) and 4.10(d) for CHAMP. In Section 4.3.2 the conclusion was drawn that the choice of $10 \leq \beta \leq 20$ seems to be appropriate for the CHAMP and the SAC-C receiver data. Together with the information from this section we note that the solutions C1 ($\beta = 3$) and C2 ($\beta = 5$) are optimal for both satellites, CHAMP and SAC-C, on the days considered. It seems that in solution C1 all outliers were actually rejected. On the other hand, some good observations may be included in solution C2 (which were excluded in C1) due to insufficient a priori information (GPS orbits, clock corrections, or a priori orbit for the LEO). These additional observations may stabilize the kinematic solution in particular in cases where otherwise only four observations would have been available.

6.2.2 Different Elevation Cut-off Angles and Elevation-dependent Weighting Functions

It is not clear a priori whether observations to satellites tracked below the local horizon of the receiver improve or deteriorate a kinematic point positioning. Such observations may be affected, e.g., by multipath. One may hope to minimize the impact of multipath by using an elevation-dependent weighting scheme (see Section 4.3.3). Using all observations but weighting them promises a gain of observation information for the kinematic solution.

Test solutions are performed with $\beta = 3$, varying elevation cut-off angles and weighting functions. Table 6.3 summarizes the solution characteristics. Figure 6.6 shows the number of interrupts and number

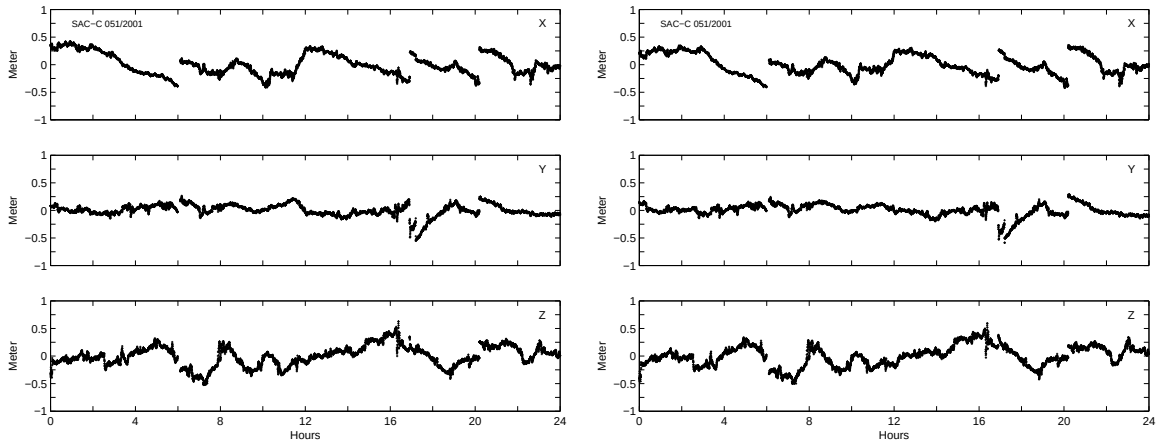

(a) Kinematic trajectory C1 – reduced-dynamic orbit C1S, RMS 0.16 m

(b) Kinematic trajectory C2 – reduced-dynamic orbit C1S, RMS 0.16 m

Figure 6.3: Orbit differences between kinematic trajectory C1 and reduced-dynamic orbit C1S (left) and between C2 and C1S (right) for SAC-C 051/2001.

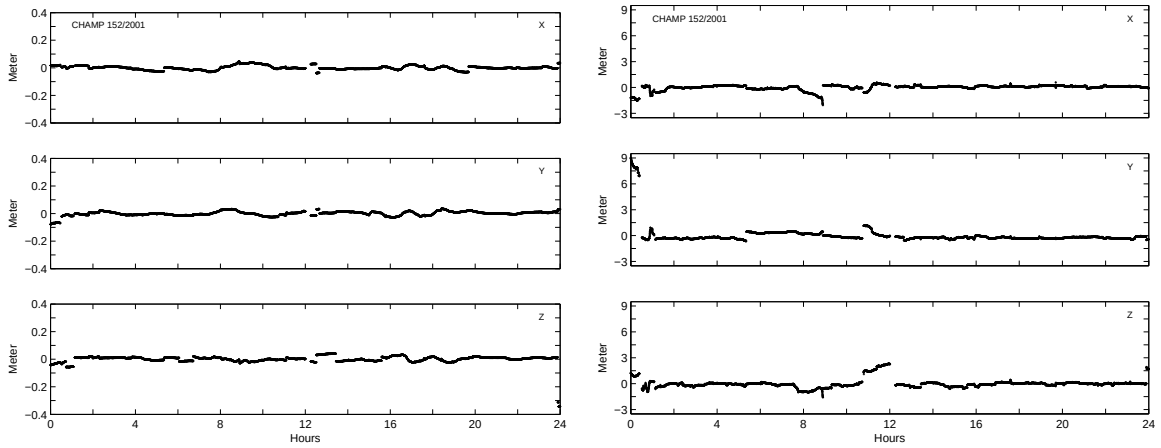

(a) Kinematic trajectories C1 – C2, RMS 0.02 m.

(b) Kinematic trajectories C1 – C5, RMS 0.72 m.

Figure 6.4: Orbit differences between kinematic trajectories C1 and C2 (left) and C1 and C5 (right) for CHAMP 152/2001.

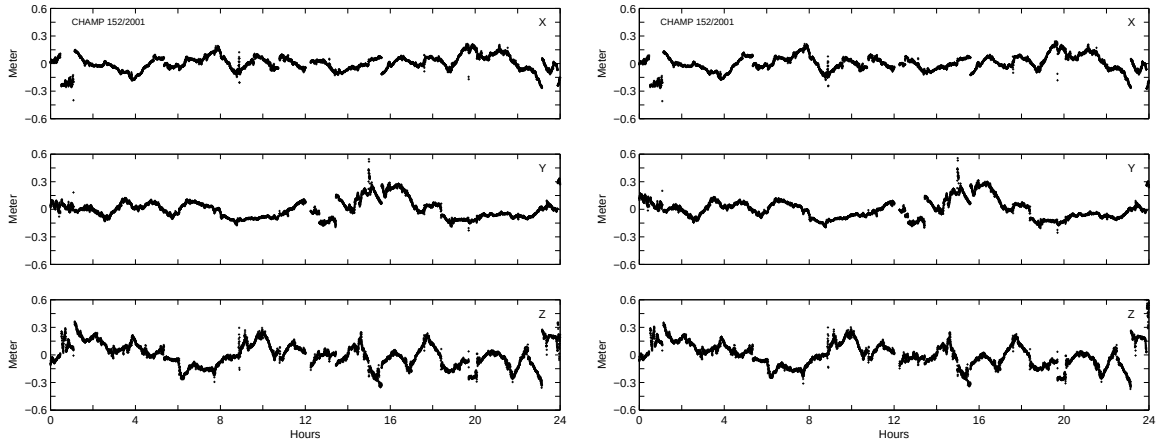

(a) Kinematic trajectory C1 – reduced-dynamic orbit C1S, RMS 0.10 m

(b) Kinematic trajectory C2 – reduced-dynamic orbit C1S, RMS 0.11 m

Figure 6.5: Orbit differences between kinematic trajectory C1 and reduced-dynamic orbit C1S (left) and between C2 and C1S (right) for CHAMP 152/2001.

Table 6.3: Solutions with different elevation cut-off angles and elevation-dependent weighting.

	C1	D1	D2	D3	D4	D5	D6
Elev. cut-off angle	no	no	0°	0°	0°	10°	10°
Elev.-dep weight.	yes	no	no	yes	yes	no	yes
Factor α	3/4	-	-	3/4	1	-	1

of jumps for SAC-C 051/2001 (top) and for CHAMP 152/2001 (bottom). Table 6.4 lists the RMS errors of the Helmert transformations between the solutions. Figure 6.7 shows the differences between D2 and D3 (Figure 6.7(a)) and between D2 and D4 (Figure 6.7(b)) for SAC-C 051/2001. Figure 6.9 shows the differences between the corresponding solutions for CHAMP 152/2001. Figure 6.8(a) shows the differences between the kinematic trajectory D2 and the reduced-dynamic orbit C1S and Figure 6.8(b) those between D4 and C1S for SAC-C 051/2001. Figures 6.10(a) and 6.10(b) show the differences between the corresponding solutions for CHAMP 152/2001.

It is obvious that the solutions D5 and D6 (elevation cut-off of 10°) are of poor quality for both satellites due to the large number of interrupts and jumps. We may conclude from this fact that observations between 0° and 10° elevation are very important for a stable point positioning solution. They have to be included into the processing.

Solutions C1 and D1 (no elevation cut-off) are the best for SAC-C regarding the number of interrupts and jumps in the kinematic trajectory. Solution D2 has the same number of interrupts but the number of jumps in the trajectory is slightly larger.

When we analyze the results from CHAMP we have to keep in mind that the CHAMP receiver is no longer tracking below the local horizon since doy 206/2001 (Section 4.3.1). This means that for the processing of data after doy 206/2001 it is no longer possible to include observations below the local horizon. Though doy 152/2001 is prior this date we have a look on the solutions D2, D3, and D4

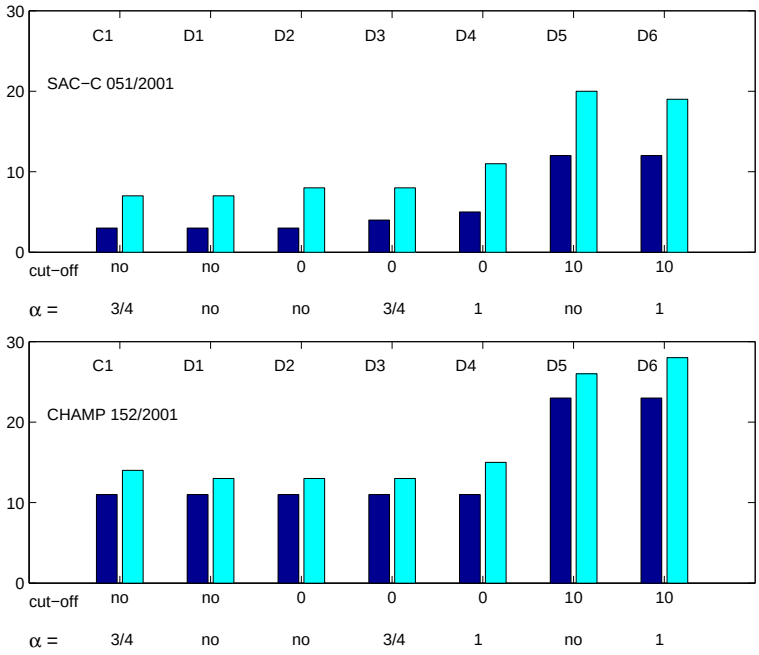

Figure 6.6: Number of interrupts due to missing phase position-differences (left bar) and number of jumps in the kinematic trajectory (right bar), solutions C1, D1 to D6, SAC-C 051/2001 (top) and CHAMP 152/2001 (bottom).

Table 6.4: RMS errors (m) of Helmert transformation between kinematic solutions and C1, D2, and C1S for SAC-C (doy 051/2001) and CHAMP (doy 152/2001).

		D1	D2	D3	D4	D5	D6
SAC-C	C1	0.04	0.06	0.04	0.08	0.19	0.20
SAC-C	D2	0.05	-	0.04	0.10	0.18	0.21
SAC-C	C1S	0.17	0.18	0.17	0.18	0.21	0.23
CHAMP	C1	0.05	0.05	0.01	0.05	0.09	0.09
CHAMP	D2	0.03	-	0.05	0.09	0.11	0.11
CHAMP	C1S	0.11	0.11	0.10	0.11	0.12	0.12

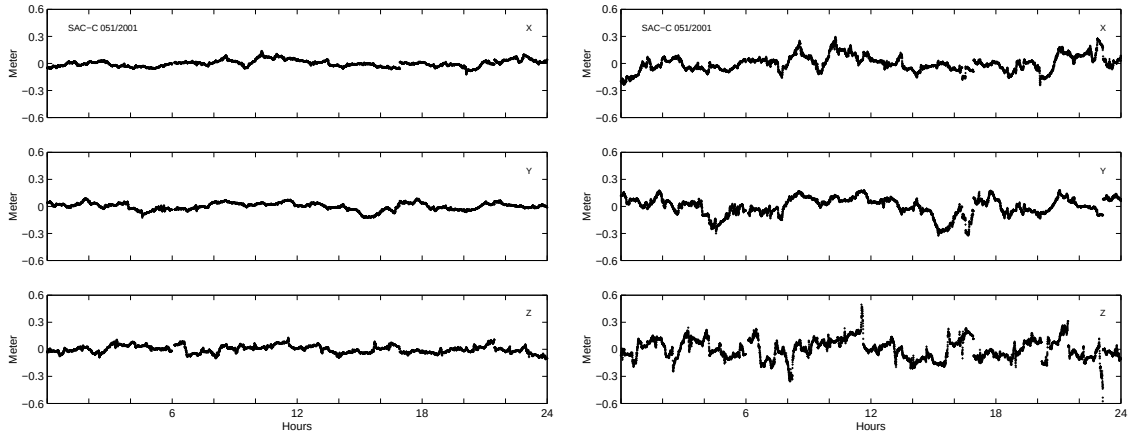

(a) Kinematic trajectories D2 – D3, RMS 0.04 m.

(b) Kinematic trajectories D2 – D4, RMS 0.10 m.

Figure 6.7: Orbit differences between kinematic trajectories D2 and D3 (left) and between D2 and D4 (right) for SAC-C 051/2001.

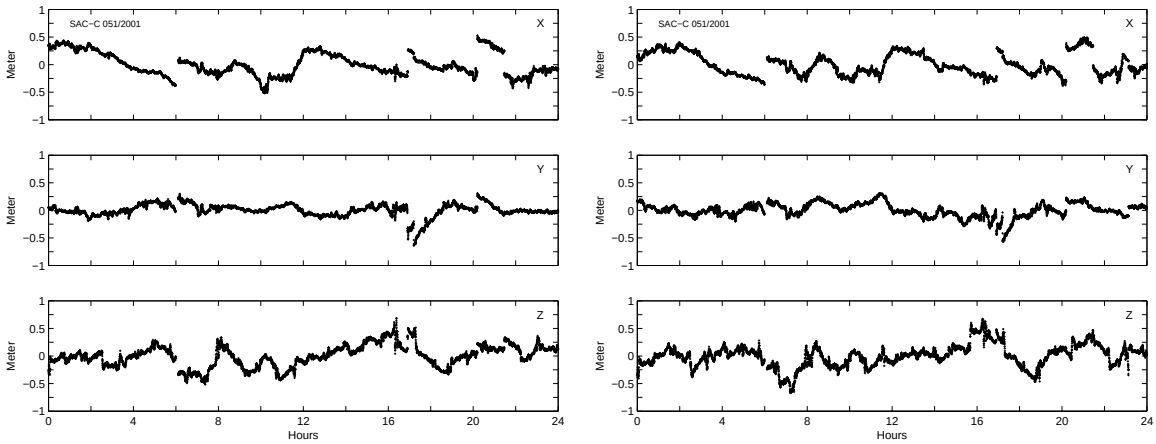

(a) Kinematic trajectory D2 – reduced-dynamic orbit C1S, RMS 0.18 m.

(b) Kinematic trajectory D4 – reduced-dynamic orbit C1S, RMS 0.18 m.

Figure 6.8: Orbit differences between kinematic trajectory D2 and reduced-dynamic orbit C1S (left) and D4 and C1S (right) for SAC-C 051/2001.

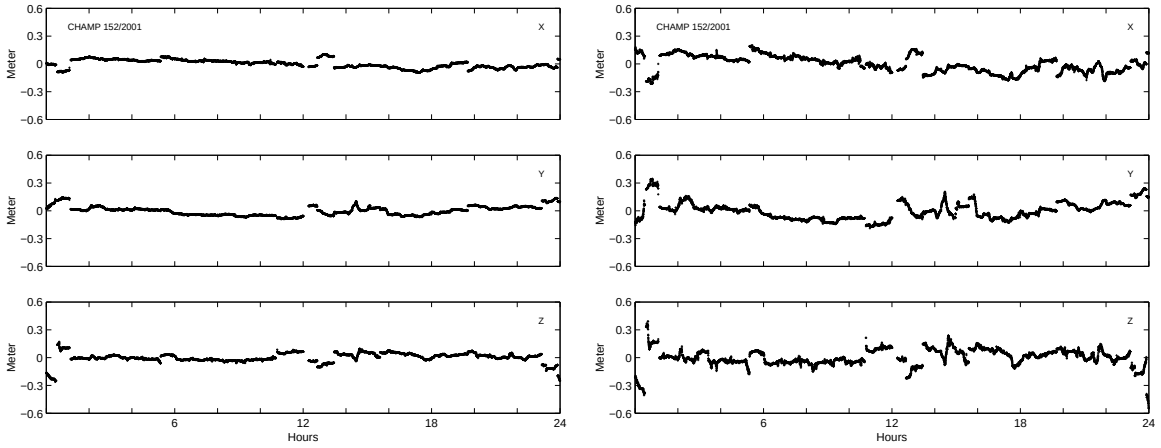

(a) Kinematic trajectories D2 – D3, RMS 0.05 m.

(b) Kinematic trajectories D2 – D4, RMS 0.09 m.

Figure 6.9: Orbit differences between kinematic trajectories D2 and D3 (left) and between D2 and D4 (right) for CHAMP 152/2001.

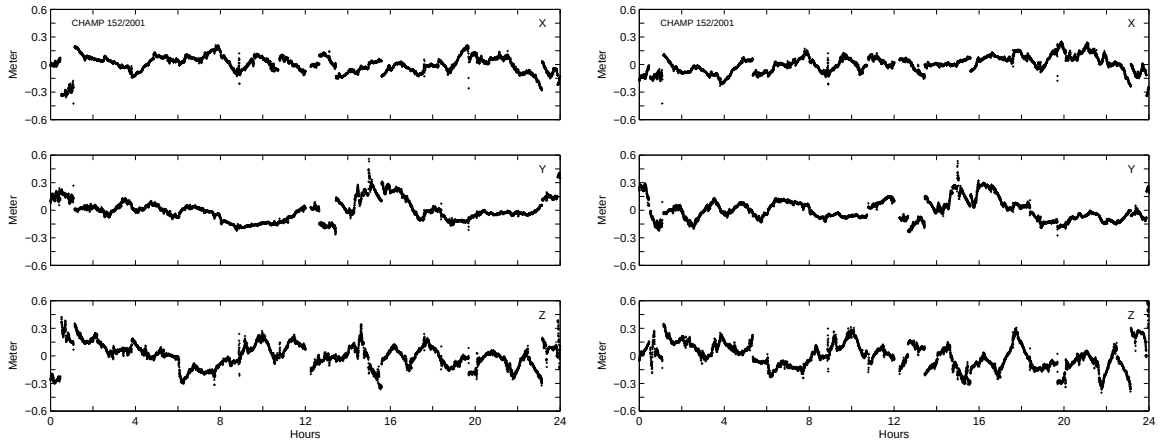

(a) Kinematic trajectory D2 – reduced-dynamic orbit C1S, RMS 0.11 m.

(b) Kinematic trajectory D4 – reduced-dynamic orbit C1S, RMS 0.11 m.

Figure 6.10: Orbit differences between kinematic trajectory D2 and reduced-dynamic orbit C1S (left) and D4 and C1S (right) for CHAMP 152/2001.

only. Concerning the number of interrupts and jumps solutions D2 and D3 are identical, solution D4 has slightly more jumps in the kinematic trajectory. Figure 6.9(a) shows the differences between the kinematic trajectories of D2 and D3. The offset of a few small sequences is remarkable. The RMS error of the Helmert transformation is five centimeters (Table 6.4). The offset between short sequences may be recognized in the differences between solution D2 and D4 (Figure 6.9(b)), as well. When we inspect the differences of the kinematic trajectories (D2 and D4) w.r.t. the reduced-dynamic orbit C1S we can recognize that solution D2 shows the bigger jumps in the kinematic trajectory.

The question whether elevation-dependent weighting of the observations is appropriate or not for CHAMP can, however, not be answered at this point of the studies.

Figure 6.6 shows that the observations below the local horizon do neither improve nor disturb the kinematic solution in the case of CHAMP. The GPS POD antenna on-board CHAMP does, however, not have a direct sight to the satellites below the local horizon. One may therefore question the sense of using these observations.

The SAC-C receiver is still tracking below the local horizon, today. The solutions C1 and D1 without applying a cut-off angle show the best performance. The observations below the local horizon slightly improve the kinematic solution. In the case of SAC-C the GPS antenna may track the satellites below the local horizon and therefore it could make sense to use these observations.

The analyzed example of one day for each satellite CHAMP and SAC-C shows the big influence of different pre-processing options on the resulting kinematic positions. Therefore it is important to find the optimum options for the pre-processing of the observations. A clear answer could be given concerning the value of β. The most reasonable choice is $\beta = 3$ or 5 because for larger values of β the bad observations remaining in the processing cannot be identified by the iterative least squares adjustment step. The studies about elevation-dependent weighting and cut-off angle options only showed clearly that the observations between 0° and 10° elevation are very important for a stable point positioning and they have to be used in the kinematic point positioning procedure in LEOKIN.

The findings of this section will be used when processing more data of CHAMP and SAC-C. The evaluation of the best pre-processing options for the kinematic point positioning of each satellite will then be easier.

6.3 IGS Test Campaign – doy 140 to 150/2001

The IGS CHAMP test campaign was initiated by the IGS LEO Pilot Project (Section 2.2.3) and covers a time interval of eleven days (May, 20 to 30, doy 140 to 150, 2001). The institutes and groups contributing to the Pilot Project processed the CHAMP GPS tracking data and produced orbits for CHAMP. The resulting orbits were compared by the Analysis Center Coordinator (ACC) of the project (Henno Boomkamp of ESOC, Darmstadt) [*TEST CAMPAIGN*, 2002].

Our (AIUB) contribution to the test campaign is based on the following input data:

- GPS orbits and ERPs from the CODE Final processing,
- GPS 30-second clock corrections (using CODE Final solutions for troposphere zenith delays and station coordinates) fixed on the 5-minute CODE Final clock corrections, and
- CHAMP L1 and L2 phase and code observations.

First we check the CHAMP GPS data quality for the eleven days of the campaign. Detailed studies of data pre-processing are performed and explained in the following section in order to select the optimal options

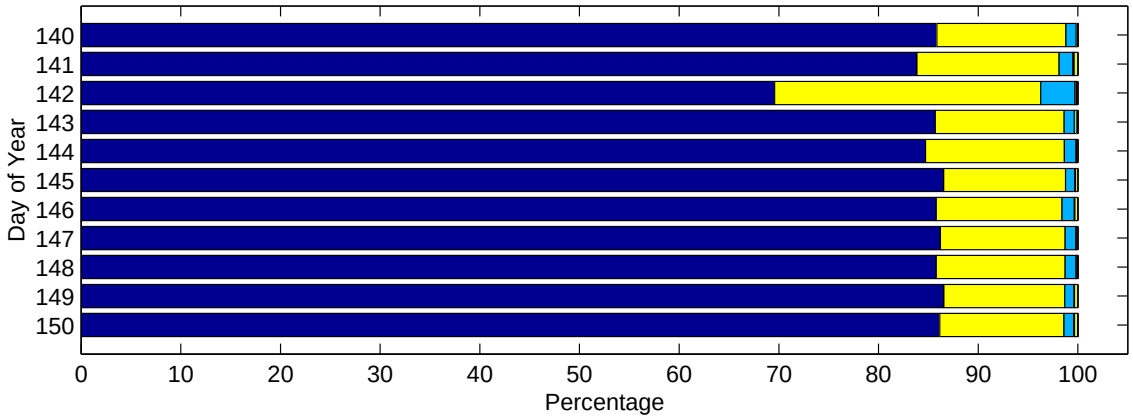

Figure 6.11: Percentage per day of effectively tracked satellites by the CHAMP GPS receiver for doy 140 to 150/2001. Black: eight satellites, white: seven satellites, gray: six satellites.

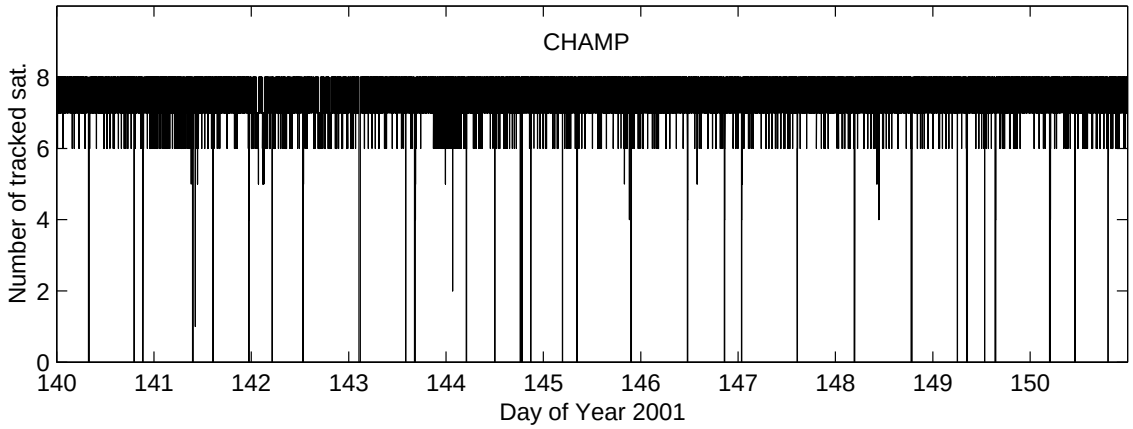

Figure 6.12: Number of tracked satellites by the CHAMP GPS receiver for doy 140 to 150/2001.

for the processing of the entire data set and the determination of the kinematic positions. Subsequently, the kinematic solutions are compared with solutions from an external source. The reduced-dynamic solution generated by the Technical University of Munich, Germany, is used for this purpose. The studies based on the data of the eleven days in 2001 for CHAMP are summarized in the concluding section.

6.3.1 Data Quality

Figure 6.11 shows for each day the fraction of the day for which a given number of satellites was tracked. During the time period of the test campaign the CHAMP receiver could track up to eight GPS satellites simultaneously (Table 4.1). The figure gives the percentage of time where eight (black), seven (white), or six (gray) satellites where tracked. Figure 6.12 shows the number of tracked satellites as a function of time for the eleven days. The CHAMP GPS receiver shows a similar performance during the entire time span. Some data gaps exist, they last from one epoch to several minutes.

6.3.2 Data Pre-processing

The pre-processing performance was studied as a function of:

- different values for the threshold β,
- the weight ratio of code and phase for the combination,
- elevation-dependent weighting of the observations,
- different a priori orbit information for the pre-screening of the data, and
- different iterative procedures to achieve the kinematic solutions.

Two basic options for data processing in LEOKIN were never changed:

- $\sigma_{c_{scr}} = 1.0$ m, $\sigma_{p_{scr}} = 0.01$ m, and
- a cut-off angle of $0°$.

The a priori orbit for the zero-difference kinematic point positioning with LEOKIN is generated by a two-step procedure (Section 3.1) in order to get an a priori orbit which has at least an accuracy of less than half a meter. Each step contains one LEOKIN and one SATORB run. We follow two different approaches (APO set C and P) for generating the reduced-dynamic orbit used as a priori orbit for the pre-screening in LEOKIN. This is done to find the most appropriate and reliable procedure for generating a reduced-dynamic orbit serving as a priori orbit. The kinematic and reduced-dynamic orbits generated for this purpose are summarized in Table 6.5.

The reduced-dynamic orbits are generated in SATORB with the following models and parameters:

- Models for gravitational forces:
  - Earth gravity field model EIGEN-1S (degree and order 120),
  - tidal potential, ocean tides,
  - third body perturbations of Sun and Moon,
  - precession, nutation, and polar motion,
- Models for non-gravitational forces:
  - atmospheric drag,
  - direct radiation pressure,
- Parameters estimated:
  - six osculating elements,
  - nine empirical parameters in RSW-directions (three constant and six periodic terms),
  - pseudo-stochastic pulses in RSW-directions with a spacing of 90 or 20 min (see Table 6.5).

Table 6.5: Kinematic (LEOKIN) and reduced-dynamic (SATORB) orbits generated in order to guarantee reliable a priori orbit information.

Solution	Source	Description
cI	LEOKIN	Kinematic code positions, generated without a priori information
cIS	SATORB	Reduced-dynamic orbit, cI positions as observations, spacing for stochastic pulses: 90 min
A priori orbit (APO) set C		
cIIβ cIIβe	LEOKIN	Kinematic code positions, cIS used as a priori information, individual value for β with elevation-dependent weighting
cIIβS cIIβSe	SATORB	Reduced-dynamic orbit, cIIβ or cIIβe positions as observations, spacing for stochastic pulses: 20 min
A priori orbit (APO) set P		
pIIβ pIIβe	LEOKIN	Combined kinematic positions based on code and phase observations, cIS used as a priori information, individual value for β with elevation-dependent weighting
pIIβS pIIβSe	SATORB	Reduced-dynamic orbit, pIIβ or pIIβe positions as observations, spacing for stochastic pulses: 20 min

Table 6.6: Summary of kinematic solutions computed for the IGS CHAMP test campaign (C stands for APO set C, P for APO set P, A for a normal code weight for the combination, B for one which is reduced by a factor of 100, e for elevation-dependent weighting).

	APO set C				APO set P			
	no elev.-dep.weight.		elev.-dep.weight.		no elev.-dep.weight.		elev.-dep.weight.	
$\beta = 3$	CA3	CB3	CA3e	CB3e	PA3	PB3	PA3e	PB3e
$\beta = 5$	CA5	CB5	CA5e	CB5e	PA5	PB5	PA5e	PB5e
$\beta =10$	CA10	CB10	CA10e	CB10e	PA10	PB10	PA10e	PB10e
$\beta =20$	CA20	CB20	CA20e	CB20e	PA20	PB20	PA20e	PB20e
$\beta =30$	CA30	CB30	CA30e	CB30e	PA30	PB30	PA30e	PB30e

Eight iterations are performed to ensure convergence of the solution.

The LEOKIN run to generate solutions cIIβ, cIIβe, pIIβ, or pIIβe is the starting point for the following set of test solutions. The pre-screening option β and elevation-dependent weighting or not dedicated to the particular test solution are used for this point positioning in LEOKIN, too. In this way we guarantee a consistent use of the same set of options throughout all steps of the procedure. This implies that we generate different a priori orbits for each solution. In some examples we will, however, use the same a priori orbit for different solutions for specific comparisons.

Table 6.6 summarizes the final kinematic solutions computed for the data set from the IGS CHAMP test campaign with LEOKIN. For all solutions code and phase observations are used. The first capital of the solution identifier stands for the a priori orbit set used (C: based on code only, cIIβS or cIIβSe, P: based on code and phase, pIIβS or pIIβSe), and the notation A or B denotes the weighting scheme for the code positions in the combination. Solution A uses the "normal" relative weight of $w_c : w_p = 2 : 100^2$ between code positions and phase position-differences for the combination. Solution B further reduces the weight of the code positions by a factor of 100 for the combination of code and phase. The number (3, 5, 10, 20, and 30) denotes the value used for β and the "e" at the end stands for elevation-dependent weighting.

The example of doy 152/2001 for CHAMP indicated no clear answer whether elevation-dependent weighting of the observations is appropriate for the GPS observations of CHAMP. In order to find an answer we produced kinematic solutions without and with elevation-dependent weighting. First we inspect the solutions without elevation-dependent weighting.

Solutions Without Elevation-dependent Weighting

Figure 6.13 shows the number of interrupts and jumps for APO set C and Figure 6.14 for APO set P. The three bars for each day stand for the number of interrupts due to missing position-differences (left bar), the number of jumps in the kinematic trajectory w.r.t. a dynamic orbit for solution A (middle bar) and for solution B (right bar). The number of interrupts needs to be given only once because it is the same for solutions A and B. Table 6.7 summarizes the mean values of the interrupts and jumps of all solutions for all eleven days. Figure 6.15 shows the percentage of deleted observations as a function of the value of β for code and phase observations and for APO set C and P for all eleven days. The top figures show the percentage of observations deleted by the pre-screening algorithm. The bottom figures show the total percentage of observations removed by the complete procedure, which is the sum of the percentage of the top figures, of observations below the cut-off angle, and of observations deleted by the iterative least squares adjustment step.

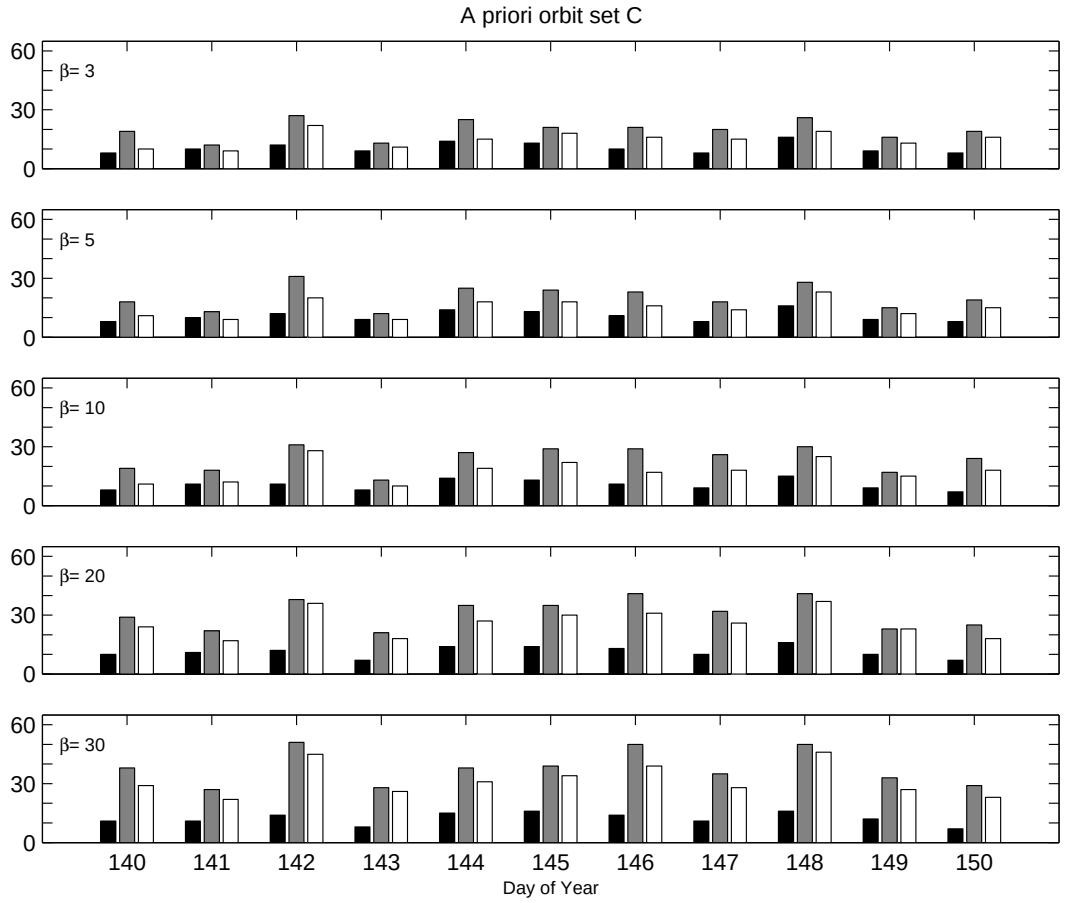

Figure 6.13: Number of interrupts due to missing phase position-differences (left bar) and number of jumps in the kinematic trajectory for solution A (middle bar) and B (right bar), without elevation-dependent weighting, doy 140 to 150/2001.

Table 6.7: Mean number of interrupts and jumps for solutions without elevation-dependent weighting, doy 140 to 150/2001.

	APO set C			APO set P		
	Interrupts	Jumps		Interrupts	Jumps	
	Sol. A and B	Sol. A	Sol. B	Sol. A and B	Sol. A	Sol. B
$\beta = 3$	11	20	15	10	19	13
$\beta = 5$	11	20	15	10	20	14
$\beta =$10	10	24	18	10	23	17
$\beta =$20	11	31	26	11	28	21
$\beta =$30	12	38	32	11	34	28

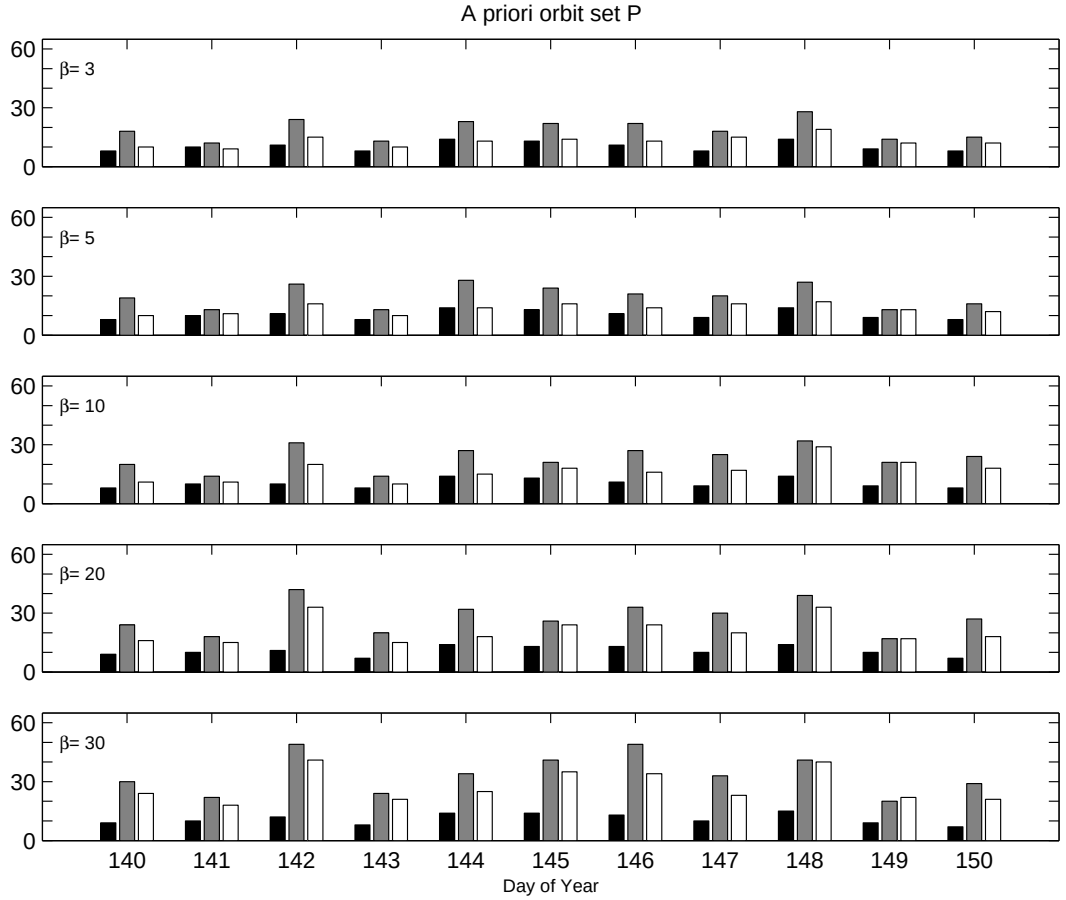

Figure 6.14: Number of interrupts due to missing phase position-differences (left bar) and number of jumps in the kinematic trajectory for solution A (middle bar) and solution B (right bar), without elevation-dependent weighting, doy 140 to 150/2001.

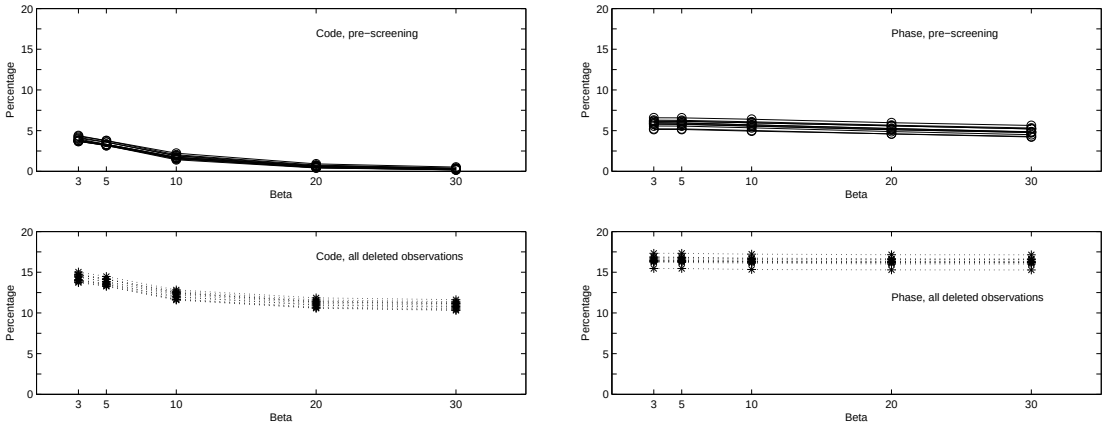

(a) Code observations, APO set C.

(b) Phase observations, APO set C.

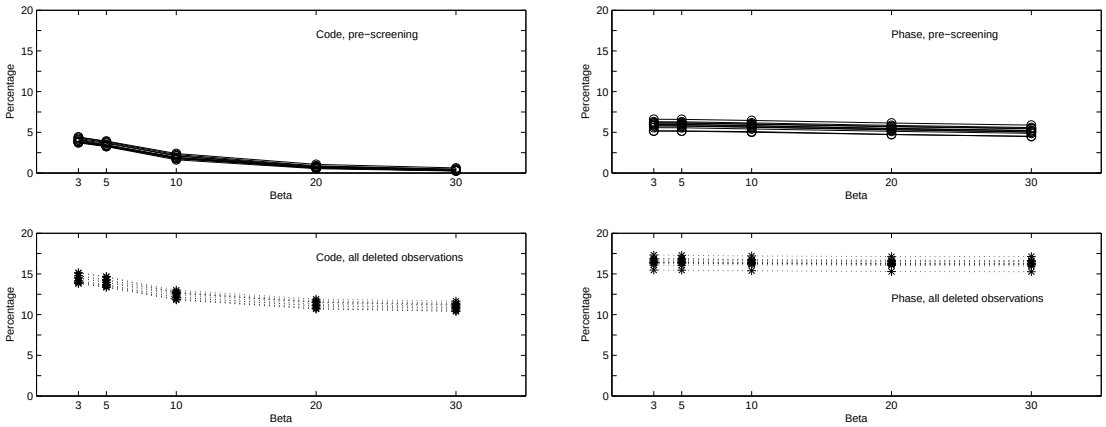

(c) Code observations, APO set P.

(d) Phase observations, APO set P.

Figure 6.15: Percentage of deleted observations after pre-screening and by entire screening procedure, solutions without elevation-dependent weighting, doy 140 to 150/2001.

The number of interrupts and the number of jumps is increasing with increasing values of β for both APO sets (Figures 6.13 and 6.14). However, the number of interrupts is increasing not as much as the number of jumps. It is remarkable that nearly all solutions A have more jumps in the kinematic trajectory than solutions B. This means that the deweighting of the code positions has a strong impact on the combined solution. As we have seen in Section 3.6.2 the deweighting causes a smoothing of the combined positions. This smoothing is reflected in the difference of the number of jumps between solution A and B. Regarding the mean number of interrupts and jumps in Table 6.7 the solutions PB show the best performance. As expected the solutions with $\beta = 3$ or 5 are the most reasonable solutions, because all bad observations are found which disturb the kinematic solutions for $\beta > 5$. The iterative least squares adjustment step cannot find these observations in the cases $\beta > 5$.

The percentage of deleted observations is similar when using either APO set C or set P. The large difference (about ten percent) between the percentage of deleted observations after the pre-screening and of all deleted observations is due to the cut-off angle of $0°$, indicating that about ten percent of the observations have an elevation angle below $0°$. These observations are already marked and excluded from the processing before the pre-screening is applied to the remaining observations. Apart from this large difference the two curves are parallel which means that during the iterative least squares adjustment step not many additional observations are excluded. This in turn means that an observation which is not excluded in the pre-screening step remains in the processing and may disturb the solution.

As mentioned in the previous section (Section 6.2) and in Section 4.2 the degree of freedom is small in the least squares adjustment step. The clear identification of an outlier is therefore not guaranteed.

The percentage of deleted code observations decreases with increasing β. The curve for deleted phase observations is flat and there is no significant difference between different values for β. This means that the differences between the solutions are mainly due to the impact of code observations which are left in the processing for big values of β.

Let us now compare different solutions. All kinematic solutions which were computed for doy 144/2001 are inspected in detail. We generated in addition a reduced-dynamic orbit in SATORB which is based on the code positions and the phase position-differences of the kinematic solution PB3 before the combination. This reduced-dynamic orbit P3S uses the same parameters as the reduced-dynamic orbit pII3S used as a priori orbit for the kinematic solutions PA3 and PB3 except that the time interval between the stochastic pulses is set to ten minutes. This reduced-dynamic orbit seems to be the best possible orbit which can be produced with the available procedures in LEOKIN and SATORB for the solutions without elevation-dependent weighting. The positions and position-differences are used as independent observation types in SATORB to avoid problems that may be introduced by jumps in the combined kinematic positions caused by missing phase position-differences.

A Helmert transformation with three translation parameter is performed between the different trajectories and the RMS errors are shown in Table 6.8. The upper part of the table lists the RMS errors of the Helmert transformations for APO set C, the middle part those for APO set P. The rightmost column gives the RMS errors for the comparisons to the reduced-dynamic orbit P3S. The two small tables at the bottom of the table are two cross comparisons of the B3 solutions with all solutions of the other APO set.

It can be seen that the differences between the A and B solutions for each APO set are rather big. These values reflect the fact that the deweighting of the code positions for the combination in solutions B has a big impact on the kinematic solution. The differences within the A or B sets of solutions, respectively, are smaller. The solutions B compare better with each other than solutions A and the solutions using APO set P compare better than the solutions using APO set C. This indicates that the value of β has a smaller impact on the kinematic positions than the downweighting of the code. The

Table 6.8: RMS errors (m) of Helmert transformation between all kinematic solutions and the reduced-dynamic solution P3S for doy 144/2001.

APO set C										
	A5	A10	A20	A30	B3	B5	B10	B20	B30	**P3S**
A3	0.04	0.11	0.16	0.17	0.14	0.15	0.17	0.20	0.21	0.17
A5	-	0.10	0.15	0.16	0.15	0.16	0.18	0.20	0.22	0.18
A10		-	0.09	0.11	0.20	0.21	0.22	0.24	0.24	0.23
A20			-	0.05	0.23	0.23	0.25	0.25	0.26	0.26
A30				-	0.24	0.24	0.25	0.26	0.26	0.27
B3					-	0.03	0.08	0.11	0.14	0.12
B5						-	0.07	0.10	0.13	0.13
B10							-	0.06	0.10	0.16
B20								-	0.08	0.19
B30									-	0.21

APO set P										
	A5	A10	A20	A30	B3	B5	B10	B20	B30	**P3S**
A3	0.04	0.10	0.16	0.17	0.14	0.14	0.15	0.17	0.17	0.17
A5	-	0.09	0.14	0.16	0.15	0.15	0.16	0.17	0.17	0.18
A10		-	0.10	0.13	0.20	0.20	0.20	0.21	0.21	0.22
A20			-	0.08	0.23	0.23	0.23	0.23	0.24	0.25
A30				-	0.23	0.23	0.23	0.23	0.23	0.25
B3					-	0.02	0.05	0.08	0.08	0.11
B5						-	0.04	0.08	0.08	0.12
B10							-	0.06	0.07	0.13
B20								-	0.04	0.15
B30									-	0.15

	CA3	CA5	CA10	CA20	CA30	CB3	CB5	CB10	CB20	CB30
PB3	0.15	0.16	0.21	0.24	0.25	0.06	0.07	0.12	0.15	0.17

	PA3	PA5	PA10	PA20	PA30	PB3	PB5	PB10	PB20	PB30
CB3	0.15	0.15	0.20	0.24	0.23	0.06	0.07	0.08	0.11	0.10

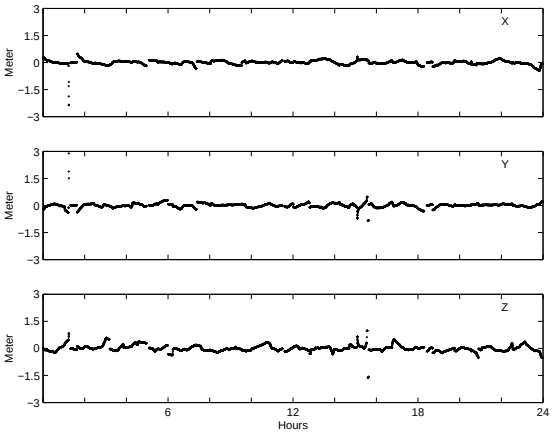

(a) Kinematic trajectories PB3 – PA3, RMS 0.14 m.

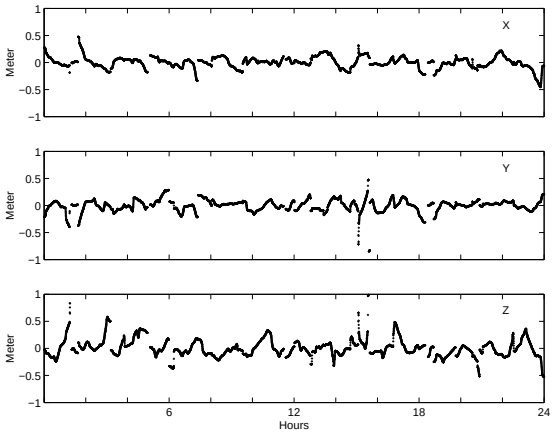

(b) Kinematic trajectories PB3 – PA3 (zoom), RMS 0.14 m.

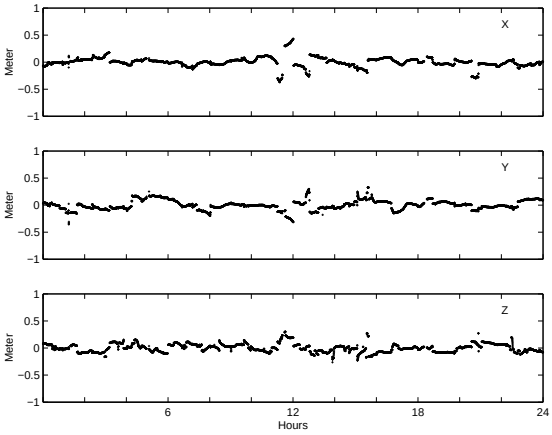

(c) Kinematic trajectories PB3 – PB30, RMS 0.08 m.

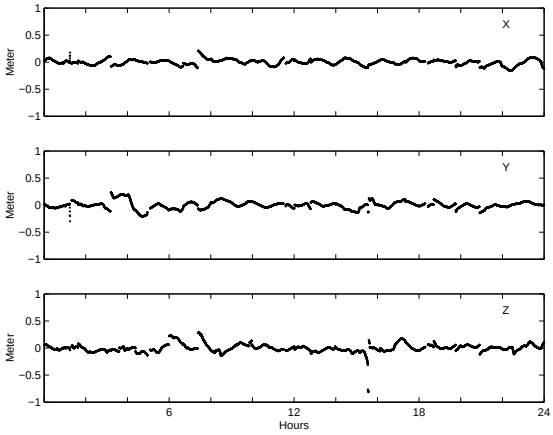

(d) Kinematic trajectories PB3 – CB3, RMS 0.06 m.

Figure 6.16: Orbit differences between kinematic trajectories for doy 144/2001.

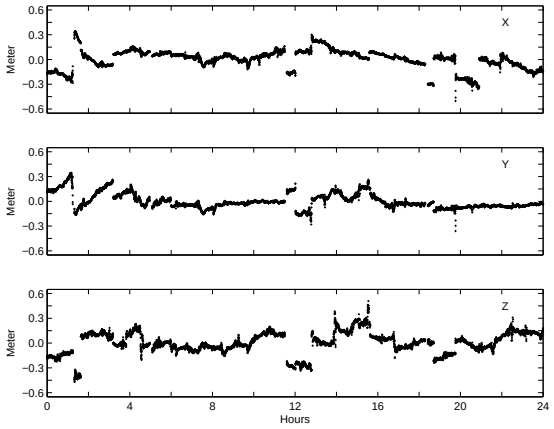

(a) Kinematic trajectory PB3 – reduced-dynamic orbit P3S, RMS 0.11 m.

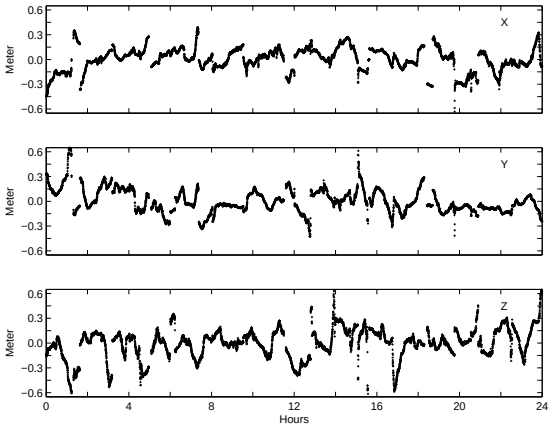

(b) Kinematic trajectory PA3 – reduced-dynamic orbit P3S, RMS 0.17 m.

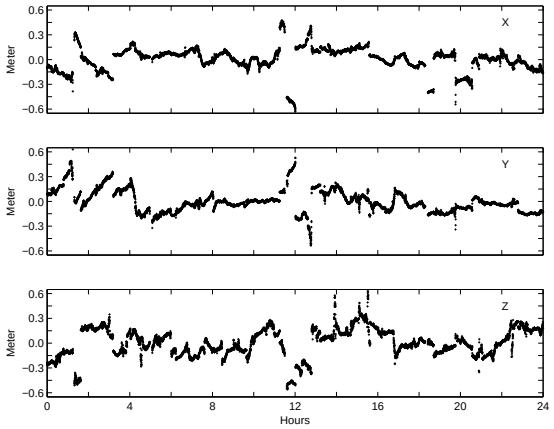

(c) Kinematic trajectory PB30 – reduced-dynamic orbit P3S, RMS 0.15 m.

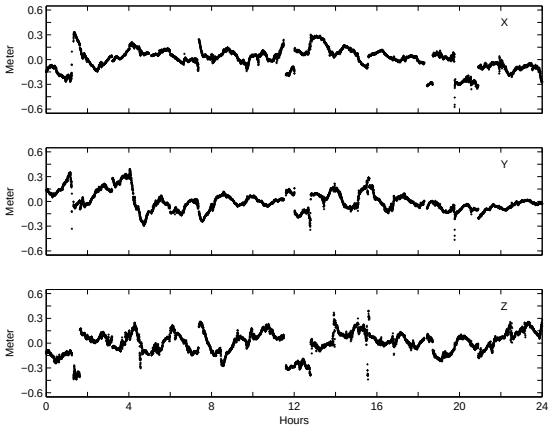

(d) Kinematic trajectory CB3 – reduced-dynamic orbit P3S, RMS 0.12 m.

Figure 6.17: Orbit differences between kinematic trajectories and post-fit reduced-dynamic orbit P3S, doy 144/2001.

impact is smaller on solutions B than on solutions A. The solution with the smallest differences to all other solutions is PB3 (APO set P, solution B, $\beta = 3$).

The following impacts on the resulting kinematic positions are inspected in more detail:

- downweighting of the code positions for the combination,
- different values for β, and
- different a priori orbits.

We take four typical solutions, PB3, PA3, PB30, and CB3. At first we will have a look at the differences of the latter three solutions w.r.t. solution PB3 (Figure 6.16) resulting after the Helmert transformation (with three translation parameters). The largest differences can be found for the comparison between PB3 and PA3 (RMS 0.14 m, Figure 6.16(a) and 6.16(b)). It seems that the differences are mainly due to a few outliers. Figure 6.16(b) is a zoom of the differences to the same scale as in Figures 6.16(c) and 6.16(d). In this figure (Figure 6.16(b)) we can recognize that the differences between solutions PB3 and PA3 are more pronounced than the differences of the two other comparisons. The differences between PB3 and PB30 are smaller (RMS 0.08 m, Figure 6.16(c)), which means that the downweighting of the code positions results in larger differences for the kinematic positions than increasing the value for β. The kinematic trajectories with the smallest differences of these three comparisons are solutions CB3 and PB3 (Figure 6.16(d)). The only difference between CB3 and PB3 is the used a priori orbit (cII3S for CB3 and pII3S for PB3). This means that the a priori orbit has some impact on the kinematic solution. The differences are rather small (RMS 0.06 m), however. More details will be provided below.

The four kinematic trajectories are also compared to the reduced-dynamic orbit P3S explained above (code positions and phase position-differences of PB3 as observations, stochastic pulses every ten minutes). Figure 6.17 shows the corresponding differences for the four solutions. The differences in Figure 6.17(a) confirm the good quality of the PB3 solution. The differences between the kinematic trajectory PB3 and the reduced-dynamic orbit P3S are the smallest. The differences in Figure 6.17(a) clearly show the jumps which are present in the kinematic trajectory of solution PB3. The differences between PA3 and P3S do not fit completely in the scale of the plot (Figure 6.17(b)). We recognize that the differences look very different to those in Figure 6.17(a). The jumps in the kinematic trajectory can be recognized, as well, but the variations in the sequences between these jumps are more pronounced than in Figure 6.17(a). These significant differences between Figures 6.17(a) and 6.17(b) are caused by the downweighting of the code positions with a factor of 100 for solution PB3. The differences between PB30 and P3S (Figure 6.17(c)) and between CB3 and P3S (Figure 6.17(d)) are larger but show similar characteristics as those between PB3 and P3S.

As a summary of these detailed comparisons we note that the downweighting of the code positions with a factor 100 has the biggest impact on the resulting kinematic positions. The impact of a different value for β is smaller but not negligible. The smallest impact results from using different a priori orbits for the pre-screening in program LEOKIN.

Solutions With Elevation-dependent Weighting of the Observations

The same solutions as described above were repeated with elevation-dependent weighting of the observations (with α =1) in order to study its impact on the kinematic solutions. Figures 6.18 and 6.19 show the number of interrupts and jumps for APO sets C and P. Table 6.9 summarizes the corresponding mean values.

Table 6.9: Mean number of interrupts and jumps for solutions with elevation-dependent weighting and α =1, doy 140 to 150/2001.

	APO set C			APO set P		
	Interrupts	Jumps		Interrupts	Jumps	
	Sol. A and B	Sol. A	Sol. B	Sol. A and B	Sol. A	Sol. B
$\beta = 3$	11	16	15	10	14	14
$\beta = 5$	10	15	14	10	14	14
β =10	13	26	23	10	16	15
β =20	10	19	18	10	17	17
β =30	12	32	30	10	22	21

The solutions are not as homogeneous as the solutions without elevation-dependent weighting (see Figures 6.13 and 6.14). We recognize outliers for APO set C, e.g., CA10e and CB10e (the "e" stands for elevation-dependent weighting, see Table 6.6) for doy 140 and 146. These solutions show a strongly increased number of interrupts and jumps in comparison to the solutions with smaller values for β. Opposed to the solutions without elevation-dependent weighting, the solutions A are of the same quality as solutions B. In a number of cases they even show the same number of jumps in the kinematic trajectory. The code observations at low elevations thus seem to be responsible for problems in the combined positions in solutions A. In the solutions with elevation-dependent weighting these problems are already taken into account for solutions A and therefore the differences to solutions B are not pronounced. In the solutions without elevation-dependent weighting these problems at low elevations are deweighted in solutions B due to the deweighting factor for the code positions. Therefore the improvements w.r.t. solutions A are larger.

This fact indicates that the elevation-dependent weighting is important mainly for the code observations. An impact on the phase observations cannot be derived from the current results.

Figure 6.20 shows the percentage of deleted observations. The curves are very similar to those of the solutions without elevation-dependent weighting (Figure 6.15). This is not surprising because the prescreening algorithm is based on unweighted observations and has therefore, except for the used a priori orbit, the same performance as for the solutions without elevation-dependent weighting. A difference may only occur in the percentage of observations excluded by the iterative least squares adjustment step.

The mean values in Table 6.9 indicate that the best solutions are those denoted by PBe. The solutions PB3e and PB5e show the best performance.

A reduced-dynamic orbit P3Se is generated with SATORB using the positions and position-differences of the kinematic solutions PB3e as input, which is the best possible orbit we may achieve with our LEOKIN and SATORB procedures. In order to get an idea of the accuracies of the best kinematic solutions from LEOKIN, we compare them with the reduced-dynamic orbit. The differences of orbit P3Se to the corresponding reduced-dynamic orbit P3S generated for the solutions without elevation-dependent weighting are shown in Figure 6.21(a). The RMS error of a Helmert transformation between the two orbits is 0.09 m. Figure 6.21(b) shows the differences between the two kinematic trajectories PB3 and PB3e. Comparison between the figures show a similar range of variations and, to a certain extent, common features. The orbit differences between the kinematic orbit PB3 and the reduced-dynamic orbit P3Se are shown in Figure 6.22(a) and those between PB3e and P3Se in Figure 6.22(b). The kinematic solution involving elevation-dependent weighting (PB3e) seems to perform marginally better in the comparison with the reduced-dynamic orbit P3Se. The differences in the patterns between the two Figures 6.22(a)

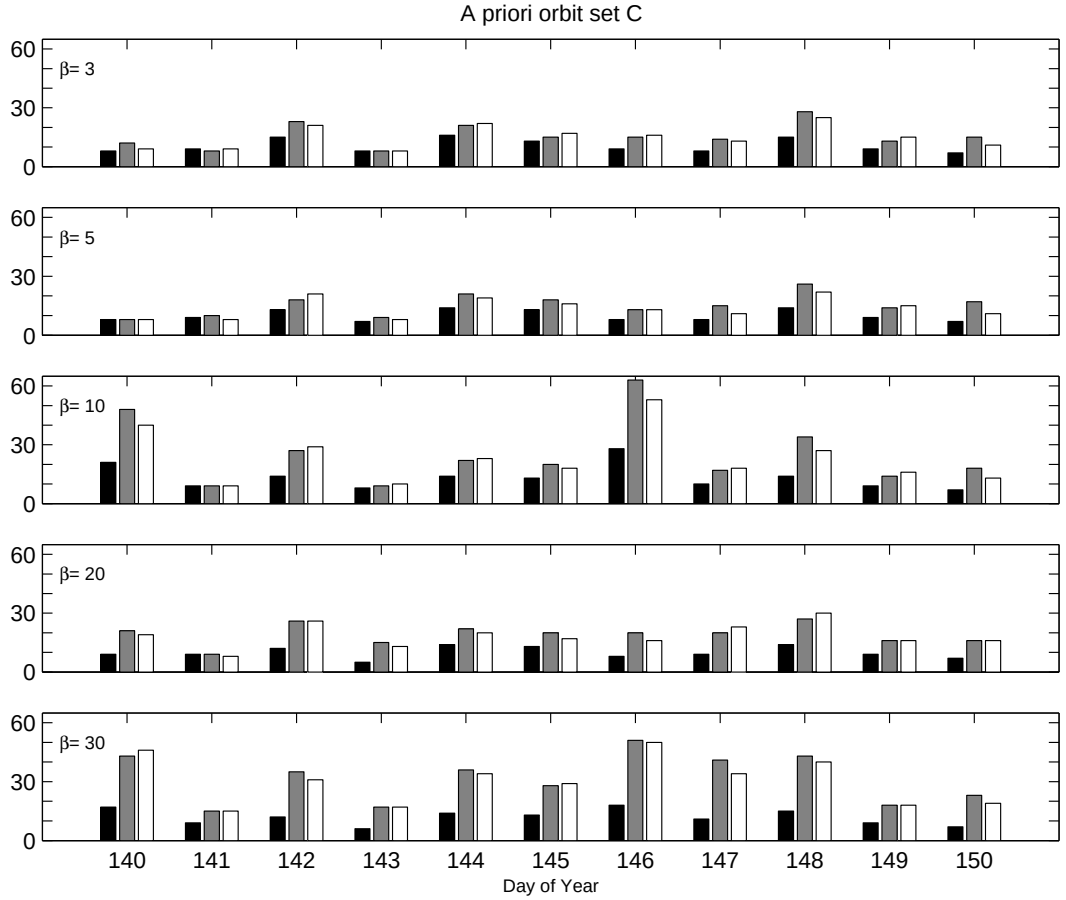

Figure 6.18: Number of interrupts due to missing phase position-differences (left bar) and number of jumps in the kinematic trajectory for solution A (middle bar) and solution B (right bar), elevation-dependent weighting, doy 140 to 150/2001.

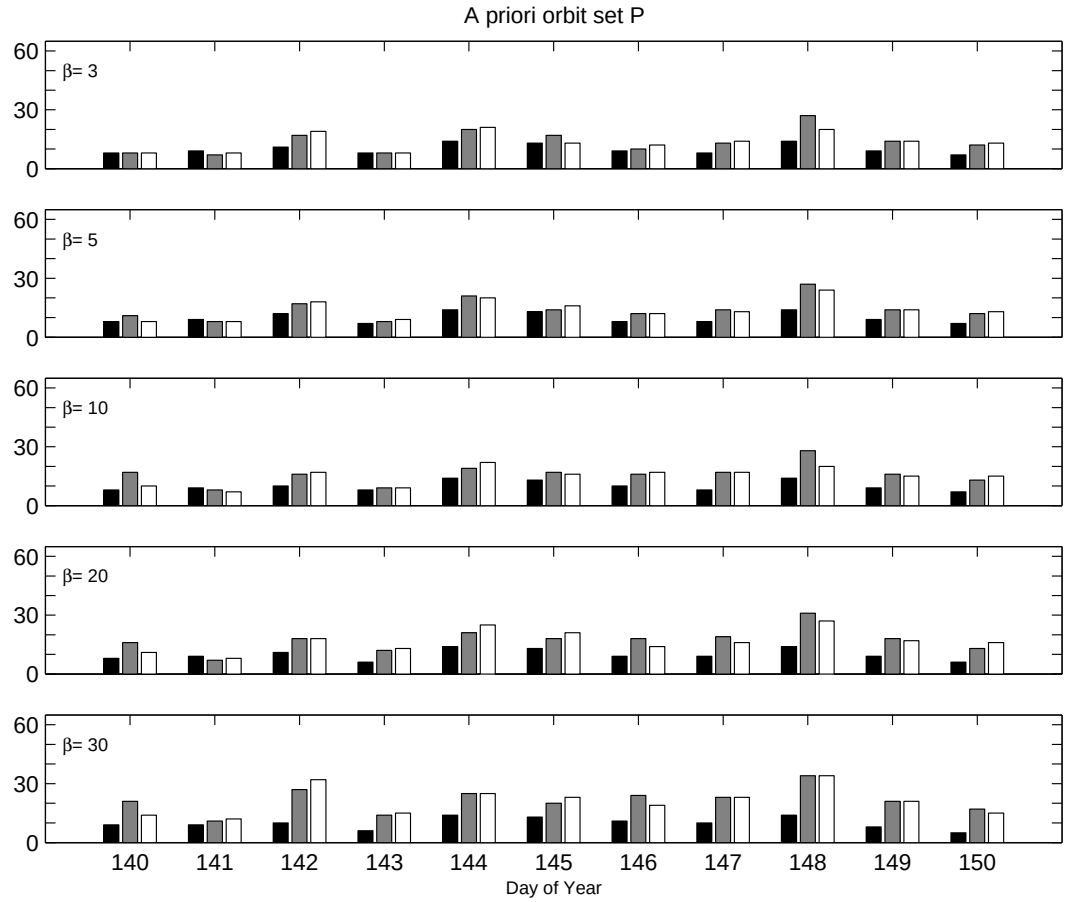

Figure 6.19: Number of interrupts due to missing phase position-differences (left bar) and number of jumps in the kinematic trajectory for solution A (middle bar) and solution B (right bar), elevation-dependent weighting, doy 140 to 150/2001.

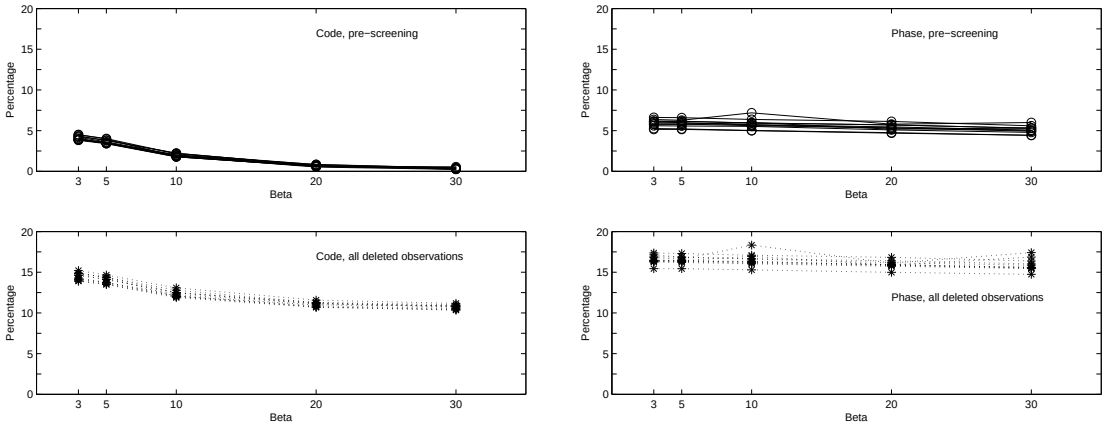

(a) Code observations, APO set C.

(b) Phase observations, APO set C.

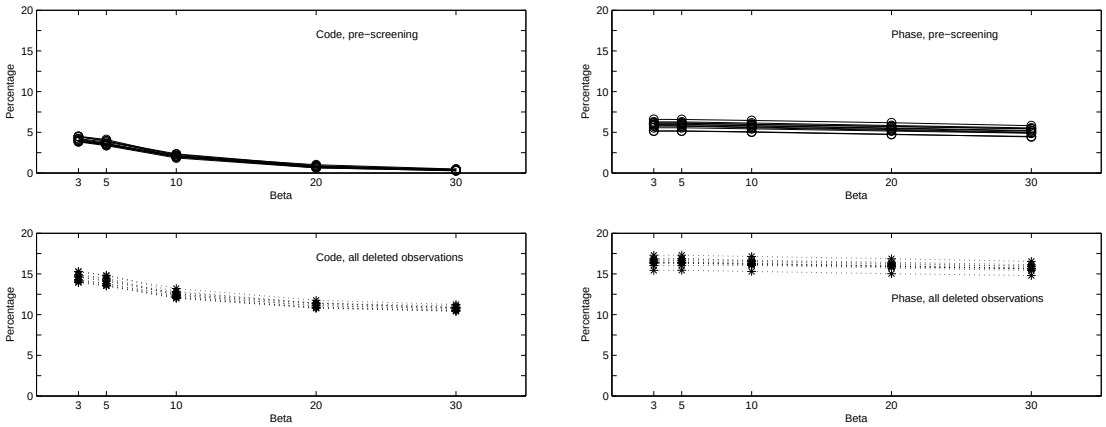

(c) Code observations, APO set P.

(d) Phase observations, APO set P.

Figure 6.20: Percentage of deleted observations after pre-screening and by entire screening procedure, solutions with elevation-dependent weighting, doy 140 to 150/2001.

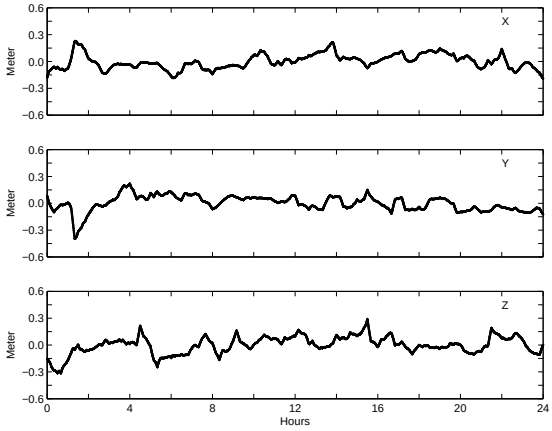

(a) Reduced-dynamic orbits P3S – P3Se, RMS 0.09 m.

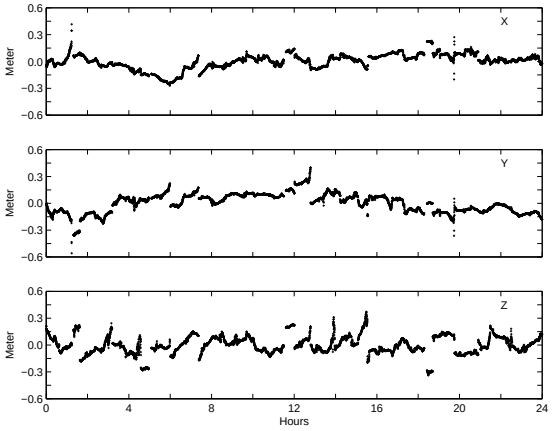

(b) Kinematic trajectories PB3 – PB3e, RMS 0.10 m.

Figure 6.21: Orbit differences between reduced-dynamic orbits P3S and P3Se (left) and kinematic trajectories PB3 and PB3e (right), doy 144/2001.

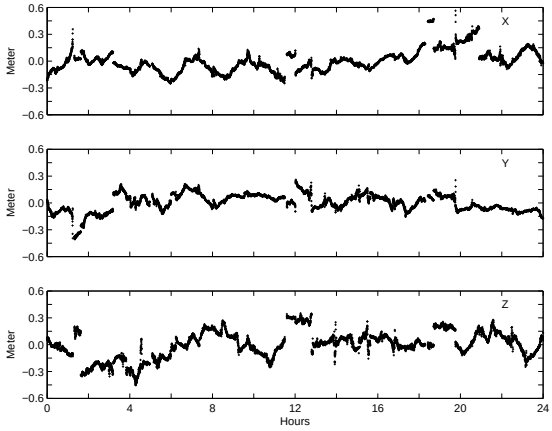

(a) Kinematic trajectory PB3 – reduced-dynamic orbit P3Se, RMS 0.12 m.

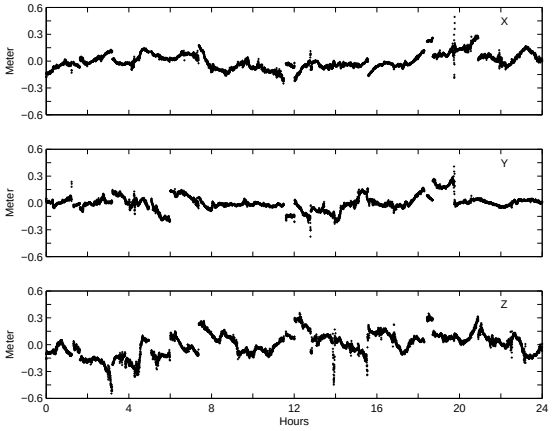

(b) Kinematic trajectory PB3e – reduced-dynamic orbit P3Se, RMS 0.10 m.

Figure 6.22: Orbit differences between reduced-dynamic orbit P3Se and kinematic trajectories PB3 (left) and PB3e (right), doy 144/2001.

and 6.22(b) are too small, however, to take a clear decision which of the two kinematic solutions is the better one.

Reduced-dynamic Orbits

The reduced-dynamic orbits (Table 6.5) serving as a priori orbits for the pre-screening in LEOKIN are of different quality because they use different solutions of code positions or combined positions as input and use a priori information or not.

First we have a look at the RMS errors per coordinate of the orbit determination using the kinematic positions in SATORB. Figure 6.23 shows the RMS errors for the cIS-orbits (code positions derived without a priori information as input). Figure 6.24 shows the RMS errors corresponding to the cIIβS- and pIIβS-orbits (without elevation-dependent weighting, $\beta = 3$, 5, and 10). Figure 6.25 shows the same RMS errors for the cIIβSe- and pIIβSe-orbits (with elevation-dependent weighting, $\beta = 3$, 5, and 10).

As expected the RMS errors for the cIS-orbits are comparatively big because the code-derived positions used as input were generated without pre-screening in LEOKIN. The RMS errors of the orbit determinations for APO set C (cIIβS, cIIβSe) are larger than those for APO set P (pIIβS, pIIβSe). The kinematic positions used for cIIβS and cIIβSe are code positions only and have therefore noise characteristics corresponding to the accuracy of the code observations. The kinematic positions used for pIIβS and pIIβSe, on the other hand, are based on a combination of code and phase-difference positions in LEOKIN. They have a lower noise and, as a consequence, the RMS errors of the orbit determination are smaller. The RMS errors are, therefore, not directly an indicator for the accuracy of the orbit. The RMS errors increase slightly with increasing value of β for the orbits derived with positions from solutions without elevation-dependent weighting (Figure 6.24). In the case of the orbits derived with positions from solutions with elevation-dependent weigthing (Figure 6.25) this behavior can only be recognized for the orbits of APO set C (Figure 6.25(a)). For the orbits of APO set P no clear tendency depending on the value β can be recognized in the RMS errors.

The reduced-dynamic orbits based on code only (APO set C) show a smaller RMS if elevation-dependent weighting is activated – indicating that the weighting scheme is appropriate for the code observations. The reduced-dynamic orbits of APO set P show smaller RMS errors for the solutions with elevation-dependent weighting, as well.

The conclusion is that the model for the elevation-dependent weighting is appropriate in particular for the code observations of the CHAMP receiver. A confirmation of this conclusion is given in Figure 6.26. It shows the residuals (RSW-directions) of the kinematic code positions from SATORB for the solution without (Figure 6.26(a)) and with (Figure 6.26(b)) elevation-dependent weighting. The residuals are smaller for the solution with elevation-dependent weighting – clearly indicating that the elevation-dependent weighting model is preferable when compared to the model without weighting.

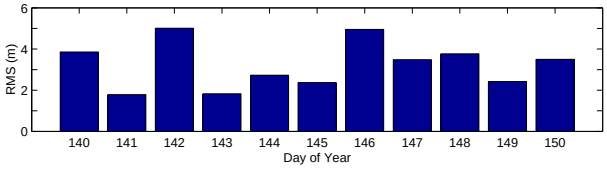

Figure 6.23: RMS errors of reduced-dynamic orbit determination in program SATORB for cIS-orbits (code positions cI derived without pre-screening used as input), doy 140 to 150/2001.

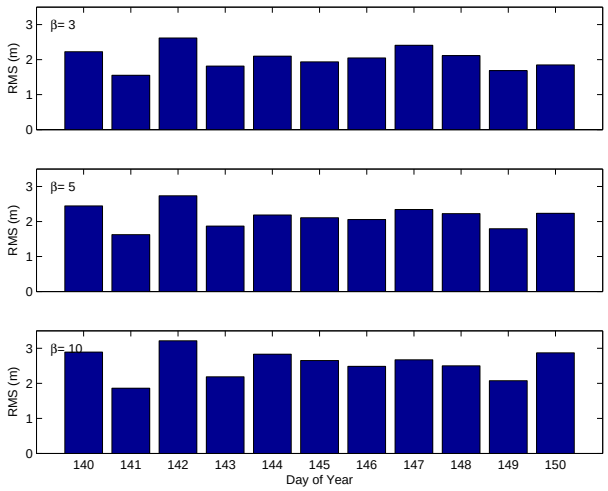

(a) cIIβS-orbits, APO set C, code positions of cIIβ used as input.

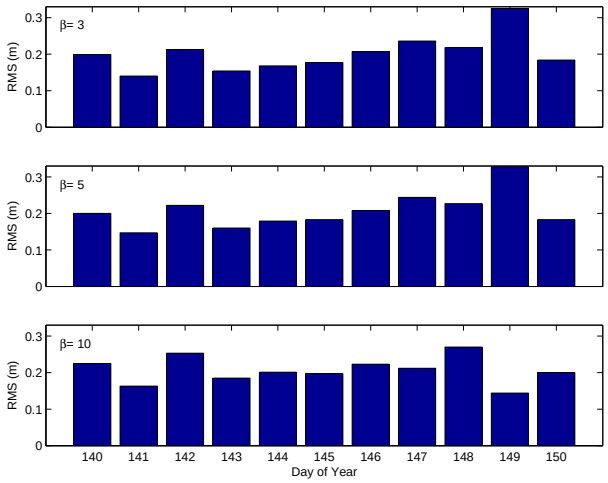

(b) pIIβS-orbits, APO set P, combined positions of pIIβ used as input.

Figure 6.24: RMS errors of reduced-dynamic orbit determination in program SATORB, without elevation-dependent weighting, doy 140 to 150/2001.

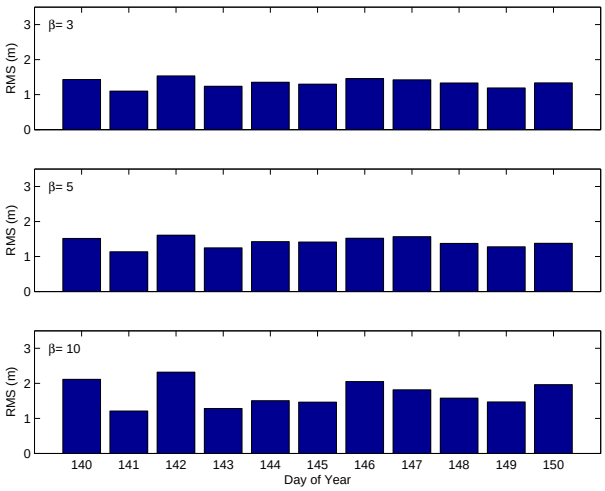

(a) cIIβSe, APO set C, code positions of cIIβe used as input.

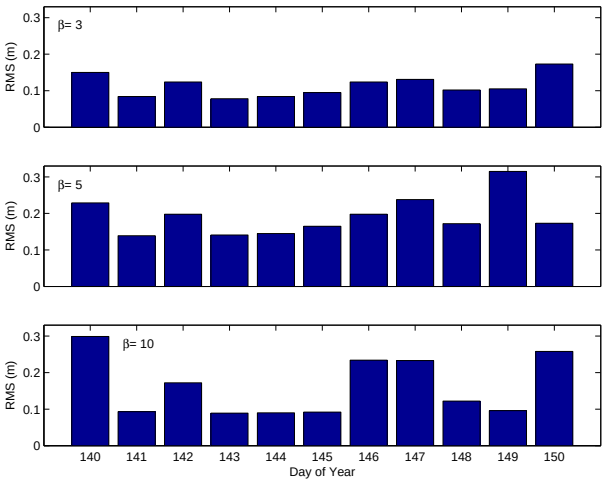

(b) pIIβSe-orbits, APO set P, combined positions of pIIβe used as input.

Figure 6.25: RMS errors of reduced-dynamic orbit determination in program SATORB, with elevation-dependent weighting, doy 140 to 150/2001.

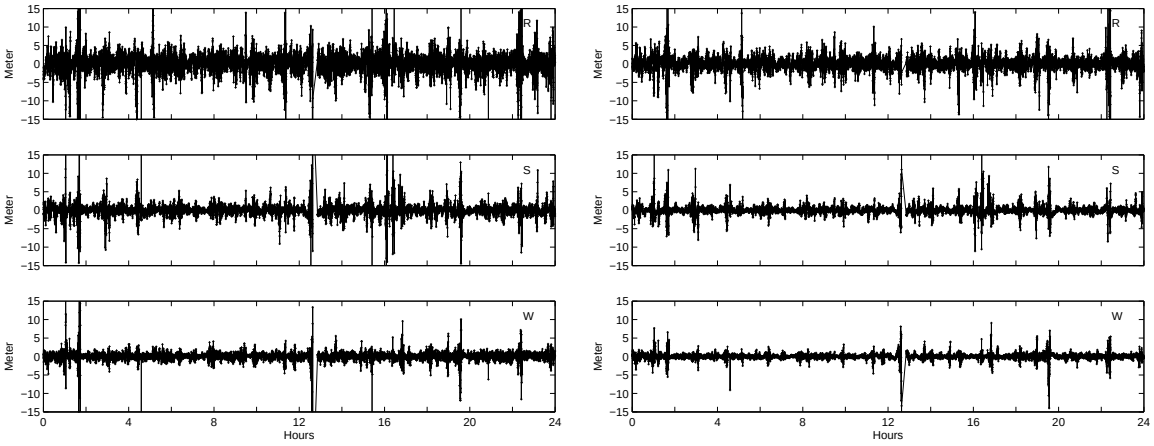

(a) Residuals of cII3 positions w.r.t. cII3S-orbit, RMS 2.62 m.

(b) Residuals of cII3e positions w.r.t. cII3Se-orbit, RMS 1.53 m.

Figure 6.26: SATORB residuals of code positions without elevation-dependent weighting (left) and with elevation-dependent weighting (right), doy 142/2001.

The same kind of analysis can be performed for the phase observables by analyzing the position-difference residuals in program SATORB for the case that positions and position-differences are used as independent observation types. No clear answer results in this case: neither of the two sets of residuals is better. This means that for the phase observation currently no clear answer may be given. Since the current implementation of LEOKIN does not allow to weight code and phase independently, we always weight the two types together in our experiments if elevation-dependent weighting is enabled.

Figure 6.27 shows the differences between the orbits of cII3S and pII3S (RMS 0.23 m) for doy 144/2001. Figure 6.27 in essence characterizes the accuracy of the APO-set-C-orbits. External comparisons will support this statement.

Nevertheless, we will inspect the differences in more detail. The differences show an offset in the x-coordinate. This is not a problem for the pre-screening because for the code screening the magnitude of this offset is small enough. For the pre-screening of the phase-difference observations this offset should not be critical either, because only position-differences of the a priori orbit are required for the pre-screening. In addition to an offset we can recognize oscillations in the differences between the reduced-dynamic orbits which have an amplitude of up to half a meter. These oscillations in the differences between cII3S and pII3S cause the differences in the kinematic trajectories shown in Figure 6.16(d).

The reduced-dynamic orbit, which is used as a priori orbit for the pre-screening in LEOKIN, is an important factor for the quality of the resulting kinematic positions when assuming that the other factors influencing the positioning are minimized (downweighting of the code positions, small value for β, and elevation-dependent weighting). This implies that we use solutions of type B, with $\beta = 3$ or 5, and with elevation-dependent weighting for the following tests. In our previous studies different a priori orbits have been used for the solutions, e.g., solution PB3e uses the a priori orbit pII3Se and PB5e the a priori orbit pII5Se. A comparison of the two kinematic trajectories would show us not only the differences due to the different value for β (3 or 5) but also the differences resulting from the different a priori orbits used (pII3Se or pII5Se).

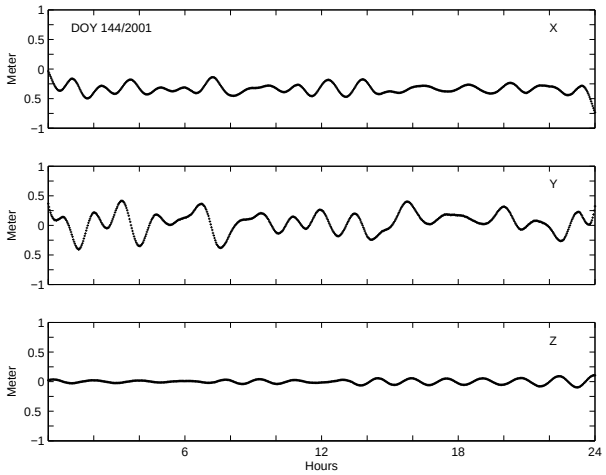

Figure 6.27: Orbit differences between reduced-dynamic orbits cII3S and pII3S without elevation-dependent weighting, doy 144/2001.

In order to separate these two influences on the solutions we repeat the computation of the kinematic solution PB3e and PB5e (this time using pII10Se as a priori orbit), and the computation of the kinematic solutions CB3e and CB5e (this time using cII10Se as a priori orbit). The orbits cII10Se and pII10Se are of different quality than the a priori orbits used originally for the solutions (cII3Se, cII5Se, pII3Se, and pII5Se) (see Figures 6.24 and 6.25). With these tests we may evaluate the impact of the a priori orbit on the resulting positions. Figures 6.28(a) and 6.28(c) show the number of interrupts and jumps for these solutions and Figures 6.28(b) and 6.28(d) show once again the corresponding information of the original solutions (Figures 6.18 and 6.19). Table 6.10 lists the mean number of interrupts and jumps of the new solutions. If we compare these mean values with the mean values in Table 6.9 we recognize a significant increase in the number of interrupts and jumps in the case of the solutions using cII10Se as a priori orbit. In the case of the solutions using the a priori orbit pII10Se there is no difference (compare Figure 6.28(c) with Figure 6.28(d)). Figure 6.28(a) shows that for some days the a priori orbit cII10Se is not of sufficient accuracy to guarantee a reliable pre-screening resulting in more interrupts and jumps than for the original solutions CB3e and CB5e (Figure 6.28(b)). Figure 6.29 shows the differences (from a Helmert transformation) between the original kinematic solutions (CB3e (left) and CB5e (right)) and the newly generated solutions with cII10Se as a priori orbit. The RMS errors of the Helmert transformation are 0.04 m and 0.08 m, respectively. Figure 6.30 shows the differences for the corresponding solutions using APO set P. The RMS errors of the Helmert transformation are 0.01 m and 0.04 m. These figures confirm the findings of Figures 6.28(a), 6.28(c), and Table 6.10. In the case of using a priori orbits of type C the reduced-dynamic orbits serving as a priori orbits are more sensitive to data problems (remaining in the code positions due to a larger β). Due to these data problems the resulting reduced-dynamic orbit may not be of sufficient accuracy to serve as reliable a priori orbit in LEOKIN. In the case of using a priori orbits of APO set P the reduced-dynamic orbits generated with combined positions based on a larger value for β the differences are small. The data problems due to larger value for β are also present in the code positions. Due to the combination with the phase-derived position-differences and the deweighting of the code positions the effect is weakened.

This shows that the a priori orbit is a key element in our zero-difference kinematic point positioning procedure. If we use different a priori orbits for our procedure we get different results. This is a

Table 6.10: Mean number of interrupts and jumps of solutions B with elevation-dependent weighting using APO cII10Se and pII10Se.

	APO cII10Se		APO pII10Se	
	Interrupts	Jumps	Interrupts	Jumps
$\beta = 3$	14	22	10	14
$\beta = 5$	14	22	10	14

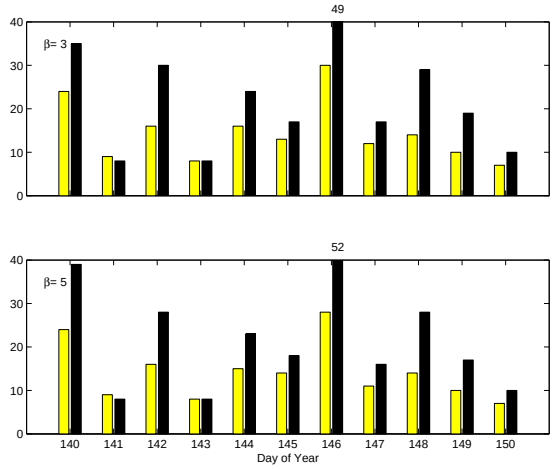

(a) A priori orbit cII10Se.

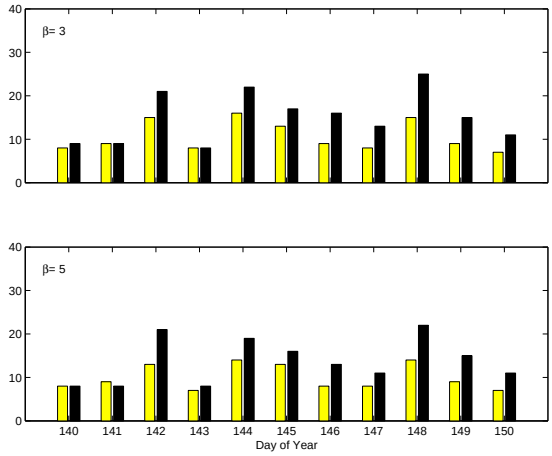

(b) Original a priori orbits cII3Se and cII5Se (see Figure 6.18, other scale).

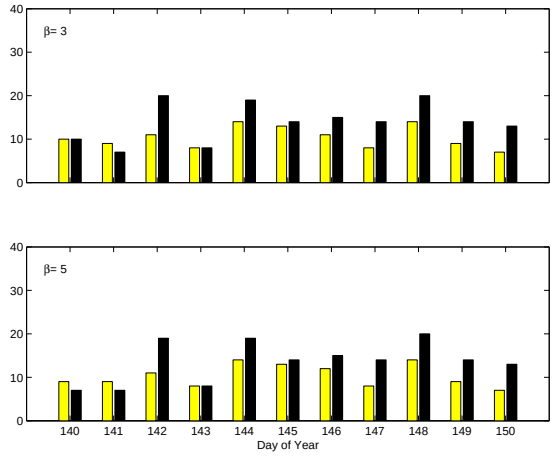

(c) A priori orbit pII10Se.

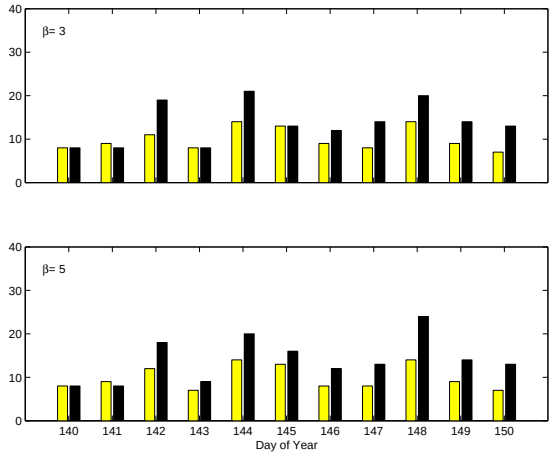

(d) Original a priori orbits pII3Se and pII5Se (see Figure 6.19, other scale).

Figure 6.28: Number of interrupts due to missing phase position-differences (left bar) and number of jumps in the kinematic trajectory (right bar), elevation-dependent weighting, cII10Se (top left) and pII10Se (bottom left) used as a priori orbits, right: plots with original a priori orbits used, doy 140 to 150/2001.

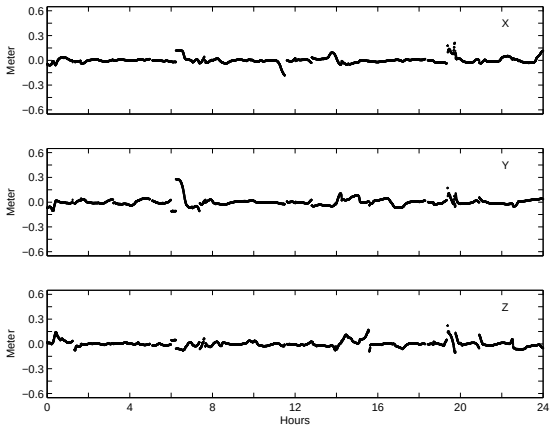

(a) Differences between original solution CB3e and CB3e using cII10Se as a priori orbit, RMS 0.04 m.

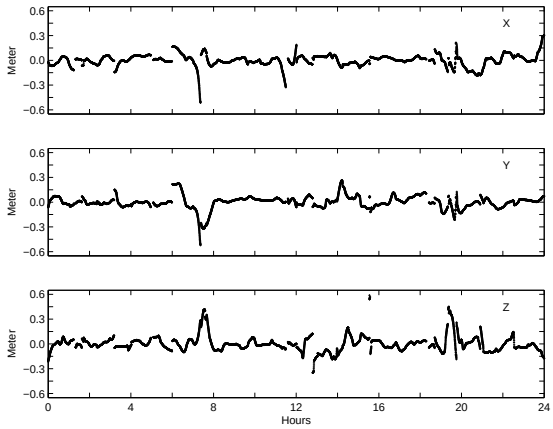

(b) Differences between original solution CB5e and CB5e using cII10Se as a priori orbit, RMS 0.08 m.

Figure 6.29: Orbit differences between kinematic trajectories using different a priori orbits of APO set C, doy 144/2001.

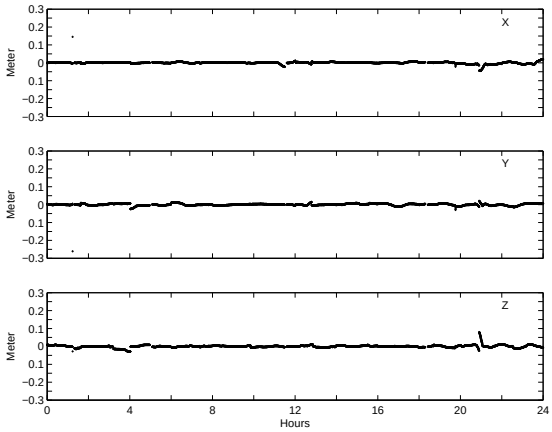

(a) Differences between original solution PB3e and PB3e using pII10Se as a priori orbit, RMS 0.01 m.

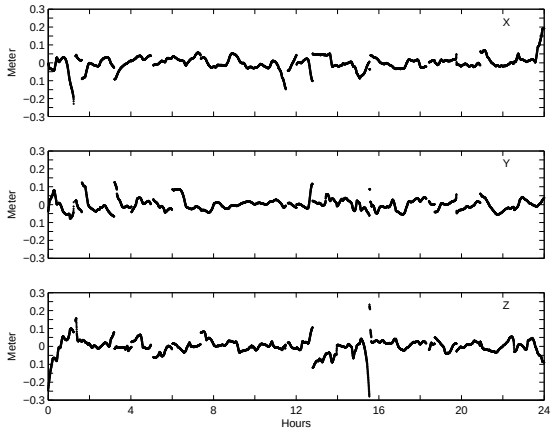

(b) Differences between original solution PB5e and PB5e using pII10Se as a priori orbit, RMS 0.04 m.

Figure 6.30: Orbit differences between kinematic trajectories using different a priori orbits of APO set P, doy 144/2001.

Table 6.11: RMS errors (cm) of improvements between kinematic trajectories of subsequent iterations.

Day	PB3 – Iter. 2	Iter. 2 – Iter. 3	Iter. 3 – Iter. 4	Iter. 4 – Iter. 5	PB3 – Iter. 5
140	9	4	2	1	11
141	4	1	1	0	4
142	41	37	10	3	11
143	4	2	1	0	4
144	4	1	0	0	5
145	5	2	1	0	6
146	5	1	0	0	7
147	6	2	1	0	10
148	6	2	1	0	7
149	8	3	1	0	11
150	5	2	1	0	6

disadvantage of this efficient point positioning procedure.

We have seen on the other hand that the pre-processing of the observations is not reliable enough for $\beta > 5$. We therefore only have to consider the solutions with $\beta = 3$ and 5. The differences showing up when we use a different a priori orbit are, in particular for APO set P, within reasonable limits.

The reduced-dynamic orbit which is used as a priori orbit for the pre-screening of the observations for the kinematic point positioning in LEOKIN has to be produced with care. The differences between APO set C and P show that the latter approach seems to be more reliable for generating a priori orbits with the requested accuracy. This means that we should use code and phase-difference observations (APO set P) for generating reduced-dynamic orbits serving as a priori orbits.

Iterative Kinematic Point Positioning

A possibility to converge to a reliable solution may be to perform an iterative kinematic point positioning in the program LEOKIN. The combined positions of the previous iterations will enter as new a priori positions into the next point positioning step. The procedure may be repeated as long as the differences between the iterations is significant.

The advantage of this procedure is that the iterations do not involve the time-consuming orbit integration step with program SATORB. A disadvantage is that excluded epochs cannot be recovered in a subsequent step.

In order to study this procedure we take as an initial point positioning solution PB3 with the corresponding APO pII3. Subsequently we process each of the eleven days and perform up to five iterations in LEOKIN. Finally we perform a Helmert transformation (with three translation parameters) between the kinematic positions from subsequent iterations. Table 6.11 lists the RMS errors of the Helmert transformations for the eleven days.

Figure 6.31 shows the improvements in the x-component of the kinematic positions with increasing iterations for doy 142 (Figure 6.31(a)) and 145/2001 (Figure 6.31(b)). The differences between the iterations are converging to zero. The solutions reach (except doy 142) a limit where the RMS errors of the improvements are smaller than two centimeters after four iterations (Table 6.11). The column on the right-hand side of Table 6.11 gives the RMS errors of the Helmert transformation between the initial solution PB3 and the solution after five iterations. These RMS errors are within eleven centimeters for

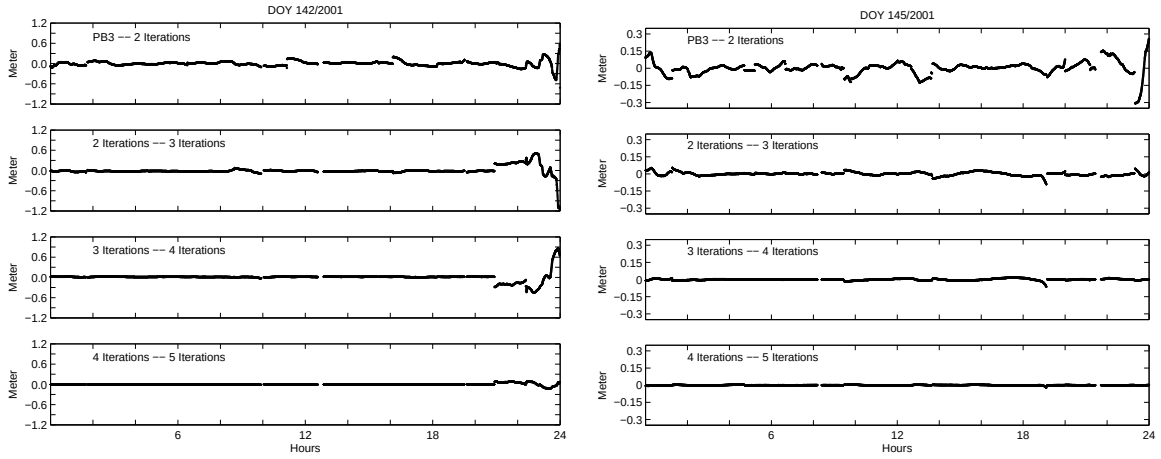

(a) DOY 142/2001.

(b) DOY 145/2001.

Figure 6.31: Improvements in the x-component of the kinematic trajectory with increasing number of iterations.

the eleven days. We will compare these kinematic positions resulting after five iterations in the next section with an independent solution for the CHAMP orbits in order to evaluate whether this iterative positioning helps to improve the kinematic trajectory.

6.3.3 Independent Comparison

In order to assess the external accuracy of the kinematic trajectory, the kinematic positions are compared with an independent external solution. Fortunately, the data from the IGS CHAMP test campaign were processed by a number of institutions. One of the best solutions in a comparison between all contributions is the solution from the Technical University of Munich (TUM), Germany. This solution was performed with an enhanced version of the Bernese GPS Software, Version 4.2. The solutions are zero-difference reduced-dynamic orbits for CHAMP generated by the main parameter estimation program GPSEST. The GPS orbits and clock corrections are assumed to be known from CODE processing. The GPS phase observations of CHAMP are directly used in the orbit estimation procedure (code observations were only used to synchronize the receiver clock). The phase ambiguities, epoch-wise LEO clock parameters, and the dynamical orbit parameter are estimated together. The reduced-dynamic orbit is parametrized with

- six initial conditions,
- nine Solar radiation pressure parameters,
- one scaling factor for the atmospheric drag, and
- pseudo-stochastic pulses every nine minutes in alongtrack (constraints: $1 \cdot 10^{-5}$ m/s), crosstrack ($1 \cdot 10^{-5}$ m/s), and radial ($2 \cdot 10^{-5}$ m/s) direction.

The TUM solution was generated without elevation-dependent weighting of the observations. Figures 6.32(a) and 6.32(b) show the RMS errors of a Helmert transformation (with three translation parameters) between our kinematic solution series A and B without elevation-dependent weighting with

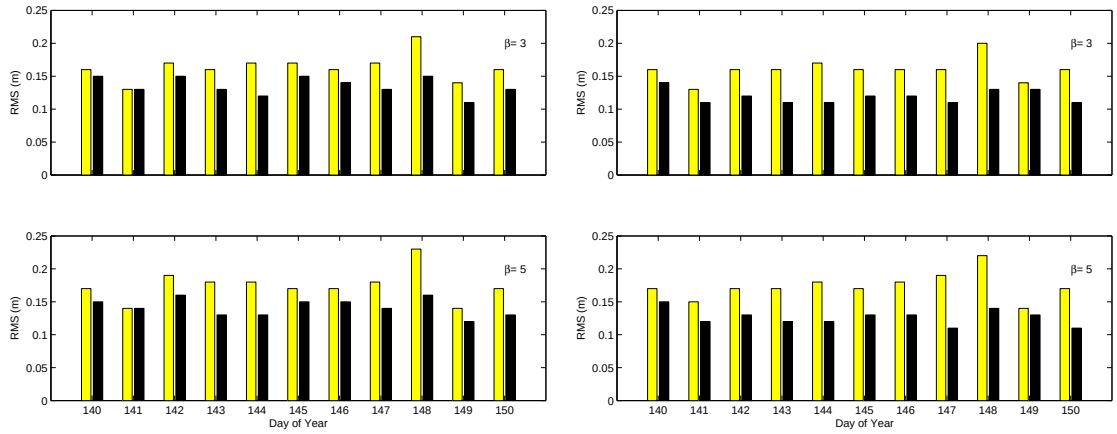

(a) A priori orbit set C.

(b) A priori orbit set P.

Figure 6.32: RMS errors of Helmert transformation between orbits from TUM and trajectories generated with LEOKIN without elevation-dependent weighting, solution A (left bar) and solution B (right bar), for doys 140 to 150/2001.

$\beta = 3$ and 5 for both APO sets and the TUM orbits. Table 6.12 summarizes the mean RMS errors for the solutions without elevation-dependent weighting in the upper part of the table. Most of solutions A are worse than solutions B.

In addition we have a look at comparisons of the solutions with elevation-dependent weighting of the observations with the TUM-solutions (Figure 6.33). It is remarkable that the solutions with $\beta = 3$ and 5 show a slightly better performance (Table 6.12 (bottom)) than the solutions without elevation-dependent weighting. This confirms our recommendation of using the elevation-dependent weighting model in LEOKIN.

Figure 6.34 shows the RMS errors of a Helmert transformation between the TUM-solutions and the reduced-dynamic solutions P3Se for all eleven days. As the comparisons between the kinematic trajectories and the TUM-solutions these comparisons are in the range of 10 to 15 cm.

Figure 6.35(a) shows the differences between the TUM-solution and solution PB3 (Helmert RMS 0.11 m) for doy 144/2001, Figure 6.35(b) those between TUM and PB3e (Helmert RMS error 0.09 m) for doy 144/2001. The differences show many jumps. These jumps are contained in the LEOKIN solutions because the TUM-solution is a reduced-dynamic orbit and is, therefore, continuous and has no jumps in the trajectory. Solutions PB3 and PB3e have both 14 interrupts due to missing position-differences. The differences for both solutions show similar characteristics. The solution with elevation-dependent weighting (PB3e) is slightly better.

Figure 6.36(a) shows the differences between the reduced-dynamic orbit P3S and TUM (Helmert RMS error 0.10 m) for doy 144/2001 and Figure 6.36(b) those between P3Se and TUM (Helmert RMS error 0.09 m).

Finally, we have a look at the differences between the TUM-solutions and the LEOKIN solutions resulting after five iterations. Figure 6.37 shows the RMS values for the differences between TUM and PB3 solutions (left bar) and between TUM and the solutions after five iterations (right bar). The kinematic positions after five iterations show no improvement in comparison with the TUM-solutions.

Table 6.12: Mean RMS errors (m) of Helmert transformation between LEOKIN solutions and TUM-solutions.

Solutions without elevation-dependent weighting				
	APO set C		APO set P	
	Solution A	Solution B	Solution A	Solution B
$\beta = 3$	0.16	0.14	0.16	0.12
$\beta = 5$	0.17	0.14	0.17	0.13

Solutions with elevation-dependent weighting				
	APO set Ce		APO set Pe	
	Solution A	Solution B	Solution A	Solution B
$\beta = 3$	0.13	0.13	0.12	0.11
$\beta = 5$	0.12	0.12	0.12	0.11

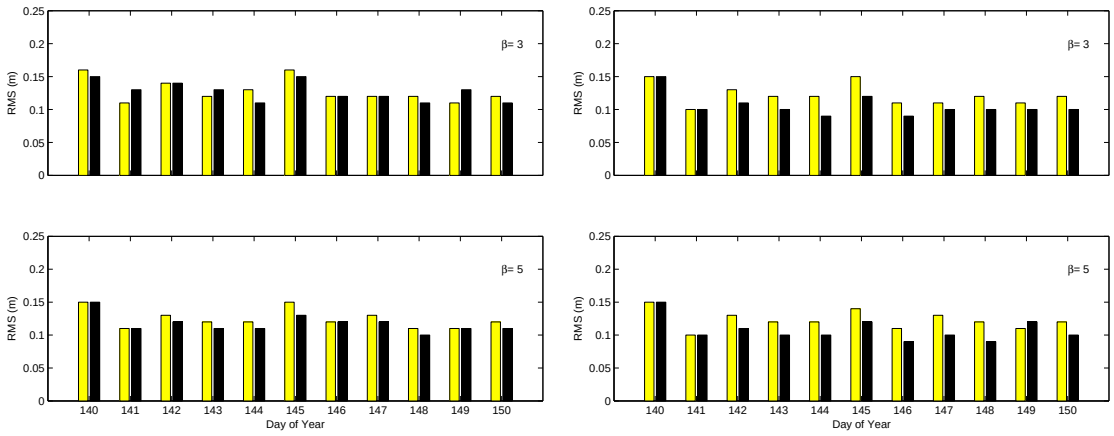

(a) A priori orbit set Ce.

(b) A priori orbit set Pe.

Figure 6.33: RMS errors of Helmert transformation between orbits from TUM and trajectories generated with LEOKIN with elevation-dependent weighting, solution A (left bar) and solution B (right bar), doy 140 to 150/2001.

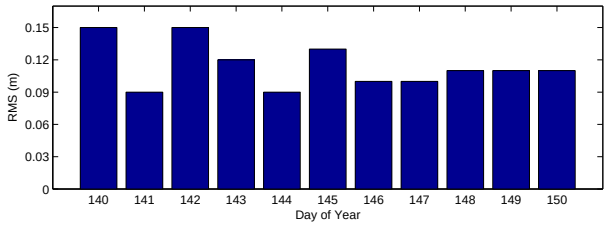

Figure 6.34: RMS errors of Helmert transformation between orbits from TUM and reduced-dynamic orbits P3Se, doy 140 to 150/2001.

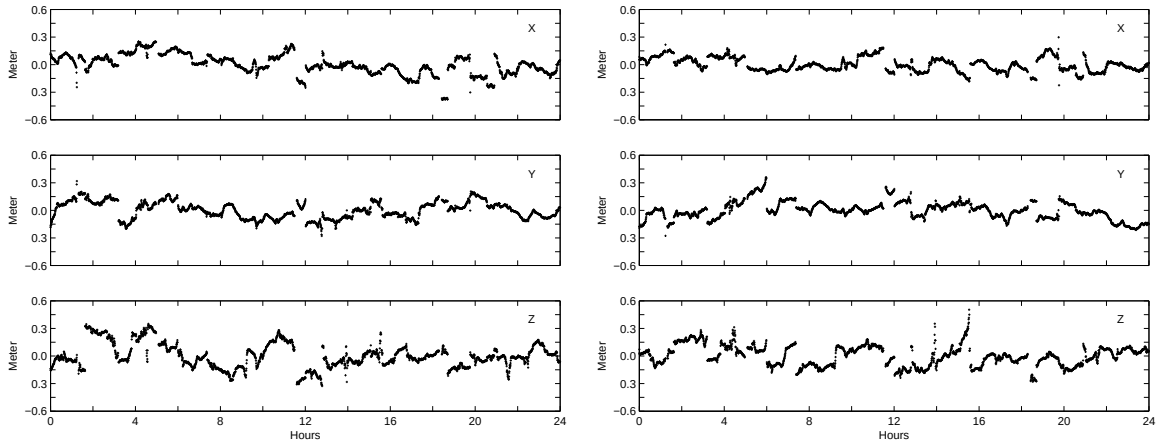

(a) Kinematic trajectory PB3 (without elevation-dependent weighting) – TUM-solution, RMS 0.11 m.

(b) Kinematic trajectory PB3e (with elevation-dependent weighting) – TUM-solution, RMS 0.09 m.

Figure 6.35: Orbit differences between kinematic trajectories (PB3 (left) and PB3e (right)) and TUM-solutions, doy 144/2001.

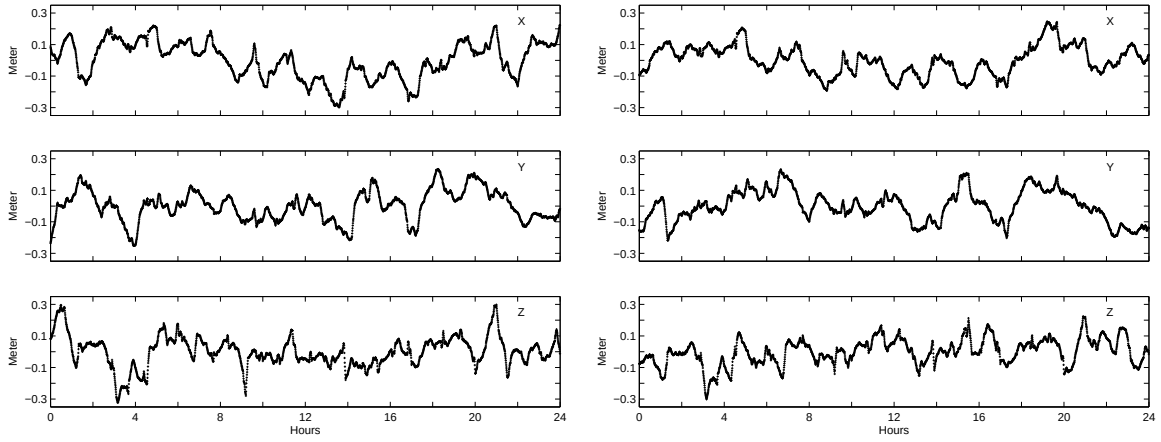

(a) Reduced-dynamic orbit P3S (without elevation-dependent weighting) – TUM-solution, RMS 0.10 m.

(b) Reduced-dynamic orbit P3Se (with elevation-dependent weighting) – TUM-solution, RMS 0.09 m.

Figure 6.36: Orbit differences between reduced-dynamic orbits (P3S (left) and P3Se (right)) and TUM-solutions, doy 144/2001.

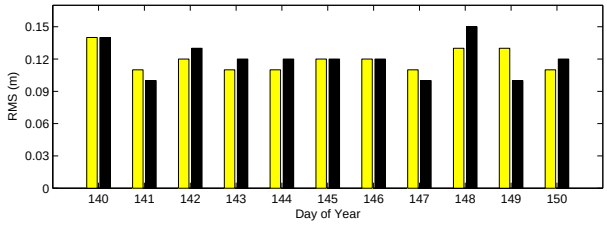

Figure 6.37: RMS errors of Helmert transformation between TUM and PB3 (left bar) and TUM and kinematic positions after five iterations (right bar).

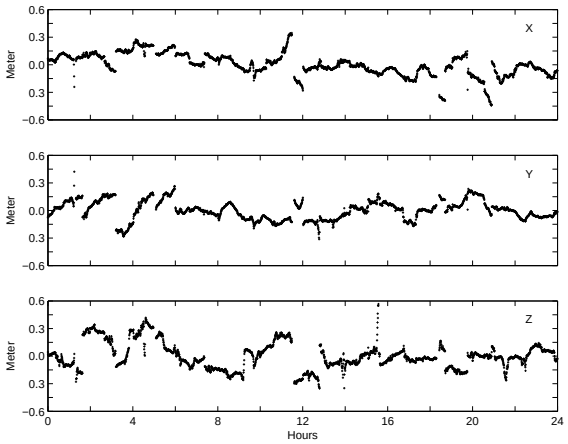

Figure 6.38: Differences between the kinematic trajectory after five iterations in LEOKIN and the TUM-solution, doy 144/2001, RMS 0.12 m.

Figure 6.38 shows the differences between the solutions for doy 144/2001.

These comparisons show that the external accuracy of the final kinematic LEOKIN and reduced-dynamic SATORB solutions is within 10 to 15 centimeters w.r.t. the TUM-solutions for an appropriate set of processing options.

6.3.4 Summary

Many kinds of LEO orbits may be generated using the programs LEOKIN and SATORB. The orbits directly emerging from LEOKIN are pure kinematic orbits. They do not make use of the fact that the LEO is obeying the equations of motion. LEOKIN may make use of a priori orbit information, but only for the purpose of screening the raw code and phase-difference observations. It is undoubtedly a disadvantage of the kinematic orbits that gaps may occur – whenever data problems did not allow it to generate point positions using code and/or position-differences using the phase observable. For many applications it is therefore appropriate and useful to consider the results of program LEOKIN only as an intermediary tool to generate a dynamic or reduced-dynamic orbit.

The orbits resulting from program SATORB are dynamic orbits or so-called reduced dynamic orbits. They are solutions of the equations of motion using rather elaborate orbit models (see section 5.1). The positions and possibly the position-differences generated by program LEOKIN are used as pseudo-observations in a conventional orbit determination process. SATORB solves for quantities characterizing

the initial state vector (six parameters), normally for nine dynamical parameters (constant and once-per-revolution terms in the three orthogonal directions R (radial), S (along track) and W (out of plane). In addition, pseudo-stochastic pulses (velocity changes) are set up in the same three directions at regularly distributed epochs (details see section 5.5). It is important that the number of unknowns is at least one to two orders of magnitude smaller than the number of pseudo-observations. One may therefore expect that the dynamic or reduced-dynamics orbits emerging from SATORB are much less prone to data problems than those resulting from LEOKIN. Also, as it is assumed that the LEO trajectory solves the equations of motion, gaps do not exist. It is thus possible to generate a table (ephemeris) of equidistant (in time) rectangular satellite positions with SATORB, either in the inertial or in the Earth-fixed system.

In order to evaluate the performance of program LEOKIN extensive studies were performed using data of the IGS CHAMP test campaign (doy 140 to 150/2001). Most of the tests confirm the conclusions drawn in Section 6.2 for the data of CHAMP for doy 152/2001.

Tests were performed to find the best possible value for the pre-screening parameter β. A choice of $\beta = 3$ or 5 is recommended. If higher values for β are used "bad" observations may still reside in the data and disturb the kinematic solution. Code observations are more delicate – for the phase observations it makes hardly any difference whether β =3 or β =30 is used. This indicates that the phase pre-screening is only important for the identification of large cycles slips and phase resets.

We studied the effect of downweighting of the code-derived positions when combining code positions and phase position-differences. Kinematic solutions not using elevation-dependent weights with the code positions downweighted by a factor of 100 (solutions B) give a better performance than the kinematic solutions with the normal relative weight of code and phase for the combination (solutions A).

Studies concerning the use of elevation-dependent weights reveal a better performance of solutions of type A and B when considering elevation-dependent weighting. The code observations at low elevations have an impact on the kinematic solutions which is expressed by outliers in the code positions leading to more jumps in the kinematic trajectory w.r.t. a reduced-dynamic orbit. In the case of solution B these outliers may be smoothed due to the deweighting of the code positions. In the case of applying an elevation-dependent weighting these observations are already deweighted in the code positioning step and may not have such a large impact on the resulting combined positions for solutions A and B. Further inspections on this issue by comparing the residuals of the orbit determinations in program SATORB using code positions derived without weighting and code positions derived with weighting confirmed the conclusion that the elevation-dependent weighting model is preferable when compared to the model without weighting.

For the phase observations no clear conclusion concerning the weighting could be drawn. Since LEOKIN currently does not allow to apply the weighting model independently on code and phase, we use always the weighting for both observations types of the CHAMP receiver. An alternative, which was not studied for this work, could be to apply the elevation-dependent weighting only to the code observations.

After an independent comparison of the kinematic solutions with solutions generated at the Technical University of Munich, Germany, the conclusion can be drawn that the application of elevation-dependent weighting on the observations slightly helps to improve the kinematic point positioning solution. This conclusion implies that we use a value for β which is smaller than ten and that the code positions are deweighted by a factor 100 for the combination with the phase-derived position-differences.

We tried to find the most reliable way to generate a reduced-dynamic orbit for the pre-screening procedure in LEOKIN. The most reasonable and reliable procedure to generate a priori orbits is to use combined code and phase-difference derived positions (APO set P) (using a reasonable value for β (i.e. $\beta \leq 5$)). For $\beta = 3$ the solutions generated with APO set C are, however, of comparable quality as

Table 6.13: Orbits generated with LEOKIN and SATORB.

Solution	Source	Description
cI	LEOKIN	Kinematic orbit based on code observations, without a priori orbit information
cIS	SATORB	cI positions as observations, 15 deterministic parameters, spacing for stochastic pulses: 90 min
cII3e	LEOKIN	Kinematic orbit based on code observations, using orbit cIS as a priori orbit, *with* elevation-dependent weighting
cII3Se	SATORB	cII3e positions as observations, 15 deterministic parameters, spacing for stochastic pulses: 20 min
cII3	LEOKIN	Kinematic orbit based on code observations, using orbit cIS as a priori orbit, *without* elevation-dependent weighting
cII3S	SATORB	cII3 positions as observations, 15 deterministic parameters, spacing for stochastic pulses: 20 min (*without* elevation-dependent weighting)
pII3e	LEOKIN	Kinematic orbit based on code and phase observations, using orbit cIS as a priori orbit *with* elevation-dependent weighting
pII3Se	SATORB	pII3e positions as observations, 15 deterministic parameters, spacing for stochastic pulses: 20 min
PB3e	LEOKIN	Kinematic orbit based on code and phase observations, using orbit pII3Se as a priori orbit *with* elevation-dependent weighting
P3Se	SATORB	PB3e positions and position-differences as observations, 15 deterministic parameters, spacing for stochastic pulses: 10 min

those generated with APO set P. The reduced-dynamic orbits of type C (using only code positions for the generation of the reduced-dynamic orbit) have an accuracy of about 30 cm, the orbits of type P (using combined positions) of about 15 cm.

In order to fix the order of magnitude of the various strategies (with LEOKIN and SATORB) we take the orbits generated for one particular day (144/2001) of the IGS test campaign in 2001 and compare ”all possible orbits” with the presumably best possible orbit, namely the one generated at TUM in a reduced-dynamics mode using the Bernese GPS software (see Section 6.3.3 for details).

The orbits are characterized in Table 6.13, their quality is described by Table 6.14 using the root mean square error (RMS_{ext}) per satellite coordinate of a Helmert transformation with three translation parameters between the orbital positions considered and the ”external” orbit positions (TUM-solutions). The error RMS_{int}, also contained in Table 6.14, characterizes the RMS error per coordinate of a transformation between the orbit considered and the presumably best possible orbit P3Se achievable with the programs LEOKIN and SATORB. Comparison of RMS_{int} with RMS_{ext} shows the rapid convergence of the described orbit determination process to an orbit comparable in quality with the best external orbit (TUM). This fact is important when dealing with LEO orbits, for which no independent estimates are available (in an operational environment, this is the normal case).

Table 6.14: LEO orbit quality using LEOKIN and SATORB, CHAMP doy 144/2001.

Solution	Code	Phase	Orbit	Program	RMS$_{int}$(m)	RMS$_{ext}$(m)
cI	Y	N	N	LEOKIN	2.71	2.56
cIS	Y	N	-	SATORB	0.47	0.48
cII3e	Y	N	Y	LEOKIN	1.38	1.36
cII3Se	Y	N	-	SATORB	0.29	0.33
cII3	Y	N	Y	LEOKIN	2.11	2.12
cII3S	Y	N	-	SATORB	0.29	0.30
pII3e	Y	Y	Y	LEOKIN	0.15	0.13
pII3Se	Y	Y	-	SATORB	0.15	0.13
PB3e	Y	Y	Y	LEOKIN	0.11	0.09
P3Se	Y	Y	-	SATORB	–	0.11

The next section deals with the kinematic solutions for a longer data series for CHAMP and SAC-C in 2002. These data sets are processed with the aim to confirm the findings from this section but also to answer additional questions concerning the data pre-processing. As a reference orbit we will use an orbit of type P3Se to compare with, because no external reference orbit is available for this time interval.

6.4 CHAMP and SAC-C – 055/2002 to 089/2002

The more recent data set we processed stems from a time interval of 35 days in 2002 (doy 055 to 089/2002). GPS data from both satellites, CHAMP and SAC-C, were analyzed.

First, we inspect the quality of the tracking data from these days. Then, we address different issues using this longer data series. A general overview of the different solutions is followed by a section that considers the kinematic solutions using CODE Rapid products as input and by a corresponding section for the solutions using CODE Final products. Finally, a summary of all solutions and results from the 2002 LEO/GPS data series is presented.

6.4.1 Data Quality

Figure 6.39 shows the number of satellites tracked by SAC-C for doy 055 to 089/2002. The SAC-C receiver tracked up to twelve satellites simultaneously for almost the whole time interval. Starting from doy 089/2002 the SAC-C receiver tracks only up to eight satellites simultaneously (see also Table 4.2). Unfortunately, the SAC-C data contain a long data gap from doy 058, $5^{\mathrm{h}}14^{\mathrm{m}}40^{\mathrm{s}}$ to doy 061, $3^{\mathrm{h}}44^{\mathrm{m}}20^{\mathrm{s}}$.

Figure 6.40 shows the number of satellites tracked by CHAMP for doy 055 to 089/2002. The GPS receiver on-board CHAMP tracked up to eight GPS satellites simultaneously prior to doy 064/2002. After that date it was able to track up to ten satellites (see also Table 4.1). The CHAMP data have a longer data gap on doy 064 from $7^{\mathrm{h}}05^{\mathrm{m}}50^{\mathrm{s}}$ to $22^{\mathrm{h}}10^{\mathrm{m}}40^{\mathrm{s}}$. During this data gap the CHAMP receiver software update was performed allowing the GPS receiver to track up to ten satellites simultaneously.

There are a few additional data gaps for both satellites lasting from one epoch up to several minutes, but in general the performance of the two spaceborne receivers was rather good (except for SAC-C after doy 086).

After the long data gap on doy 064 for CHAMP the number of gaps per day has decreased. Most of the days even show no data loss at all. Starting from doy 077 a barely visible, but important, change

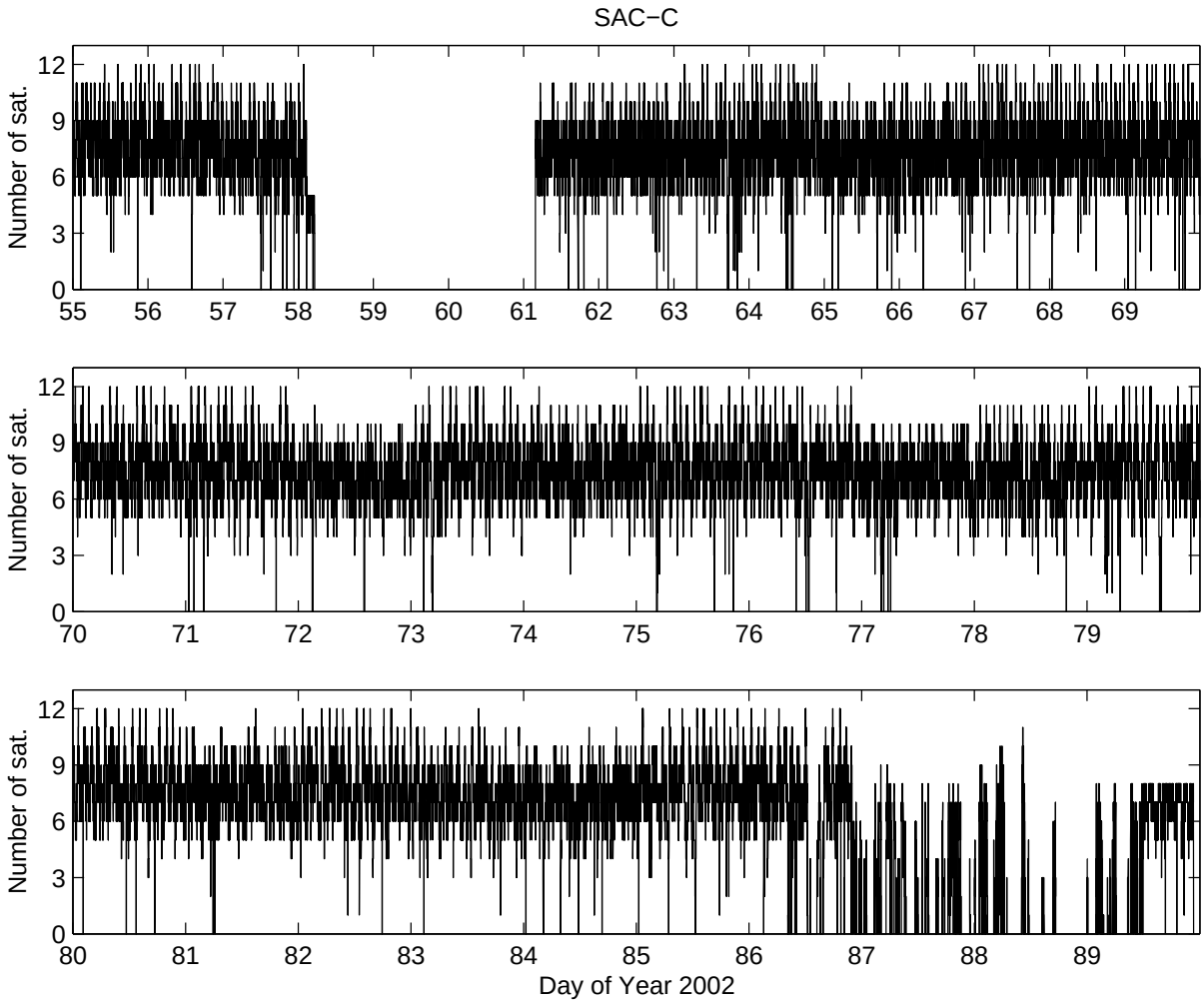

Figure 6.39: Number of tracked satellites by SAC-C for doy 055 to 089/2002.

in the data performance has occurred: the number of epochs with only four or five tracked satellites has decreased. This is a big advantage for kinematic point positioning, because at least four observations are needed to determine a position. If we have more than four observations available the redundancy of the solution increases, and therefore the solutions are better controllable.

There are only two days without data gap (doy 070 and 074) for SAC-C. Starting with doy 086 the receiver performance is very bad. The time intervals without any tracked satellites are longer than the time intervals with more than three tracked satellites. It is, therefore, difficult to generate reliable kinematic solutions after doy 085.

6.4.2 Data Processing

In addition to the GPS data of the two LEO satellites with a sampling of ten seconds the following input data were needed and used for our tests:

- CODE Rapid GPS orbits,

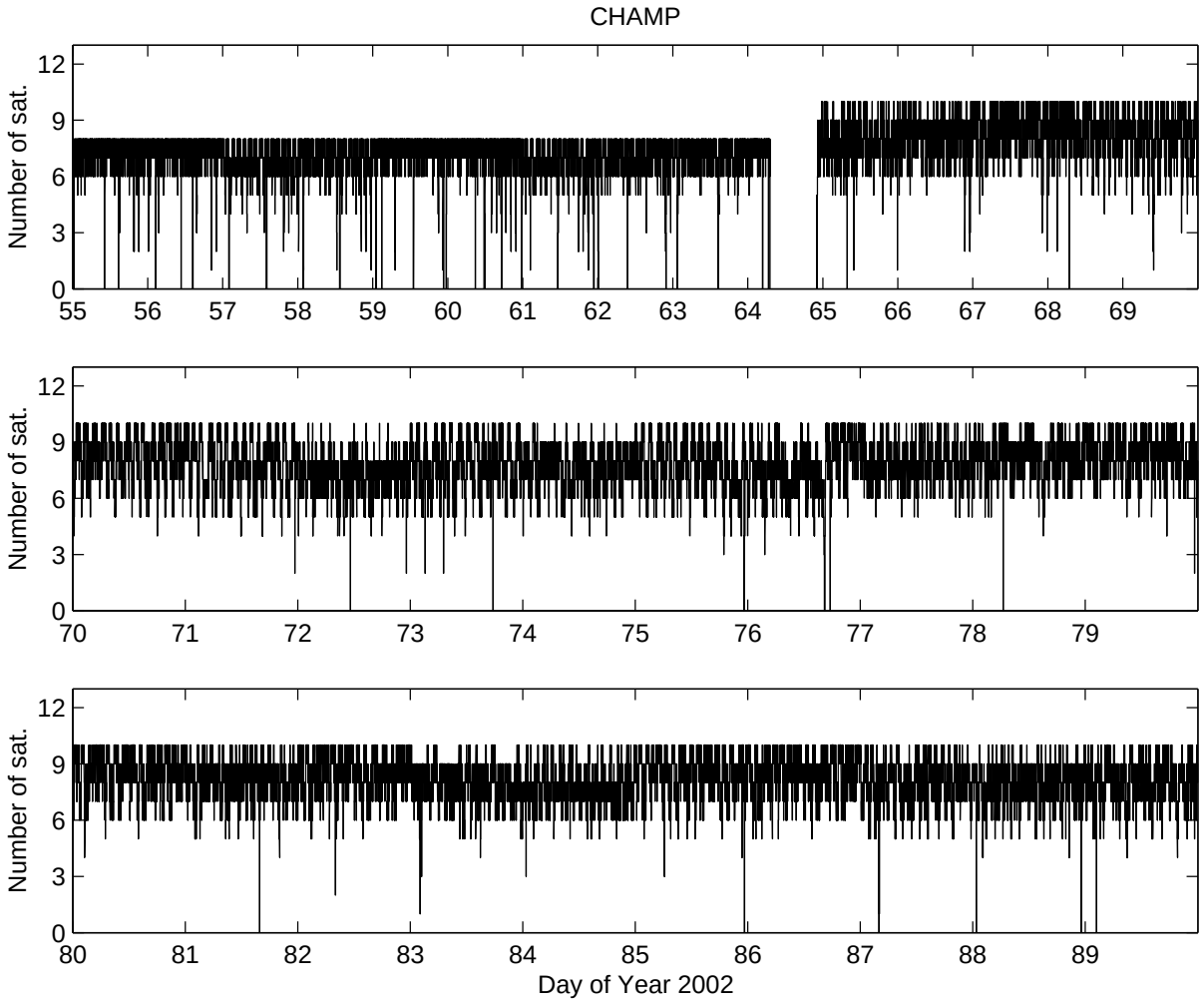

Figure 6.40: Number of tracked satellites by CHAMP for doy 055 to 089/2002.

- ERPs of the CODE Rapid processing, and
- 30-second clock corrections for the GPS satellites with the GPS broadcast clock corrections used for alignment to GPS time.

For doy 055 to 069/2002 we used in addition a second set of input data

- CODE Final GPS orbits,
- ERPs of the CODE Final processing, and
- 30-second clock corrections for the GPS satellites constrained to the CODE Final 5-minute clock corrections.

These two sets of input data are used to compare kinematic results as a function of input information of different accuracy. The official IGS Rapid product is available with a delay of 17 hours after the day considered and the IGS Final product with a delay of 10 days after the week considered. The analysis centers have to provide their results before the combination of all contributions may take place. For the Rapid products not as many GPS observation data may be used as for the Final products. The Final products have a better quality than the Rapid products. For more details about the IGS products we refer e.g., to [*Weber and Springer,* 2002] and [*IGSCB,* 2002].

Solutions with the following input data and options in LEOKIN are performed and analyzed for CHAMP and SAC-C:

- DOY 055 – 089/2002: CODE Rapid products
  1. no elevation-dependent weighting and a cut-off angle of $0°$,
  2. elevation-dependent weighting and a cut-off angle of $0°$.
- DOY 055 – 069/2002: CODE Final products
  1. no elevation-dependent weighting and a cut-off angle of $0°$,
  2. elevation-dependent weighting and a cut-off angle of $0°$,
  3. CODE Final 5-minute clock corrections as GPS clock information (using linear interpolation) and elevation-dependent weighting with a cut-off angle of $0°$,
  4. SAC-C: no elevation-dependent weighting and no cut-off angle.

Table 6.15 summarizes the solution types. The common values of $\sigma_{c_{scr}} = 1.0$ m and $\sigma_{p_{scr}} = 0.01$ m are used. We have seen in the previous examples that $\beta > 10$ results in outliers residing in the "screened" data. We have seen this problem also in the kinematic solutions for $\beta = 10$ and partly for $\beta = 5$. We want to see whether the kinematic solutions of the 2002 data series show the same sensitivity mainly for the code observations. Indeed we use β =5 and 10 only for the solutions generated using the CODE Rapid products. For the remaining solutions we confine ourselves to the best possible kinematic solution with $\beta = 3$. The two procedures (APO set C and P) to generate reduced-dynamic orbits serving as a priori orbits explained in the previous section are used (see Table 6.5). The options for the reduced-dynamic orbits in SATORB are the same as for the reduced-dynamic orbits of the IGS CHAMP test campaign (six osculating elements, nine empirical parameters in RSW, stochastic pulses every 90 and 20, respectively, see Section 6.3.2). Solutions A (normal relative weight $2 : 100^2$ between code positions

Table 6.15: Summary of kinematic solutions computed for CHAMP and SAC-C for doy 055 to 089/2002 (R stands for Rapid, F for Final, S for SAC-C, C for APO set C, P for APO set P, A for a normal code weight for the combination, B for a code weight reduced by a factor of 100, and e for elevation-dependent weighting).

	CODE Rapid products, doy 055 to 089/2002							
	APO set C				APO set P			
	no elev.-dep.weight.		elev.-dep.weight.		no elev.-dep.weight.		elev.-dep.weight.	
$\beta = 3$	RCA3	RCB3	RCA3e	RCB3e	RPA3	RPB3	RPA3e	RPB3e
$\beta = 5$	RCA5	RCB5	RCA5e	RCB5e	RPA5	RPB5	RPA5e	RPB5e
$\beta =10$	RCA10	RCB10	RCA10e	RCB10e	RPA10	RPB10	RPA10e	RPB10e
	A priori orbits from processing with CODE Final products							
$\beta = 3$		RFCB				RFPB		

	CODE Final products, doy 055 to 069/2002							
	APO set C				APO set P			
	no elev.-dep.weight.		elev.-dep.weight.		no elev.-dep.weight.		elev.-dep.weight.	
$\beta = 3$	FCA	FCB	FCAe	FCBe	FPA	FPB	FPAe	FPBe

	Official 5-minute GPS clock corrections from CODE Final processing used							
$\beta = 3$							F5PAe	F5PBe

	SAC-C							
	no cut-off angle				no cut-off angle			
$\beta = 3$	SCA	SCB			SPA	SPB		

and phase position-differences) and B (code positions deweighted with a factor 100 for the combination) are computed for nearly all versions.

We start with the solutions based on the CODE Rapid products as input for the GPS orbits and clock corrections. We analyze the solutions for SAC-C first and then those for CHAMP. Finally, the solutions using the CODE Final products are inspected, again first for SAC-C and then for CHAMP.

6.4.3 Solutions with CODE Rapid Products

SAC-C: No Elevation-dependent Weighting and Cut-off Angle $0°$

Let us first study the reduced-dynamic orbits (RcIS, RcIIS, and RpIIS, see Table 6.5, R stands for Rapid) used as a priori orbits for the pre-screening in LEOKIN. Figure 6.41 shows the RMS errors per coordinate of the reduced-dynamic orbit determinations for the solutions without elevation-dependent weighting for SAC-C in program SATORB.

The RMS errors for the RcIS-orbits (Figure 6.41(a)) are the largest which is no surprise because they are based on code positions only. These code positions are derived without a priori orbit information in LEOKIN and therefore no pre-screening of the data was possible. SATORB allows it to screen the "observations". No use was made of this option, however. These RcIS-orbits are the basis for all subsequent kinematic solutions computed with the CODE Rapid products as input for SAC-C.

The RMS errors for the RcIIβS- and RpIIβS-orbits are smaller. The RMS errors for the RcIIβS-orbits (APO set C) (Figure 6.41(b)) are around two meters. These are code-only orbits, as well. The corresponding code positions (RcIIβ) were, however, generated in LEOKIN using the pre-screening option (using the RcIS-orbit). The RMS errors reflect the accuracy of the code positions of SAC-C.

The RMS errors for the reduced-dynamic orbits of APO set P (RpIIβS) (Figure 6.41(c)) are for most days < 30 cm. These reduced-dynamic orbits are based on combined code positions and phase position-differences. The combined positions obviously have a much better accuracy than the code-only positions used for APO set C.

The RMS errors are missing for some days. For doy 059 and 060 no data are available. For doy 087 and 088 it is impossible with LEOKIN to compute a reasonable kinematic solution with the few data available (see Figure 6.39). For doy 081 it is impossible to generate reduced-dynamic orbits for APO set P with SATORB. The RcIS-orbit has an RMS error of 54 m for the orbit determination of the reduced-dynamic orbit with code-only positions in program SATORB. This shows already that there are severe data problems for this day. Even if we choose the screening option in program SATORB it is not possible to generate a reasonable orbit for this day. At about noon probably a maneuver took place because if we set up a new arc after 740 minutes (12^h20^m) the results for the two arcs are reasonable.

We want to follow the same processing procedure for all days considered and do not make any exception by splitting up the 24-hours arc, for example. It is obvious that it is not recommended to use the reduced-dynamic orbits of type C for doy 081/2002 for the pre-screening in LEOKIN but with this example we may show what happens if we nevertheless do it.

Figure 6.42 shows the results of the RCβ- and RPβ-solutions for doy 055 to 089 (cut-off angle $0°$, no elevation-dependent weighting). Each day is characterized by three bars. The left bar gives the number of interrupts due to missing position-differences, the middle bar the number of jumps in the kinematic trajectory for solution A, and the right bar the corresponding number of jumps for solution B. Table 6.16 summarizes the minimum, mean, and maximum numbers for all solutions. Figure 6.43 shows the percentage of deleted observations for the code and the phase observations.

The number of interrupts and jumps for doy 086 is comparatively large for all solutions. This is due

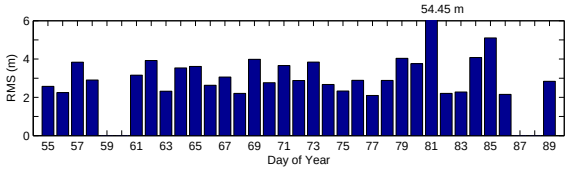

(a) RcIS-orbits (code positions RcI derived without pre-screening used as input).

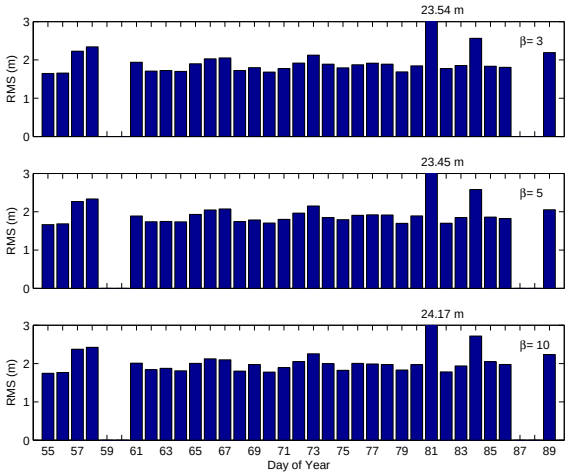

(b) RcIIβS-orbits, APO set C, code positions of RcIIβ used as input.

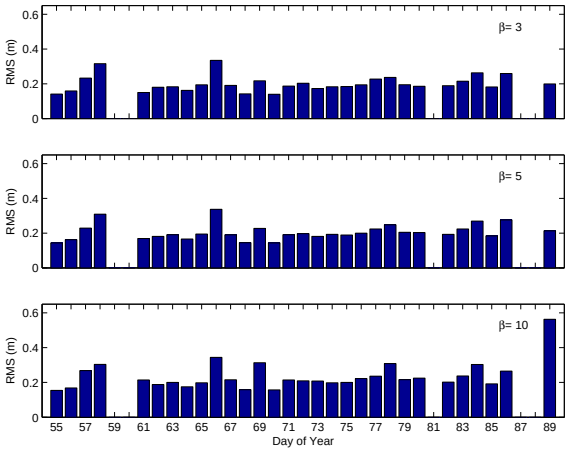

(c) RpIIβS-orbits, APO set P, combined positions of RpIIβ used as input.

Figure 6.41: RMS errors per coordinate of orbit determination in program SATORB, SAC-C, no elevation-dependent weighting, CODE Rapid products, doy 055 to 089/2002.

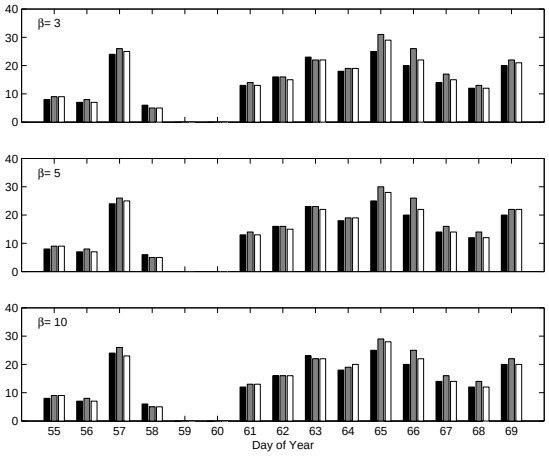

(a) APO set C, doy 055 to 069/2002.

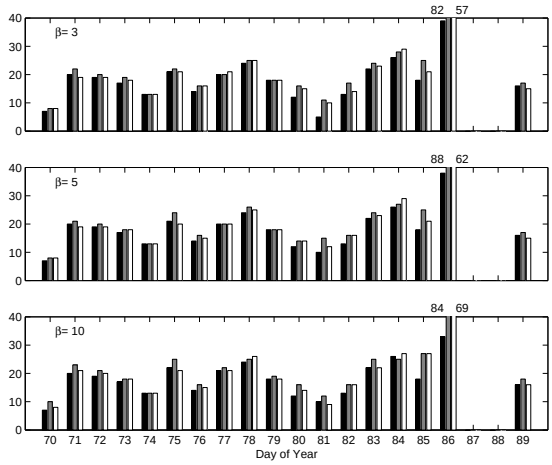

(b) APO set C, doy 070 to 089/2002.

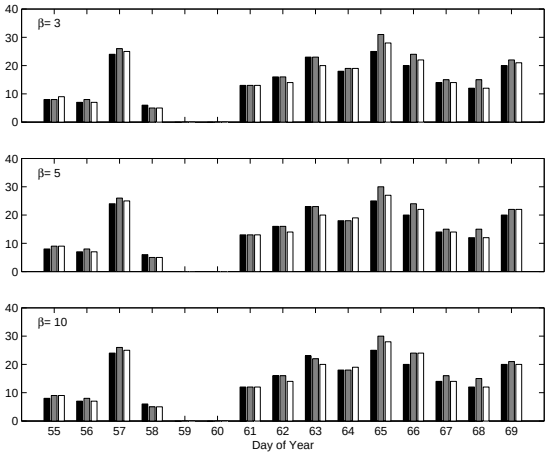

(c) APO set P, doy 055 to 069/2002.

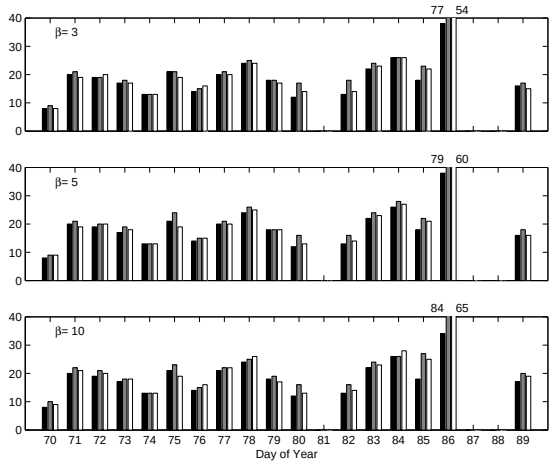

(d) APO set P, doy 070 to 089/2002.

Figure 6.42: Number of interrupts due to missing phase position-differences (left bar) and number of jumps in the kinematic trajectory for solution A (middle bar) and B (right bar), CODE Rapid products, no elevation-dependent weighting, SAC-C, doy 055 to 089/2002.

Table 6.16: Minimum, mean, and maximum number of interrupts and jumps for solutions without elevation-dependent weighting using CODE Rapid products (RCβ, RPβ), SAC-C, doy 055 to 089/2002.

	APO set C									APO set P								
	Interrupts			Jumps						Interrupts			Jumps					
	Sol. A and B			Sol. A			Sol. B			Sol. A and B			Sol. A			Sol. B		
$\beta = 3$	6	17	39	5	20	82	5	18	57	6	18	38	5	20	77	5	18	54
$\beta = 5$	6	17	38	5	20	88	5	19	62	6	18	38	5	20	79	5	19	60
$\beta = 10$	6	17	33	5	20	84	5	19	69	6	17	34	5	21	84	5	19	65

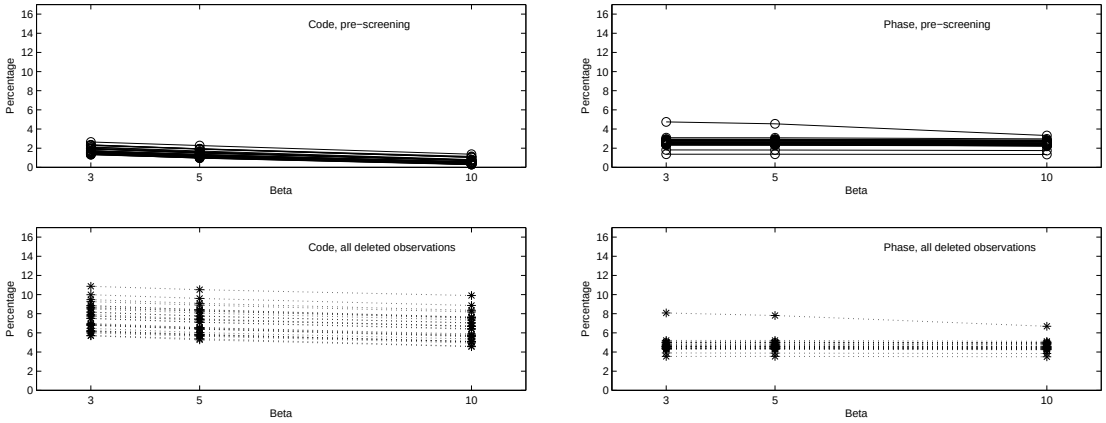

(a) Code observations, APO set C.

(b) Phase observations, APO set C.

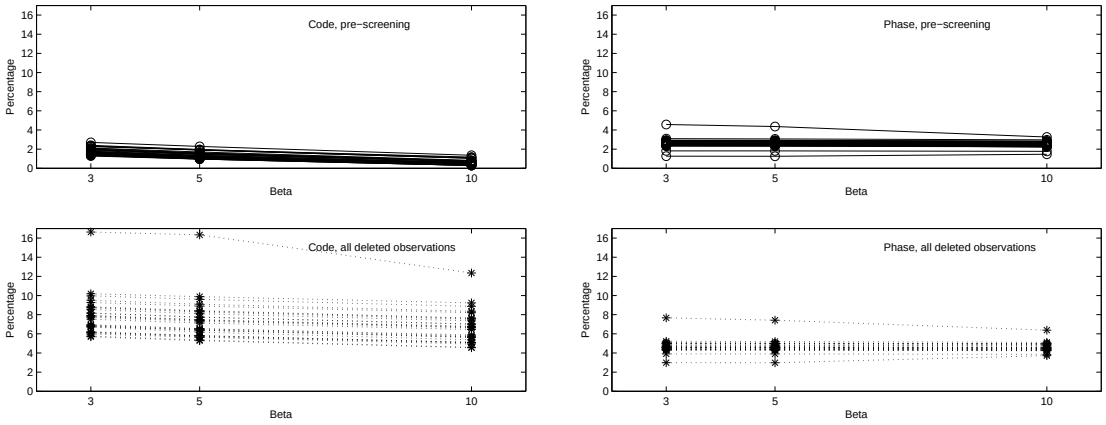

(c) Code observations, APO set P.

(d) Phase observations, APO set P.

Figure 6.43: Percentage of deleted observations for solutions using CODE Rapid products and not applying elevation-dependent weighting, SAC-C, doy 055-089/2002.

to the data performance which gets worse during this day (see Figure 6.39). Many data gaps and epochs with fewer than four tracked satellites do occur. The data quality of this day is barely sufficient for our kinematic positioning approach in LEOKIN.

On nearly all days the number of jumps for solution A is larger than for solution B. We already saw a similar behavior for the CHAMP solutions of the 2001 IGS CHAMP test campaign. The code observations at low elevations may be responsible for problems in the combined positions in solutions A.

The number of interrupts and jumps does not significantly increase with increasing values of β as it was observed in previous examples. There is no significant difference between the solutions for APO set C and P. The numbers in Table 6.16 are similar for all solution types. All maximum numbers correspond to the problematic day 086.

Figure 6.43(a) shows the percentage of deleted code observations and Figure 6.43(b) the percentage of deleted phase observations when using APO set C. Each curve represents one of the 30 days. For doys 059, 060, 087, and 088 no solutions exist and the percentage of deleted observations for doy 081 is out of range (more than 40 % for code and more than 20 % for phase observations). The percentage of *all deleted observations* includes the observations excluded by the pre-screening, by the iterative least squares adjustment step, and due to the cut-off angle. The curves for the deleted code observations show a slight decrease with increasing value of β. The curves representing the percentage of deleted phase observations are in most cases rather flat. The percentage is nearly the same for most values of β considered. The differences in the resulting kinematic positions are therefore mainly due to the different amount of deleted code observations for different values of β.

We mentioned that the percentage of deleted observations is out of range for doy 081 for APO set C. This underlines that a priori orbits with an RMS in SATORB larger than ten meters are simply not acceptable for further analysis.

Figure 6.43(c) and 6.43(d) show the corresponding curves for the solutions with APO set P. They have in essence the same characteristics as those using APO set C. The uppermost curve in the bottom figure of Figure 6.43(c) corresponds to the solutions for doy 089. As we can see in Figure 6.39 the data performance of this day is still bad and it is not an ideal day for a kinematic point positioning of the satellite. The reason for the high percentage of deleted code observations in Figure 6.43(c) is thus due to bad data performance, which does not allow for a reliable kinematic point positioning. The a priori orbits generated based on only few point positions have reasonable small RMS errors for the orbit determination but the bad data performance is, as in the case of doy 086, at the limit of being usable for a kinematic point positioning with LEOKIN.

The solutions using the CODE Rapid products as input data, no elevation-dependent weighting of the observations, and a cut-off angle of 0° are of similar quality for all days except doys 081, and 086 to 089. The different values for β do not have such a large impact as expected from the previous examples.

SAC-C: Elevation-dependent Weighting and Cut-off Angle 0°:

Figure 6.44 shows the RMS errors per coordinate for the reduced-dynamic orbit determination in SATORB for APO set C and P, when applying an elevation-dependent weighting of the observations in LEOKIN. The differences w.r.t. Figure 6.41 are in most cases not significant. The largest difference may be recognized for the a priori orbits of APO set P with $\beta = 10$. The RMS errors in Figure 6.44(b) are slightly larger than those in Figure 6.41(c). It seems that observations which are not excluded from the data due to the larger value of β have a larger impact on the kinematic solution and the a priori orbit if we use an elevation-dependent weighting of the observations.

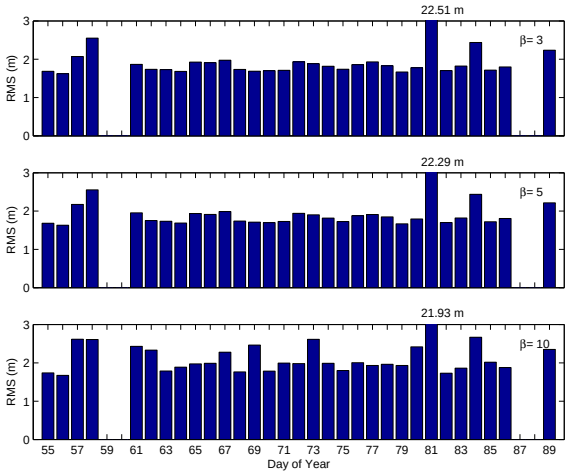

(a) RcIIβSe-orbits, APO set C, code positions of RcIIβe used as input.

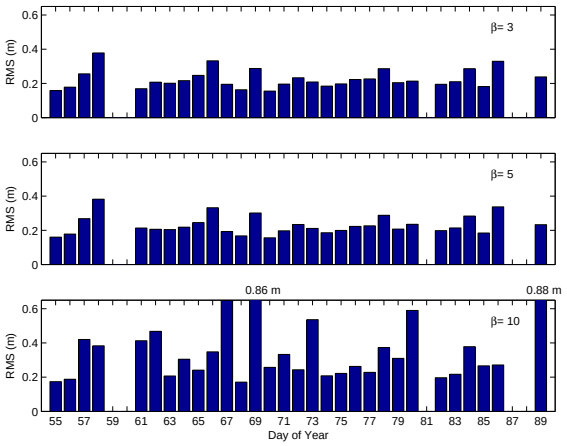

(b) RpIIβSe orbits, APO set P, combined positions of RpIIβe used as input.

Figure 6.44: RMS errors per coordinate for reduced-dynamic orbit determination in program SATORB, SAC-C, elevation-dependent weighting, CODE Rapid products, doy 055 to 089/2002.

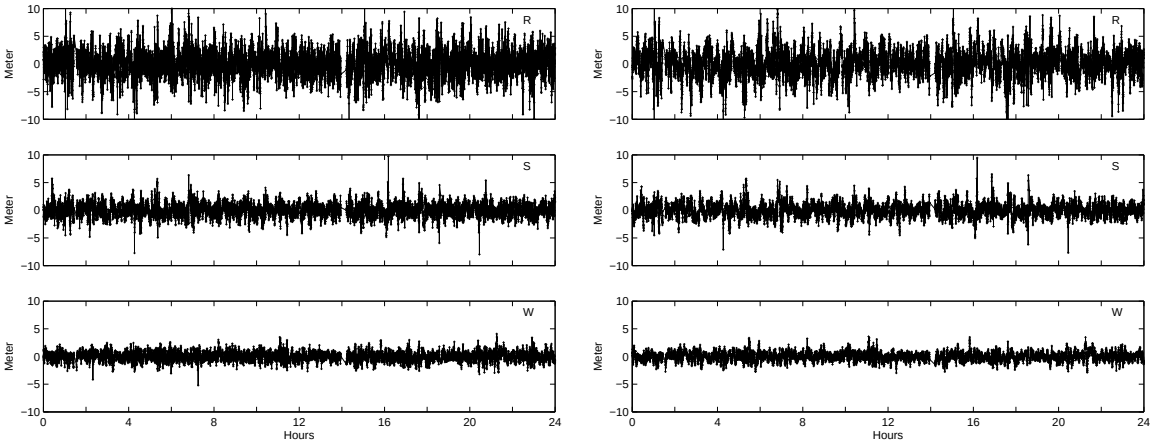

(a) Residuals of RcII3 positions w.r.t. RcII3S orbit, RMS 1.66 m.

(b) Residuals of RcII3e positions w.r.t. RcII3Se orbit, RMS 1.64 m.

Figure 6.45: SATORB residuals of code positions without weighting (left) and with weighting (right), SAC-C doy 056/2002.

Figure 6.46 shows the number of interrupts and number of jumps in the kinematic trajectory for the RCβe-, and RPβe-solutions (cut-off angle 0°, elevation-dependent weighting with $\alpha = 1$) for SAC-C. We cannot recognize significant differences to Figure 6.42. Many solutions A show more jumps in the kinematic trajectory than solutions B. This does not agree with the observations made for the corresponding solutions of the IGS CHAMP test campaign: There we have seen that the performance of solution A is improving when elevation-dependent weighting of the observations is enabled. This behavior points to problems with code observations at low elevations (multipath) for CHAMP. For SAC-C this difference for solution A between the solutions without and with elevation-dependent weighting cannot be recognized. In order to confirm that the quality of the code positions for SAC-C are not significantly better when elevation-dependent weighting is applied we inspect the residuals (RSW-directions) of the kinematic code positions in SATORB for the reduced-dynamic orbit RcII3S without (Figure 6.45(a)) and the orbit RcII3Se with (Figure 6.45(b)) elevation-dependent weighting. The residuals show no significant difference and when we compare these figures with Figures 6.26(a) and 6.26(b) we see that, in contrary to CHAMP, the elevation-dependent weighting has more or less no influence on the code positioning results in LEOKIN for SAC-C. Therefore no clear answer may be given at this point whether the weighting model is appropriate for the code observations of SAC-C or not. The code observations in general seem to be worse than in the case of CHAMP, however.

Table 6.17 lists the minimum, mean, and maximum numbers of interrupts and jumps for the RCβe- and RPβe-solutions. The mean numbers are as homogeneous but slightly better than the mean numbers of the RCβ- and RPβ-solutions (Table 6.16). The values for the minimum and maximum numbers are comparable for the solutions with and without elevation-dependent weighting.

Figure 6.47 shows the percentage of deleted observations. Figures 6.47(a) and 6.47(b) show the percentage for APO set C and Figures 6.47(c) and 6.47(d) for APO set P. There are no significant differences between the APO sets. The percentage of deleted observations shows no significant difference to the corresponding percentage of deleted observations for the solutions without elevation-dependent weighting

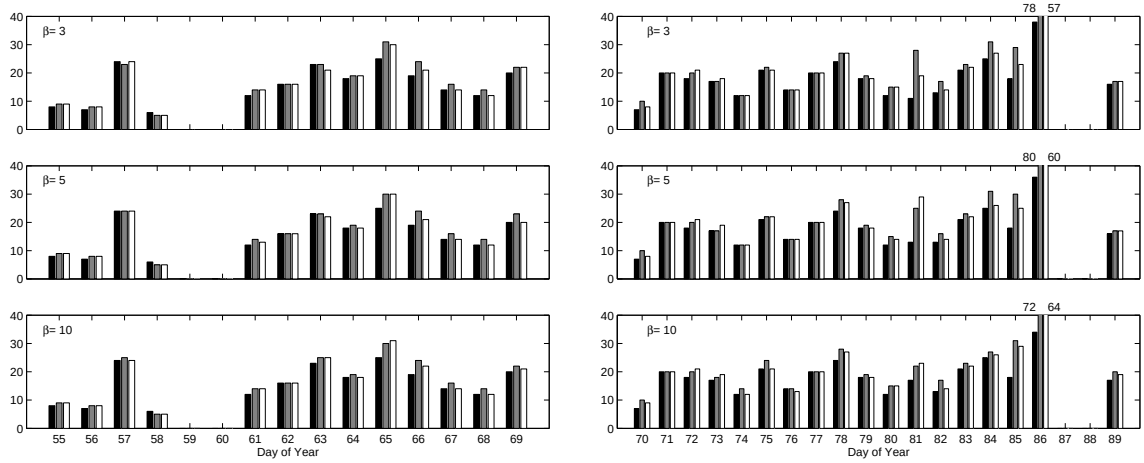

(a) APO set C, doy 055 to 069/2002.

(b) APO set C, doy 070 to 089/2002.

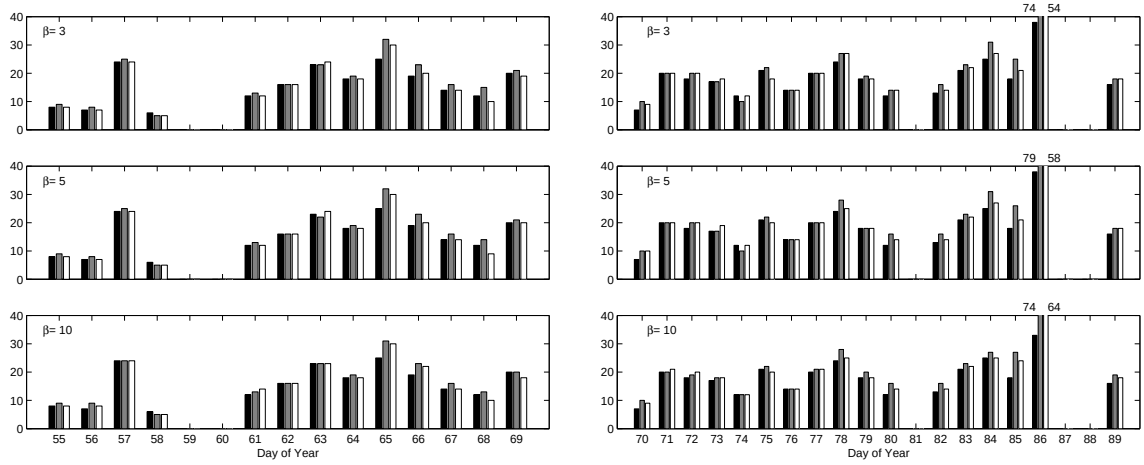

(c) APO set P, doy 055 to 069/2002.

(d) APO set P, doy 070 to 089/2002.

Figure 6.46: Number of interrupts due to missing phase position-differences (left bar) and number of jumps in the kinematic trajectory for solution A (middle bar) and B (right bar), CODE Rapid products, elevation-dependent weighting, SAC-C, doy 055 to 089/2002.

Table 6.17: Minimum, mean, and maximum number of interrupts and jumps for solutions with elevation-dependent weighting using CODE Rapid products (RCβe, RPβe), SAC-C.

	APO set C									APO set P								
	Interrupts			Jumps						Interrupts			Jumps					
	Sol. A and B			Sol. A			Sol. B			Sol. A and B			Sol. A			Sol. B		
$\beta = 3$	6	17	38	5	20	78	5	19	57	6	17	38	5	20	74	5	18	54
$\beta = 5$	6	17	36	5	21	80	5	19	60	6	17	38	5	21	79	5	19	58
$\beta =$10	6	17	34	5	21	72	5	20	64	6	17	33	5	20	74	5	19	64

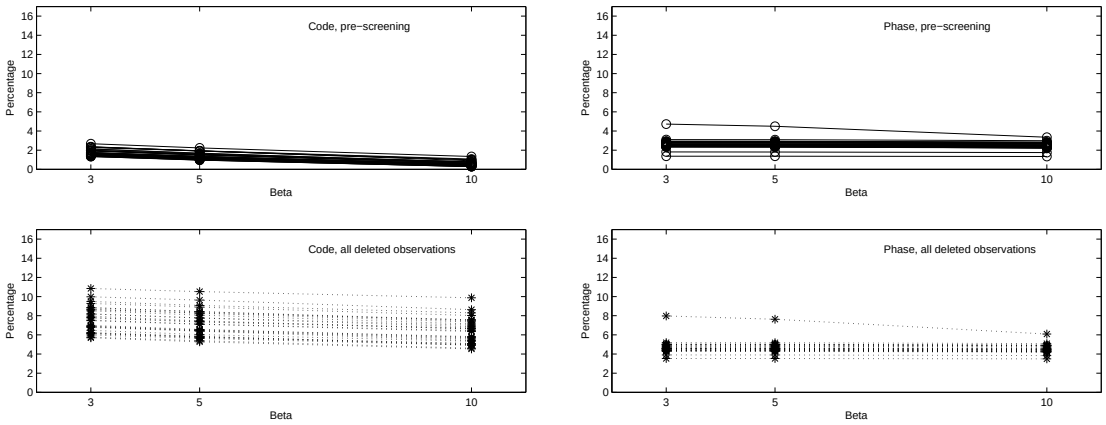

(a) Code observations, APO set C.

(b) Phase observations, APO set C.

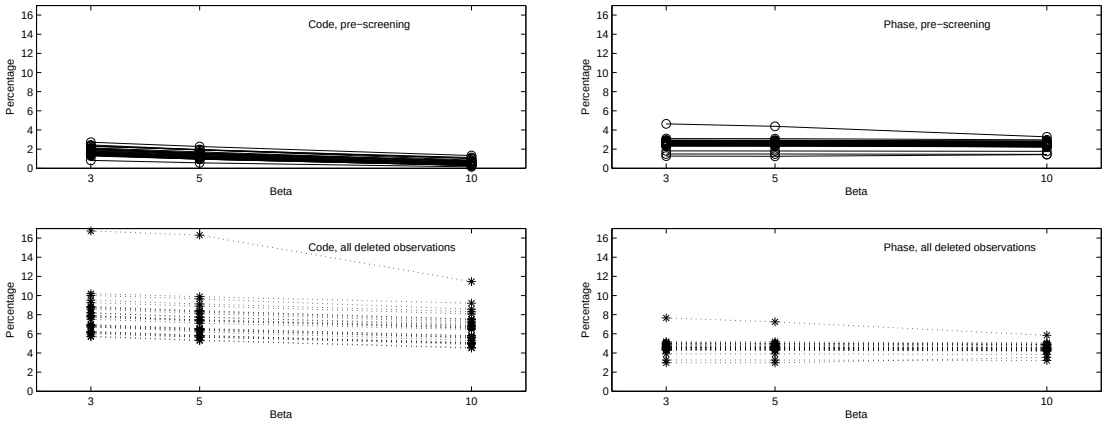

(c) Code observations, APO set P.

(d) Phase observations, APO set P.

Figure 6.47: Percentage of deleted observations for solutions using CODE Rapid products and applying elevation-dependent weighting, SAC-C, doy 055-089/2002.

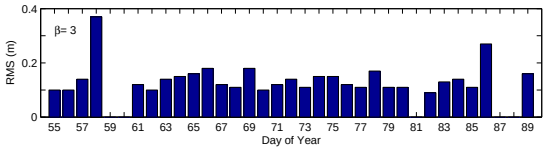

Figure 6.48: RMS errors of Helmert transformation between kinematic trajectories RCB3 and RCB3e, SAC-C, doy 055 to 089/2002.

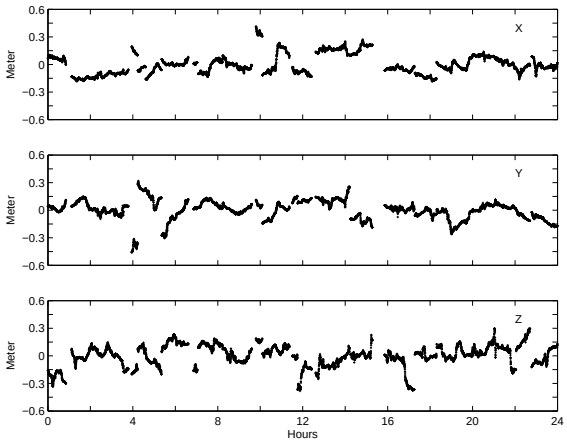

Figure 6.49: Differences between kinematic trajectories RCB3 and RCB3e, SAC-C, doy 079/2002.

(Figure 6.43).

In general we have seen that the solutions computed with the CODE Rapid products for SAC-C are of a good quality except for a few days with serious data problems. Neither the solution without nor the solution with elevation-dependent weighting is outstandingly good or bad.

Figure 6.48 shows the RMS errors of a Helmert transformation between the kinematic solutions RCB3 and RCB3e for the 35 days. Most RMS errors are between 10 cm and 20 cm. Two days show, however, larger RMS errors (up to 40 cm). Doy 079/2002 is a typical day which has no special problems and we use it for illustrations. Figure 6.49 shows the differences between the kinematic trajectories RCB3 and RCB3e for doy 079/2002. The offsets between sequences of phase-connected positions are in most cases in excess of ten centimeters.

For APO set P we generate the best possible reduced-dynamic orbits with SATORB with code positions and phase position-differences of the kinematic solutions RPB3 ($\rightarrow$ reduced-dynamic solution RP3S) and RPB3e ($\rightarrow$ RP3Se). These reduced-dynamic orbits may help to evaluate the kinematic solutions.

Figure 6.50(a) shows the RMS errors of a Helmert transformation between the kinematic solutions RPB3 and RPB3e and Figure 6.50(b) those for a transformation between the reduced-dynamic orbits RP3S and RP3Se. Figure 6.52 shows the RMS errors of a Helmert transformation between the kinematic trajectories (RPB3 and RPB3e) and the reduced-dynamic orbits (RP3S and RP3Se). The values are all of the same size for all four comparisons. Figure 6.51(a) shows the differences between the kinematic trajectories RPB3 and RPB3e for doy 079/2002 and Figure 6.51(b) those between the reduced-dynamic orbits RP3S and RP3Se.

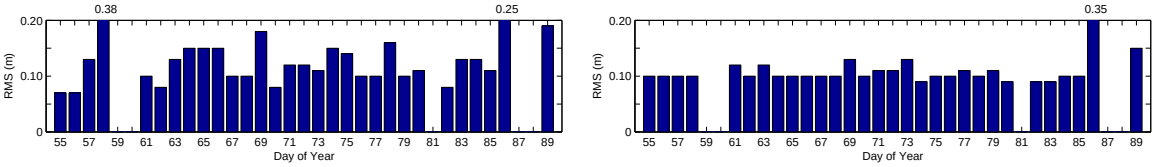

(a) Kinematic trajectories RPB3 – RPB3e.

(b) Reduced-dynamic orbits RP3S – RP3Se.

Figure 6.50: RMS errors of Helmert transformation between RPB3 and RPB3e (left) and between RP3S and RP3Se (right), SAC-C, doy 055 to 089/2002.

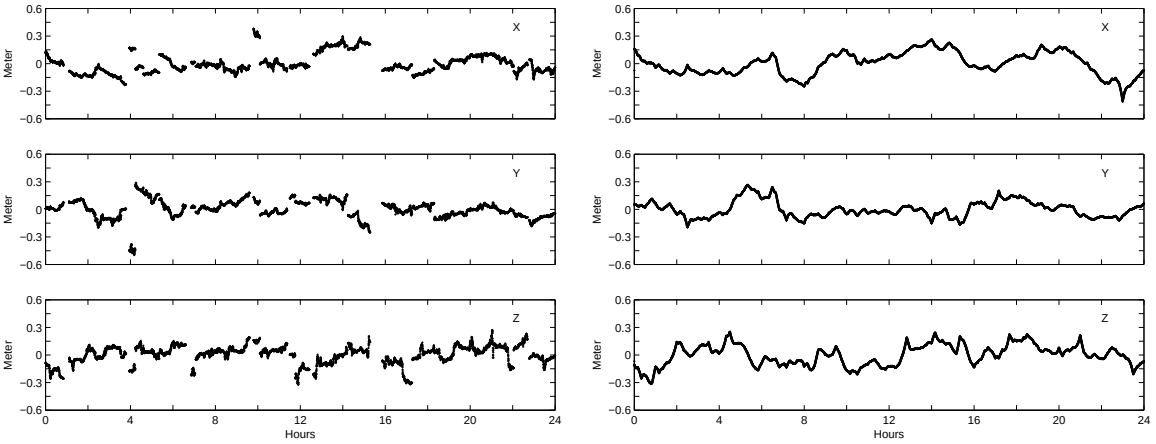

(a) Kinematic trajectories RPB3 – RPB3e, RMS 0.10 m.

(b) Reduced-dynamic orbits RP3S – RP3Se, RMS 0.11 m.

Figure 6.51: Differences between RPB3 and RPB3e (left) and between RPS3 and RPS3e (right), SAC-C, doy 079/2002.

The offsets between the sequences of phase-connected positions in Figure 6.51(a) have the same size as for the corresponding differences for APO set C (Figure 6.49). The frequent interrupts and the resulting offsets in the kinematic trajectory are a problem of the kinematic point positioning procedure in LEOKIN and they cannot be avoided. Figures 6.53(a) and 6.53(b) show the differences between the kinematic trajectory RPB3 and the reduced-dynamic orbit RP3S (left) and between RPB3e and RP3Se (right) for doy 079/2002, respectively. The large offsets of the kinematic trajectories w.r.t. the reduced-dynamic orbit make it very difficult to evaluate the accuracy of the particular solutions.

From these comparisons it cannot be concluded which of the two solutions is the better one (without or with elevation-dependent weighting). The answer is not as clear as in the case of CHAMP for the 2001 campaign. Further investigations on this issue are necessary in order to find an answer.

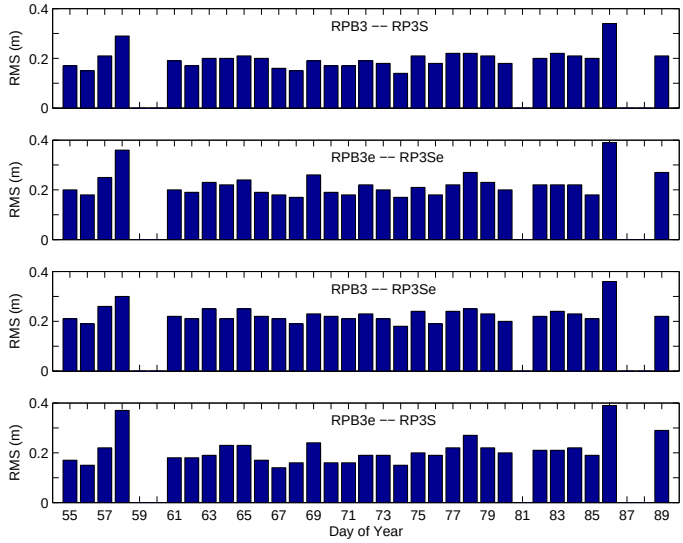

Figure 6.52: RMS errors of Helmert transformation between kinematic (RPB3, RPB3e) and reduced-dynamic orbits (RP3S, RP3Se), SAC-C, doy 055 to 089/2002.

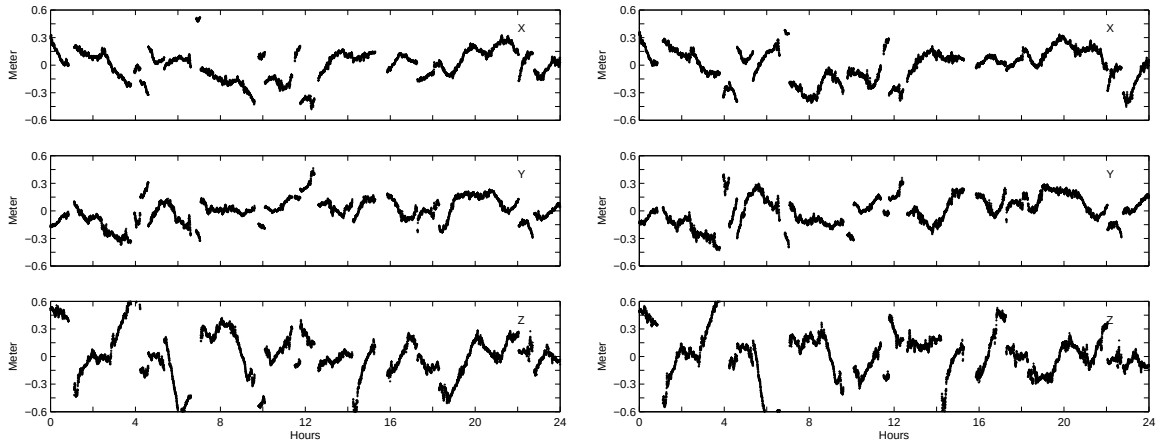

(a) Kinematic trajectory RPB3 – reduced-dynamic orbit RP3S.

(b) Kinematic trajectory RPB3e – reduced-dynamic orbit RP3Se.

Figure 6.53: Differences between RPB3 and RP3S (left) and between RPB3e and RP3Se (right), SAC-C, doy 079/2002.

CHAMP: No Elevation-dependent Weighting, Cut-off Angle 0°

The kinematic solutions for the 35 days in 2002 of CHAMP GPS observations may be compared with those from the eleven days of the IGS CHAMP test campaign and with results from SAC-C.

Satellites below the local horizon are no longer tracked for the 2002 time interval considered. In addition the CHAMP receiver started to track up to ten satellites simultaneously on doy 064/2002 (Figure 6.40). We therefore expect to have a better data performance and therefore better results for these 35 days, especially after doy 064, than for the eleven days in 2001. The kinematic solutions without elevation-dependent weighting of the observations are analyzed first.

Figure 6.54 shows the RMS errors per coordinate for the reduced-dynamic orbit determinations in SATORB. Figure 6.54(a) shows the values for reduced-dynamic orbits RcIS (using code positions derived without a priori orbit information in LEOKIN) which are the basis for all following solutions using the CODE Rapid products as input data for CHAMP. The RMS errors are clearly smaller than those for SAC-C (Figure 6.41(a)).

The RMS errors for the reduced-dynamic orbits of APO set C (RcIIβS, Figure 6.54(b)) are about one meter. This is a factor of two smaller than the corresponding values for SAC-C (Figure 6.41(b)). The code observations of CHAMP thus seem to be of better quality than the code observations of SAC-C. The values for doy 064 are missing because we split the day into two intervals. The first arc refers to the observations before and the second to the observations after the data gap. Therefore, we have two short reduced-dynamic orbits for doy 064, which are not included in these figures.

The reduced-dynamic orbits for APO set P (RpIIβS, Figure 6.54(c)) have RMS errors below 15 cm for all days considered (for $\beta = 3$ and 5). The RMS errors are slightly smaller than the corresponding values for SAC-C (Figure 6.41(c)) and very homogeneous over the 35 days.

Figure 6.55 shows the number of interrupts and number of jumps for the kinematic solutions considered. The three bars for each day have the same meaning as in the corresponding figures for SAC-C (Figure 6.42). The differences between the solutions with APO set C (Figures 6.55(a) and 6.55(b)) and the solutions with APO set P (Figures 6.55(c) and 6.55(d)) are not significant. In many cases solutions A show more jumps in the kinematic trajectory than solutions B. A sudden increase of the quality of the kinematic solutions can be observed on doy 077. The numbers of interrupts and jumps are significantly smaller than for the days before. No obvious change in the data performance starting on doy 077 may be recognized however (see Figure 6.40), except that the number of epochs with fewer than six tracked satellites is reduced starting with doy 077. This may be very important because kinematic point positioning with LEOKIN requires at least four observations. With four observations we may determine a kinematic position but there is no redundancy in the adjustment and therefore no quality control is possible for this position.

Observe that the kinematic solution for doy 086 has no interrupts due to missing position-differences and that no jumps in the kinematic trajectory could be found. Therefore, doy 086 is an ideal test day without data gaps and data problems.

Compared to the results of the IGS CHAMP test campaign (Table 6.7) the mean number of interrupts and jumps are significantly smaller (Table 6.18). Figure 6.56 shows the percentage of deleted observations for the 35 days. The curves may be characterized as the corresponding curves for SAC-C (Figure 6.43).

The solutions without elevation-dependent weighting for the 35 days in 2002 for CHAMP show similar characteristics concerning the number of interrupts and jumps, and the percentage of deleted observations. Partly, solutions A show more jumps than solutions B, but mainly for the days before doy 077. The values for the interrupts and jumps themselves are smaller than the corresponding values for

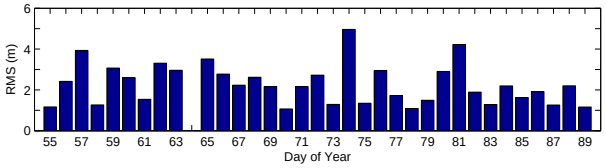

(a) RcIS-orbits.

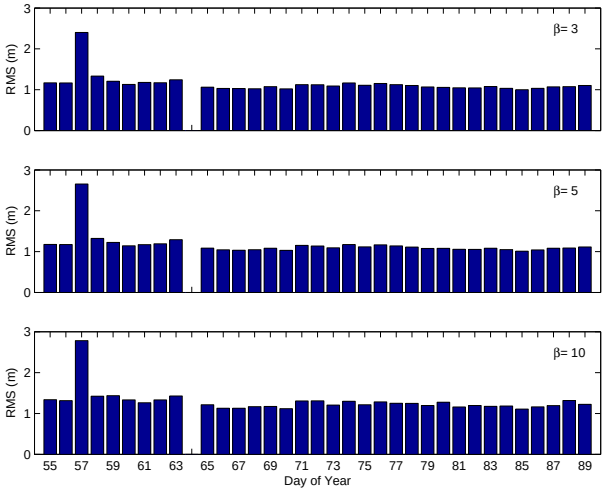

(b) RcIIβS-orbits, APO set C.

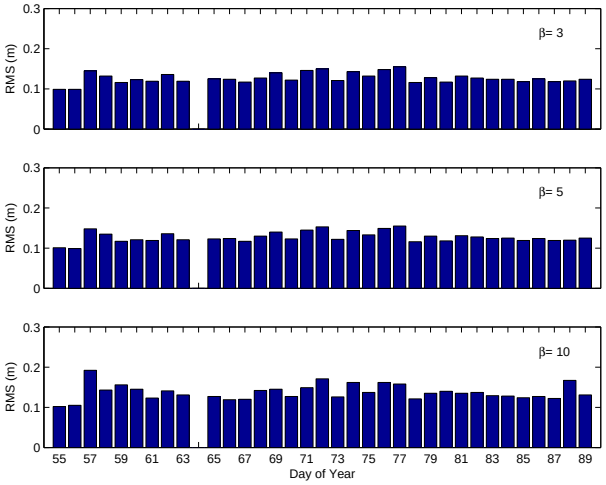

(c) RpIIβS-orbits, APO set P.

Figure 6.54: RMS errors per coordinate for reduced-dynamic orbit determination in program SATORB, CHAMP, no elevation-dependent weighting, CODE Rapid products, doy 055 to 089/2002.

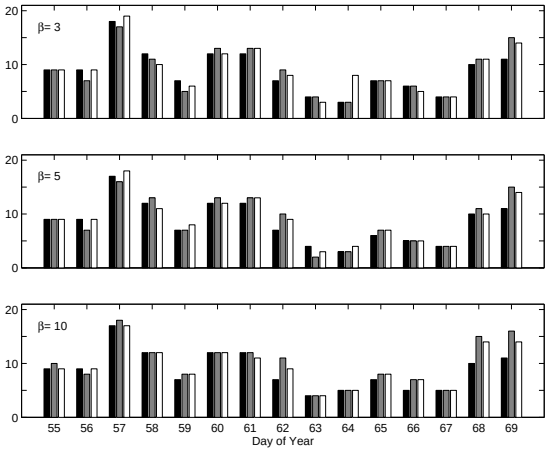

(a) APO set C, doy 055 to 069/2002.

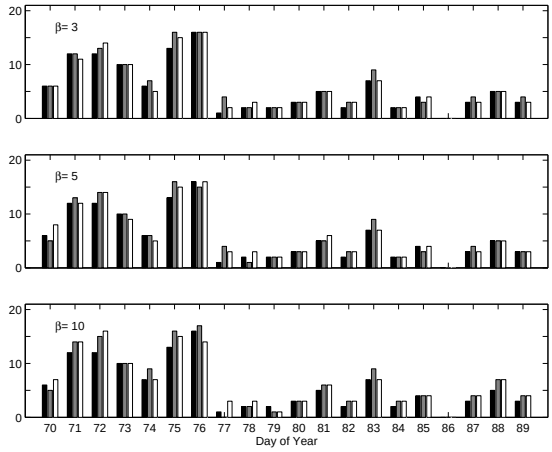

(b) APO set C, doy 070 to 089/2002.

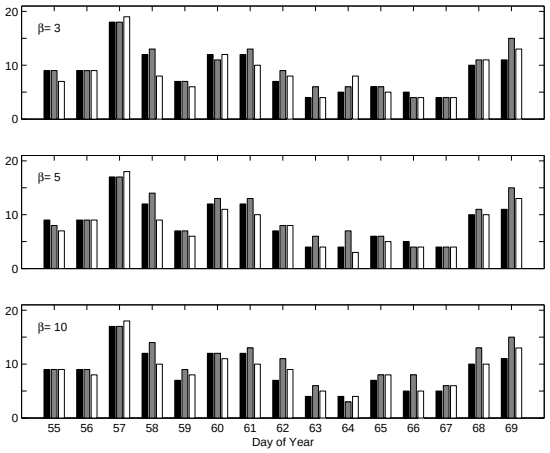

(c) APO set P, doy 055 to 069/2002.

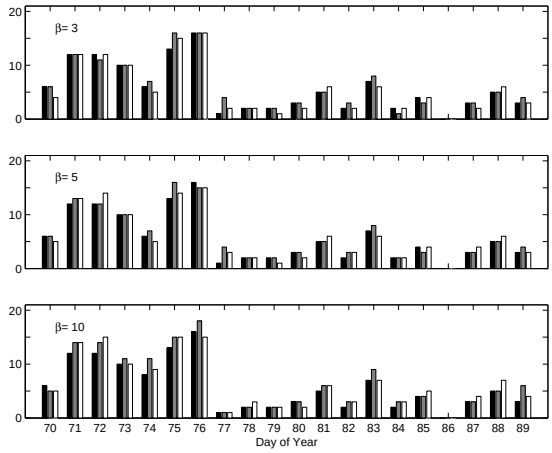

(d) APO set P, doy 070 to 089/2002.

Figure 6.55: Number of interrupts due to missing phase position-differences (left bar) and number of jumps in the kinematic trajectory for solution A (middle bar) and B (right bar), CODE Rapid products, no elevation-dependent weighting, CHAMP, doy 055 to 089/2002.

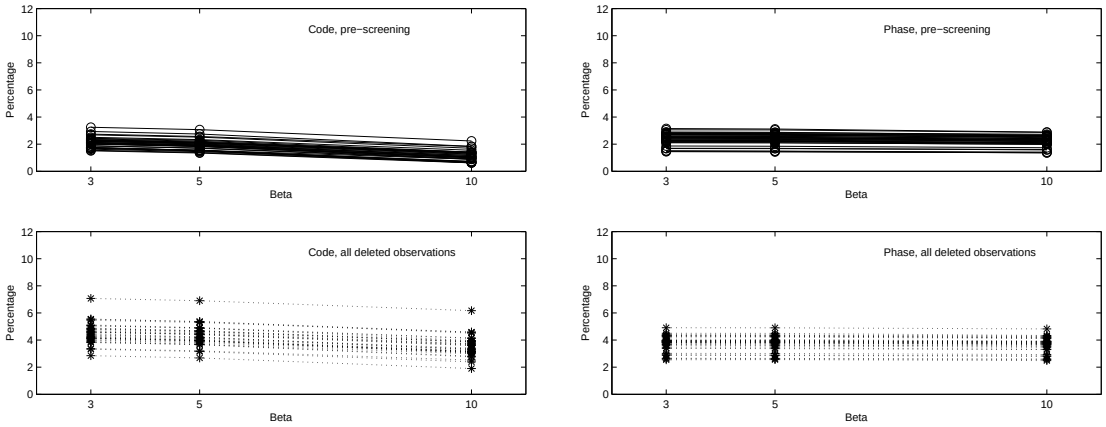

(a) Code observations, APO set C.

(b) Phase observations, APO set C.

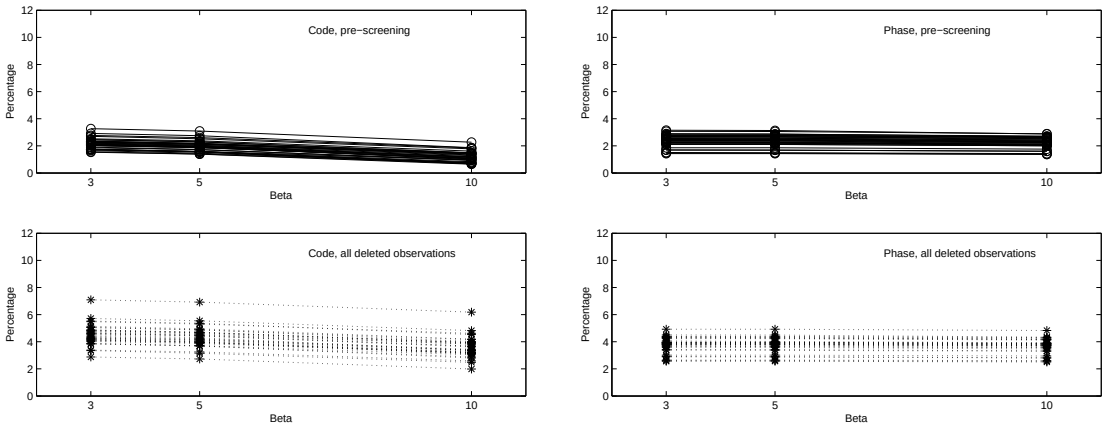

(c) Code observations, APO set P.

(d) Phase observations, APO set P.

Figure 6.56: Percentage of deleted observations for solutions using CODE Rapid products and not applying elevation-dependent weighting, CHAMP, doy 055-089/2002.

Table 6.18: Minimum, mean, and maximum number of interrupts and jumps for solutions without elevation-dependent weighting using CODE Rapid products (RCβ, RPβ), CHAMP.

	APO set C									APO set P								
	Interrupts			Jumps						Interrupts			Jumps					
	Sol. A and B			Sol. A			Sol. B			Sol. A and B			Sol. A			Sol. B		
$\beta = 3$	0	7	18	0	7	17	0	7	19	0	7	18	0	7	18	0	7	19
$\beta = 5$	0	7	17	0	7	16	0	7	18	0	7	17	0	8	17	0	7	18
$\beta = 10$	0	7	17	0	8	18	0	8	17	0	7	17	0	8	18	0	8	18

the 2001 IGS CHAMP test campaign. This is the case for the RMS errors of the reduced-dynamic orbit determinations in SATORB, as well. This indicates that the data performance and quality of the CHAMP data has significantly improved in 2002.

CHAMP: Elevation-dependent Weighting, Cut-off Angle 0°

Figure 6.57 shows the RMS errors per coordinate for the orbit determination in SATORB for the reduced-dynamic orbits RcIIβSe and RpIIβSe. The RMS errors for APO set C (Figure 6.57(a)) are slightly smaller than those for the solutions without elevation-dependent weighting (Figure 6.54(b)) which was expected due to the findings for the 2001 IGS test campaign that elevation-dependent weighting has to be applied to the code observations of CHAMP. The RMS errors of the orbit determination of the reduced-dynamic orbits RcII10Se are less homogeneous than those for the reduced-dynamic orbits RcII10S. The RMS errors for APO set P (Figure 6.57(b)) are equal to those in Figure 6.54(c). Except for $\beta = 10$ this is not the case and it can be stated that the choice of $\beta = 10$ is not good enough.

Figure 6.58 shows the number of interrupts and number of jumps for the RCβe- and RPβe-solutions of CHAMP. Table 6.19 summarizes the minimum, mean and maximum numbers for the different RCβe- and RPβe-solutions.

The number of interrupts and number of jumps in Figure 6.58 shows the pattern already noticed in the examples for the IGS CHAMP test campaign: The solution A shows a similar number of jumps as solution B. The kinematic solutions get better starting from doy 077 onwards. The best performance of the solutions can be found in Figures 6.58(c) and 6.58(d) for solution B using APO set P with elevation-dependent weighting of the observations. The curves with the percentage of deleted observations are not shown for these solutions with elevation-dependent weighting because they are very similar to those of the solutions without elevation-dependent weighting (Figure 6.56).

The RMS errors per coordinate of the Helmert transformation between the solution RPB3 and RPB3e for the 35 days may be found in Figure 6.59. The values are smaller than the corresponding values for SAC-C (Figure 6.50(a)). The reason may be that the solutions for SAC-C have in average more interrupts than the solutions for CHAMP. If these interrupts have different size for the solution with and without elevation-dependent weighting this leads to larger differences between the kinematic trajectories.

We generate, in addition, the best possible reduced-dynamic orbits RP3Se in SATORB with the code positions and phase position-differences from RPB3e as input. Figure 6.60(a) shows the RMS errors of the Helmert transformations between the kinematic trajectory RPB3 and the reduced-dynamic orbit RP3Se (top) and between RPB3e and RP3Se (bottom). The RMS errors of the Helmert transformation between RPB3e and RP3Se (mean RMS error 9.6 cm) are in average smaller than those for the comparison between RPB3 and RP3Se (mean RMS error 11.5 cm). A reason for this is that the orbits RPB3e

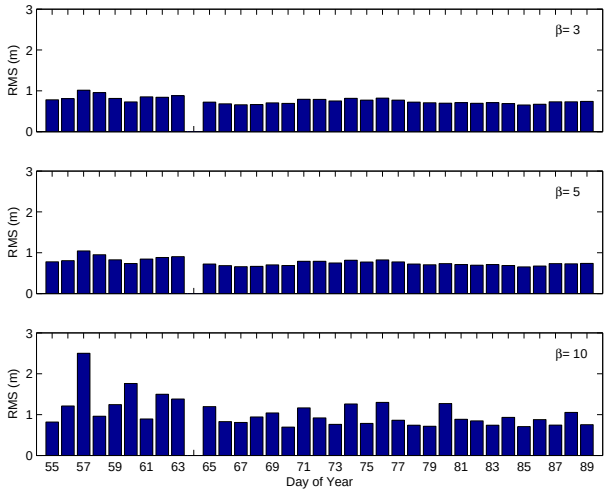

(a) RcIIβSe-orbits, APO set C.

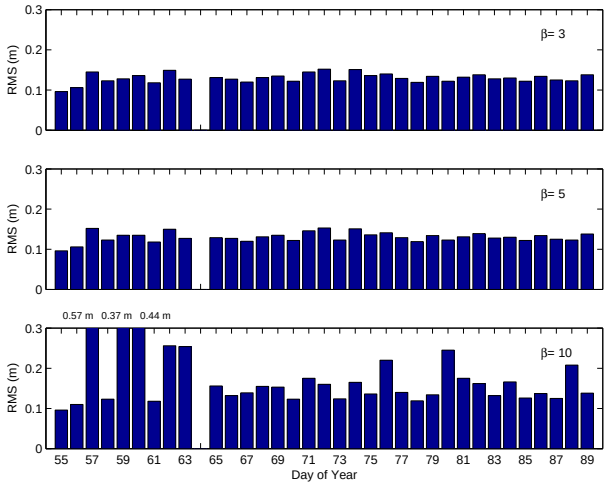

(b) RpIIβSe-orbits, APO set P.

Figure 6.57: RMS errors per coordinate for reduced-dynamic orbit determination in program SATORB, CHAMP, elevation-dependent weighting, CODE Rapid products, doy 055 to 089/2002.

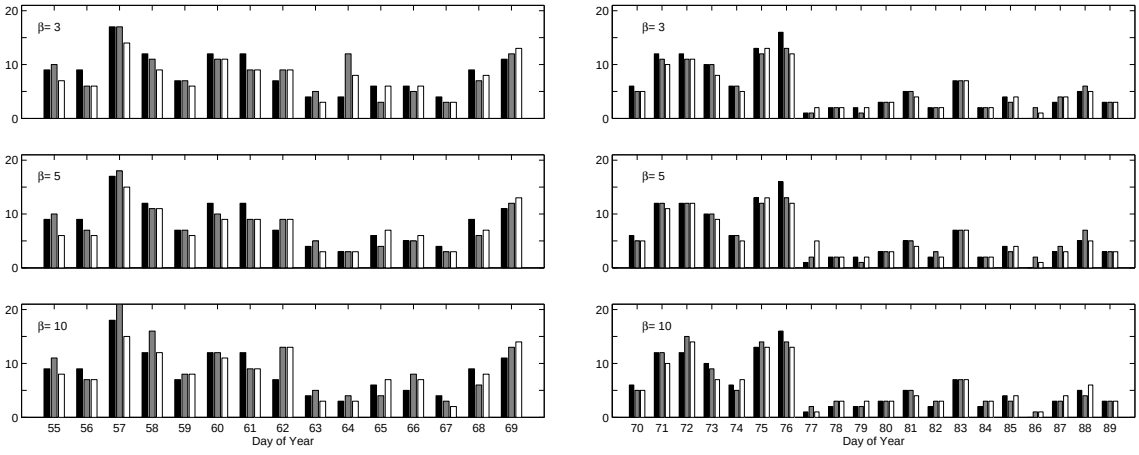

(a) APO set C, doy 055 to 069/2002.

(b) APO set C, doy 070 to 089/2002.

(c) APO set P, doy 055 to 069/2002.

(d) APO set P, doy 070 to 089/2002.

Figure 6.58: Number of interrupts due to missing phase position-differences (left bar) and number of jumps in the kinematic trajectory for solution A (middle bar) and B (right bar), CODE Rapid products, elevation-dependent weighting, CHAMP, doy 055 to 089/2002.

Table 6.19: Minimum, mean, and maximum number of interrupts and jumps for solutions with elevation-dependent weighting using CODE Rapid products (RCβe, RPβe), CHAMP.

	APO set C									APO set P								
	Interrupts			Jumps						Interrupts			Jumps					
	Sol. A and B			Sol. A			Sol. B			Sol. A and B			Sol. A			Sol. B		
$\beta = 3$	0	7	17	1	7	17	1	6	14	0	7	17	1	7	17	0	7	14
$\beta = 5$	0	7	17	1	7	18	1	6	15	0	7	17	1	7	17	0	6	15
$\beta = 10$	0	7	18	1	7	21	1	7	15	0	7	17	1	7	16	0	7	15

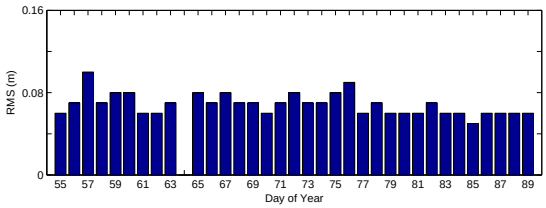

Figure 6.59: RMS errors of Helmert transformation between kinematic solutions RPB3 and RPB3e, CHAMP, doy 055 to 089/2002.

and RP3Se are related to each other: The reduced-dynamic orbit RP3Se is generated using positions and position-differences from the RPB3e solution. If we perform Helmert transformations between the kinematic trajectories RPB3 and RPB3e and the reduced-dynamic orbit RP3S (generated using positions and position-differences of RPB3 solution without elevation-dependent weighting) (Figure 6.60(b)) we find a mean RMS error of 11.1 cm for the comparisons between RPB3 and RP3S and 11.2 cm for the comparisons between RPB3e and RP3S. The larger values for all other comparisons indicate that the small RMS between the trajectories RPB3e and RP3Se is not only due to the relation between them. The solutions with elevation-dependent weighting (RPB3e (kinematic) and RP3Se (reduced-dynamic)) show the best performance and this underlines that the elevation-dependent weighting is appropriate for CHAMP.

Figure 6.61 shows the differences between the RPB3 and RPB3e solutions for doy 079 for CHAMP. As expected from Figures 6.55(d), and 6.58(d) we cannot recognize many offsets caused by interrupts (two for RPB3 and RPB3e) between the kinematic trajectories. The differences between the solutions without and with elevation-dependent weighting do not show offsets disturbing and confusing the pictures. Figure 6.62(a) shows the differences between the kinematic trajectory RPB3 and the reduced-dynamic orbit RP3Se and Figure 6.62(b) those between RPB3e and RP3Se.

The better data quality reflected by Figure 6.40 of these 35 days of CHAMP results in an improved quality of the kinematic point positioning with LEOKIN.

6.4.4 Solutions with CODE Final Products

For doy 055 to 069/2002 we generate kinematic solutions based on the CODE Final products as input and compare these results with the kinematic solutions for doy 055 to 069 derived from the CODE Rapid products. The difference between the CODE Rapid and CODE Final products are the GPS orbits and clock corrections used. The differences between the GPS orbits of the two products are in the order of

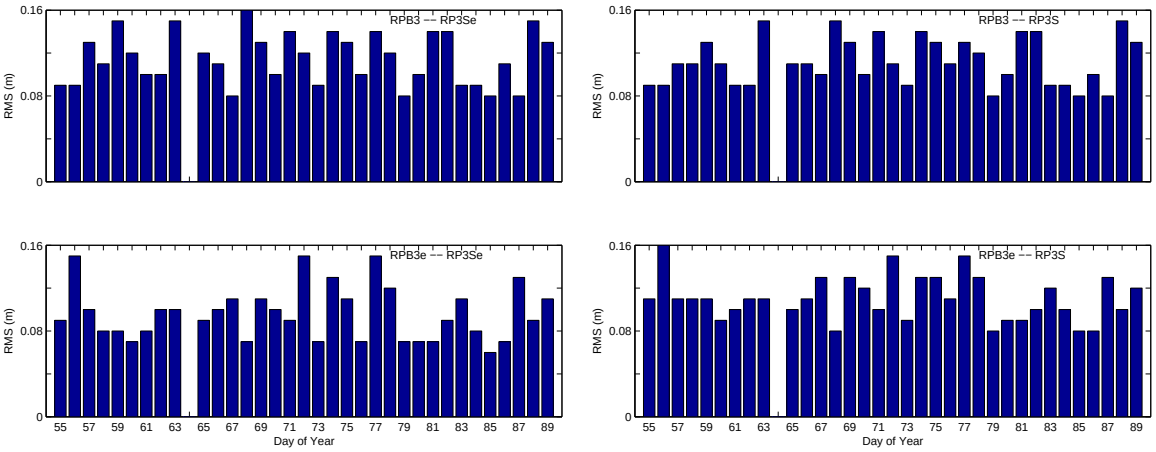

(a) Kinematic trajectories RPB3 (top), RPB3e (bottom) – reduced-dynamic orbit RP3Se.

(b) Kinematic trajectories RPB3 (top), RPB3e (bottom) – reduced-dynamic orbit RP3S.

Figure 6.60: RMS errors of Helmert transformation between kinematic trajectories RPB3 (top), RPB3e (bottom) and reduced-dynamic orbits RP3Se (left) and RP3S (right), CHAMP, doy 055 to 089/2002.

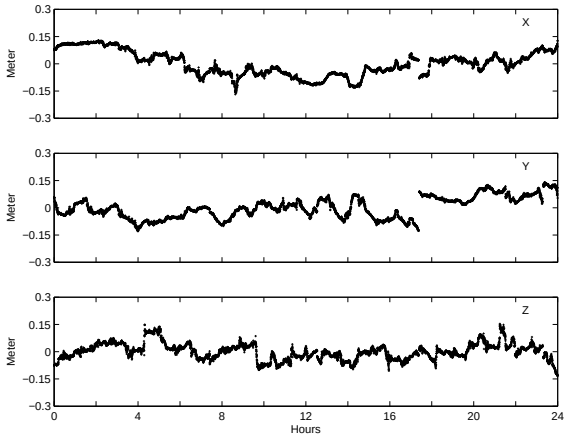

Figure 6.61: Differences between kinematic solutions RPB3 and RPB3e, CHAMP, doy 079/2002, RMS 0.06 m.

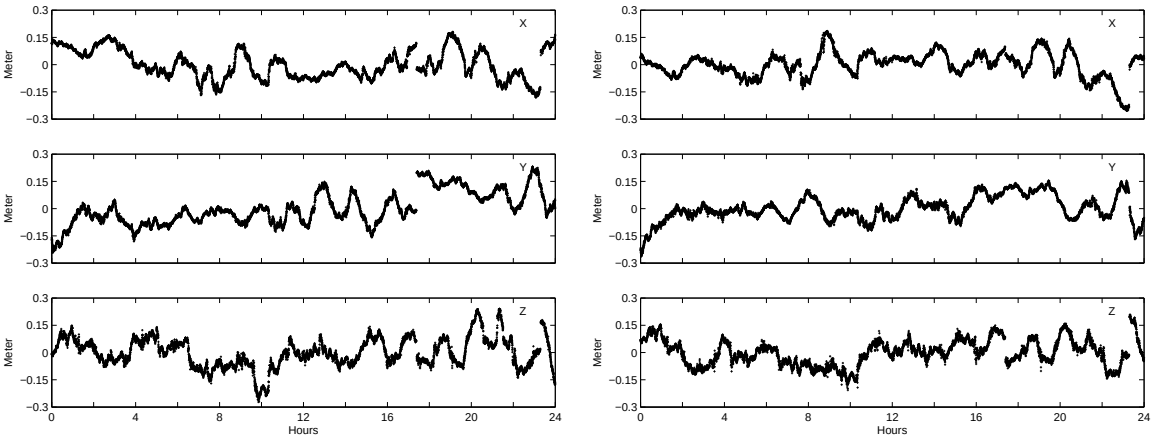

(a) Kinematic trajectory RPB3 – reduced-dynamic orbit RP3Se, RMS 0.08 m.

(b) Kinematic trajectory RPB3e – reduced-dynamic orbit RP3Se, RMS 0.07 m.

Figure 6.62: Differences between kinematic trajectory RPB3 and reduced-dynamic orbit RP3SE (left) and between RPB3e and RP3Se (right), CHAMP, doy 079/2002.

three to six centimeters (RMS error of a Helmert transformation). This should not cause large differences in the resulting trajectories of the LEO. The clock corrections, on the other hand, are generated with two different procedures. The 30-second GPS clock corrections used together with the CODE Rapid orbits are aligned to the GPS broadcast clock corrections and the reference clock is arbitrarily chosen (normally it is a receiver clock of a station known to have a good quality). These so-called “free” 30-second clock corrections are not as consistent with the CODE Rapid orbits as the 30-second clock corrections used together with the CODE Final orbits. These 30-second clock corrections are constrained to the CODE Final 5-minute clock corrections. Therefore we may expect differences in the kinematic trajectories of the LEOs mainly due to these different clock generation procedures.

In addition we want to study the impact on kinematic positions when using the precise 5-minute clock correction of the CODE Final processing as clock information in the LEOKIN procedure (instead of the 30-second clock corrections used so far). The 5-minute clock corrections are linearly interpolated to the epochs needed (as it was also done with the 30-second clock corrections). Finally, the SAC-C data are processed without a cut-off angle for the observations in order to assess the quality of the observations below the local horizon. All kinematic solutions using CODE Final products are generated using exclusively β = 3. When we are using a solution generated with the CODE Rapid products for comparison we always use the corresponding solution generated with $\beta = 3$.

SAC-C: No Elevation-dependent Weighting, Cut-off Angle 0°

Figure 6.63 shows the number of interrupts and number of jumps in the way previously explained. Table 6.20 summarizes the minimum, mean, and maximum numbers for the thirteen days. The numbers are not significantly different from those referring to the solutions using CODE Rapid products (Figures 6.42(a) and 6.42(c)).

Let us now analyze the differences in the kinematic trajectories due to the use of different a priori

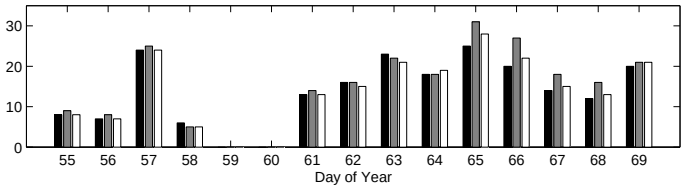

(a) APO set C.

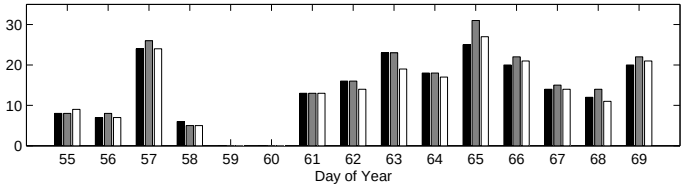

(b) APO set P.

Figure 6.63: Number of interrupts due to missing phase position-differences (left bar) and number of jumps in the kinematic trajectory for solution A (middle bar) and B (right bar), CODE Final products, no elevation-dependent weighting, SAC-C, doy 055 to 069/2002.

Table 6.20: Minimum, mean, and maximum number of interrupts and jumps for solutions without elevation-dependent weighting using CODE Final products (FC, FP), SAC-C.

APO set C									APO set P								
Interrupts			Jumps						Interrupts			Jumps					
Sol. A and B			Sol. A			Sol. B			Sol. A and B			Sol. A			Sol. B		
6	16	25	5	18	31	5	16	28	6	16	25	5	17	31	5	16	27

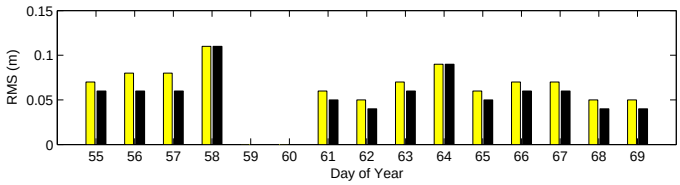

(a) Helmert transformation between RC and FC.

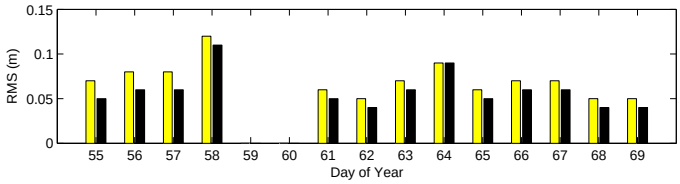

(b) Helmert transformation between RP and FP.

Figure 6.64: RMS errors of Helmert transformation between corresponding kinematic solutions using CODE Rapid (RC and RP) and using CODE Final products (FC and FP), no elevation-dependent weighting, SAC-C, doy 055 to 069/2002. Left bar: solution A, right bar: solution B.

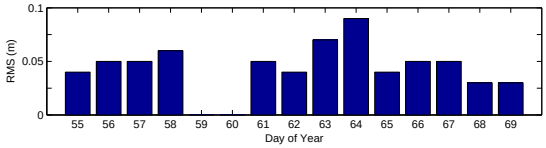

Figure 6.65: RMS errors of Helmert transformation between post-fit reduced-dynamic orbits RPS and FPS, doy 055 to 069/2002, SAC-C.

information for the GPS orbits and clock corrections.

Figure 6.64 shows the RMS errors of the Helmert transformation between the kinematic solutions using either CODE Rapid products (RC and RP) or the CODE Final products (FC and FP). The two bars represent the RMS error for the comparison of solutions A (left bar) and of solutions B (right bar). The RMS errors corresponding to solutions A are in most cases slightly larger than those of solution B. Table 6.21 summarizes the mean RMS errors of the Helmert transformation. Figure 6.65 shows the RMS errors of a Helmert transformation between the post-fit reduced-dynamic orbits RPS and FPS.

Figure 6.66(a) shows, as an example, the differences between the post-fit reduced-dynamic orbits RPS and FPS for doy 055 (RMS 0.04 m). Figure 6.66(b) shows the differences between the kinematic trajectories of solutions RPB and FPB for doy 055 (RMS 0.05 m). Since both, different a priori orbits and different a priori information for the GPS orbits and clock corrections are used for the two solutions the evaluation of the comparisons is difficult.

In order to independently evaluate the influence of different a priori information for GPS orbits and clock corrections on the kinematic trajectory the solutions RCB and RPB were repeated with the a priori

Table 6.21: Mean RMS errors (cm) of Helmert transformation between corresponding kinematic solutions using CODE Rapid (RC and RP) and using CODE Final products (FC and FP) and between corresponding reduced-dynamic solutions (RPS and FPS), SAC-C.

RC ↔ FC.		RP ↔ FP.		RPS ↔ FPS
Sol. A	Sol. B	Sol. A	Sol. B	
7.0	6.0	7.1	5.9	5.0

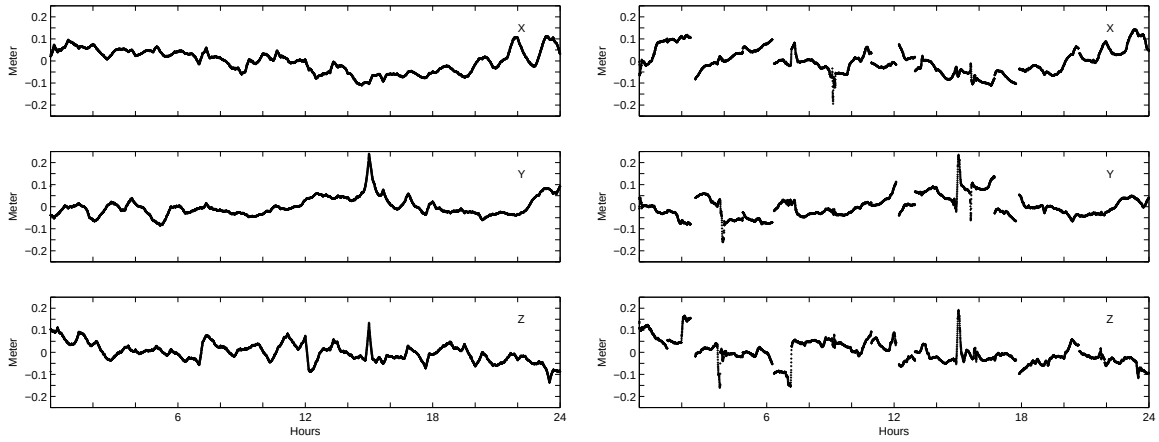

(a) Reduced-dynamic orbits RPS – FPS, RMS 0.04 m.

(b) Kinematic trajectories RPB – FPB, RMS 0.05 m.

Figure 6.66: Differences between reduced-dynamic orbit RPS and FPS (left) and kinematic trajectories RPB and FPB (right) for doy 055, SAC-C.

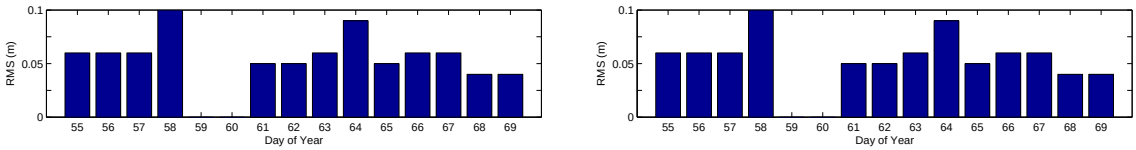

(a) APO set C. (b) APO set P.

Figure 6.67: RMS errors of the Helmert transformation between solutions FCB and RFCB and between FPB and RFPB, SAC-C, doy 055 to 069/2002.

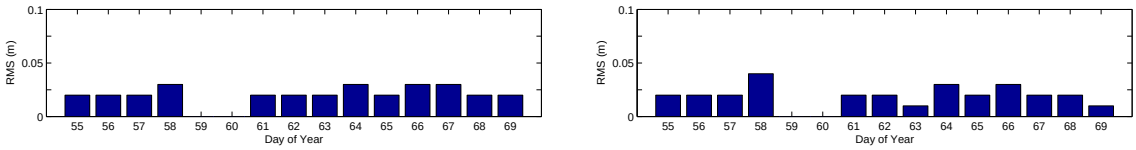

(a) APO set C. (b) APO set P.

Figure 6.68: RMS errors of the Helmert transformation between solutions RCB and RFCB, and between RPB and RFPB, SAC-C, doy 055 to 069/2002.

orbits FcIIS and FpIIS, respectively (solutions RFCB and RFPB).

The RMS errors of the Helmert transformation between the resulting kinematic trajectories of RFCB and RPB with the corresponding solutions FCB and FPB may be found in Figure 6.67. Figure 6.68 shows the RMS errors of the Helmert transformation between the kinematic trajectories of RFCB and RCB and between RFPB and RPB.

The differences between the original solution RCB and solution RFCB (exchanging the a priori orbit) for doy 055 (Figure 6.69(a)) have an RMS error per coordinate of 0.02 m in the Helmert transformation. The differences between the solution FCB and solution RFCB (using the a priori orbit FcIIS) for doy 055 (Figure 6.69(b)) have an RMS error of 0.06 m. These results indicate that the impact on the kinematic results of different input data like CODE Rapid products or CODE Final products is larger than the impact of a different a priori orbit.

As mentioned above the different procedures to generate the 30-second clock corrections used together with the CODE Rapid and the CODE Final products are the main difference between the two types of input data. These differences explain the differences in Figure 6.69(b).

SAC-C: Elevation-dependent Weighting, Cut-off Angle 0°

We computed also the solutions with elevation-dependent weighting using the CODE Final products.

Figure 6.70 shows the number of interrupts and number of jumps for these solutions using APO set C and P. Table 6.22 lists the minimum, mean, and maximum number of interrupts and jumps. Figure 6.71 shows the RMS errors of the Helmert transformation between the corresponding kinematic solutions using CODE Rapid and using CODE Final products as input data. Figure 6.72 shows the RMS errors of the Helmert transformation between the post-fit reduced-dynamic orbits RPSe and FPSe. In Table 6.23 the mean RMS errors for these comparisons are listed.

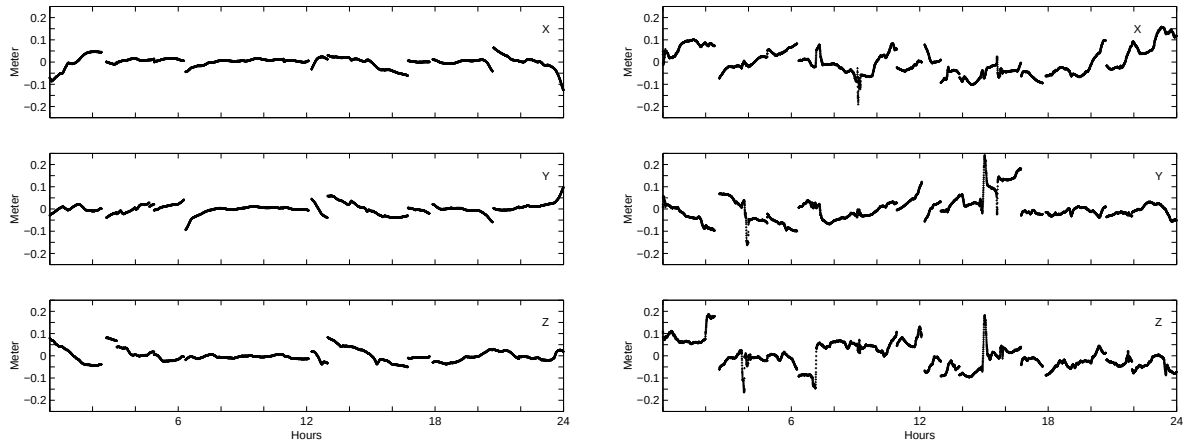

(a) Differences between RCB and RFCB, RMS 0.02 m.

(b) Differences between FCB and RFCB, RMS 0.06 m.

Figure 6.69: Differences between kinematic trajectories for doy 055, SAC-C.

Table 6.22: Minimum, mean, and maximum number of interrupts and jumps for solutions with elevation-dependent weighting using CODE Final products (FCe, FPe), SAC-C.

APO set C									APO set P								
Interrupts			Jumps						Interrupts			Jumps					
Sol. A and B			Sol. A			Sol. B			Sol. A and B			Sol. A			Sol. B		
6	16	25	5	17	30	5	17	30	6	16	25	5	17	31	5	16	29

These results do not indicate whether the solutions without or with elevation-dependent weighting are better in the case of SAC-C. Even the differences between solution A and B are similar for both solution types (without and with elevation-dependent weighting).

The RMS errors of the Helmert transformation between orbit solutions using CODE Rapid and using CODE Final products are larger for the solutions with elevation-dependent weighting (compare Table 6.21 with Table 6.23).

Table 6.23: Mean RMS errors (cm) of the Helmert transformation between corresponding kinematic solutions using CODE Rapid (RCe and RPe) and using CODE Final products (FCe and FPe) and between corresponding reduced-dynamic solutions RPSe and FPSe, SAC-C.

RCe ↔ FCe		RPe ↔ FPe		RPSe ↔ FPSe
Sol. A	Sol. B	Sol. A	Sol. B	
8.3	6.5	8.4	6.5	5.8

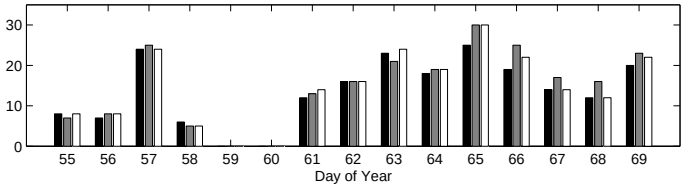

(a) APO set C.

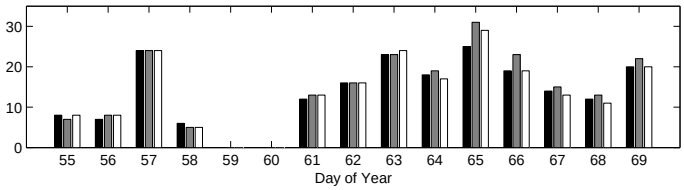

(b) APO set P.

Figure 6.70: Number of interrupts due to missing phase position-differences (left bar) and number of jumps in the kinematic trajectory for solution A (middle bar) and B (right bar), CODE Final products, elevation-dependent weighting, SAC-C, doy 055 to 069/2002.

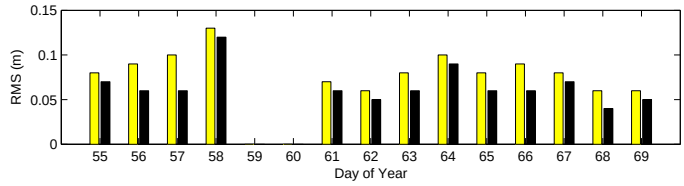

(a) APO set C.

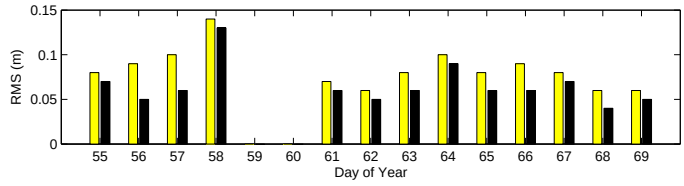

(b) APO set P.

Figure 6.71: RMS errors of the Helmert transformation between kinematic solutions using CODE Rapid and using CODE Final products, elevation-dependent weighting, SAC-C, doy 055 to 069/2002.

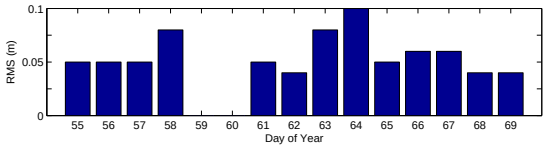

Figure 6.72: RMS errors of the Helmert transformation between reduced-dynamic orbits RPSe and FPSe, SAC-C, doy 055 to 069/2002.

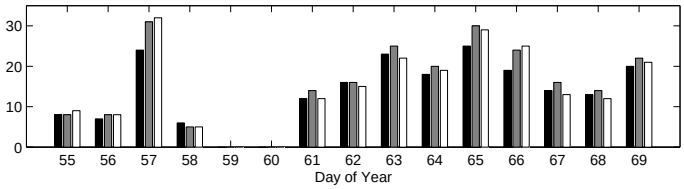

(a) Number of interrupts and number of jumps for solution F5PAe and F5PBe.

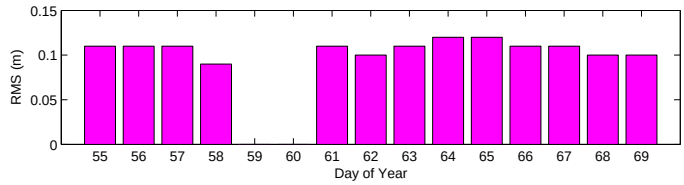

(b) RMS errors of Helmert transformation between solutions F5PBe and FPBe.

Figure 6.73: CODE Final products and CODE Final 5-minute clock corrections as clock information, SAC-C, doy 055 to 069/2002.

SAC-C: CODE Final 5-minute Clock Corrections Used as Clock Information

In Section 3.7 we used interpolated 5-minute clock corrections instead of interpolated 30-second clock corrections in LEOKIN. The resulting differences on the kinematic positions using simulated error-free observations had an RMS error of a Helmert transformation of 2.5 to 4 cm.

In order to evaluate the impact of using the interpolated 5-minute clock corrections those simulation results were performed without a data screening. In the test with real data the data screening is enabled and therefore problems stemming from bad satellite clocks are removed.

In the following we have replaced the 30-second clock corrections used in LEOKIN with the 5-minute clock corrections from the CODE Final product. The 5-minute clock corrections are linearly interpolated to 10-second observation epochs. Solutions FPAe and FPBe are repeated with the interpolated clock information (F5PAe and F5PBe). The a priori orbits used are the same as for the original solutions FPe (FpIISe). The only difference between the two solutions are the GPS clock corrections used.

The number of interrupts and jumps is given in Figure 6.73(a) in the usual way. There is no significant difference to Figure 6.70(b) (except a few small differences, e.g., doy 057 and 066/2002). Figure 6.73(b)

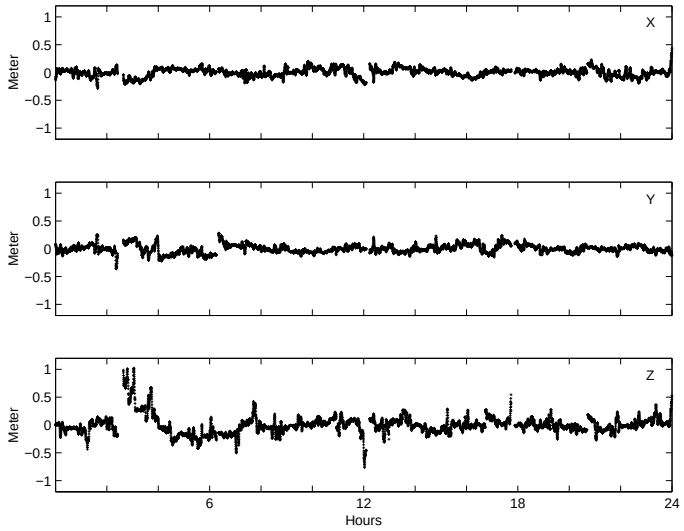

Figure 6.74: Differences between solutions F5PBe and FPBe for doy 055, SAC-C, RMS 0.11 m.

shows the RMS errors of the Helmert transformation between the new solutions F5PBe and the original solutions FPBe. The RMS errors are around ten centimeters for all thirteen days considered. The values are larger than the values from the simulations in Section 3.7. The simulations are performed with error-free observations and therefore no interrupts due to data problems were in the data. This explains the larger values for the real data.

Figure 6.74 shows the differences between the two corresponding solutions for doy 055. The differences are of the order of up to one meter at a few epochs.

The results of this section are of greatest importance for practice: It is obviously possible to generate kinematic (or reduced-dynamic) LEO orbits with a quality of a few decimeters using readily available IGS orbits and clock information (5-minute satellite clock corrections are available from individual IGS analysis centers and as an official IGS product).

SAC-C: No Elevation-dependent Weighting, no Cut-off Angle

In Section 6.2 we have seen that the observations below the local horizon are of rather good quality in the case of SAC-C. This is why we also generate kinematic orbits with all available observations for SAC-C.

The additional observations for these solutions have elevation angles between zero and minus ten degrees. The percentage of these observations compared to the total number is about one to two percent for the thirteen days. This is a significantly smaller percentage than in the case of doy 051/2001 processed in Section 6.2 (about ten percent). The test shall show whether this small amount of observations improves the point positioning result.

Figure 6.75 shows that the number of interrupts and jumps is of the same order as in Figure 6.63 (representing the solutions with a cut-off angle of $0°$).

Figure 6.76 shows the differences in the kinematic trajectory between the solutions FCB and SCB for doy 055. The differences are very small (RMS 0.01 m). It is not clear whether the kinematic solution improves due to the use of the one to two percent low elevation data.

Since the gain of using a small amount of low elevation data is marginal we do not further pursue the issue and recommend a cut-off angle of $0°$ in the case of SAC-C.

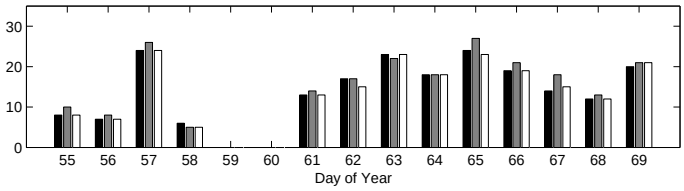

(a) APO set C.

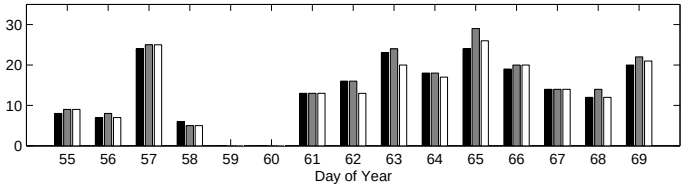

(b) APO set P.

Figure 6.75: Number of interrupts due to missing phase position-differences and number of jumps in the kinematic trajectory, CODE Final products, no elevation-dependent weighting, no cut-off angle, SAC-C, doy 055 to 069/2002.

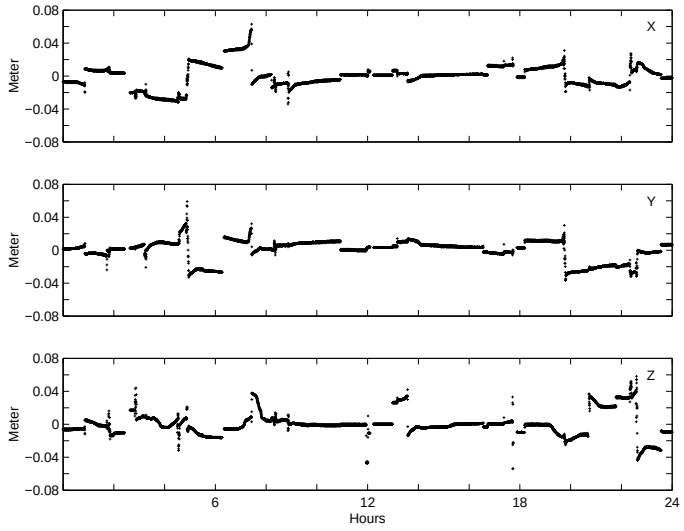

Figure 6.76: Differences between kinematic trajectories FCB (cut-off angle 0°) and SCB (no cut-off angle) for doy 055, SAC-C, RMS 0.01 m.

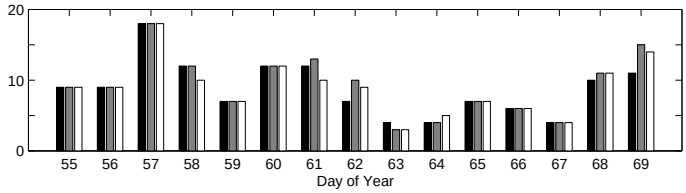

(a) APO set C.

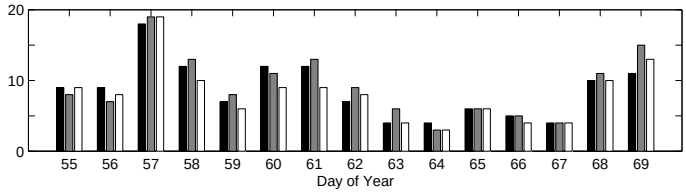

(b) APO set P.

Figure 6.77: Number of interrupts due to missing phase position-differences (left bar) and number of jumps in the kinematic trajectory for solution A (middle bar) and B (right bar), CODE Final products, no elevation-dependent weighting, CHAMP, doy 055 to 069/2002.

Table 6.24: Minimum, mean, and maximum number of interrupts and jumps for solutions without elevation-dependent weighting using CODE Final products (FC, FP), CHAMP.

APO set C									APO set P								
Interrupts			Jumps						Interrupts			Jumps					
Sol. A and B			Sol. A			Sol. B			Sol. A and B			Sol. A			Sol. B		
4	9	18	3	9	18	3	9	18	4	9	18	3	9	19	3	8	19

CHAMP: No Elevation-dependent Weighting, Cut-off Angle 0°

The CHAMP data for doy 055 to 069/2202 are processed with the CODE Final products as input, as well. The solutions without elevation-dependent weighting are analyzed first.

Figure 6.77 shows the number of interrupts and jumps in the known format. Table 6.24 summarizes the corresponding minimum, mean, and maximum numbers of the solutions. Concerning data screening there are no significant differences to the corresponding solutions using CODE Rapid products. We compare the kinematic trajectories of the RC and RP with those of FC and FP. Figure 6.78 shows the RMS errors of the Helmert transformation between the solutions. The values for the comparisons between the solutions A are larger than those for solutions B. The mean RMS errors of the Helmert transformations are listed in Table 6.25. The values are smaller than those for SAC-C (Table 6.21).

As in the case for SAC-C we repeat the computation of RCB and RPB using the corresponding reduced-dynamic orbits FcIIS and FpIIS as a priori orbits. This is done in order to isolate the differences caused by different a priori orbits and caused by different input data. Figure 6.79 shows the RMS errors of the Helmert transformation between the resulting trajectories and the solutions FCB and FPB,

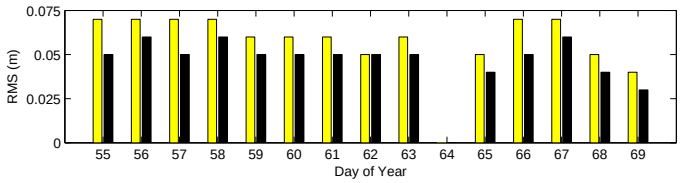

(a) APO set C.

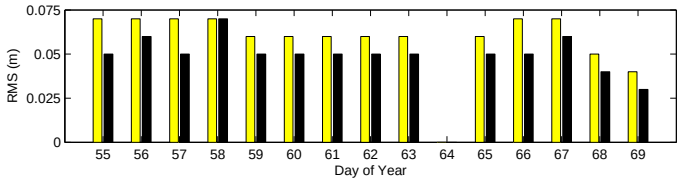

(b) APO set P.

Figure 6.78: RMS errors of the Helmert transformation between corresponding kinematic solutions using CODE Rapid (RC and RP) and using CODE Final products (FC and FP), no elevation-dependent weighting, CHAMP, doy 055 to 069/2002. Left bar: solution A, right bar: solution B.

Table 6.25: Mean RMS errors (cm) of the Helmert transformation between corresponding kinematic solutions using CODE Rapid (RC and RP) and using CODE Final products (FC and FP), CHAMP.

RC $\leftrightarrow$ FC		RP $\leftrightarrow$ FP	
Sol. A	Sol. B	Sol. A	Sol. B
6.1	4.9	6.2	5.1

respectively. Figure 6.80(a) shows the RMS errors of the Helmert transformation between the resulting trajectories of the new solutions RFCB and the solution RCB and Figure 6.80(b) shows the RMS errors of the Helmert transformation between solutions RFPB and RPB. The values have the same order of magnitude as the corresponding values for SAC-C (Figures 6.67 and 6.68). Figure 6.81(a) shows the differences between the kinematic solutions RCB and RFCB derived with the a priori orbit of FcIIS for doy 056. Figure 6.81(b) shows the differences between FCB and the new solution RFCB. The differences in Figure 6.81(a) reflect, therefore, the differences in the used a priori orbit. Those in Figure 6.81(b) reflect the differences in the input data (satellite clock corrections in particular).

The effect on the kinematic solutions for CHAMP is as expected similar to the effect on the kinematic solutions for SAC-C. The difference is only that the effect of using different input data (CODE Final products instead of CODE Rapid products) is somewhat smaller for the CHAMP solutions.

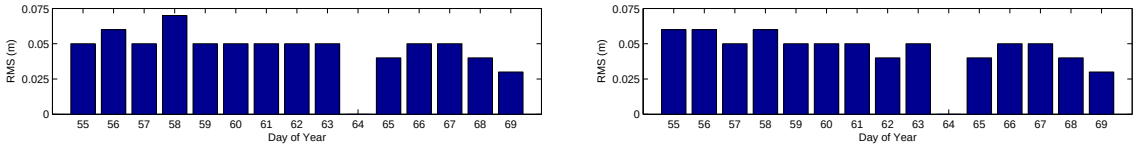

(a) APO set C. (b) APO set P.

Figure 6.79: RMS errors of Helmert transformation between solutions FCB and RFCB, and between FPB and RFPB, CHAMP, doy 055 to 069/2002.

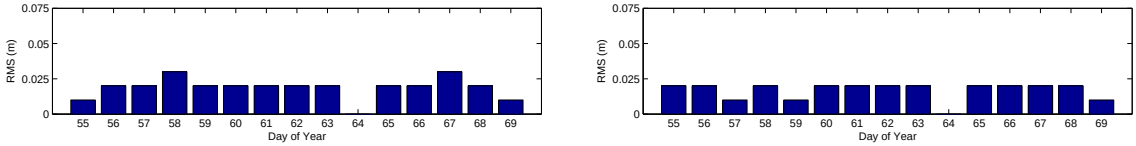

(a) APO set C. (b) APO set P.

Figure 6.80: RMS errors of Helmert transformation between solutions RCB and RFCB, and between RPB and RFPB, CHAMP, doy 055 to 069/2002.

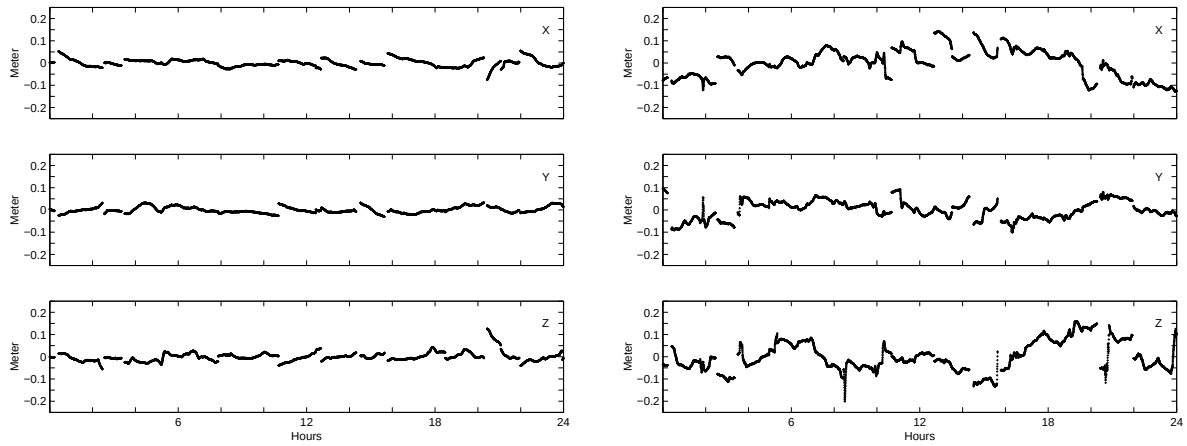

(a) Differences between RCB and RFCB, RMS 0.02 m. (b) Differences between FCB and RFCB, RMS 0.06 m.

Figure 6.81: Differences between kinematic trajectories of doy 056, CHAMP.

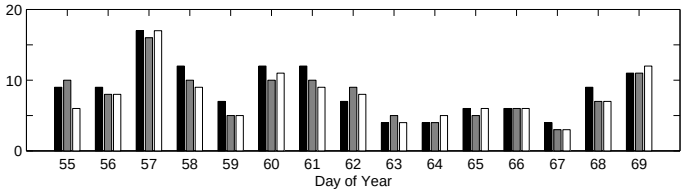

(a) APO set C.

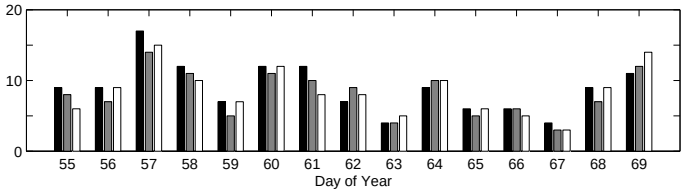

(b) APO set P.

Figure 6.82: Number of interrupts due to missing phase position-differences (left bar) and number of jumps in the kinematic trajectory for solution A (middle bar) and B (right bar), CODE Final products, elevation-dependent weighting, CHAMP, doy 055 to 069/2002.

Table 6.26: Minimum, mean, and maximum number of interrupts and jumps for solutions with elevation-dependent weighting using CODE Final products (FCe, FPe), CHAMP.

APO set C									APO set P								
Interrupts			Jumps						Interrupts			Jumps					
Sol. A and B			Sol. A			Sol. B			Sol. A and B			Sol. A			Sol. B		
4	9	17	3	8	16	3	8	17	4	9	17	3	8	14	3	8	15

CHAMP: Elevation-dependent Weighting, Cut-off Angle 0°

The solutions with elevation-dependent weighting for CHAMP are computed, as well. Figure 6.82 shows the corresponding number of interrupts and jumps for the kinematic solutions. Table 6.26 summarizes the minimum, mean, and maximum numbers for the 15 days considered.

As expected the differences to the solutions without elevation-dependent weighting (Figure 6.77) are not significant except the notice that, as in previous examples for CHAMP, the solutions A have for some days a better performance than the solutions A without elevation-dependent weighting.

Figure 6.83 shows the RMS errors of the Helmert transformation between the solutions using CODE Rapid products (RCe and RPe) and the solutions using CODE Final products (FCe and FPe). Table 6.27 summarizes the mean RMS errors for these comparisons. These mean RMS errors are about one centimeter larger than the corresponding mean RMS errors for the solutions without elevation-dependent weighting (Table 6.25). This was also the case for the solutions for SAC-C (Tables 6.21 and 6.23). The reason for this fact could not be found yet.

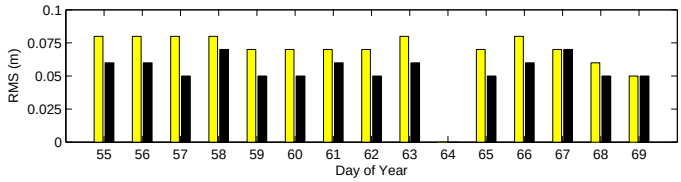

(a) APO set C.

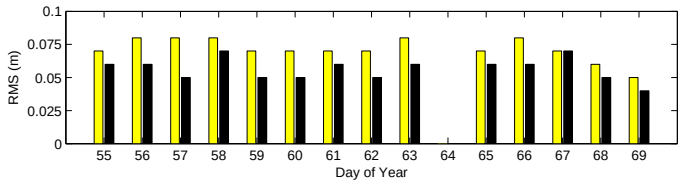

(b) APO set P.

Figure 6.83: RMS errors of the Helmert transformation between corresponding kinematic solutions using CODE Rapid (RCe and RPe) and using CODE Final products (FCe and FPe), with elevation-dependent weighting, CHAMP, doy 055 to 069/2002. Left: solution A, right: solution B.

Table 6.27: Mean RMS errors (cm) of the Helmert transformation between corresponding kinematic solutions using CODE Rapid (RCe and RPe) and using CODE Final products (FCe and FPe), CHAMP.

RC ↔ FC		RP ↔ FP	
Sol. A	Sol. B	Sol. A	Sol. B
7.2	5.6	7.1	5.6

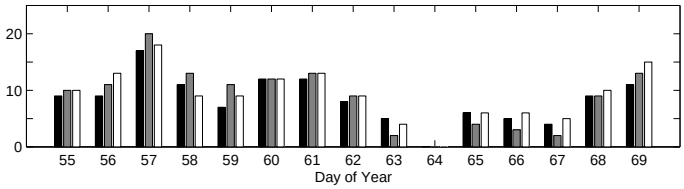

(a) Number of interrupts and number of jumps.

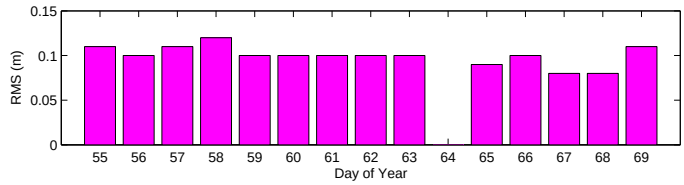

(b) RMS errors of Helmert transformation between solutions F5PBe and FPBe.

Figure 6.84: CODE Final products and CODE Final 5-minute clock corrections as clock information, CHAMP, doy 055 to 069/2002.

CHAMP: CODE Final 5-minute Clock Corrections Used as Clock Information

Interpolated CODE Final 5-minute clock corrections are used for doy 055 to 069/2002 of CHAMP, as well. As in the case of SAC-C we repeated solutions FPA3e and FPB3e with the interpolated 5-minute clock corrections (to 10-second intervals).

Figure 6.84(a) shows the number of interrupts and jumps for these new solutions. The number of jumps is in a few cases (e.g., doy 056 and 057) slightly higher than in Figure 6.82 (top). On the other hand, the number of interrupts and jumps is smaller for doy 058. Figure 6.84(b) shows the RMS errors of the Helmert transformation between solutions F5PBe and FPBe. Doy 064 is left out because of the long data gap on that day (see Figure 6.40). The RMS errors are of the same order of magnitude as the corresponding values for SAC-C (Figure 6.73(b)). Figure 6.85 shows the differences between the two corresponding solutions for doy 055 (F5PBe and FPBe). The differences show similar characteristics as the corresponding differences for SAC-C (Figure 6.74).

6.4.5 Summary

The studies made based on the data series of 35 days for CHAMP and SAC-C in 2002 confirm in essence the conclusions already drawn from the previous examples (CHAMP 152/2001, SAC-C 051/2001, and IGS CHAMP test campaign (doy 140 to 150/2001)).

The solution B with a cut-off angle of $0°$, $\beta = 3$, and a priori orbits from APO set P leads to reliable, robust, and accurate kinematic point positioning results with LEOKIN. For CHAMP we have seen already for the 2001 campaign that the elevation-dependent weighting model is appropriate for the code observations. For SAC-C this cannot be concluded as clearly as in the case of CHAMP because no significant differences between the two models (without and with elevation-dependent weighting)

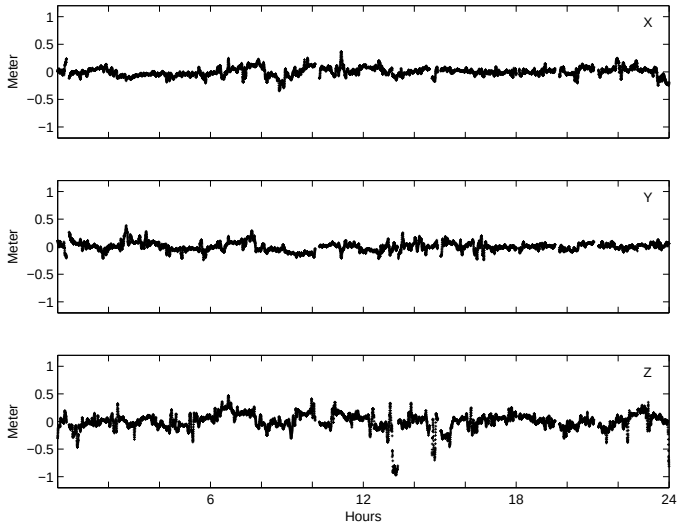

Figure 6.85: Differences between solutions F5PBe and FPBe for doy 055, CHAMP, RMS 0.11 m.

could be identified. We have recognized, on the other hand, that the quality of the kinematic solutions for CHAMP and SAC-C does not depend as much on the value of β as in the previous examples for CHAMP 152/2001, SAC-C 051/2001, and the IGS CHAMP test campaign. The data quality is better in 2002 than in 2001 for both satellites. The remaining outliers can be detected reliably. After data screening there are still enough satellites available to generate kinematic point positions of good quality.

Additional studies were performed concerning the use of different GPS orbits and clock corrections. We used, on the one hand, CODE Rapid products as a priori information and, on the other hand, CODE Final products. The differences between corresponding solutions are below ten centimeters. They are smaller for the solutions without elevation-dependent weighting for both satellites and the reason for this is still unclear.

The differences between the kinematic solutions using CODE Rapid products and the solutions using CODE Final products are mainly due to the GPS clock correction sets used. The differences in the GPS orbits are too small to have a big impact on the results. The Rapid and Final GPS clock correction sets are derived by two slightly different procedures. The 30-second clock corrections used with the CODE Rapid products are so-called “free” clock corrections which are only aligned to the broadcast clock corrections. The 30-second clock corrections used with the CODE Final products, on the other hand, are constrained to the precise CODE Final 5-minute clock corrections.

The differences between the solutions using CODE Rapid products and using CODE Final products are smaller for the CHAMP solutions than the differences for the SAC-C solutions.

The use of interpolated 5-minute clock corrections instead of interpolated 30-second clock corrections in LEOKIN for processing 10-second data leads to highly accurate solutions, as well. The maximal differences in the kinematic trajectories may reach one meter in one component but the RMS errors of a Helmert transformation between the orbit sets are only about ten centimeters. The use of interpolated 5-minute clock corrections is possible and may be recommended if the accuracy requirements are of the order of a few decimeters. This conclusion is of great importance because we do not need to have 30-second clock correction available but may directly use official clock products from the IGS.

The observations tracked below the horizon by SAC-C do not improve the kinematic solution sig-

Table 6.28: RMS (m) errors of Helmert transformation between solutions for doy 144/2001, CHAMP, italic: LEOKIN solutions, non-italic: SATORB solutions, bold: best solutions.

	cIS	*cII3*	cII3S	*cII3e*	cII3Se	*pII3e*	pII3Se	*PB3e*	**P3Se**	**TUM**
cI	2.58	2.86	2.55	2.30	2.52	2.50	2.56	2.60	2.71	2.56
cIS	-	2.13	0.42	1.42	0.51	0.51	0.50	0.48	0.47	0.48
cII3		-	2.10	1.71	2.10	1.89	2.12	1.98	2.11	2.12
cII3S			-	1.37	0.35	0.32	0.32	0.30	0.29	0.30
cII3e				-	1.33	1.35	1.36	1.36	1.38	1.36
cII3Se					-	0.32	0.31	0.33	0.29	0.33
pII3e						-	0.08	0.13	0.15	0.13
pII3Se							-	0.13	0.15	0.13
PB3e								-	0.11	0.09
P3Se									-	0.11

nificantly. The amount of additional observations is, however, very small (one to two percent). We recommend to disregard them for the kinematic point positioning with SAC-C GPS data.

For the CHAMP receiver the maximum number of tracked satellites was increased from eight to ten on doy 064/2002. Interestingly enough, this change did not directly improve the kinematic point positioning results. From doy 077/2002 onwards the results are, however, much better. From doy 077/2002 onwards the number of epochs with only four tracked satellites decreased significantly. With four tracked satellites we can determine a position for the satellite but we have no redundant observation to control the result. The improved redundancy is a possible explanation for the improved kinematic positions starting with doy 077/2002.

In Section 6.3.4 we performed comparisons (Helmert transformation) of many orbits for doy 144/2001 with an external solution from TUM and the best reduced-dynamic orbit (P3Se) we could produce with our procedures in LEOKIN and SATORB. For the data of 2002 we have no external solution available. We can perform, therefore, only internal comparisons.

We review the comparisons for doy 144/2001 for CHAMP and perform, in addition, all cross comparisons between the orbits considered. The description of the orbit solutions may be found in Table 6.13. Table 6.28 shows the RMS errors per coordinate of the Helmert transformations. Table 6.29 shows the corresponding information for doy 086/2002 which is the day with the best data quality for CHAMP for the campaign in 2002. For SAC-C the RMS errors of the Helmert transformations are shown in Table 6.30 for doy 055/2002. The solutions generated with LEOKIN are written in italics in order to distinguish them from the reduced-dynamic SATORB solutions.

The last two columns in Table 6.28 are identical with the last two columns of Table 6.14. Some comparisons indicate that the corresponding solutions are related with each other such as, e.g., pII3e and pII3Se with an RMS error of 0.08 m for the Helmert transformation: The combined positions of pII3e are used as observations for the generation of the reduced-dynamic pII3Se-orbit. The convergence of the orbit solutions to the best solutions in the list (TUM) is nevertheless obvious. In addition, the difference in quality between the kinematic trajectories cII3e and cII3 can clearly be noticed. The code positions of cII3e are generated with elevation-dependent weighting and those of cII3 without weighting. The RMS errors of the Helmert transformations show clearly that the code positions with weighting are significantly better ($\sim$ 30%) than those without weighting. This fact can be recognized in Table 6.29, as well. This underlines our finding that the elevation-dependent weighting model is appropriate for the

Table 6.29: RMS (m) errors of Helmert transformation between solutions for doy 086/2002 using CODE Rapid products, CHAMP, italic: LEOKIN solutions, non-italic: SATORB solutions, bold: best solutions.

	cIS	*cII3*	cII3S	*cII3e*	cII3Se	*pII3e*	pII3Se	*PB3e*	**P3Se**
cI	1.91	1.94	1.95	1.81	1.96	1.96	1.96	1.95	1.95
cIS	-	1.09	0.44	0.78	0.47	0.51	0.48	0.42	0.44
cII3		-	1.07	0.73	1.08	1.05	1.06	1.04	1.04
cII3S			-	0.74	0.13	0.37	0.32	0.33	0.32
cII3e				-	0.73	0.67	0.68	0.67	0.67
cII3Se					-	0.32	0.26	0.28	0.27
pII3e						-	0.13	0.15	0.12
pII3Se							-	0.15	0.13
PB3e								-	0.08

Table 6.30: RMS (m) errors of Helmert transformation between solutions for doy 055/2002 using CODE Rapid products, SAC-C, italic: LEOKIN solutions, non-italic: SATORB solutions, bold: best solutions.

	cIS	*cII3*	cII3S	*cII3e*	cII3Se	*pII3e*	pII3Se	*PB3e*	*PB3*	**P3Se**	**P3S**
cI	2.57	2.31	2.58	2.02	2.58	2.58	2.60	2.60	2.60	2.58	2.59
cIS	-	1.66	0.24	1.70	0.26	0.41	0.37	0.37	0.38	0.35	0.35
cII3		-	1.65	1.10	1.64	1.62	1.67	1.65	1.65	1.65	1.65
cII3S			-	1.69	0.12	0.32	0.27	0.28	0.29	0.23	0.23
cII3e				-	1.69	1.67	1.71	1.70	1.71	1.68	1.69
cII3Se					-	0.33	0.29	0.32	0.33	0.24	0.27
pII3e						-	0.16	0.16	0.18	0.21	0.19
pII3Se							-	0.12	0.13	0.18	0.15
PB3e								-	0.07	0.20	0.17
PB3									-	0.21	0.17
P3Se										-	0.10

code observations of CHAMP. The code positions in general are of better quality in the 2002 campaign.

The comparisons for SAC-C (Table 6.30) show that the code positions are of lower quality than for CHAMP (in 2002). This could be an explanation for the larger differences between the solutions using CODE Rapid products and the solutions using CODE Final products for SAC-C than for CHAMP. Differences in the quality of the code positions with (cII3e) and without (cII3) elevation-dependent weighting cannot be identified for SAC-C. For this example, the solution without elevation-dependent weighting even seems to compare better with the other orbits than the solution with elevation-dependent weighting.

The orbit results of the programs LEOKIN and SATORB are for CHAMP and SAC-C of good quality. Even reduced-dynamic orbits generated with code positions only (cIS, cIIS, and cIISe) have an accuracy of half a meter or better. Comparisons with an external solution (TUM) have shown that the final kinematic (PB3, PB3e) and reduced-dynamic orbit solutions (P3S, P3Se) of our procedures have an accuracy of the order of a decimeter.

6.5 Use of Different Gravity Field Models for the Reduced-dynamic Orbit Modeling

The LEO satellites are orbiting in an altitude where the modeling of the forces due to high degree and order terms of the gravity field is important (Table 5.2). There are many different Earth gravity field models available. They differ (among other) in the maximum order and degree of the coefficients and the data used for generating the model.

Until recently the accuracy of the higher order terms of the available models were not sufficient to model the gravitational forces acting on a satellite at CHAMP's altitude with high precision. Since gravity models are available using also CHAMP data for the computation of the coefficients (TEG-4, and EIGEN-1S) the situation has improved and the new models represent the gravity field experienced by CHAMP much better than the older gravity models.

Subsequently we study the impact of gravity models by determining dynamic and reduced-dynamic orbits with program SATORB.

A first pure dynamic solution is generated using the following parametrization in program SATORB:

- six initial conditions (osculating elements),
- nine empirical (three constant and six once-per-revolution) parameters in RSW-directions, and
- scaling factors for atmospheric drag and direct Solar radiation pressure.

In order to solve for the latter scale factors, the a priori models for atmospheric drag and direct radiation pressure have to be turned on.

A second reduced-dynamic solution is performed using the following options:

- six initial conditions (osculating elements),
- three constant parameters in RSW-directions,
- pseudo-stochastic pulses (velocity changes) every 20 minutes in three orthogonal directions (RSW) constrained to zero with a standard deviation of 10 mm/s.

The a priori force model is the same in both cases. Eight iterations were performed to determine the orbits in order to make sure that full convergence was reached. The two types of orbits are determined using either of the five following Earth gravity field models:

- JGM3 (70x70) [*Tapley et al.*, 1996],
- EGM96 (120x120) [*Lemoine et al.*, 1998],
- GRIM5-S1 (120x120) [*Biancale et al.*, 2000],
- TEG-4 (120x120) [*Tapley et al.*, 2000], and
- EIGEN-1S (120x120) [*Reigber et al.*, 2002].

The last two models include CHAMP data. We use two different types of pseudo-observations for the orbit generation in SATORB (see Section 5.1). First we use the combined positions of FPB3e from doy 065 to 068/2002 as input for program SATORB. The second type are the code positions and phase position-differences from the same kinematic solution in LEOKIN. In the latter case we have, therefore, two independent pseudo-observation types in SATORB.

Table 6.31: RMS error (m) per satellite coordinate of orbit determination in SATORB.

		SAC-C		CHAMP	
Model	DOY	Dynamic	Pulses	Dynamic	Pulses
JGM3	065	1.29	0.11	1.94	0.06
	066	0.38	0.07	1.76	0.06
	067	0.31	0.06	2.80	0.06
	068	1.61	0.06	1.86	0.06
EGM96	065	1.32	0.11	1.62	0.05
	066	0.38	0.07	1.62	0.05
	067	0.32	0.06	2.27	0.05
	068	1.63	0.06	1.62	0.05
GRIM5-S1	065	1.31	0.11	3.08	0.08
	066	0.34	0.07	2.74	0.08
	067	0.29	0.06	3.67	0.08
	068	1.56	0.06	2.31	0.07
TEG-4	065	1.32	0.11	0.74	0.04
	066	0.34	0.07	1.25	0.03
	067	0.28	0.06	1.39	0.03
	068	1.58	0.06	0.68	0.03
EIGEN-1S	065	1.28	0.11	0.78	0.04
	066	0.33	0.07	1.31	0.03
	067	0.30	0.06	1.54	0.03
	068	1.56	0.06	0.72	0.03

6.5.1 Combined Positions as Pseudo-observations

Table 6.31 summarizes the RMS errors per coordinate of the orbit determination using the combined positions in SATORB. Figure 6.86 shows the values of the estimated stochastic pulses for the different solutions for SAC-C on doy 065/2002. Figure 6.87 shows the same information for CHAMP on the same day.

The RMS errors in Table 6.31 tell that different gravity fields have no significant effect on the orbit representation for SAC-C, which is orbiting at a height of about 700 km. For days 065 and 068 the RMS errors of the pure dynamic solution is four to five times larger than the values on the two middle days 066 and 067, which may be due to data problems. For the solutions containing stochastic pulses every 20 minutes the RMS errors are the same for each gravity field model. The stochastic pulses in Figure 6.86 are very similar for the five gravity models considered.

The situation is different for CHAMP. The RMS errors for the dynamic solutions are different for the five gravity models used. With the models TEG-4 and EIGEN-1S the best fit is achieved for the four days. This is an expected result because the models include CHAMP data. The GRIM-S1 model shows the worst performance. Even the JGM3 model which provides coefficients only up to degree and order 70, gives better orbit results. The orbit quality achieved with stochastic pulses show differences related to the gravity models, as well. The models TEG-4 and EIGEN-1S show the best and the GRIM5-S1 model shows the worst RMS errors. The values for the stochastic pulses are different for the five gravity models (Figure 6.87). It can be seen very clearly that for the two models TEG-4 and EIGEN-1S the pulses

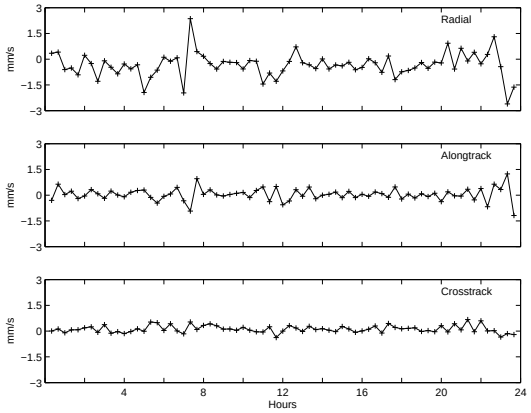

(a) JGM3.

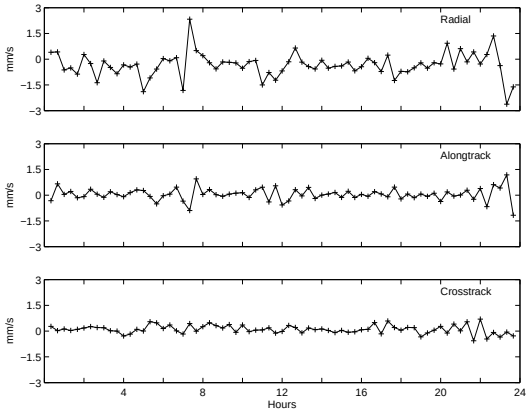

(b) EGM96.

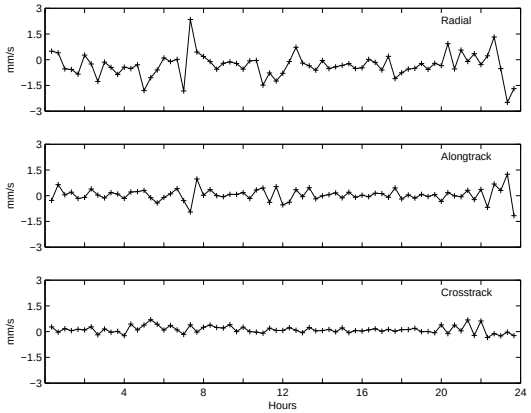

(c) GRIM5-S1.

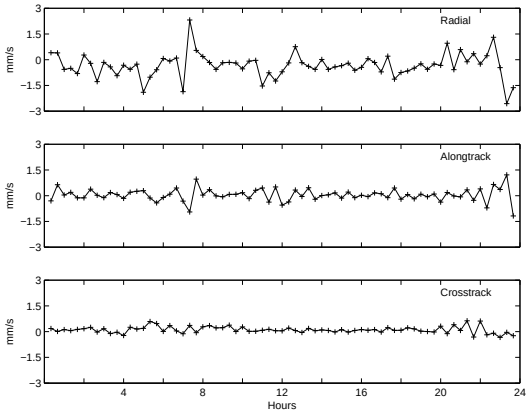

(d) TEG-4.

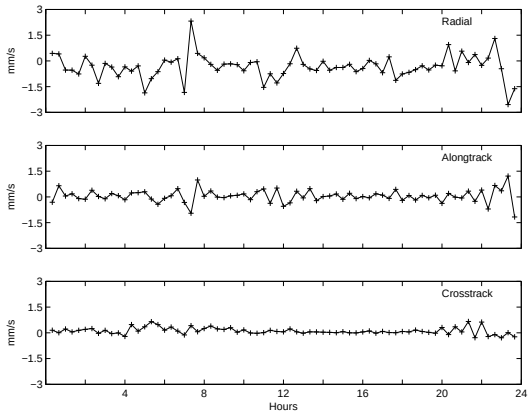

(e) EIGEN-1S.

Figure 6.86: Stochastic pulses estimated based on combined positions and different a priori gravity fields, SAC-C, doy 065/2002.

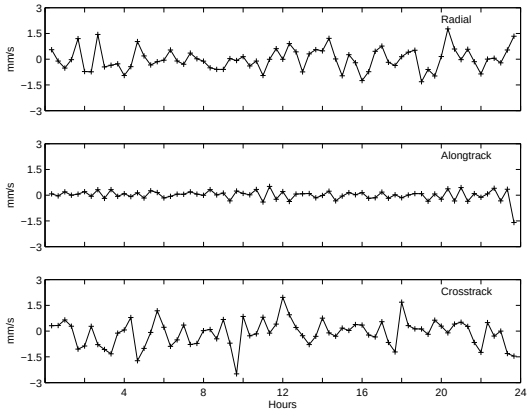

(a) JGM3.

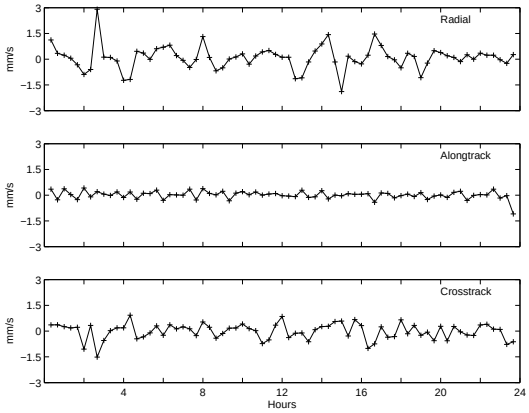

(b) EGM96.

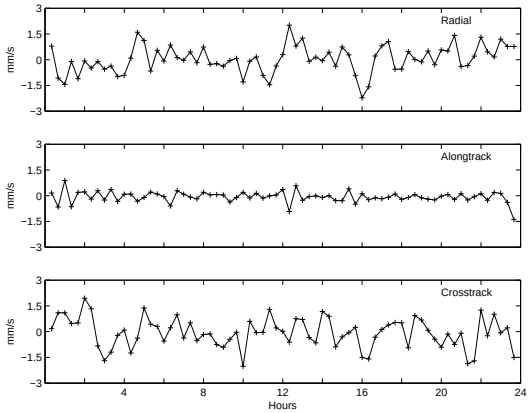

(c) GRIM-S1.

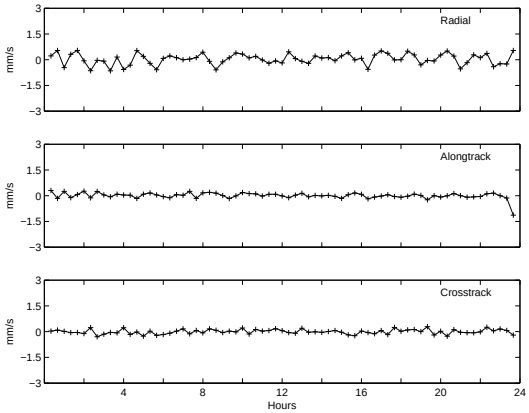

(d) TEG-4.

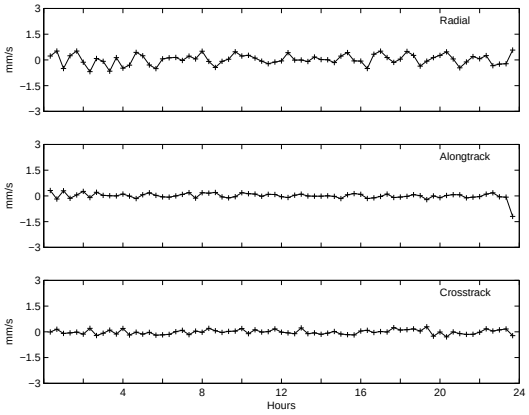

(e) EIGEN-1S.

Figure 6.87: Stochastic pulses estimated based on combined positions and different a priori gravity fields, CHAMP, doy 065/2002.

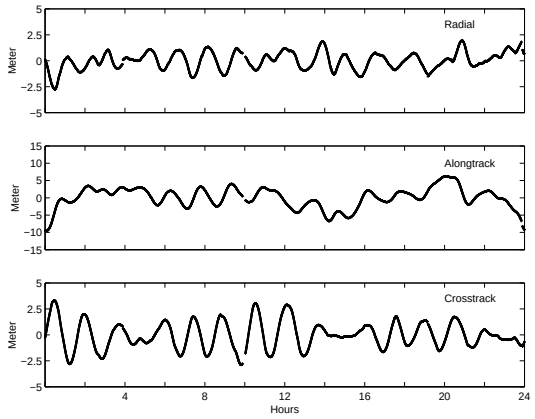

(a) JGM3.

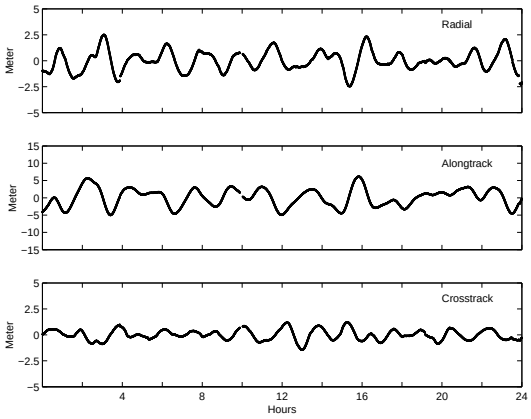

(b) EGM96.

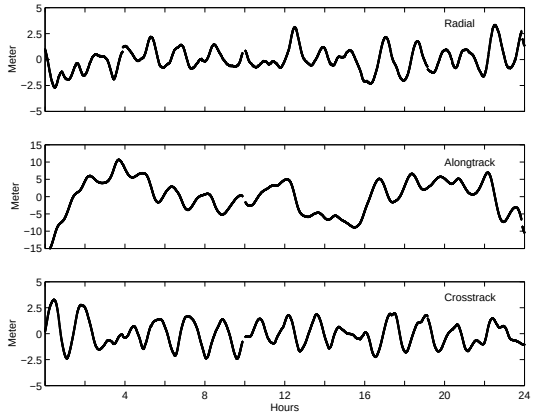

(c) GRIM-S1.

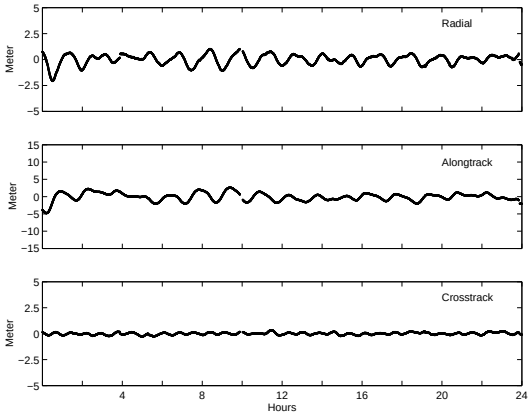

(d) TEG-4.

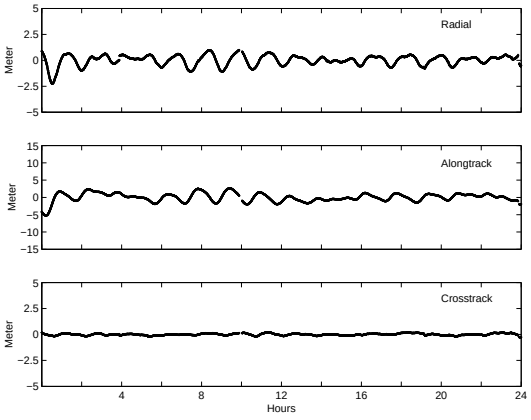

(e) EIGEN-1S.

Figure 6.88: Residuals of purely deterministic orbit determination, CHAMP, doy 065/2002.

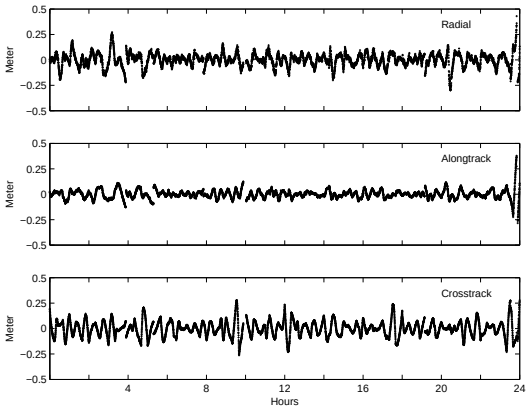

(a) JGM3.

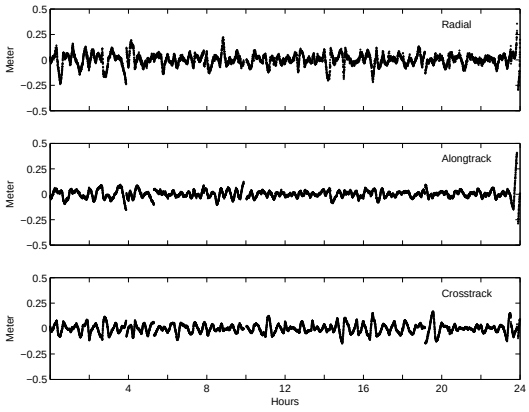

(b) EGM96.

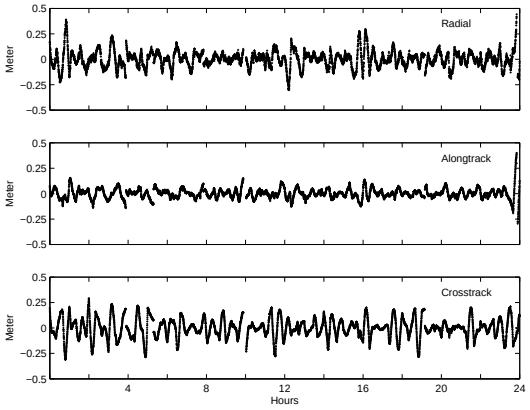

(c) GRIM-S1.

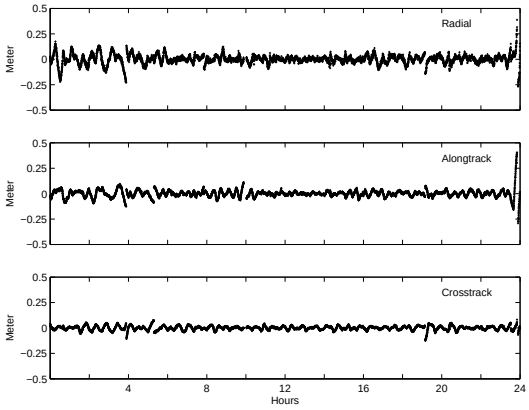

(d) TEG-4.

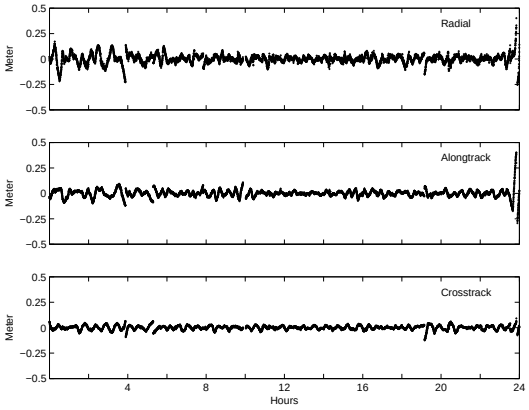

(e) EIGEN-1S.

Figure 6.89: Residuals of orbit determination including stochastic pulses, CHAMP, doy 065/2002.

are smallest. The largest pulses may be found for the models GRIM5-S1 and JGM3. Interestingly, the biggest differences may be recognized in the values for the crosstrack pulses. The crosstrack pulses are close to zero for TEG-4 and EIGEN-1S. For each of the three other models the crosstrack pulses show a different pattern.

Figure 6.88 shows the residuals of the five deterministic orbit determinations for doy 065 for CHAMP, Figure 6.89 those of the reduced-dynamic orbit determinations including stochastic pulses. In Figure 6.88 the residuals lie within -5 m to 5 m for the radial and crosstrack directions, for the alongtrack directions a range of -15 m to 15 m is covered. In Figure 6.89 all residuals lie within -0.5 m to 0.5 m. The residuals underline our findings from Table 6.31 and Figure 6.87. The models TEG-4 and EIGEN-1S are best suited to model the orbit of CHAMP.

In the case of SAC-C, orbiting about 300 km above CHAMP, the differences between the gravity models are hardly noticeable implying that all gravity models considered are sufficient for orbit modeling (for our purpose).

Signals in the residuals of the deterministic orbit determination for SAC-C stem mainly from data problems (jumps in the combined positions) and the insufficient modeling of the non-gravitational forces. In the case of CHAMP it is a mixture of all, data problems, insufficient modeling of the non-gravitational forces, and insufficient modeling of the gravity field of the Earth.

6.5.2 Code Positions and Phase Position-differences as Pseudo-observations

Orbits for the four days (065 to 068/2002) were also derived using the code positions and phase position-differences as independent observation types in SATORB. The options and parameters are the same as in the solution using stochastic pulses described above.

The RMS errors per coordinate of the orbit determination process cannot directly be compared to the RMS errors when using combined positions because we have two different observation types with two different RMS errors for these analyses. One refers to the code positions and the other to the phase-derived position-differences. Residuals may not be compared due to the same reason. Therefore, we focus on the estimated values of the stochastic pulses. Figure 6.90 shows them for SAC-C, doy 065/2002, and Figure 6.91 for CHAMP, doy 065/2002.

For SAC-C we confine ourselves to showing only the values of the stochastic pulses for the solution using the GRIM5-S1 model. The values are very similar for the other four gravity models considered. The characteristics of the pulses are different from those related to the combined positions (compare Figures 6.90 and 6.86). Their values are on average larger in the case of using combined positions. The differences are mainly due to the jumps in the kinematic trajectories when using combined positions. In the case of using positions and position-differences such problems do not show up in the pseudo-observations and therefore the stochastic pulses do not have to account for them. In this case the stochastic pulses mainly have to compensate for the insufficient modeling of the non-gravitational forces.

For CHAMP the absolute values of the stochastic pulses are slightly smaller when using code positions and phase position-differences independently as pseudo-observations. The characteristics of the pulses are similar to that of the orbit fits using combined positions. These facts confirm the above conclusion that in the case of CHAMP the stochastic pulses compensate data problems, insufficient modeling of the non-gravitational forces, and insufficient modeling of the gravity field of the Earth. Data problems do not influence significantly the estimated pulses.

Figure 6.92 shows the resulting orbit differences (residuals of Helmert transformation with three translation parameters) using the two types of pseudo-observations. The orbit differences refer to orbits

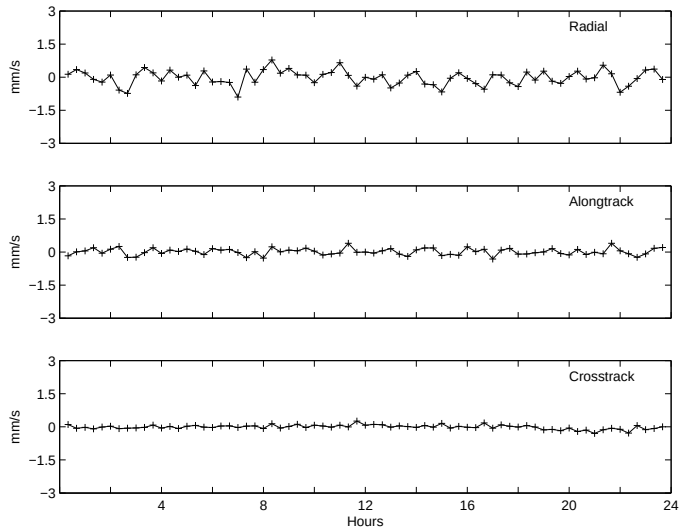

Figure 6.90: Stochastic pulses from orbit determination with gravity model GRIM5-S1 using code positions and phase position-differences, SAC-C, doy 065/2002.

determined using the gravity field model GRIM5-S1.

The orbit differences are of the same order of magnitude for both satellites, indicating that the combined positions show data problems (jumps) due to the interrupts (25 in the case of SAC-C and 6 in the case of CHAMP) and the resulting short sequences of connected positions. If we use the code positions and phase position-differences independently from each other as pseudo-observations in SATORB problems due to unconnected phase position-differences do not show up.

Figure 6.93 shows the differences between orbits from the orbit fit using the GRIM5-S1 model on one side and using the TEG-4 model on the other side. These are reduced-dynamic orbits derived from code positions and phase position-differences. The differences for SAC-C (Figure 6.93(a)) are small ($<$ 10 cm). The force model used in SATORB seems to be adequate for the SAC-C satellite. The differences for CHAMP (Figure 6.93(b)) are larger but they show similar characteristics as the differences between the two different orbits derived with the GRIM5-S1 model (Figure 6.92(b)). Figure 6.94 shows the orbit differences between the orbit generated with combined positions using the GRIM5-S1 model and the orbit generated with positions and position-differences using the TEG-4 model. Interestingly, these differences are significantly smaller than those in Figures 6.92(b) and 6.93(b). This indicates that the orbit generated with combined positions represents the true trajectory of the satellite better than an orbit based on positions and position-differences, if a bad gravity field model is used (GRIM5-S1 instead of TEG-4). The reason is that the combined positions are computed in LEOKIN without using any model information. They therefore represent the satellite trajectory according to the "true" gravity field. Positions and position-differences are, on the other hand, combined in SATORB based on the physical orbit model (which is in this case not perfect due to the bad gravity field model GRIM5-S1).

Table 6.32 summarizes the RMS errors for these comparisons for the four days considered. The RMS errors are similar for the different comparisons for each of the four days. The column denoted A represents the differences shown in Figure 6.92, column B those from Figure 6.93, and column C those from Figure 6.94. For SAC-C the differences between the reduced-dynamic orbits generated with positions and position-differences and either the GRIM5-S1 or the TEG-4 model are the smallest (column

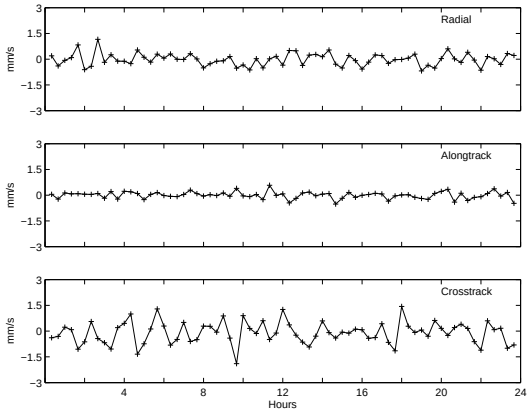

(a) JGM3.

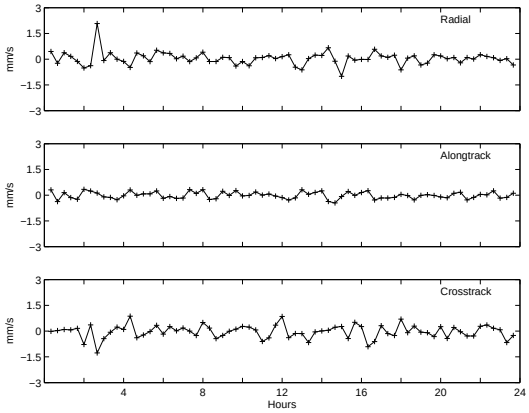

(b) EGM96.

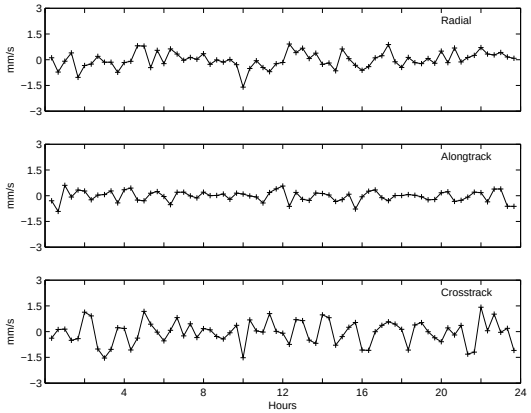

(c) GRIM5-S1.

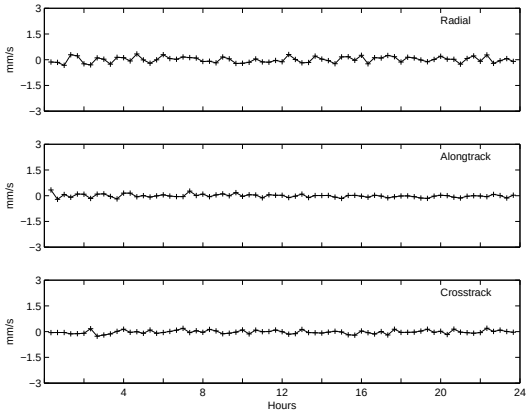

(d) TEG-4.

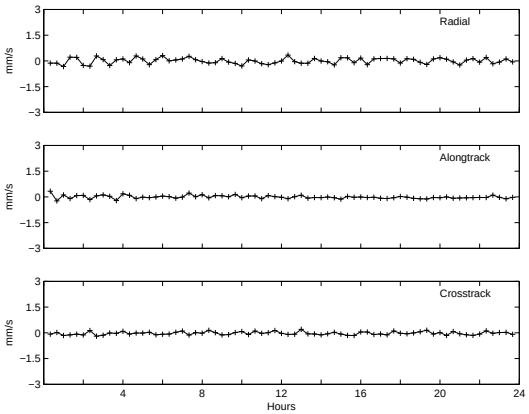

(e) EIGEN-1S.

Figure 6.91: Values for the stochastic pulses for different orbit fits using code positions and phase position-differences in SATORB, CHAMP, doy 065/2002.

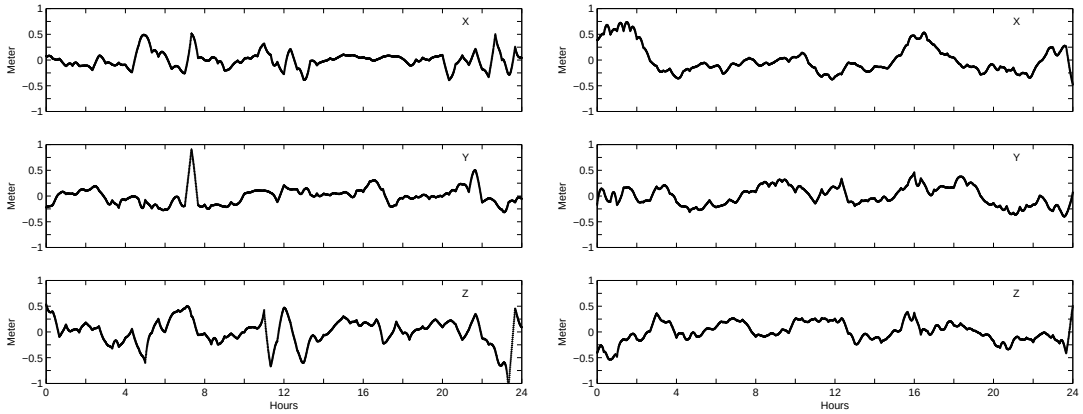

(a) SAC-C, doy 065/2002, RMS 0.19 m.

(b) CHAMP, doy 065/2002, RMS 0.21 m.

Figure 6.92: Orbit differences when using either combined positions or positions and position-differences, GRIM5-S1 model, reduced-dynamic orbits, CHAMP, doy 065/2002.

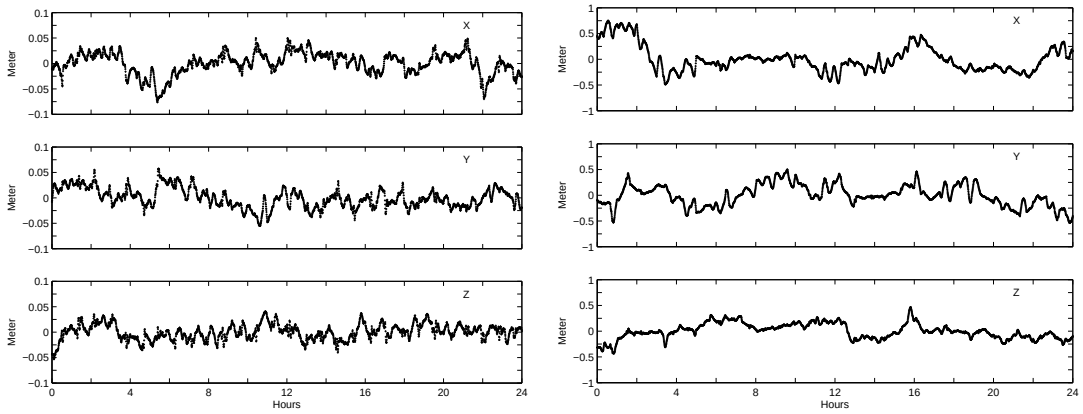

(a) SAC-C, doy 065/2002, RMS 0.02 m.

(b) CHAMP, doy 065/2002, RMS 0.21 m.

Figure 6.93: Orbit differences when using either the GRIM5-S1 model or the TEG-4 model, positions and position-differences, reduced-dynamic orbits, CHAMP, doy 065/2002.

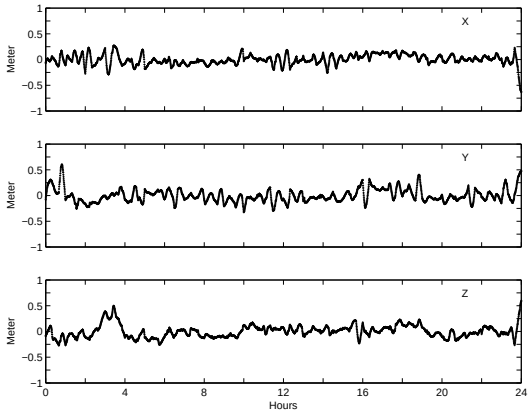

Figure 6.94: Orbit differences when using either combined positions with GRIM5-S1 model or positions and position-differences with TEG-4 model, CHAMP, doy 065/2002, RMS 0.12 m.

Table 6.32: RMS errors (m) of Helmert transformation between reduced-dynamic orbits from different orbit determinations; A: GRIM5-S1, combined positions vs. positions and position-differences, B: positions and position differences, GRIM5-S1 vs. TEG-4, C: combined positions, GRIM5-S1 vs. positions and position-differences, TEG-4.

Satellite	Doy	A	B	C
SAC-C	065	0.19	0.02	0.19
	066	0.14	0.02	0.15
	067	0.13	0.02	0.13
	068	0.15	0.02	0.15
CHAMP	065	0.21	0.21	0.12
	066	0.18	0.20	0.10
	067	0.20	0.19	0.11
	068	0.23	0.23	0.10

B) which was expected due to the finding that the gravity field model is not important for the reduced-dynamic orbit modeling for SAC-C. In the case of CHAMP the differences between the reduced-dynamic orbits generated with combined positions and the GRIM5-S1 model and the orbits generated with positions and position-differences and the TEG-4 model (column C) are the smallest. The reason for this is explained above.

These tests show that the use of different gravity field models may have a considerable impact on the resulting orbit from SATORB depending on the satellite considered. For SAC-C, a LEO orbiting at a height of 702 km, the impact is hardly noticeable. For CHAMP, which is orbiting at a height of about 400 km, the influence of the gravity field is considerable and we should not use the gravity models generated without CHAMP data for the dynamic orbit modeling. Even when setting up a modest number of stochastic pulses at pre-defined epochs, the insufficiencies of “older” gravity models cannot be completely absorbed.

6.6 Stochastic Pulses and Accelerometer Measurements

In Section 5.4 we introduced the measurements stemming from the CHAMP accelerometer. The specific instrument type is used for the first time on-board CHAMP. It is also used by the GRACE satellites, now. The measurements may be used in the dynamical orbit determination process to replace the models for the non-gravitational forces, but the accelerometer measurements have to be calibrated. The calibration parameters (biases and scale factors, see eqn. (5.7)) are made available to the user community of the CHAMP data [*Perosanz et al.*, 2003]. The calibration parameters are frequently improved due to better calibration strategies. In our tests (in the dynamical orbit determination process) we tried to estimate these calibration parameters with the program SATORB and compared the estimates with those officially available.

Maneuver information is also available for CHAMP. The attitude maneuvers are not performed at pre-defined epochs and therefore the epochs and durations are made available to the users of the CHAMP data. We generate different solutions with SATORB in order to study two different issues, namely

- the impact of using the accelerometer measurements and of estimating their biases and scale factors and
- the impact of setting up stochastic pulses at pre-defined equidistant epochs or at the maneuver epochs.

For all tests we use the same kinematic solutions for doy 065 to 068/2002 as in Section 6.5 (FPB3e, APO set P, solution B, $\beta = 3$, elevation-dependent weighting) as input for program SATORB.

First we generate a solution *ref* for all four days which does not use the accelerometer measurements in order to have a reference for the following solutions. The options for this solution are:

- gravity field model EIGEN-1S 120x120,
- Estimation of
  - six osculating elements,
  - nine empirical parameters (three constant, six periodic) in RSW-directions,
  - scaling factor for atmospheric drag, and
  - scaling factor for direct radiation pressure.

Two arcs of twelve hours were formed and the parameters were estimated per arc. The orbit was established in eight iteration steps. The general options for the orbit solutions using the accelerometer measurements are:

- gravity field model EIGEN-1S 120x120,
- Estimation of
  - six osculating elements,
  - three biases $b(i), i = 1, 2, 3$ (eqn. (5.7)) for the accelerometer measurements,

As opposed to the first run no a priori models for atmospheric drag and direct radiation pressure were used; the accelerometer data were introduced instead. Again, two arcs of twelve hours were established in eight iteration steps with the parameters estimated per arc. Based on these general options we generate different reduced-dynamic orbits with the following additional options:

- Solution 1:
  - Estimation of six periodic parameters in RSW-directions.
- Solution 2:
  - Estimation of six periodic parameters in RSW-directions and set up of stochastic pulses in RSW-directions every 90 minutes.
- Solution 3:
  - Set up of stochastic pulses in RSW-directions every 20 minutes.
- Solution 4:
  - Estimation of six periodic parameters in RSW-directions and set up of stochastic pulses in RSW-directions at epochs where attitude maneuvers took place with a duration longer than 0.5 seconds.

The scale factors for the accelerometer measurements are set to one ($a(i) = 1, i = 1, 2, 3$) for these solutions.

For the following two solutions we introduced the values for the accelerometer biases published together with the accelerometer data as known into the orbit generation process.

- Solution 5:
  - Estimation of
    - six periodic parameters in RSW-directions and
    - the three scale factors $a(i), i = 1, 2, 3$ (eqn. (5.7)) for the accelerometer measurements per arc.
- Solution 6:
  - Estimation of
    - six periodic parameters in RSW-directions and
    - the three scale factors $a(i), i = 1, 2, 3$ for the accelerometer measurements per arc,
  - set up of stochastic pulses in RSW-directions every 90 minutes.

We estimate only the six periodic parameters in RSW-directions because the constant parameters in the RSW-directions are fully correlated with the biases of the accelerometer measurements. The 24 hours are split up into two twelve-hours arcs in order to have more independent estimations available for the biases and scale factors. Table 6.33 gives a summary of the different options for the reduced-dynamic orbit solutions.

Figure 6.95 shows the RMS errors per coordinate for the solution *ref* and solution 1 for the four days considered. Each day is represented by two bars. The left bar corresponds to the first twelve-hours-arc and the right bar to the second one. It can be seen that the reference solutions *ref* using the models for the non-gravitational forces have an RMS at least two times higher than solutions 1 using the accelerometer measurements. This shows that the models presently used in SATORB are not good enough to represent the non-gravitational forces acting on the CHAMP satellite. The use of the accelerometer measurements considerably improves the dynamic orbit modeling for CHAMP.

Table 6.33: Summary of options for different reduced-dynamic orbit solutions.

	Six osculat. elements	Empirical param.		Scale factor		Accelerometer data		Stoch. pulses
		const.	period.	atm. drag	rad. press.	scal.fact.	biases	
ref	yes	yes	yes	yes	yes	no	no	no
1	yes	no	yes	no	no	no	yes	no
2	yes	no	yes	no	no	no	yes	90 min
3	yes	no	no	no	no	no	yes	20 min
4	yes	no	yes	no	no	no	yes	maneuver
5	yes	no	yes	no	no	yes	yes	no
6	yes	no	yes	no	no	yes	yes	90 min

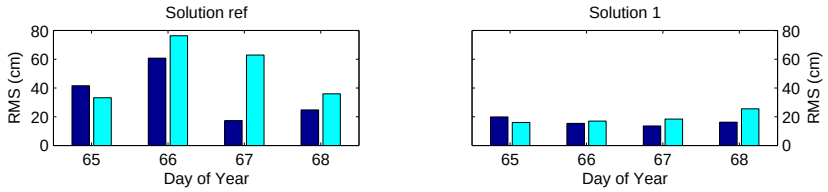

Figure 6.95: RMS errors (cm) per coordinate of the orbit determination in SATORB for the solutions *ref* and 1.

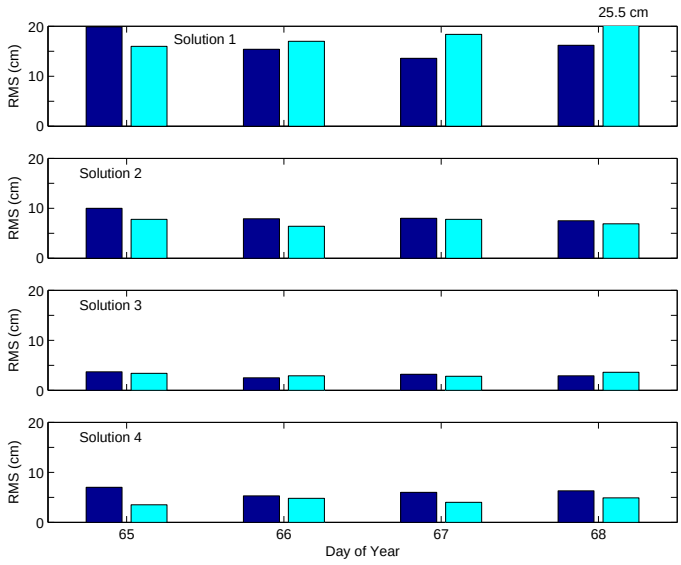

Figure 6.96: RMS errors (cm) per coordinate of the orbit determination in SATORB for solutions 1 to 4.

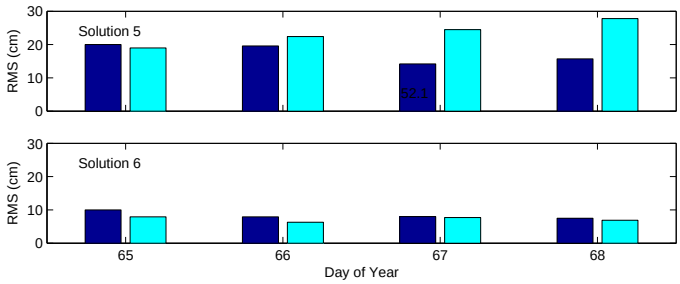

Figure 6.97: RMS errors (cm) per coordinate of the orbit determination in SATORB for solutions 5 and 6.

Figure 6.96 shows the RMS errors per coordinate of the orbit determinations in SATORB for solutions 1 to 4. Solution 1 is the only solution containing no stochastic pulses. For solution 2 stochastic pulses are estimated at 90 minutes intervals. As expected, solutions 1 are of lower quality than solutions 2, 3, and 4, which promise to be of an accuracy clearly below the five centimeter level.

Biases and Scale Factors for the Accelerometer Measurements

Figure 6.98 shows the estimated biases $b(i)$ of the accelerometer measurements in the three directions R, S, W (radial, alongtrack, and crosstrack) for solutions 1 to 4. The estimates are given together with their one sigma error bars. The horizontal lines in the figures represent the official values distributed together with the accelerometer data. The estimates have small errors. The estimated biases are of the same order of magnitude as the official values but they do not directly confirm these values.

For solutions 5 and 6 we introduced the official values for the biases into the orbit generation process and estimated the scale factors for the accelerometer measurements. We do not estimate the biases and scale factors together because these parameters are highly correlated.

Figure 6.97 shows the RMS errors per coordinate of the orbit determination. As expected, solutions 5 are of lower quality than solutions 6. The RMS errors for solutions 5 are comparable with those of solutions 1 and the values for solution 6 with those of solution 2. One would expect a slightly better solution by introducing the accelerometer biases as known and estimating the scale factors. The estimated values for the scale factors (Figure 6.99) show in the case of the alongtrack and the crosstrack component a bad agreement with the official values (horizontal lines in the plots). The scale factor of the radial component shows the best agreement.

The calibration of the biases and the scale factors is not a trivial task. The methods used to do it are described in [*Perosanz et al.*, 2003]. Longer data series have to be considered and correlations with other parameters such as, e.g., pseudo-stochastic pulses or empirical parameters, need to be minimized.

It seems problematic to determine the calibration parameters for the accelerometer measurements in SATORB (despite the fact that this is technically possible). A significant effort would be needed to develop strategies to reliably estimate these parameters. We should be able to use the officially available calibration values without further improvement in the dynamical orbit determination procedure. We have seen that the introduction of accelerometer measurements into the dynamical orbit procedure improves the dynamical orbit. If we perform a reduced-dynamic modeling using stochastic pulses it does not matter whether we use the models or the accelerometer measurements because the pulses compensate problems stemming from data problems, insufficient modeling of the forces acting on the satellite, or possible insufficiencies in the accelerometer data. One should mention, however, that only few pseudo-stochastic

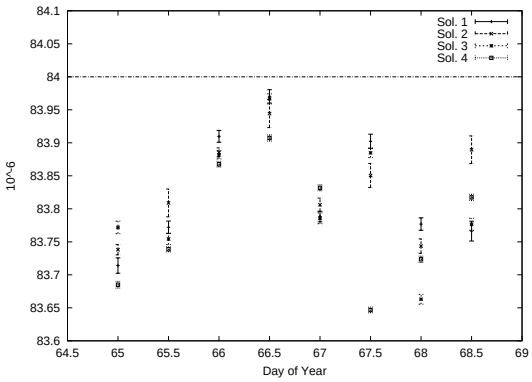

(a) Radial direction.

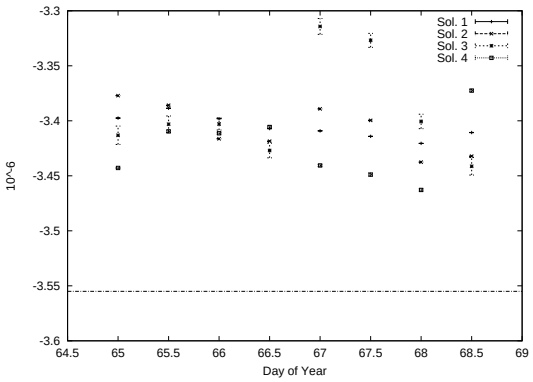

(b) Alongtrack direction.

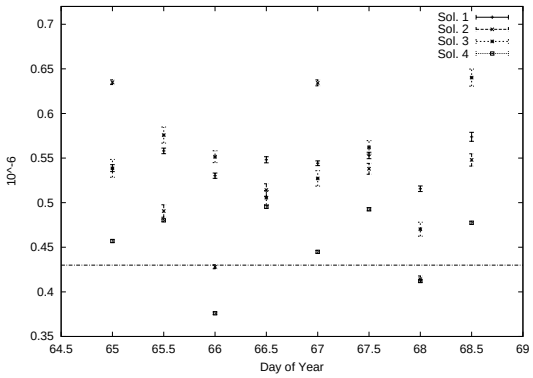

(c) Crosstrack direction.

Figure 6.98: Estimated biases $b(i)$ with error bars for solutions 1, 2, 3, and 4 (the horizontal line represents the published value).

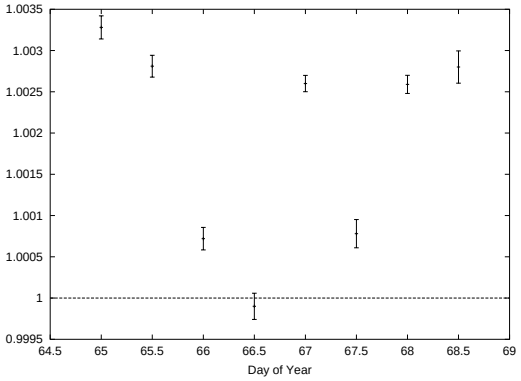

(a) Radial scale factors, solution 5.

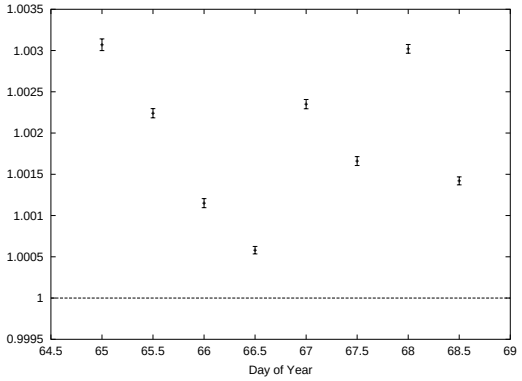

(b) Radial scale factors, solution 6.

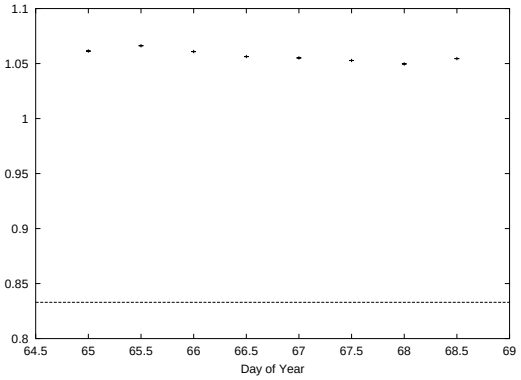

(c) Alongtrack scale factors, solution 5.

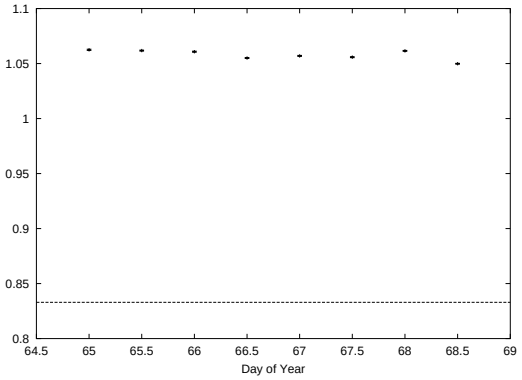

(d) Alongtrack scale factors, solution 6.

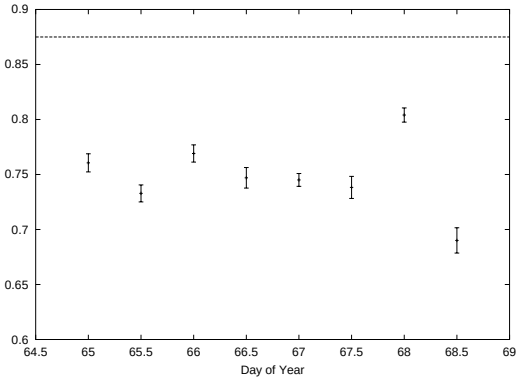

(e) Crosstrack scale factors, solution 5.

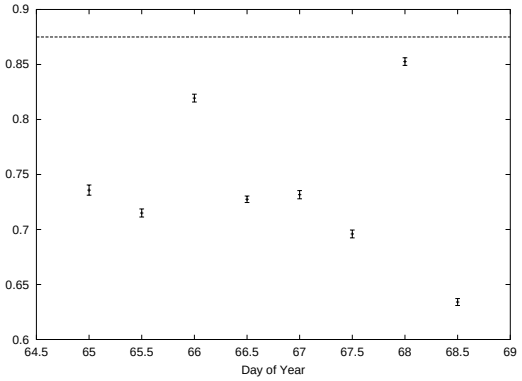

(f) Crosstrack scale factors, solution 6.

Figure 6.99: Estimated scale factors $a(i)$ with error bars for solutions 5 and 6 (the horizontal line represents the published value).

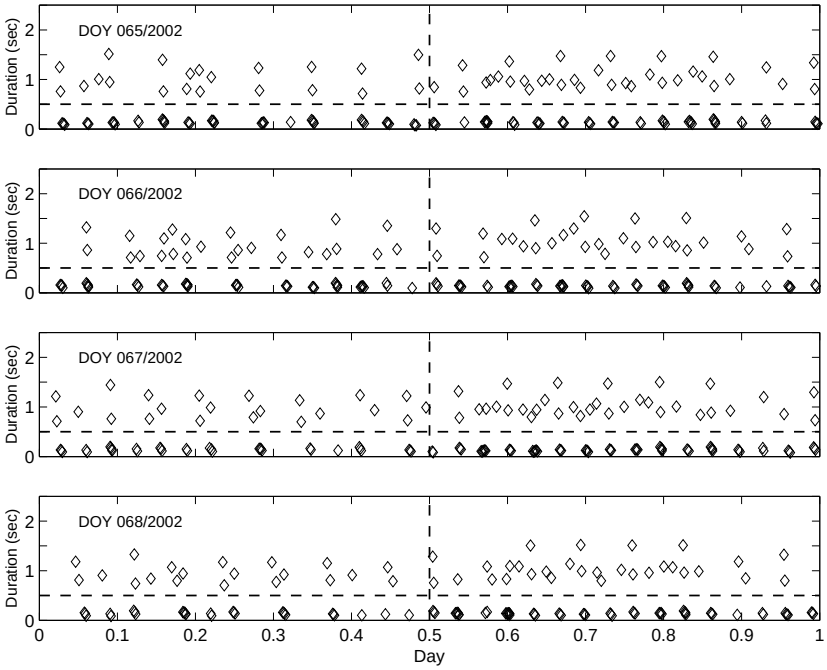

Figure 6.100: Maneuvers performed by CHAMP for days 065 to 068/2002.

Table 6.34: Number of epochs, where stochastic pulses in RSW-directions are set up.

	Day of Year							
	065		066		067		068	
Sol. 2	7	7	7	7	7	7	7	7
Sol. 3	35	35	35	35	35	35	35	35
Sol. 4	21	34	25	29	22	33	20	30

pulses have to be set up when using the accelerometer data.

Stochastic Pulses at pre-defined Intervals or at Maneuver Epochs

What is the effect of different set-up strategies for pseudo-stochastic pulses? Obviously we have to focus on the solution types 2, 3, and 4 to answer this question. Table 6.34 lists the number of epochs per arc with stochastic pulses in the RSW-directions. Note that the number of epochs with maneuvers in solutions 4 is smaller than the number of epochs with pulses in solution 3.

Figure 6.100 shows the duration of the attitude maneuvers performed for CHAMP in the four days considered. There are many maneuvers for which no stochastic pulses were set up because the duration of these maneuvers was shorter than 0.5 seconds. These are mainly small correction maneuvers for iteratively reaching the nominal attitude following a main maneuver. We only set up pulses for the maneuvers with a duration longer than 0.5 seconds.

Figure 6.96 shows that the RMS errors for solutions 4 are larger than those for solutions 3. This is not surprising because for solutions 4 less stochastic pulses are set up.

Figures 6.101 and 6.102 show the values for the stochastic pulses estimated for solutions 2 to 4 for

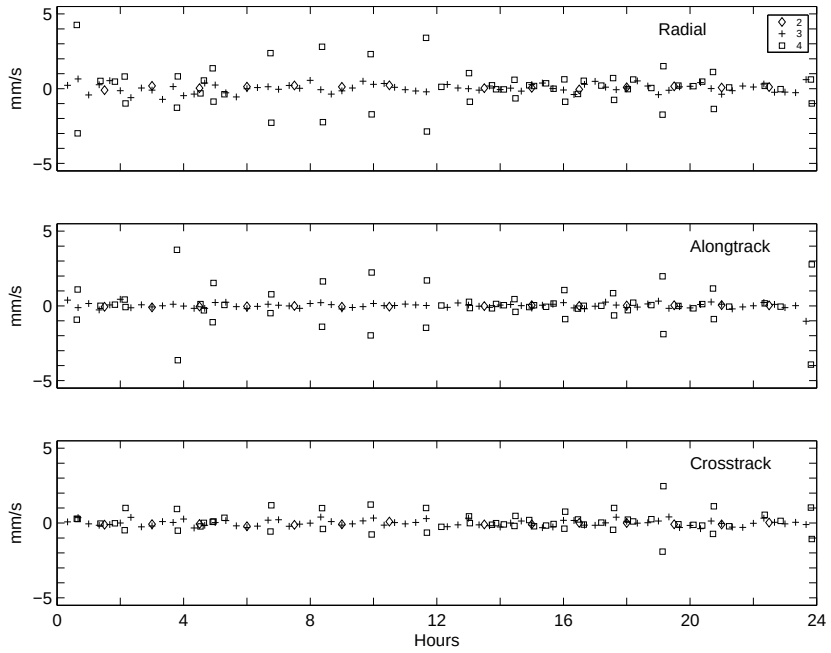

(a) Doy 065/2002.

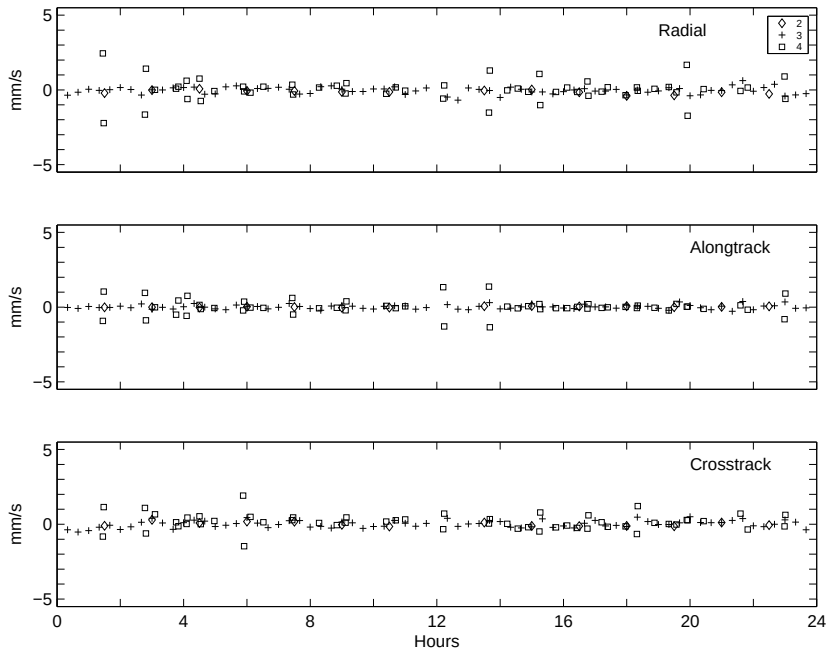

(b) Doy 066/2002.

Figure 6.101: Estimated stochastic pulses in solutions 2, 3, and 4 for doy 065 and 066/2002.

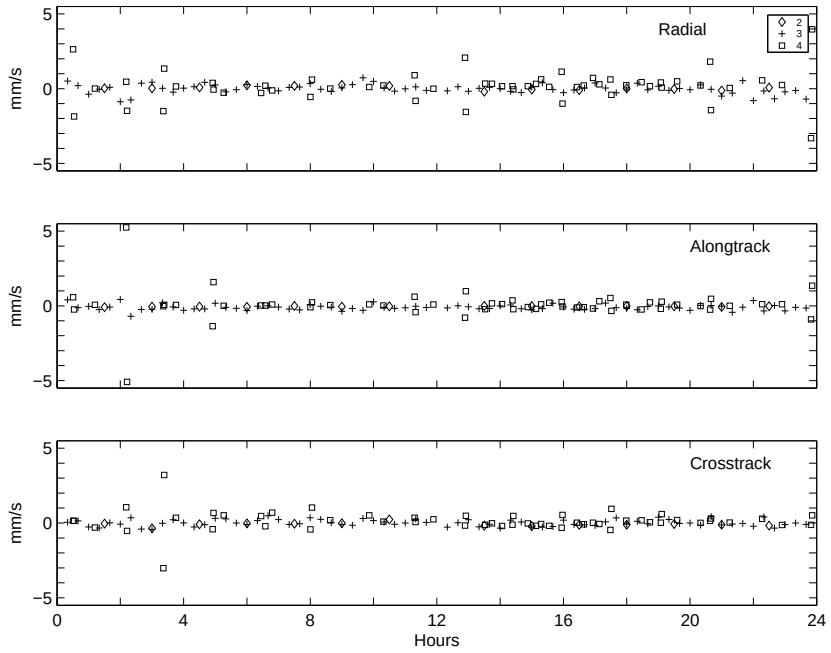

(a) Doy 067/2002.

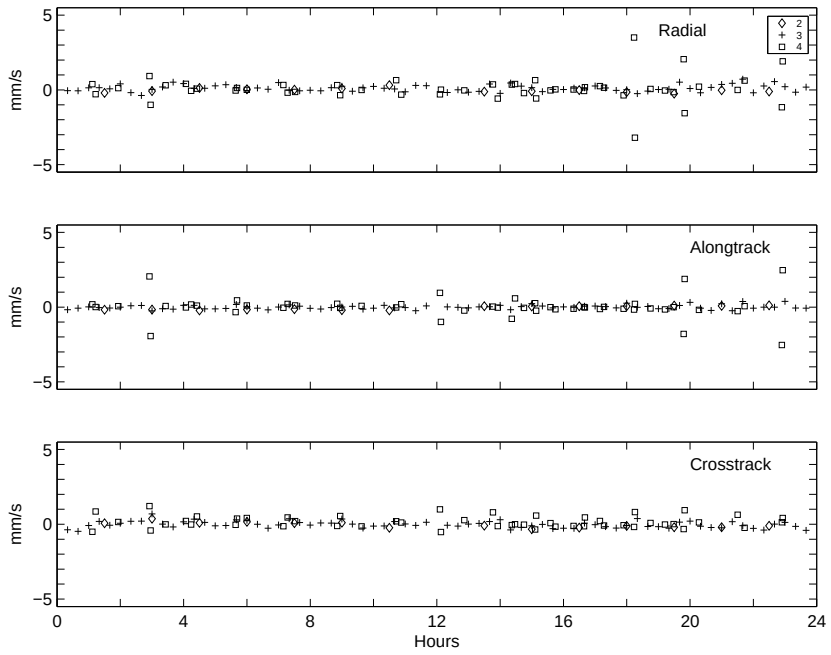

(b) Doy 068/2002.

Figure 6.102: Estimated stochastic pulses in solutions 2, 3, and 4 for doy 067 and 068/2002.

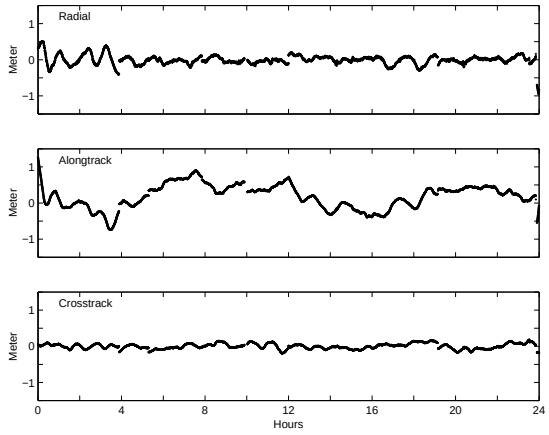

(a) Solution 1, without stochastic pulses.

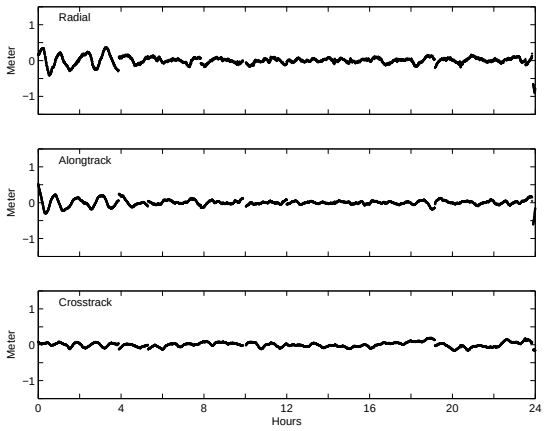

(b) Solution 2, stochastic pulses each 90 minutes.

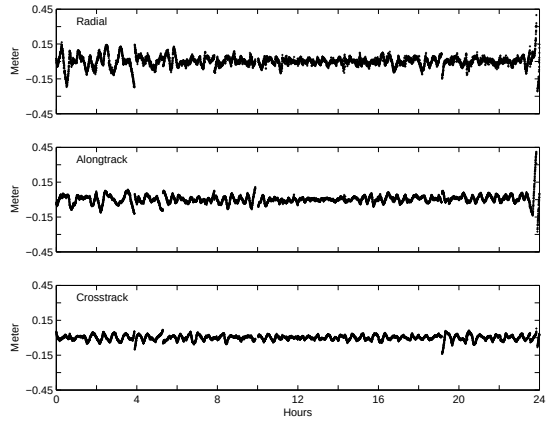

(c) Solution 3, stochastic pulses each 20 minutes.

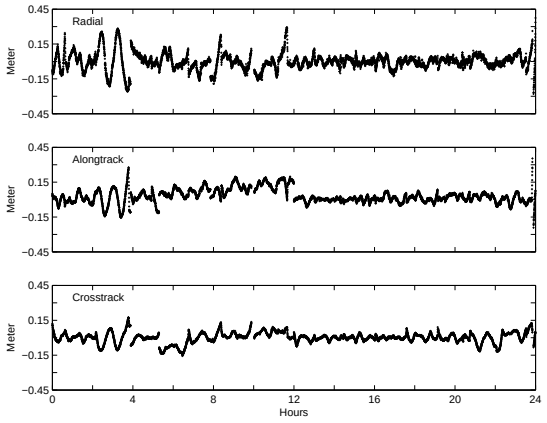

(d) Solution 4, stochastic pulses at epochs with maneuvers.

Figure 6.103: Residuals for solutions 1, 2, 3, and 4 for doy 065.

the four days considered. The pulses for solutions 4 are often following each other within a short time interval due to a rapid sequence of maneuvers (Figure 6.100). The pulses are then in most cases of the same size but of opposite direction, which means that they are compensating each other. Due to the high correlation between a pair of adjacent pulses, the absolute values of such a pair may become unreasonably large. The pulses for the two other solution types are smaller than one millimeter per second. Figure 6.101 and 6.102 indicate that it does not improve the orbits if we set up stochastic pulses at maneuver epochs. Better solutions are obtained by setting up pulses at regular time intervals.

Figure 6.103 shows the residuals of the kinematic positions used as pseudo-observations for the orbit generation in SATORB for solutions 1 to 4 for doy 065. The residuals for solution 1 show large variations in alongtrack direction which disappear in all other solutions due to the stochastic pulses.

The conclusion from these studies is that it is useful for the dynamic orbit determination process to use the measurements of the accelerometer instrument. It is possible to estimate the accelerometer biases and scale factors in the orbit generation procedure in SATORB. It is nevertheless not recommended to do this because it is a complex issue and not as simple (see [*Perosanz et al.*, 2003]). The official calibration parameters for the accelerometer measurements are made available together with the data themselves. These values are reliable and we should adopt them and introduce them in the orbit generation process, if we want to use the accelerometer measurements for the dynamic orbit modeling.

The pseudo-stochastic pulses should be set up at pre-defined time intervals. If we set them up at the maneuver epochs the time intervals between subsequent pulses are often too short. This causes mathematical correlation of these pulses leading to problematic results. The stochastic pulses do not only account for the small velocity changes provoked by the attitude maneuvers but also for problems in the combined positions. In order to compensate only for the small velocity changes from the attitude maneuvers, the stochastic pulses should be set up only in the directions defined by the maneuver (these directions are made available for the users, as well) and with a stronger constrain to zero (e.g., with a standard deviation of 0.01 mm/s). Data problems would, however, not be compensated by such pulses.

6.7 Data Screening Procedure for a Permanent Ground Network

6.7.1 Comparison with MAUPRP

In Section 4.4 we proposed a data screening procedure based on LEOKIN for a permanent ground network. This procedure is applied to a data set of the IGS station network and the results are compared with the data screening procedure performed on the same data set with the program MAUPRP used in the Bernese GPS Software.

Data set and Processing Options

GPS observation data from 175 IGS stations (30-second sampling) from doy 055 to 069/2002 serve as test data. Our analysis is based on

- the CODE Final GPS orbits,
- the ERPs of the CODE Final processing,
- 30-second clock corrections for the GPS satellites constrained to the CODE Final 5-minute clock corrections,
- troposphere zenith delays from the CODE Final processing, and

- station coordinates from the CODE Final processing.

The options for the pre-processing in LEOKIN are the following

- $\sigma_{c_{scr}} = 1.0$ m, $\sigma_{p_{scr}} = 0.014$ m.
- $\beta_c = 3$, $\beta_p = 20$ (see eqn. (4.6)).
- Minimum number of observations connected by one initial phase ambiguity parameter is set to 25.
- Maximum number of ambiguities is set to 300.

The options for pre-processing in the MAUPRP program correspond to those of LEOKIN as close as possible in order to ensure that both programs have the same basic conditions.

The observations of the terrestrial stations are independently pre-processed with both programs. The procedure related to LEOKIN is performed with the following programs of the Bernese GPS Software

- RXOBV3 - import RINEX [*Gurtner*, 1994] observation data to the Bernese GPS Software,
- LEOKIN - data screening of the observations, write a file with actions to do,
- SATMRK - mark the observations listed in the file generated by LEOKIN,
- CODSPP - synchronize the receiver clock to GPS time, and
- GPSEST - kinematic point positioning using the phase observations of the station processed.

The procedure related to MAUPRP is performed with the following programs of the Bernese GPS Software

- RXOBV3 - import RINEX observation data to the Bernese GPS Software,
- CODSPP - synchronize the receiver clock to GPS time,
- MAUPRP - data screening of the phase observations, and
- GPSEST - kinematic point positioning using the phase observations of the station processed.

Figures 6.104 and 6.105 show statistical results from LEOKIN and MAUPRP for eight stations arbitrarily selected as examples. The RMS errors (per coordinate) of the kinematic point positioning in GPSEST are given in the top row of the two figures. The left bars for each day represent the RMS errors corresponding to the data screened with LEOKIN, the right bars to those for the data screened with MAUPRP.

The two different screening procedures are based on rather different principles and exclude possibly different observations. Therefore, the kinematic point positioning in GPSEST is based on different observations. The total number of observations for one day of 30-second data is about 23,000. The difference between the number of observations used in the procedure with LEOKIN and in the procedure with MAUPRP is provided in the bottom line of Figures 6.104 and 6.105. A positive number means that more observations passed the screening with LEOKIN than the screening with MAUPRP, a negative number means that LEOKIN removed more observations than MAUPRP.

The performance is different for the eight stations. The stations ALBH (Figure 6.104(a)), ALGO (Figure 6.104(b)), ZWEN (Figure 6.104(d)), and ZIMM (Figure 6.105(b)) show a stable RMS for all

days and the RMS errors for both procedures are nearly the same for all days. For the station ZIMM MAUPRP removed more observations, for all other stations LEOKIN removed more observations.

There are three days for BRAZ (Figure 6.104(c)) with big RMS errors (43.5 cm, 53.7 cm, 169.6 cm) for the point positioning procedure in GPSEST, but only for data screened with MAUPRP. The RMS errors of the point positioning for BRAZ (for both procedures) are larger for the other seven days than for the other stations considered, but they have all the same size (two to three centimeters). The point positioning for station MAW1 (Figure 6.105(a)) has unusually big RMS errors for both procedures for doy 056. For doy 066 the data screened by LEOKIN gives rise to a three times larger RMS error for the point positioning than for the screening with MAUPRP.

The stations FAIR (Figure 6.105(c)) and MALI (Figure 6.105(d)) are exceptions (observe the differences in scale). For FAIR three days (056, 066, and 069) have a big RMS when using data screened by MAUPRP. For days 059, 066, and 067 no solution was possible using the data screened by LEOKIN due to too many ambiguities set up during the day. The differences in the number of observations used for the point positioning is quite large for the days 055 to 062. On these days the screening procedure in MAUPRP deleted about 50% of the observations and therefore the differences to the data screened by LEOKIN are as large as can be seen in Figure 6.105(c) (bottom). MALI has three to four times larger RMS errors for the point positioning with data screened by LEOKIN. This means that the screening algorithm in LEOKIN did not find the observations responsible for the deterioration of the point positioning.

Figure 6.106(a) shows the mean RMS errors for all stations for one particular day. The large values for some days for the MAUPRP procedure are due to individual bad stations deteriorating this mean value. Figure 6.106(b) shows the mean differences between the observations used for the different point positioning runs in GPSEST. The RMS errors show that on average the data screened by LEOKIN have a better quality. The number of observations left after the screening is about the same for both procedures.

Currently the LEOKIN procedure has the problem, that for few stations too many ambiguities are set up, because a new ambiguity is set up after each "bad" phase-difference identified between successive observations to a particular satellite (Section 4.4.2). As LEOKIN analyzes only pairs of successive phase observations it cannot decide whether the problem encountered is caused by an outlier or a cycle slip. MAUPRP can bridge gaps of a few epochs and is therefore in a position to better identify the nature of a bad phase-difference.

The LEOKIN procedure has the advantage that the code and phase observations are screened in one and the same procedure. Applications requiring screened code and phase observations may benefit from this feature.

Extended studies on longer time series of data may show, which of the two programs, LEOKIN and MAUPRP, better fits the requirements of zero-difference data cleaning. A combination of the advantages of both programs may lead to a very efficient and robust zero-difference data cleaning tool.

The results presented above are encouraging and most promising. One should consider that MAUPRP is an "old established" program (it was created in 1990/91 in preparation of the CODE participation in the IGS, but the zero-difference part was only realized in 2001). The application of LEOKIN to data screening was only a by-product of this general investigation. We believe that with an investment of about 0.5 person years LEOKIN could be used as the general purpose zero-difference screening program with a better performance than both, the currently available MAUPRP and LEOKIN realizations.

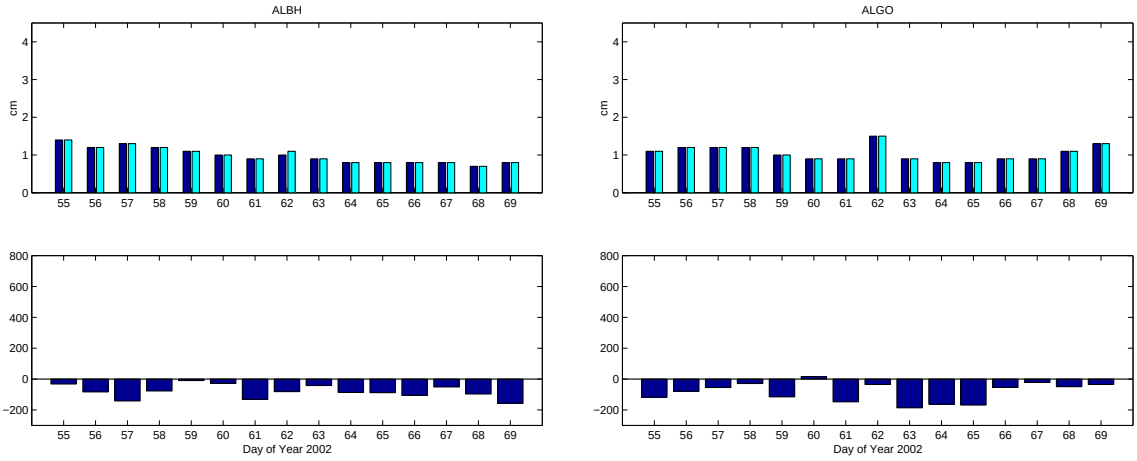

(a) Albert Head, Canada, North America.

(b) Algonquin, Canada, North America.

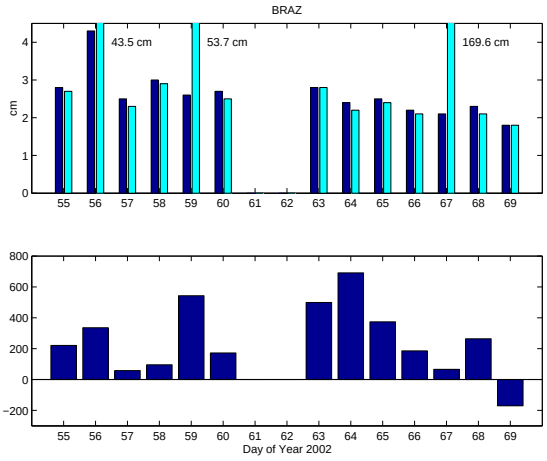

(c) Brasilia, Brazil, South America.

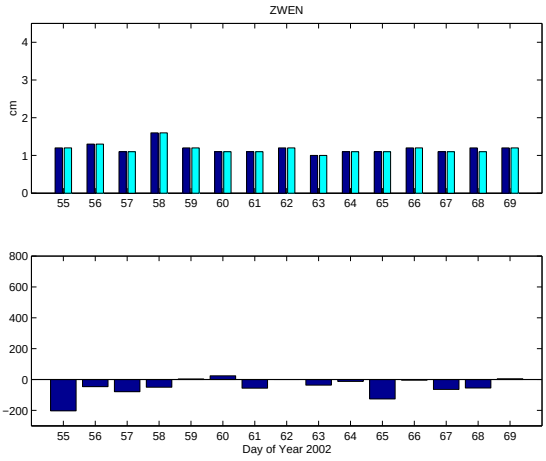

(d) Zwenigorod, Russia, Asia.

Figure 6.104: Top: RMS errors for kinematic positioning in GPSEST after screening with LEOKIN (left bar) and MAUPRP (right bar); Bottom: Difference in number of observations used for positioning, LEOKIN minus MAUPRP.

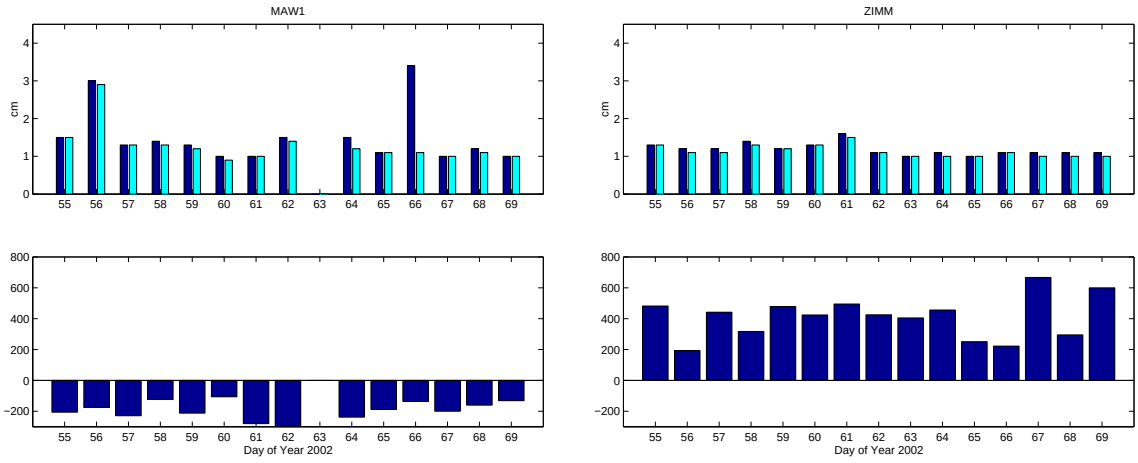

(a) Mawson, Antarctica.

(b) Zimmerwald, Switzerland, Europe.

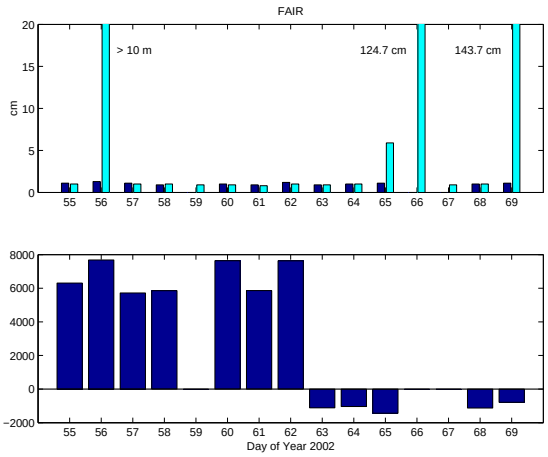

(c) Gilmore Creek Observatory, Fairbanks, Alaska, USA, North America.

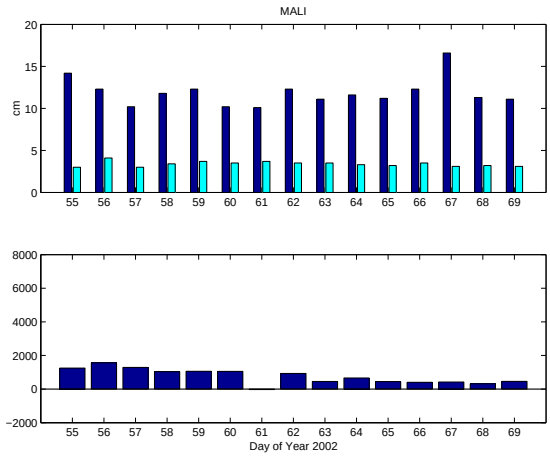

(d) Malindi, Kenya, Africa.

Figure 6.105: Top: RMS errors for kinematic positioning in GPSEST after screening with LEOKIN (left bar) and MAUPRP (right bar); Bottom: Difference in number of observations used for positioning, LEOKIN minus MAUPRP.

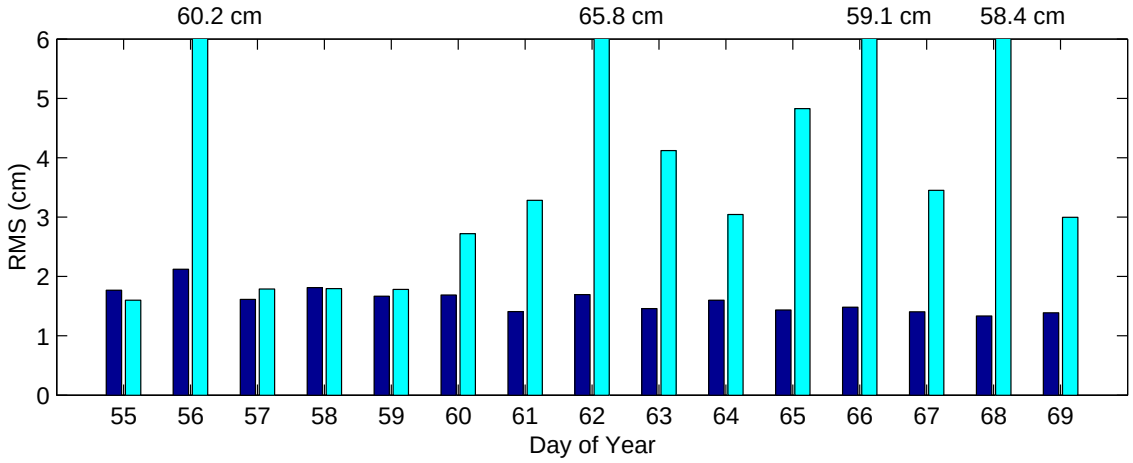

(a) Mean RMS errors of point positioning for all stations for one day, left bar: LEOKIN, right bar: MAUPRP.

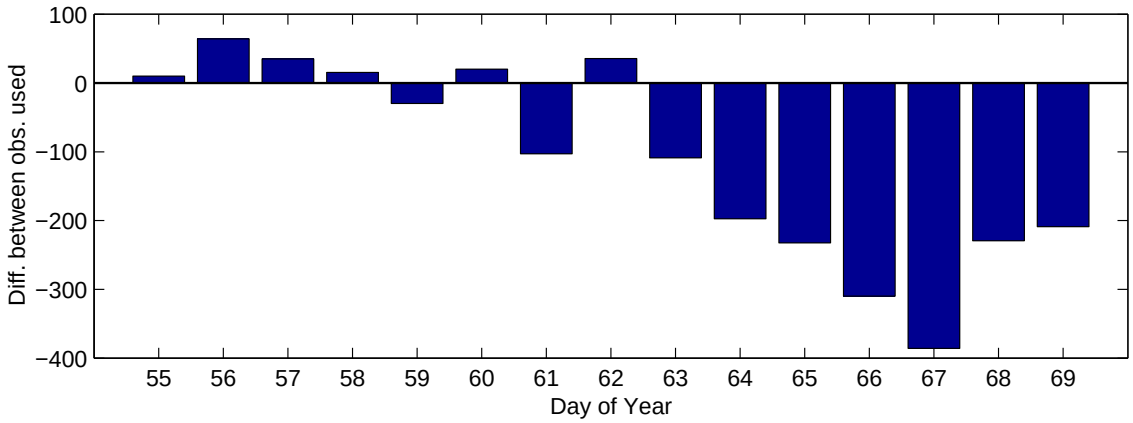

(b) Mean difference of number of observations used for the kinematic positioning in GPSEST, LEOKIN minus MAUPRP.

Figure 6.106: Doy 055 to 069/2002, data screening differences.

7. Summary and Outlook

The main part of this work dealt with the development and evaluation of efficient methods for precise orbit determination of LEOs. A kinematic approach using GPS zero-difference observations was developed (program LEOKIN) and a procedure for generation of dynamic and reduced-dynamic orbits was presented (program SATORB). The procedures have been tested using long GPS data series gathered by two LEO satellites, namely CHAMP and SAC-C.

An external comparison was available for the time interval of the eleven days of the IGS CHAMP test campaign (May 20 to 30, 2001). The orbit solution generated at the Technical University of Munich (TUM), Germany, using the Bernese GPS Software was used for this purpose. The TUM-solution is believed to be one of the best solutions contributing to the IGS test campaign. Comparisons with this solution showed that both our best kinematic trajectory and a post-fit reduced-dynamic orbit based on this kinematic solution compare within an RMS error per coordinate (of a Helmert transformation) of about 10 cm with the TUM-solutions. This indicates that LEO orbits with a quality of about 10 cm result from our analyses. The goal of developing efficient methods for precise orbit determination of LEOs is therefore achieved with the zero-difference kinematic point positioning procedure in LEOKIN and the program SATORB to generate reduced-dynamic orbits. It is worth mentioning that the procedure, when using only code observations as input, results in reduced-dynamic orbits with a quality of already 30 cm RMS.

The kinematic approach in LEOKIN is an epoch-by-epoch procedure using code observations and differences between phase observations from subsequent epochs. We are using phase-differences between epochs in order to eliminate the initial phase ambiguities from the processing. This step significantly reduces the required computer resources. The epoch-by-epoch positions determined from code observations and position-differences determined from phase-difference observations are combined to define a kinematic trajectory of the LEO.

It is, however, a disadvantage of the procedure that the mathematical correlations between subsequent phase-difference observations are not taken into account. The solution is therefore not completely correct from the statistical point of view. It is, however, a good approximation and we have shown that our results are within a decimeter (RMS per coordinate) to statistical correct solutions.

The method for kinematic point positioning leads to interrupts when a data gap occurs or when “bad” phase observations corrupt a solution of a particular epoch-difference. At the epochs with interrupts a jump in the kinematic trajectory may occur because the sequences before and after the interrupt (internally connected by the phase measurement) may have a different absolute definition given by the code positions. The code positions have an accuracy corresponding to the GPS code observation (0.3 to 1 meter) and therefore the magnitude of these jumps between the sequences may reach in the worst cases up to half a meter (for very short data spans). These jumps cannot be avoided when using our kinematic approach for the orbit determination of a LEO. The number can, however, be minimized by an elaborate screening procedure developed for the kinematic approach.

This screening procedure makes use of a priori information about the orbit of the LEO. This a priori

orbit is a reduced-dynamic orbit generated with the SATORB program using positions from LEOKIN as observations. The data screening in LEOKIN heavily depends on the quality of the reduced-dynamic orbit. The better the orbit the more reliable the pre-screening of the data.

Two procedures for producing a reliable and good enough reduced-dynamic orbit serving as a priori orbit were studied. The first procedure uses only code observations and positions for the generation of the reduced-dynamic orbits (APO set C). The second procedure uses combined positions derived from code and phase observations to generate the reduced-dynamic orbits (APO set P). Both procedures are reliable and useful for the kinematic point positioning in LEOKIN. The computation of the orbits for APO set C is slightly less time consuming than the alternative procedure due to the use of only one observation type. Nevertheless, the procedure for APO set P is better and more reliable. It is not as sensitive to data problems which may remain in the code-derived positions: The code positions are deweighted relative to the phase position-differences by a factor 100 (on top of $w_c : w_p = 2 : 100^2$) for the combination and therefore these problems are smoothed for the generation of the reduced-dynamic orbit. The accuracy of the reduced-dynamic orbits of APO set P is about 15 cm RMS error (Helmert transformation to best possible orbits) and that of the reduced-dynamic orbits of APO set C is about 30 cm RMS.

The pre-screening algorithm depends not only on the quality of the a priori orbit. Different options may be selected and have to be adapted to the quality of the GPS data processed from different satellites. An option which is central is the threshold value β for the outlier rejection. Due to the dependency of the pre-screening algorithm on the quality of the a priori orbit we have provided the possibility to use a large variety of threshold values β. We believed that this would help in the case of a bad a priori orbit to avoid rejecting observations erroneously flagged as outliers. There was hope that "moderately bad" observations could be recognized and removed in the least squares adjustment step. The studies have shown, however, that the β-value has to be lower than six. If we use a larger value for β the pre-processing of the data (consisting of the pre-screening and the following iterative least squares adjustment step) does not work properly. The pre-screening algorithm is much more robust than the least squares adjustment step to find outliers because only the receiver clock correction has to be estimated whereas the position is fixed to its a priori value. In the least squares adjustment step the degree of freedom is very small due to the epoch-wise processing and the often quite low number of tracked satellites.

The question whether an elevation-dependent weighting should be used for the processing of GPS LEO data can be answered for CHAMP. These results have shown that there are problems with code observations at low elevation angles disturbing the kinematic solution (multipath effects). The comparison of the code positioning with and without elevation-dependent weighting clearly shows that the elevation-dependent weighting model is appropriate and has to be used for the code observations. No clear answer can be given concerning the weighting of code observations for SAC-C. The code positions are of the same quality for the solutions with and without weighting.

The BlackJack GPS receiver on-board CHAMP tracks up to ten satellites simultaneously since March 5, 2002. The data performance has become better shortly after this change of the receiver software. The number of data gaps is reduced and the number of epochs with fewer than five tracked satellites has decreased significantly. The resulting kinematic trajectories show therefore fewer interrupts due to missing phase position-differences and the outlier rejection is very reliable and robust.

The BlackJack GPS receiver on-board SAC-C performs slightly worse than the CHAMP receiver. During some time intervals the receiver has, however, tracked up to twelve satellites simultaneously. Today, the SAC-C receiver tracks only up to eight satellites (status April 10, 2003). The code observations are not as much affected by multipath as in the case of CHAMP, but in general the observation quality is worse. Comparing the kinematic code-only positions with reduced-dynamic orbits it can be seen that the code positions of SAC-C have a lower quality than the corresponding kinematic code-only positions

from CHAMP.

The GPS antennas on-board the LEOs track partially below the local horizon of the satellite. The question arose whether it makes sense to use this observation information. For CHAMP this question does not matter because the receiver does no longer track satellites below the local horizon. For SAC-C the situation is different even though the amount of observations tracked below the local horizon today is only of the order of one to two percent (of all observations). The low-elevation observations do not seem to improve the kinematic point positioning result. Therefore we recommend to reject them.

We used different input data for our kinematic point positioning procedure in LEOKIN in order to study the impact of different information about GPS orbits and clock corrections on the kinematic result. We used either products (GPS orbits and clock corrections) from the Rapid processing at CODE or products from the Final processing at CODE. Differences of a few centimeters result when exchanging the input data, because the 30-second clock corrections were generated by two different procedures and the clock corrections associated with the CODE Rapid orbits are of slightly lower quality. The differences between the results using either CODE Rapid or CODE Final products for the kinematic point positioning in LEOKIN are mainly caused by the clock correction quality.

The official IGS/GPS clock products are 5-minute clock corrections available from each of the eight analysis centers and as a combined IGS product. Here we used normal 30-second clock corrections generated by our own procedures (interpolated to 10-second sampling) for the kinematic positioning of the LEOs. We also answered the question whether the officially available IGS clock corrections would be sufficiently accurate for use in our LEOKIN procedure. For these tests the 5-minute clock corrections are linearly interpolated to the 10-second observation epochs. The results are promising. We conclude that the 5-minute clock corrections can be used for our kinematic point positioning procedure in LEOKIN when the accuracy requirements are of the order of a few decimeters. If only code observations are processed in LEOKIN, the quality difference in the results is hardly noticeable when using the 5-minute clock corrections instead of the 30-second clock corrections. When using phase observations differences result in comparison (Helmert transformation) to our best possible solution with an RMS error of the order of a decimeter.

The program SATORB was used for the generation of dynamic and reduced-dynamic LEO orbits. The reduced-dynamic orbits serving as a priori orbits for the pre-screening of the observations for the kinematic point positioning are one output used from SATORB. In addition we have produced reduced-dynamic orbits using the code positions and phase position-differences of the best possible kinematic solution as independent observation types in SATORB. These reduced-dynamic orbits are the best orbits we can generate with our LEOKIN and SATORB procedures.

Additional studies focussed on the impact of different Earth gravity field models for the dynamic and reduced-dynamic orbit modeling. We performed these tests with different observation types as input in SATORB. On one hand, we used combined kinematic positions and, on the other hand, the two observation types of code positions and phase position-differences. We have seen that for SAC-C it makes no difference which of the Earth gravity models is used. The height of SAC-C is about 300 km higher (702 km) than that of CHAMP (350 to 400 km). The gravity models considered seem to be accurate enough at the altitude of SAC-C. For CHAMP this is different. We recognized significant differences when using different gravity field models. The main advantage of using “better” gravity models resides in a significant reduction of the number of pseudo-stochastic pulses which are required to absorb (among other) the deficiencies of the a priori gravity model. With a good gravity field model the use of code-derived positions and phase-derived position-differences as pseudo-observations in SATORB is superior to the use of the positions combined in LEOKIN (from the code and phase results). In the case, when the physical model is not as good, (e.g., when we use an older gravity field model which does not include

CHAMP data) it is better to use the combined positions from LEOKIN as input for the reduced-dynamic orbit generation. The results are better than in the case of using, separately, code positions and phase position-differences as input. The reason is that the combined positions are computed in LEOKIN without using any model information. The combined positions therefore follow the real force field. Positions and position-differences are, on the other hand, combined in SATORB based on the physical orbit model (which may be different from the "truth").

For CHAMP the choice of the gravity model is important for the dynamic and the reduced-dynamic orbit modeling. This is not surprising because the CHAMP mission is designed to contribute to the generation of a high-resolution gravity field model for the Earth.

For CHAMP there is an additional measurement type available, namely the readings of the accelerometer instrument on-board the satellite. This accelerometer measures the non-gravitational forces acting on the satellite. These measurements may be introduced into the orbit generation process instead of modeling the non-gravitational forces. The tests have shown that it is possible to use these accelerometer measurements in SATORB and that the dynamic orbit modeling results improve significantly compared to a dynamic orbit fit using the models for the non-gravitational forces. In addition, it would be technically possible to estimate the calibration parameter for the accelerometer measurements in SATORB (biases and scale factors). The calibration of an accelerometer is, however, a complex task. We therefore recommend to use the officially available values distributed together with the data.

CHAMP performs maneuvers to keep the satellite as close as possible to its nominal flight attitude. The attitude is changed by a sequence of velocity changes within a short time interval. In theory attitude changes should not affect the satellite's orbital velocity. In practice this may, however, happen. Stochastic pulses may be set up at the "main" maneuver epochs in order to compensate for possible small velocity changes. The success of such a procedure was, however, marginal. It has been proved to be preferable to set up stochastic pulses at pre-defined equidistant epochs.

Finally, we proposed a data screening procedure for zero-difference observations of a permanent GPS network. The pre-screening algorithm primarily developed for the screening of the zero-difference LEO GPS data in LEOKIN was slightly modified and then used for the cleaning of GPS observations of terrestrial stations in a permanent network. The results of the new procedure based on LEOKIN were compared to results gained with the zero-difference data cleaning tool MAUPRP of the Bernese GPS Software. The comparison suggests that a combination of the advantages of both procedures might lead to a reliable and efficient data cleaning tool for zero-difference observations. Additional tests and developments are required for this purpose.

The goal of this work was achieved with the development of the zero-difference kinematic procedure in LEOKIN and the reduced-dynamic procedure in SATORB. We will apply these efficient methods to other LEO satellite missions using GPS for POD, e.g., JASON-1, GRACE, and ICESat. This will increase the data basis and allow for an extended use of the developed procedures for other satellites with the goal of an extended evaluation of the achievable accuracy and reliability of the algorithms. It is planned to use the procedures on a routinely basis for the upcoming GOCE mission for the generation of rapidly available orbit information.

The kinematic trajectories for this work were computed using GPS orbits and clock corrections from the CODE Rapid or Final products. Due to their processing delay these products are not available for a near real-time processing of the LEO data. In order to evaluate the efficiency of the approach in a near real-time processing environment, the performance, quality, and accuracy of the procedure must be studied when using IGS products (Ultra-rapid products), which are available at the time of downloading LEO GPS data. This aspect may be of particular interest for atmospheric sounding missions such as

COSMIC.

Orbit results from other procedures and from independent observation types, e.g., SLR measurements, will be taken into account for comparisons in order to further improve our procedures.

Bibliography

Bancroft, S. (1985), An Algebraic Solution of the GPS Equations, *IEEE Transactions on Aerospace and Electronic Systems, AES–21*(6), 56–59.

Battrick, B. (ed.) (1999), *Gravity Field and Steady-state Ocean Circulation,* The Four Candidate Earth Explorer Core Missions, ESA Publications Division, ESTEC, The Netherlands, July 1999, ESA SP-1233(1).

Bertiger, W.I., and S. Wu (1996), Single Frequency GPS Orbit Determination For Low Earth Orbiters, in *Proceedings of the National Technical Meeting (ION): Technology and Operations: Partnerships for Success in Navigation,* pp. 463–473, JPL/Caltech.

Bertiger, W.I., Y.E. Bar-Sever, E.J. Christensen, E.S. Davis, J.R. Guinn, B.J. Haines, R.W. Ibanez-Meier, J.R. Lee, S.M. Lichten, W.G. Melbourne, R.J. Muellerschoen, T.N. Munson, Y. Vigue, S.C. Wu, T.P. Yunck, B.E. Schutz, P.A.M. Abusali, H.J. Rim, M.M. Watkins, and P. Willis (1994), GPS precise tracking of TOPEX/POSEIDON: Results and implications, *Journal of Geophysical Research, 99*(C12), 24449–24464.

Beutler, G. (2004), *Methods of Celestial Mechanics,* two volumes, Springer, Heidelberg, in preparation.

Beutler, G., W. Gurtner, M. Rothacher, U. Wild, and E. Frei (1990), Relative Static Positioning With the Global Positioning System: Basic Technical Considerations, in *Global Positioning System: An Overview*, IAG Symposium No. 102, pp. 1–23, ISBN 0-387-97266-8.

Beutler, G., E. Brockmann, W. Gurtner, U. Hugentobler, L. Mervart, M. Rothacher, and A. Verdun (1994), Extended orbit modeling techniques at the CODE processing center of the international GPS service for geodynamics (IGS): theory and initial results, *Manuscripta Geodaetica, 19,* 367–386.

Biancale, R., G. Balmino, J.-M. Lemoine, J.-C. Marty, B. Moynot, F. Barlier, P. Exertier, O. Laurain, P. Gegout, P. Schwintzer, C. Reigber, A. Bode, T. Gruber, R. Koenig, F.-H. Massmann, J.C. Raimondo, R. Schmidt, and S.Y. Zhu (2000), A New Global Earth's Gravity Field Model from Satellite Orbit Perturbations: GRIM5-S1, *Geophysical Research Letters, 27,* 3611–3614.

Bisnath, S.B., and R.B. Langley (2001), High-Precision Platform Positioning with a Single GPS Receiver, in *Paper presented at ION GPS 2001, 11-14 September 2001, Salt Lake City, Utah, USA.*

Bock, H., G. Beutler, S. Schaer, T.A. Springer, and M. Rothacher (2000), Processing aspects related to permanent GPS arrays, *Earth Planets Space, 52,* 657–662.

Bock, H., U. Hugentobler, and G. Beutler (2003), Kinematic and Dynamic Determination of Trajectories for low Earth Satellites Using GPS, in *First CHAMP Mission Results for Gravity, Magnetic and Atmospheric Studies,* edited by C. Reigber *et al.*, pp. 65–69, Springer, Berlin, ISBN 3-540-00206-5.

Boomkamp, H. (2002), IGS LEO position paper for IGS Workshop Ottawa 2002-04-02, in *Draft version, March 2002.*

Byun, S.H. (2003), Satellite orbit determination using triple-differenced GPS carrier phase in pure kinematic mode, *Journal of Geodesy, 76,* 569–585.

CDDIS (2002), IGS Data Center, CDDIS, Crustal Dynamics Data Information System, NASA, GSFC, USA, `ftp://cddisa.gsfc.nasa.gov`.

CHAMP (2002), CHAllenging Minisatellite Payload, GFZ, Potsdam, Germany, `http://op.gfz-potsdam.de/champ`.

Colombo, O.L. (1989), The Dynamics of Global Positioning Orbits and the Determination of Precise Ephemerides, *Journal of Geophysical Research, 94*(B7), 9167–9182.

Eanes, R. and S. Bettadpur (1995), The CSR 3.0 global ocean tide model, *Technical Memorandum, CSR-TM-95-06, Center for Space Research, University of Texas.*

Ferland, R. (2002), Reference Frame Working Group Technical Report, *IGS Technical Report 2000,* pp. 61–70.

Foerste, Ch. (2001), Preprocessing of accelerometer and attitude data, Meeting of CHAMP Project, 9 November 2001, GFZ Potsdam, Germany.

Fu, L., E.J. Christensen, C.A. Yamarone, M. Lefebvre, Y. Ménard, M. Dorrer, and P. Escudier (1994), TOPEX/POSEIDON mission overview, *Journal of Geophysical Research, 99*(C12), 24369–24381.

GFO (2002), Geosat Follow On, `http://gfo.bmbcoe.org/Gfo`.

GOCE (2002), Gravity field and steady-state Ocean Circulation Explorer, `http://www.esa.int/export/esaLP/goce.html`.

GRACE (2003), Gravity Recovery And Climate Experiment, `http://essp.gsfc.nasa.gov/grace` or `http://www.csr.utexas.edu/grace`.

Grejner-Brzezinska, D.A., S. Ge, J. Kwon, C.K. Shum, and C.Y. Zhao (2002), GPS/LEO Rapid Orbit Determination in Support of GPS Meteorology: Status and Future Plans, *Presented at the First CHAMP Science Meeting, 22 – 25 January, 2002, GFZ Potsdam, Germany.*

Grunwaldt, L. (2002), Personal communication, by e-mail.

Grunwaldt, L., and T.K. Meehan (2003), CHAMP Orbit and Gravity Instrument Status, in *First CHAMP Mission Results for Gravity, Magnetic and Atmospheric Studies,* edited by C. Reigber *et al.*, pp. 3–10, Springer, Berlin, ISBN 3-540-00206-5.

Gurtner, W. (1994), RINEX: The Receiver-Independent Exchange Format, *GPS World, 5*(7), 48–52.

Hedin, A.E. (1987), The MSIS-86 Thermospheric Model, *Journal of Geophysical Research, 92*(A5), 4649–4662.

Hedin, A.E. (1991), Extension of the MSIS-86 Thermosphere Model into the Middle and Lower Atmosphere, *Journal of Geophysical Research, 96*(A2), 1159–1172.

Heuberger, H. (1984), Performance of the GPS Package on LANDSAT5, *IEEE Position Location and Navigation Symposium.*

Hofmann-Wellenhof, B., H. Lichtenegger, and J. Collins (2001), *GPS: Theory and Practice*, Springer, ISBN 3-211-83534-2.

Hugentobler, U., S. Schaer, and P. Fridez (eds.) (2001), *Bernese GPS Software Version 4.2*, Astronomical Institute, University of Berne, Switzerland, February 2001.

Hugentobler, U., S. Schaer, T. A. Springer, G. Beutler, H. Bock, R. Dach, D. Ineichen, L. Mervart, M. Rothacher, U. Wild, A. Wiget, E. Brockmann, G. Weber, H. Habrich, and C. Boucher (2002), CODE IGS Analysis Center Technical Report 2000, in *IGS - 2000 Technical Reports*, edited by K. Gowey *et al.*, pp. 73–82, IGS Central Bureau, JPL, Pasadena, California, USA, November 2002.

ICD (2000), Interface Control Document - Navstar GPS Space Segment / Navigation User Interfaces, ICD-GPS-200C.

ICESat (2002), `http://icesat.gsfc.nasa.gov`.

IGSCB (2002), IGS Central Bureau, JPL, Pasadena, California, USA, `http://www.igscb.jpl.nasa.gov/` or `ftp://igscb.jpl.nasa.gov/`.

JASON-1 (2003), `http://www.aviso.oceanobs.com`.

Kleusberg, A., and P. J. G. Teunissen (eds.) (1996), *GPS for Geodesy*, Lectures Notes in Earth Sciences, Springer Verlag.

Koenig, R., G. Baustert, K.-H. Neumayer, H. Meixner, V. Schweiger, S. Zhu, and C. Reigber (2001), Precise orbit determination for CHAMP, *Paper presented at EGS XXVI General Assembly, Nice, France*.

Koenig, R., S. Zhu, C. Reigber, K.-H. Neumayer, H. Meixner, R. Galas, G. Baustert, and P. Schwintzer (2002), CHAMP Rapid Orbit Determination for GPS Atmospheric Limb Sounding, *Advances in Space Research*, *30*(2), 289–293.

Lang, K.R. (1992), *Astrophysical Data: Planets and Stars*, Springer-Verlag, New York, Berlin, Heidelberg.

Lemoine, F.G., S.C. Kenyon, J.K. Factor, R.G. Trimmer, N.K. Pavlis, D.S. Chinn, C.M. Cox, S.M. Klosko, S.B. Luthcke, M.H. Torrence, Y.M. Wang, R.G. Williamson, E.C. Pavlis, R.H. Rapp, and T.R. Olsen (1998), *The Development of the Joint NASA GSFC and the National Imagery and Mapping Agency (NIMA) Geopotential Model EGM96*, NASA/TP–1998-206861, National Aeronautics and Space Administration.

Loyer, S. (2000), Personal communication.

Martin, C., H. Lewis, and R. Walker (2001), Studying the MEO & GEO Space Debris Environments with the Integrated Debris Evolution Suite (IDES) Model, in *Proceedings of the Third European Conference on Space Debris, ESOC, Darmstadt, Germany*, pp. 351–354.

McCarthy, D.D. (ed.) (1996), *IERS Standards 1996*, Obs. de Paris, July 1996, IERS Technical Note 21.

Melbourne, W.G., E.S. Davis, C.B. Duncan, G.A. Hajj, K.R. Hardy, E.R. Kursinski, T.K. Meehan, L.E. Young, and T.P. Yunck (1994), *The Application of Spaceborne GPS to Atmospheric Limb Sounding and Global Change Monitoring*, Jet Propulsion Laboratory, April 1994, JPL Publication 94-18.

Ørsted (2002), `http://web.dmi.dk/projects/oersted`.

Perosanz, F., R. Bianchale, S. Loyer, J.-M. Lemoine, A. Perret, P. Touboul, B. Foulon, G. Pradels, L. Grunwaldt, T. Fayard, N. Vales, and M. Sarrailh (2003), On Board Evaluation of the STAR Accelerometer, in *First CHAMP Mission Results for Gravity, Magnetic and Atmospheric Studies*, edited by C. Reigber *et al.*, pp. 11–18, Springer, Berlin, ISBN 3-540-00206-5.

Press, W.H., S.A. Teukolsky, W.T. Vetterling, and B.P. Flannery (1992), *Numerical Recipes in Fortran 77*, Cambridge, University Press, Second Edition.

Reigber, C., H. Lühr, and P. Schwintzer (1998), Status of the CHAMP Mission, in *Towards an Integrated Global Geodetic Observing System (IGGOS)*, IAG Symposium No. 120, edited by R. Rummel *et al.*, pp. 63–65, Springer, Berlin, ISBN 3-540-67079-3.

Reigber, C., G. Balmino, P. Schwintzer, R. Biancale, A. Bode, J.-M. Lemoine, R. Koenig, S. Loyer, H. Neumayer, J.-C. Marty, F. Barthelmes, F. Perosanz, and S.Y. Zhu (2002), A high quality global gravity field model from CHAMP GPS tracking data and Accelerometry (EIGEN-1S), *Geophysical Research Letters*, *29*(14), doi:10.1029/2002GL015064.

Remondi, B.W. (1989), Extending the National Geodetic Survey Standard GPS Orbit Formats, *Technical Report NOS 133 NGS 46*, NOAA, USA.

Rothacher, M. (1992), *Orbits of Satellite Systems in Space Geodesy*, Vol. 46 of *Geodätisch-geophysikalische Arbeiten in der Schweiz*, Schweizerische Geodätische Kommission.

Rothacher, M., T. A. Springer, S. Schaer, and G. Beutler (1998), Processing Strategies for Regional GPS Networks, in *Advances in Positioning and Reference Frames*, IAG Symposium No. 118, edited by F. K. Brunner, pp. 93–100.

SAC-C (2002), `http://www.gsfc.nasa.gov/gsfc/service/gallery/fact_sheets/spacesci/sac-c.htm`.

Schaer, S. (1999), *Mapping and Predicting the Earth's Ionosphere Using the Global Positioning System*, Vol. 59 of *Geodätisch-geophysikalische Arbeiten in der Schweiz*, Schweizerische Geodätische Kommission.

Schutz, L.E., B.D. Tapley, P.A.M. Abusali, and H.J. Rim (1994), Dynamic orbit determination using GPS measurements from TOPEX/POSEIDON, *Geophysical Research Letters*, *21*(19), 2179–2182.

Seidelmann, P.K. (ed.) (1992), *Explanatory supplement to the Astronomical Almanach*, University Science Books, ISBN 0-935702-68-7.

Springer, T.A. (2000), *Modeling and Validating Orbits and Clocks Using the Global Positioning System*, Vol. 60 of *Geodätisch-geophysikalische Arbeiten in der Schweiz*, Schweizerische Geodätische Kommission.

Standish, E.M. (1990), The Observational Basis for JPL's DE200, the Planetary Ephemerides of the Astronomical Almanac, *Astronomy and Astrophysics, 233*, 252–271.

Sunsat (2002), `http://sunsat.ee.sun.ac.za`.

Svehla, D., and M. Rothacher (2002), Kinematic Orbit Determination of LEOs Based on Zero or Double-difference Algorithms Using Simulated and Real SST GPS Data, in *Vistas for Geodesy in the New Millenium*, IAG Symposium No. 125, pp. 322–328, ISBN 3-540-43454-2.

Tapley, B.D., M.M. Watkins, J.C. Ries, G.W. Davis, R.J. Eanes, S.R. Poole, H.J. Rim, B.E. Shutz, C.K. Shum, R.S. Nerem, F.J. Lerch, J.A. Marshall, S.M. Klosko, N.K. Pavlis, and R.G. Williamson (1996), The Joint Gravity Model-3, *Journal of Geophysical Research, 101*(B12), 28029–28049.

Tapley, B.D., D. Chambers, M. Cheng, M. Kim, S. Poole, and J.C. Ries (2000), The TEG-4 Gravity Field Model, 25th General Assembly, EGS, Nice, France, April 2000.

Test Campaign (2002), CHAMP Test Campaign, ESOC, Darmstadt, Germany, `http://nng.esoc.esa.de/gps/igsleo.html`.

Visser, P.N.A.M., and J. van den IJssel (2000), GPS-based precise orbit determination of the very low Earth-orbiting gravity mission GOCE, *Journal of Geodesy, 74*, 590–602.

Weber, R., and T.A. Springer (2002), Analysis Activities, in *IGS 2000 Annual Report*, pp. 14–17, IGS Central Bureau, JPL, Pasadena, California, USA.